Investigating the role of FUS, TDP-43 and DYNC1H1 mutations in the etiology of adult and childhood-onset motor neuron disease.

Ryan Liam Green

Doctor of Philosophy in Neuroscience

University of Sussex

August 2016

Acknowledgements

I wish to firstly thank Dr. Majid Hafezparast for the opportunity to study in his lab at Sussex University and develop my skills in scientific research. His guidance throughout my PhD has been invaluable and I would like to thank him for all his expert appraisals of my work throughout this time. Additionally, I appreciate all of his patience and advice given to me over the years, all of which I am very grateful for.

Secondly, I would like to thank all the laboratory group members of the Hafezparast lab. Specifically, Muruj Barri and Fabio Simoes for both their experience and productive discussions that have been enjoyable to be a part of.

I would also like to thank my family for their unbelievable support throughout my entire education, without them I would not be where I am today and for that I am eternally grateful.

Also I wish to thank all of my good friends that I am lucky to have for their continued encouragement and support.

Lastly I wish to acknowledge and thank the Hans and Marit Rausing scholarship for their funding contribution towards my PhD research.

Contents

Chapter 1- Introduction 18
1.0 Motor neuron disease 1
1.1 Amyotrophic lateral sclerosis (ALS) 1
1.2 An introduction to ALS 1
1.3 Adult onset motor neuron diseases and neuropathies 4
1.3.1 Motor neuron degeneration and associated clinical symptoms 6
1.3.2 ALS and frontotemporal dementia (FTD) 7
1.4 Treatment for ALS 8
1.5 The molecular genetics of ALS 9
1.5.1 Cu Zn Super-oxide dismutase 1 (*SOD1*) 13
1.5.2 Structure and function of SOD1 14
1.5.3 TAR DNA-binding protein (*TARDBP*) 15
1.5.4 Structure and function of TDP-43 15
1.5.5 TDP-43 dependent transcription and its autoregulation 18
1.5.6 TDP-43 and splicing of pre-mRNA 18
1.5.7 TDP-43 and micro RNA (miRNA) biogenesis 19
1.5.8Transport of mRNA granules via TDP-43 20
1.5.9 TDP-43 and the stress granule response 20
1.5.10 TDP-43 mouse models 21
1.5.11 Fused in sarcoma (*FUS*)/Translocated in liposarcoma (*TLS*) 24
1.5.12 Structure and function of FUS 24
1.5.13 FUS dependent transcription and autoregulation 27
1.5.14 RNA binding properties of FUS 28
1.5.15 FUS regulated splicing of pre-mRNA 28
1.5.16 The role of FUS in mRNA stability 29
1.5.17 FUS regulation of miRNA processing 29
1.5.18 Long non-coding RNA (lncRNAs) and nuclear paraspeckles 30
1.5.19 FUS associated mRNA transport 31
1.5.20 Response to DNA damage 31
1.5.21 FUS mouse models 32
1.5.22 Hexanucleotide repeat expansion in *C9orf72* 35
1.5.23 Structure and function of C9ORF72 35
2.0 ALS pathology 39
2.1 Protein aggregation 39
2.2 Defective RNA metabolism 40

2.3 TDP-43 mutations and aberrant axonal transport 44
2.4 Gliosis and excitotoxicity of motor neurons 44
2.5 Oxidative stress and its potential detriment in ALS 45
2.6 Mitochondrial damage in ALS 46
2.7 DNA damage and neurodegeneration 47
2.7.1 Nucleotide excision repair (NER) 47
2.7.2 Base excision repair (BER) 48
2.7.3 Single strand break repair (SSBR) 48
2.7.4 Double strand break repair (DSBR) 49
3.0 Childhood-onset motor neuron diseases 49
3.1 Spinal muscular atrophy (SMA) 49
3.3 Spinal muscular atrophy with lower extremity pre-dominance (SMA-LED) 52
3.2 Clinical characteristics of SMA-LED 53
3.4 Molecular genetics of SMA-LED 55
3.5 Molecular motors 55
3.5.1 Dynein families 56
3.5.2 The structure and function of the Dynein complex 57
3.5.3 The ATPase activity of Dynein 60
3.5.4 The dynein adaptor dynactin 60
3.5.5 Dynein-dynactin-microtubule structural organisation 62
3.5.6 The dynein adaptor BICD2 63
3.5.7 Other co-factors of cytoplasmic dynein 65
3.5.8 Dynein, axonal transport and microtubules 67
3.5.9Endocytic vesicle transport 67
3.6 Transport independent roles of dynein 68
3.6.1 Dynein at the Golgi apparatus 68
3.6.2 Cortical and nuclear dynein 71
3.7.1 R399G mutation 71
3.8 SMA-LED mouse models 72
3.8.1 *Loa* mouse model 72
3.8.2 *Cra1* mouse model 76
3.8.3 *Swl* mouse model 76
3.8.4 *Arl* mouse model 77
3.9 Research aims and objectives 78
Chapter 2- Materials and methods 80

4.0 Genotyping 81
4.1 DNA preparation 81
4.2 *Arl* genotyping 81
4.3 TDP-43 ^{F210I} genotyping 84
4.4 *Fus* ^{D520G} genotyping 88
4.5 DYNC1H1 ^{R399G} genotyping 90
5.0 Cell culture and tissue dissection 93
5.1 Dissection and culture of murine embryonic fibroblasts 93
5.2 Dissection and culture of cerebral cortex neurons 94
Biochemistry and cell assays 99
5.3 Preparation of cell lysates 101
5.4 SDS-PAGE 102
5.5 Immunoblotting of membranes and quantification 102
5.6 Co-immunoprecipitation 103
5.7 Sucrose density gradient analysis of dynein in DYNC1H1$^{R399G/R399G}$ mutants 104
5.8 Immunocytochemistry of primary cells 105
5.9 Dynein and Golgi apparatus co-localisation 106
5.10 Golgi polarisation assay in DYNC1H1^{R399G} mutants 107
5.11 The Azimuthal average quantification of Golgi polarisation 107
5.12 Endosomal trafficking in DYNC1H1 ^{R399G} human fibroblasts 108
5.13 Wound healing assay 109
5.14 Single strand break assays with topoisomerase I inhibitor camptothecin (CPT) 110
5.15 Transfection and UVA microirradiation assays 111
5.16 RNA polymerase I and II inhibition 112
5.17 Preparation and cryo-sectioning of murine brains 112
5.18 Cresyl violet staining 113
5.19 Propagation and preparation of plasmid DNA 114
5.19.1 Transformation of competent DH5-α E.coli 114
5.19.2 Midiprep of plasmid DNA 115
5.19.3 Maxiprep of plasmid DNA 115
5.20 Transfection of primary and immortalised cells 116
5.20.1 Electroporation of primary human fibroblasts 116
5.20.2 Transfection of cells using lipofection 117
5.21 Image acquisition and analysis 117

5.22 Matlab Image analysis 118
5.23 Quantification of western blots 119
5.23 Statistical analysis 119
Chapter 3- Investigating the roles of FUS and TDP-43 in DNA damage repair 120
6.0 Introduction 121
6.1 Results 122
6.1.1 Endogenous FUS re-localises to DNA lesions induced by UVA laser-induced oxidative damage. 122
6.1.2 TDP-43-GFP re-localises away from DNA lesions induced by UVA laser-induced oxidative damage 125
6.1.3 FUS re-localises to nuclear foci after camptothecin exposure in human fibroblasts 127
6.1.4 Camptothecin does not induce TDP-43 nuclear foci formation in human fibroblasts 129
6.1.5 Nuclear re-localisation of FUS after camptothecin treatment in murine wild-type and p.D520G mutant cortical neurons 131
6.1.6 TDP-43 forms nuclear foci localised with FUS after camptothecin exposure in wild-type murine cortical neurons 134
6.1.7 The FUS recruitment to nucleoli associated foci is inhibited by caffeine in murine wild-type cortical neurons 137
6.1.8 Nucleoli associated FUS foci are induced by polymerase II inhibition but not polymerase I inhibition 141
6.1.9 FUS foci formation is inhibited by dipyridamole in murine wild-type cortical neurons 145
6.10 Chapter 3 Summary 148
6.11 Chapter 3 discussion 149
6.11.1 FUS and TDP-43 re-localise after UVA microirradiation in A549 cells 149
6.11.2 FUS, but not TDP-43 form nuclear foci in human fibroblasts after topoisomerase I inhibition with CPT 151
6.11.3 FUS and TDP-43 form nuclear foci after CPT treatment in neurons 153
6.11.4 The recruitment of FUS to the nucleolus is inhibited by caffeine 154
6.11.5 RNA polymerase II inhibition produces nucleoli associated FUS foci 155
6.11.6 Formation of nucleoli associated FUS foci is inhibited by dipyridamole 157
Chapter 4- The DYNC1H1 ^{R399G} mutation in SMA-LED 161
7.0 Introduction 162

7.1 Results....164
7.1.1 Analysis of the dynein complex in p.R399G homozygous fibroblasts 164
7.1.2 The p.R399G mutation causes Golgi fragmentation in human fibroblasts 168
7.1.3 DYNC1H1-Halotag transfection restores a compact Golgi morphology in p. R399G homozygous fibroblasts 171
7.1.4 Investigating Golgi orientation and morphology in p.R399G mutants in migrating fibroblasts....174
7.1.5 The p.R399G mutation results in an increased interaction between dynein and Golgin 160 recapitulated with nocodazole treatment in wild-type fibroblasts 177
7.1.6 The p.R399G mutation in human fibroblasts results in a depletion of acetylated tubulin at Lysine 40....180
7.1.7 Elucidating the rate of α-tubulin deacetylation at Lysine 40 in p.R399G homozygous fibroblasts....184
7.1.8 Dynein depletion on the Golgi apparatus in p.R399G fibroblasts is not rescued by increasing acetylated tubulin 186
7.1.9 Increasing acetylated tubulin in p.R399G homozygous mutants rescues Golgi fragmentation....190
7.1.10 Increasing acetylated tubulin at Lysine 40 results in a down-regulation of golgin 160 192
7.1.11 The maturation of endosomes is impaired in p. R399G mutant fibroblasts 194
7.12 Chapter 4 summary 199
7.13 Chapter 4 Discussion 199
7.13.1The p.R399G mutation does not affect the dynein complex 199
7.13.2 The p.R399G mutation causes Golgi fragmentation and perturbed morphology during migration in human fibroblasts 201
7.13.3 The p.R399G mutation results in an increased interaction between golgin 160 and dynein.....202
7.13.4 The p.R399G mutation causes depletion of acetylation at Lys40 .203
7.13.5 Evaluating the rate of α-tubulin deacetylation in p.R399G homozygous fibroblasts....205
7.13.6 Homozygous p.R399G mutant fibroblasts show dynein depletion on the Golgi apparatus which cannot be rescued through increasing acetylated tubulin....206
7.13.7 Increasing microtubule acetylation through HDAC6 inhibition in p.R399G homozygous mutants rescues Golgi fragmentation....207
Increasing acetylation at Lysine 40 results in a down-regulation of golgin 160....210

The maturation of endosomes is impaired in p.R399G mutant fibroblasts 210
Chapter 5- Analysing the impact of the *Arl* mutation on cell migration and brain morphology 212
8.0 Introduction 213
8.1 Results 214
8.1.1 The *Arl*/+ mutation results in delayed cell migration in mouse embryonic fibroblasts. 214
8.1.2 The organisation of cortical layers is impaired in *Arl*/+ adult mice...217
8.1.3 The *Arl*/+ mutation causes a collapse of the third ventricle and condensation of the dentate gyrus. 220
8.1.4 The corpus callosum and dentate fascia brain regions are condensed in *Arl*/+ mice 224
8.1.5 Cortical organisation is disrupted in p4 *Arl*/+ mice in comparison with littermates 226
8.6 Chapter 5 summary 229
8.7 Chapter 5 discussion 229
8.7.1 The *Arl* mutation causes delayed cell migration in mouse embryonic fibroblasts 229
8.7.2 The organisation of cortical layers is impaired in *Arl*/+ mice 231
8.7.3 The *Arl*/+ mutation causes a collapse of the third ventricle and condensation of the dentate gyrus 232
8.7.4 The corpus callosum and the dentate fascia brain regions are condensed in *Arl*/+ mice 233
Chapter 6- Conclusion and general discussion 235
9.0 Conclusion 236
9.1 General discussion 237
References 242

Publications

Rulten, S.L. et al., 2013. PARP-1 dependent recruitment of the amyotrophic lateral sclerosis-associated protein FUS/TLS to sites of oxidative DNA damage. *Nucleic acids research*, pp.1–8.

List of figures and tables

Figures

1.1 The corticospinal tract……3

1.2 Proportion of genes associated with familial and sporadic ALS……10

1.3 TDP-43 protein structure……17

1.4 FUS protein structure……26

1.5 C9ORF72 isoforms……36

1.6 Roles of TDP-43 in RNA metabolism……42

1.7 Roles of FUS in RNA metabolism……...43

1.8 Example of lower limb wasting in SMA-LED……54

1.9 DHC diagram and schematic……...68

2.0 Dynactin diagram…….....62

2.1 Dynein and dynactin interaction……..64

2.2 Structure of the Golgi……70

2.3 DHC schematic with mutations……...75

2.4 *Arl* Genotyping……83

2.5 TDP-43 ^{F210I} PCR product……58

2.6 TDP-43 ^{F210I} Sequence and primers……...86

2.7 TDP-43 ^{F210I} genotyping primer specificity……87

2.8 FUS ^{D520G} PCR product and sequence……..89

2.9 FUS ^{D520G} genotyping Alw I restriction sites……..90

3.0 DYNC1H1 ^{R399G} genotyping……92

3.1 Plate positioning for wound healing assay……..110

3.2 Endogenous FUS re-localises to DNA lesions induced by UVA laser-induced oxidative damage……121

3.3 TDP-43-GFP re-localises away from DNA lesions induced by UVA laser-induced oxidative damage……126

3.4 FUS re-localises to nuclear foci after camptothecin exposure in human fibroblasts……128

3.5 Camptothecin does not induce TDP-43 nuclear foci formation in human fibroblasts……130

3.6 Nuclear re-localisation of FUS after camptothecin treatment in murine wild-type and p.D520G mutant cortical neurons……...133

3.7 TDP-43 forms nuclear foci localised with FUS after camptothecin exposure in wild-type murine cortical neurons……136

3.8 The FUS recruitment to nucleoli associated foci is inhibited by caffeine in murine wild-type cortical neurons……139

3.9 Nucleoli associated FUS foci are induced by polymerase II inhibition but not polymerase I inhibition…….....143

4.0 FUS foci formation is inhibited by dipyridamole in murine wild-type cortical neurons…….....147

4.1 PDE-CREB pathway……..…….159

4.2 Proposed responses of FUS and TDP-43 to DNA damage ...…….160

4.3 Analysis of the dynein complex in p.R399G homozygous fibroblasts……166

4.4 The p.R399G mutation causes Golgi fragmentation in human fibroblasts ……..166

4.5 DYNC1H1-Halotag transfection restores a compact Golgi morphology in p. R399G homozygous fibroblasts…….....172

4.6 Investigating Golgi orientation and morphology in p.R399G mutants in migrating fibroblasts……..176

4.7 The p.R399G mutation results in an increased interaction between dynein and Golgin 160 recapitulated with nocodazole treatment in wild-type fibroblasts ……179

4.8 The p.R399G mutation in human fibroblasts results in a depletion of acetylated tubulin at Lysine 40……182

4.9 Elucidating the rate of α-tubulin deacetylation at Lysine 40 in p.R399G homozygous fibroblasts……185

5.0 Dynein depletion on the Golgi apparatus in p.R399G fibroblasts is not rescued by increasing acetylated tubulin……..188

5.1 Increasing acetylated tubulin in p.R399G homozygous mutants rescues Golgi fragmentation……..191

5.2 Increasing acetylated tubulin at Lysine 40 results in a down-regulation of golgin 160……193

5.3 The maturation of endosomes is impaired in p. R399G mutant fibroblasts……196

5.4 p.R399G model……209

5.5 The *Arl*/+ mutation results in delayed cell migration in mouse embryonic fibroblasts……216

5.6 The organisation of cortical layers is impaired in *Arl*/+ adult mice……..219

5.7 The *Arl*/+ mutation causes a collapse of the third ventricle and condensation of the dentate gyrus……...222

5.8 The corpus callosum and dentate fascia brain regions are condensed in *Arl*/+ mice……...225

5.9 Cortical organisation in *Arl*/+ littermates……..228

Tables

1.1 Adult onset motor neuron diseases and neuropathies……4

1.2 Main mutated genes in ALS……11

1.3 Mouse models of TDP-43……22

1.4 FUS mouse models……...34

1.5 The immunoreactivity of protein aggregates in ALS……41

1.6 Childhood onset motor neuron diseases……...51

1.7 Co-factors of cytoplasmic dynein……66

1.8 Key Golgi proteins……70

1.9 DYNC1H1 mutations in SMA-LED……..74

2.0 Human fibroblast / Mouse embryonic fibroblast media……96

2.1 Cortical neurobasal media……96

2.2 Triturating solution (50 ml)……96

2.3 Tissue culture and lab plastics……..97

2.4 Tissue culture and lab glassware……98

2.5 Primary Antibodies……99

2.6 Secondary antibodies……100

2.7 Antibiotics used for transformation……...114

Abbreviations used in this study

ADHD	Attention deficit hyperactivity disorder
ALS FTD	ALS frontotemporal dementia
ALS	Amyotrophic lateral sclerosis
ANOVA	Analysis of variance
ATM	Ataxia telangiectasia mutated
ATP	Adenosine triphosphate
ATR	ATM-Rad3-related
BER	Base excision repair
BICD2	Bicaudal D2
BSA	Bovine serum albumin
BVVL	Brown-Vialetto-Van Laere syndrome
C9orf72	Chromosome 9 Open Reading Frame 72
CLIP	Cross linking immunoprecipitation
CMT	Charcot-Marie-Tooth disease
CPT	Camptothecin
CTFR	Conductance Regulator Gene
DAPI	4' 6-diamidino-2-phenylindole
DENN	Differentially expressed in normal and neoplasia
DHC	Dynein heavy chain
DIC	Dynein intermediate chain
DLC	Dynein light chain
DLIC	Dynein light intermediate chain
DMSO	Dimethyl sulfoxide
DPBS	Dulbecco's phosphate-buffered saline
DRB	5 6-dichloro-1-beta-D-ribofuranosylbenzimidazole
DSBR	Double strand break repair
ECL	Enhanced chemiluminescence
EGF	Epidermal growth factor
fALS	Familial ALS
FDA	Food and drug administration
FUS	Fused in Sarcoma
GEF	Guanine nucleotide exchange factor
GFP	Green fluorescent protein
HIV-1	Human immunodeficiency virus 1
hnRNPs	Heterogeneous nuclear ribonucleoproteins
HSP	Hereditary spastic paraplegia
LB	Lysogeny broth
LIS1	Lissencephaly
LMN	Lower motor neuron
lncRNA	Long non-coding RNA
MCD	Malformations of cortical development
MEF	Mouse embryonic fibroblast
miRNA	Micro RNA
MMA	Monomelic amyotrophy

MMN	Multifocal motor neuropathy
MRC	Medical research council
mRNA	Messenger RNA
MTOC	Microtubule organising centre
NER	Nucleotide excision repair
NudE	Nuclear distribution protein E
PBS	Phosphate buffer solution
PCR	Polymerase chain reaction
PDE	Phosphodiesterase
PFA	Paraformaldehyde
PIKK	Phosphatidylinositol 3-kinase-related kinases
PLS	Primary lateral sclerosis
PMA	Progressive muscular atrophy
PVDF	Polyvinylidene difluoride
RBP	RNA binding protein
RIPA	Radioimmunoprecipitation assay
RMM1	RNA recognition motif 1
RNA	Ribonucleic acid
ROS	Reactive oxidative species
sALS	Sporadic ALS
SDS	Sodium dodecyl sulfate
siRNA	Small interfering RNA
SMA-LED	Spinal muscular atrophy-lower extremity predominance
SMN	Survival motor neuron
snRNPs	Small nuclear ribonucleo proteins
SOD1	Superoxide dismutase 1
SSBR	Single strand break repair
TARDBP	TAR DNA binding protein
TCR	Transcription coupled excision repair
TLS	Translocated in liposacoma
UMN	Upper motor neuron

Abstract

Amyotrophic lateral sclerosis (ALS) and spinal muscular atrophy with lower extremity predominance (SMA-LED) represent two distinctive types of motor neuron disease, the first of which ALS manifests usually as an adult-onset, rapidly progressive, terminal neurodegenerative disorder. Conversely, SMA-LED a childhood-onset disease is mainly characterised by lower limb wasting and intermittently compounded by intellectual disability. Firstly, this thesis represents investigations in the roles of both Fused in Sarcoma (FUS) and TAR-DNA binding protein (TDP-43), two mutated proteins in ALS. Secondly, this thesis explores the implications of SMA-LED mutations in the cytoplasmic dynein heavy chain (DYNC1H1) to investigate disease pathogenesis.

Mutations found in RNA binding proteins FUS and TDP-43 are pathogenic in the adult-onset form of motor neuron disease ALS. These proteins are known to interact with DNA and it is suggested in the literature that FUS in particular has a protective role to repair DNA after lesions. FUS was shown to localise to sub-nuclear regions of UVA induced oxidative damage as well as nucleoli foci after induction of DNA single strand breaks through RNA polymerase II inhibition in mitotic cells and neurons. This re-localisation was inhibited by both caffeine and dipyridamole indicating FUS recruitment via phophodiesterases (PDEs). TDP-43 was found to vacate regions of oxidative damage and showed neuronal specific re-localisation to nucleoli in response to polymerase II inhibition that was not observed in mitotic cells.

These data for the first time show that both FUS and TDP-43 re-localise after DNA damage events. FUS is shown to respond to transcriptional stress perhaps to protect nascent RNA, whereas the expulsion of TDP-43 may indicate a role in transcription coupled excision repair or heterochromatin remodelling.

The SMA-LED autosomal dominant *DYNC1H1* mutation p.R399G causes lower limb weakness and muscle atrophy as well as cognitive impairment but the pathogenesis remains unknown. p.R399G mutant fibroblasts exhibit a fragmented Golgi apparatus phenotype rescuable by HDAC6 inhibition in conjunction with a reduced localisation of the dynein complex to the Golgi membranes. Furthermore, western blot and immunoprecipitation assays showed decreased acetylation in mutant fibroblasts as well as an increased interaction between dynein and golgin160 in p.R399G mutants. These data for the first time show that mutations in dynein can modulate acetylation of microtubules and caffect dynein recruitment to the Golgi apparatus. This suggests a novel mechanism in which perturbed dynein-mediated regulation of microtubule acetylation and dynein-Golgi interaction underpin SMA-LED.

Finally, the *Dync1h1* mutant *Arl* SMA-LED mouse model recapitulates phenotypes of the human disease and presents with motor phenotypes. However, this mouse model is yet to be fully characterised and the extent of any aberrant brain development is unknown. Analysis of the model indicated defective cortical organisation in addition to defective cell migration seen in *Arl*/+ fibroblasts. Furthermore, collapse of the third ventricle and condensation of the corpus callosum was also observed in this model.

These data show that the *Arl* p.Trp1206Arg mutation in the tail domain of Dync1h1 results in defective cellular migration as well as gross morphological brain deficits that mirror malformation of cortical development (MCD) in patients with SMA-LED. This is likely related to microtubule instability, Golgi abnormalities or impaired force production of dynein leading to suppressed cell migration and neuronal arborisation.

Chapter 1- Introduction

1.0 Motor neuron disease

Motor neuron disease is a broad classification for a group of neurological diseases in which the deterioration of motor neurons results in an impairment of muscle innervation. The disease itself can manifest as either an adult onset or childhood onset condition in which both upper and lower motor neurons can be affected (see Figure 1.1). This predominantly results in muscle atrophy confounded by a multitude of other clinical presentations. Primarily, this thesis will focus on amyotrophic lateral sclerosis (ALS), an adult onset motor neuron disease and spinal muscular atrophy with lower extremity pre-dominance (SMA-LED) a type of congenital motor neuron disease.

1.1 Amyotrophic lateral sclerosis (ALS)

1.2 An introduction to ALS

Amyotrophic lateral sclerosis (OMIM#105400) is a progressive disease of the nervous system in which upper and lower motor neurons degenerate and become denervated (see Table 1.1). The word amyotrophic comes from the Greek word ‘amyotrophia’ which means ‘no muscle nourishment’. The word ‘lateral’ indicates the part of the spinal cord that becomes damaged and ‘sclerosis’ is the Greek word for ‘hard’ reflecting the scarring of the tissue (Morris 2015).The disease is also referred to as Lou Gehrig’s disease in the United States after the famous baseball player who suffered with the condition until 1941 (Morris 2015).

This neurological disease can be characterised by a rapid onset and fast progression of neurodegeneration typically occurring between 50 – 75 years of age (Laferriere & Polymenidou 2015). These severe progressing features of the disease include muscle atrophy, paralysis, and eventually respiratory failure leading to death (see Table 1.1). This occurs usually within five years of the onset of the disease and has an incidence of around 2 in every 100,000 people (Laferriere & Polymenidou 2015).

Figure 1.1

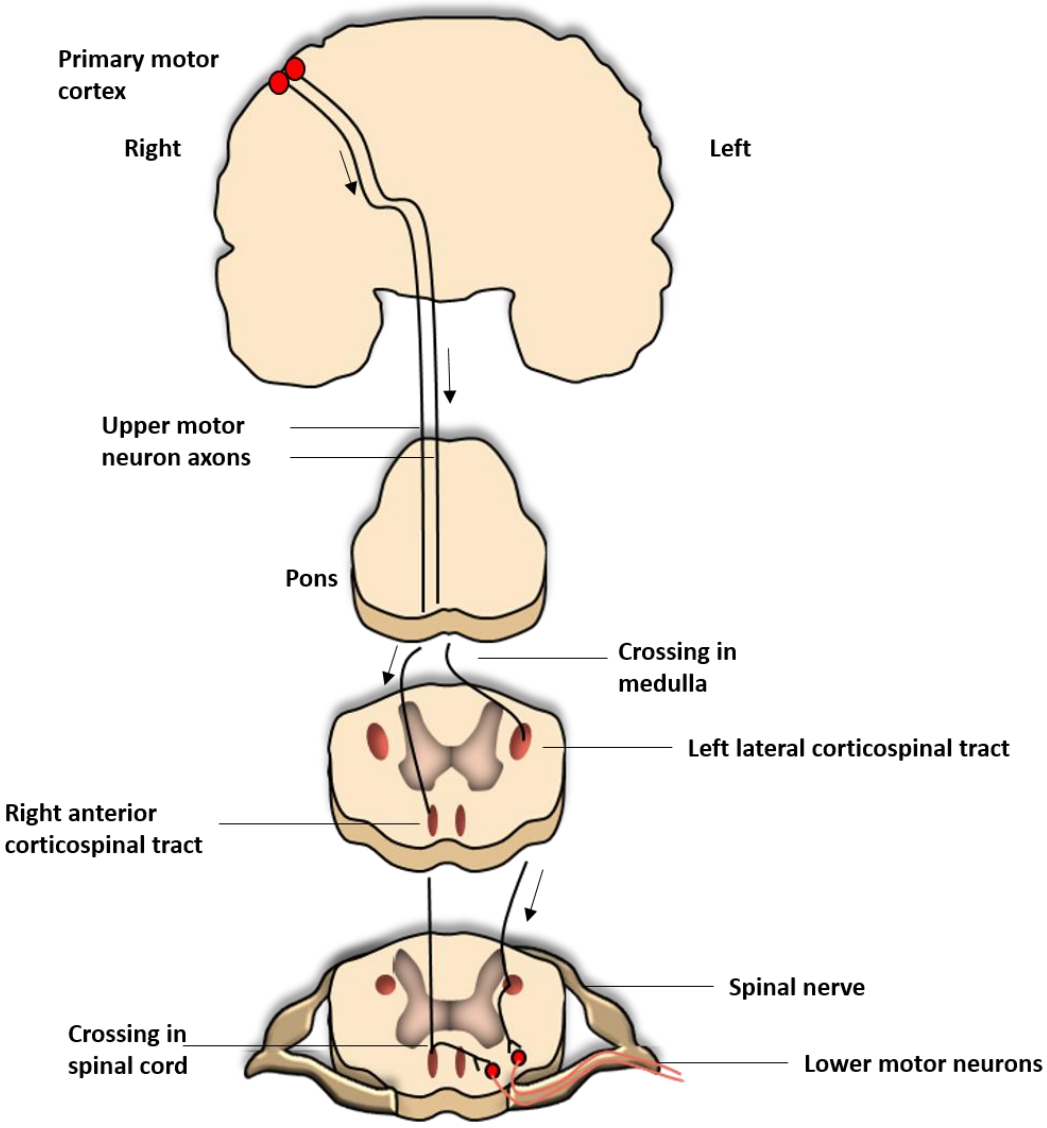

Figure 1.1- The anatomy of the corticospinal tract. Upper motor neurons originate in the primary motor cortex; in contrast lower motor neurons typically originate from the pons or lower lumbrosacral regions.

1.3 Adult onset motor neuron diseases and neuropathies

Table 1.1- Adult onset motor neuron diseases and neuropathies

Motor neuron disease	Disease characteristics and clinical features	References
ALS **ALS – Frontotemporal dementia (FTD)**	Upper and lower motor neuron involvement resulting in deterioration of the spinal cord, brainstem and motor cortex, affects 2 in every 100,000. **Upper motor neuron characteristics** • Hyperreflexia • Spasticity • Inability to communicate and detect sensory stimuli (dysphasia and agnosia) **Lower motor neuron characteristics** • Muscle weakness • Muscle cramps • Impaired or lack of reflexes • Muscle hypotonia and flaccid paralysis **FTD symptoms** • Change in personality • Apathy • Disinhibition • Hallucinations	(Morris 2015; Lattante et al. 2015)
Charcot-Marie-Tooth disease (CMT) **(Hereditary and sensory neuropathy)**	CMT is the most common hereditary neuromuscular neuropathy (40 in every 100,000). • Lower motor and sensory nerves affected. • Pre-dominance of distal limb wasting. • Muscle weakness and sensory loss.	(Pareyson & Marchesi 2009)
Distal hereditary motor neuropathy (dHMN) **(Spinal CMT)**	A neuropathy which resembles Charcot-Marie-Tooth (CMT) disease, but lacks sensory involvement.	(Luigetti et al. 2016; Devic et al. 2012)

Table 1.1- ***cont.***

Motor neuron disease	Disease characteristics and clinical features	References
Monomelic amyotrophy (MMA) **(Hirayama disease)**	Predominantly affects young men with no involvement of sensory neuron deterioration. The disease is non-progressive although it can lead to morbidity. • Onset of limb weakness and thinning restricted to either a single upper or lower limb. • Lower motor neuron deterioration only. • Typically worsens progressively over a 2-4 year period.	(Nalini et al. 2004; Vibha et al. 2015)
Multifocal motor neuropathy (MMN)	A neuropathy characterised by nerve conduction block through an immune response. • Lower motor neuron deterioration. • Distal limb progressive weakness. • Common involvement of upper extremities. • Muscle weakness without wasting. • No sensory involvement.	(Vlam et al. 2015; Muley & Parry 2012)
Primary lateral sclerosis (PLS)	A rare neurological disorder usually seen in the sixth decade of life with a slower rate of progression compared to ALS. • Degeneration of upper motor neurons with no lower motor neuron involvement. • Spastic paresis. • Usually develops in the lower extremities. • Progresses with pseudobulbar features.	(Agosta et al. 2014)
Progressive muscular atrophy (PMA)	Progressive muscular atrophy (or lower motor neuron disease) with sporadic onset in adulthood. • Lower motor neuron deterioration only. • Progressive muscle weakness. • Loss of anterior horn cells. • Similar to the progression of ALS although life expectancy can be longer.	(Bogucki et al. 2016; Visser et al. 2008)

Table 1.1 – Adult onset motor neuron diseases and neuropathies with associated motor neuron involvement and clinical features.

1.3.1 Motor neuron degeneration and associated clinical symptoms

The clinical presentation of ALS results from deterioration of either upper or lower motor neurons or both (see Figure 1.1). Upper motor neurons (UMN) originate in the primary motor cortex and span from the sylvian fissure to the cingulate gyrus. These neurons project a minimum of 12cm from cortical layer 5 in a caudal direction towards lower motor neurons (LMN). Lower motor neurons are organised in a columnar fashion spanning from the pons to the lumbrosacral region of the spinal cord over a distance of 55 cm and consist of mainly alpha motor neurons (Ravits 2014). Table 1.1 highlights the clinical symptoms associated with the loss of motor neurons from either pathway. Limb ALS refers to degeneration of neurons driving leg and arm function whereas bulbar ALS refers to primary degeneration of neurons controlling swallowing and speech.

ALS motor phenotypes can be categorised into five main observations, the first is the random and localised onset of the disease. The symptoms may first appear in the tongue or facial muscles, for example, (bulbar ALS) or in the limbs in a unilateral fashion (limb ALS). This highlights the appearance of a random focal onset characteristic of the disease (Ravits 2014). Secondly, the spread of the disease appears to occur in a contact-dependent proximal nature. This arises from the fact that the area where the motor symptoms arise tends to worsen over a course of time. Additionally, the deterioration of the motor neurons progresses into neighbouring regions, from one side of the body to the other (Ravits 2014). This suggests neuroanatomical spread of the disease from one region to another. Thirdly, whilst the initial symptoms are focal in either a UMN or LMN region or both, the deterioration is maximal in all of the affected areas where the disease

first begins. This suggests that the disease is triggered within a network encompassing both UMN's and LMN's (Ravits 2014).

The next important and fourth observation is that once the disease is progressing in a contiguous manner, the progression of the disease at the UMN and LMN levels seem disharmonious (Ravits 2014). For example, if the onset of disease occurs in one arm at a LMN level, the progression of the disease can spread to the other arm. In an instance when the disease begins at the UMN level for example the progression can spread from an arm to the leg on the same side of the body (Ravits 2014). Overall, this observation suggests the segregation and independent spread of motor neuron deterioration at UMN and LMN levels.

Lastly, although the degeneration of motor neurons and the muscles they innervate seem to progress at the anatomical level, the disease progression is likely related to specific disease kinetics. Studies of rate of disease progression have mainly focussed upon functional deficiencies rather than regional disease progression. The molecular underpinnings of diffusion of motor neuron loss and how this differs at both the UMN and LMN levels are still to be determined (Ravits 2014).

1.3.2 ALS and frontotemporal dementia (FTD)

Clinically reported incidences of psychiatric disturbance or dementia in association with clinical presentations of ALS were recognised in the early 20th century (Bak & Hodges 2001). Increased recognition of behavioural abnormalities in ALS patients began to gather pace in the 1990's (Van Langenhove et al. 2012).

FTD is a disease in which specific atrophy of the anterior and frontal lobes of the brain is accompanied with typical dementia. The prevalence of FTD is around 10 per 100,000 and clinically presents around 45 to 65 years of age (Sieben et al. 2012). It represents the second most common type of dementia second to Alzheimer's disease.

Currently it is estimated that ALS criteria are met in around 15% of FTD patients and similarly around 15% of ALS patients can present with dementia-like symptoms that agree with the FTD definition (Ringholz et al. 2005; Wheaton et al. 2007). Both ALS and FTD are recognised as an interrelated broad neuropathological disorder which are linked both genetically and pathologically (Ling et al. 2013).

1.4 Treatment for ALS

The only current available drug for ALS is rilluzole which is a treatment which only modestly improves life span of patients. Riluzole was approved by the FDA in 1995 for the treatment for ALS and remains to date the only treatment available. This drug has been found to have a multitude of varying effects in terms of neuronal survival across a dose range of 1-1000 μM. The greatest clinical efficacy of intracellular riluzole concentrations are observed at 5 μM. At this concentration riluzole is expected to depress neuronal hyper-excitability by decreasing the firing frequency of neurons through reducing Na^+ influx. The effects of riluzole has been comprehensively reviewed by Bellingham (Bellingham 2011).

1.5 The molecular genetics of ALS

The first description of ALS came in the 19th century in which Aran (1848), Cruveilhier (1852), and Charcot and Joffroy (1869) had all played a part. At this time the disease was thought to be non-heritable and it wasn't until 1955 when Kurland and Mulder suggested that the disease could have heritable elements (Kurland & Mulder 1955; Visser et al. 2008).

ALS today is recognised to be 10% familial ALS (fALS) and 90% deemed sporadic ALS (sALS) (Marangi & Traynor 2015). Of the 10% that is heritable around two thirds of the genes implicated have been discovered with the final third yet to be identified (see Figure 1.2). The so-called sporadic contribution to the disease is thought to be at least 23% attributable to genetics according to genome-wide studies (Keller et al. 2014). Table 1.2 outlines the major genes implicated in both fALS and sALS (also see 'ALSoD' database for a comprehensive list).

Figure 1.2

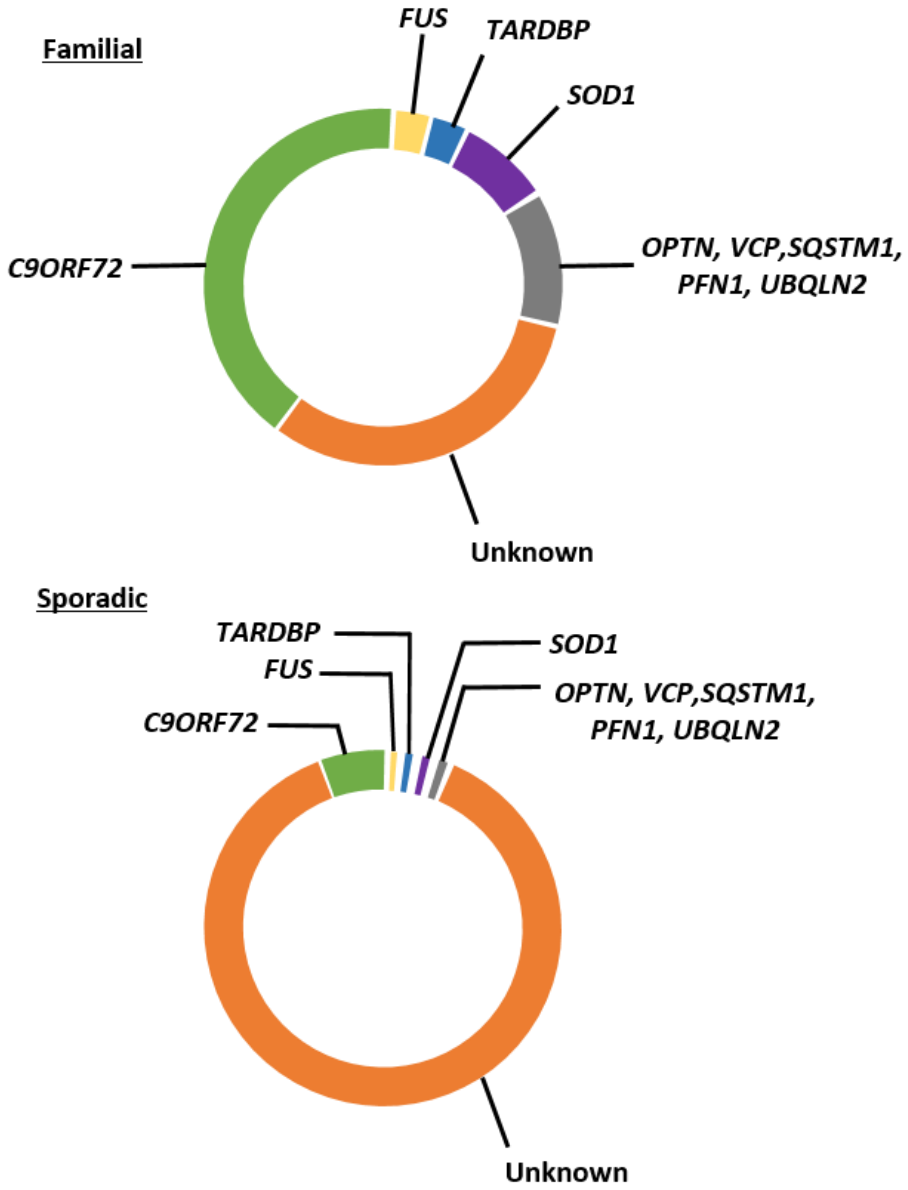

Figure 1.2- A schematic representation of the proportion of ALS associated genes with mutations in both familial and sporadic ALS.

Table 1.2- Main mutated genes in ALS

Gene	Protein	Function	fALS	sALS	MOI
SOD1	SOD	Antioxidant	fALS1	Yes	AD/AR
Alsin	ALS2	TRAF, ESCRT	f+jALS2	No	AR
SETX	Senetaxin	Replication	f+jALS4	No	AR
SPG11	Spatacsin	Unclear	f+jALS5	No	AR
FUS/TLS	FUS	RBP	f+jALS6	Yes	AD/AR
VAPB	VAMP	ERGP, TRAF	fALS8	No	AD
ANG	Angiogenin	RBP, angiogenesis	fALS9	Yes	AD
TARDBP	TDP-43	RBP	fALS10	Yes	AD
FIG4	FIG4	PRD,ERGP,TRAF	fALS11	Yes	AD
OPTN	Optineurin	PRD,ERGP,TRAF	fALS12	Yes	AD/AR
VCP	VCP	PRD	fALS14	No	AD
UBQLN2	Ubiquilin-2	PRD	f+jALS15	Yes	XR
SigMAR1	Sigma rec.1	ERGP	f+jALS16	No	AR
PFN1	Profilin	Actin polymerisation	fALS18	Yes	AD
ERBB4	ERBB4	TRAF	fALS19	No	AD
C9orf72	Unknown	TRAF	fALS	Yes	AD
CHMP2B	Unknown	PRD, TRAF,ESCRT	fALS	Yes	AD
DAO	D-AA oxidase	AA oxidation	fALS	No	AD
DCTN1	Dynactin	TRAF	fALS	Yes	AD
SQSTM1	P62	PRD	fALS	Yes	AD
hnRNPA1	hnRNPA1	RBP	fALS	Yes	NP
Erlin2	Erlin	ER lipid rafts	jALS	Yes	No
UNC13A	UNC13	Regulates transmitters	No	Yes	No

Table 1.2 ***Cont.***

Gene	Protein	Function	fALS	sALS	MOI
NEFH	Neurofilament	TRAF	No	Yes	AD
PRPH	Peripherin	TRAF	No	Yes	No
TAF15	TBP factor 15	RBP	No	Yes	AD
GRN	Progranulin	Cell growth regulator	No	Yes	No
EWSR1	EWSR1	RBP	No	Yes	No
ATXN2	Ataxin-2	Repeat expansion	No	Yes	AD
DJ1	DJ-1	Antioxidant	Yes	No	AR
TUBA4a	Tubulin	Cytoskeleton	Yes	No	AD

Table 1.2- Main mutated proteins found in ALS adapted from Finsterer and Burgunder, Hanagasi et al., and Smith (Finsterer & Burgunder 2014; Hanagasi et al. 2016; B. N. Smith et al. 2014). Abbreviations are as follows: TRAF: trafficking, ESCRT: endosomal sorting complexes required for transport, AA: amino acid, PRD: protein degradation, ERGP: ER-Golgi pathway, jALS: juvenile ALS, FTLD: fronto-temporal lobe degeneration, RBP: RNA binding protein, AD: autosomal dominant, AR: autosomal recessive, XR: x-linked recessive.

1.5.1 Cu Zn Super-oxide dismutase 1 (*SOD1*)

Linkage analysis provided the first common genetic factor contributing to fALS and alluded to the potential underlying pathogenesis of the disease. In 1993 dominant missense mutations were identified in the *SOD1* gene in fALS patients (Rosen et al. 1993). This gene codes for an enzyme which binds Cu and Zn and catalyses the reaction of O_2^- (a toxic anion) to O_2 and H_2O_2, this toxic H_2O_2 species is then neutralised by the catalase enzyme (Rosen et al. 1993; Kirkman & Gaetani 2007).

Overall data from population studies have revealed that mutations in *SOD1* account for about 1% of all sporadic cases of ALS and 12% of familial cases (Chiò et al. 2008). It is also important to note that over 100 mutations have been reported in *SOD1* and are presumed to contribute to the disease pathogenesis however, many of these mutations are lacking validation as causative through either statistics or mouse models (Andersen 2006).

The majority of *SOD1* mutations exhibit a high penetrance with an autosomal dominant mode of inheritance (Marangi & Traynor 2015). Despite this a D90A mutation has been identified in a Scandinavian population which exhibits recessive inheritance (Andersen et al. 1996). Only a small number of mutations can be shown to correlate with phenotypic presentations from a prognostic point of view. The A4V mutation is the most common in North America and represents a particularly lethal form of ALS in which patients die within a year of the onset of the disease (Cudkowicz et al. 1997).

1.5.2 Structure and function of SOD1

SOD1 is an enzyme found in the intermembrane space of mitochondria as well as both the nuclear and cytoplasmic compartments of eukaryortic cells. The protein consists of 153 residues (32-kDa) which homodimerise to form the functional enzyme (Valentine et al. 2005). Each subunit of SOD1 contains a copper and zinc binding region. The structure of the monomer is highly conserved between species and are structured centrally around a β-barrel. Each monomer contains two large loops which are structured regions of the protein termed the 'electrostatic' and 'zinc' loops that encompass the metal binding region of the protein (Valentine et al. 2005).

The function of SOD1 as previously alluded to is to convert superoxide ions to both oxygen and hydrogen peroxide with the interaction of both zinc and copper catalysing this conversion (Bunton-Stasyshyn et al. 2014; Zelko et al. 2002). The superoxide reactive oxygen species (ROS) at high levels are toxic and can affect many cellular processes (see oxidative stress) as well as cause DNA damage (Carrì et al. 2015). ROS are generated through oxygen metabolism and thus can be increased through high levels of cellular metabolism which is particularly elevated in motor neurons due to their size and function (Briese et al. 2005). Interestingly, in yeast only around 1% of SOD1 is needed to carry out this anti-oxidative role. This has led to other proposed functions of SOD1 including RNA metabolism, signalling, and as an endoplasmic reticulum (ER) stress sensor (Bunton-Stasyshyn et al. 2014).

1.5.3 TAR DNA-binding protein (*TARDBP*)

A major breakthrough in understanding the genetics and potential pathogenic mechanisms in ALS came from the discovery of TDP-43 (coded by *TARDBP*) positive cellular inclusions in 2006 (discussed in ALS pathology). This finding was swiftly followed by the discovery of mutations in *TARDBP* in 2008 in families with autosomal dominant ALS and FTD (Sreedharan et al. 2008; Chiò et al. 2010). TDP-43 is a protein which is involved in the processing of transcripts by binding to nascent pre-RNA molecules (see below) (Ratti & Buratti 2016).

Mutations found in *TARDBP* contribute to around 4% of fALS cases and a smaller number of sALS cases of around 1% (Chio et al. 2012; Marangi & Traynor 2015). Mutations in *TARDBP* are found worldwide with some regional variation, the A382T mutation is particularly prevalent in Sardinia perhaps due to a founder effect (Chiò et al. 2011). Overall there are 47 missense mutations and one truncating mutation that have currently been reported (Lattante et al. 2013).

1.5.4 Structure and function of TDP-43

TDP-43 encoded by the *TARDBP* gene is a 43 kDa protein comprised of 414 amino acids located on chromosome 1p36.2 (see Figure 1.3). This protein is ubiquitously expressed, highly conserved, and localises predominantly in the nucleus (Banks et al. 2008). Originally in 1995, it was first identified as a transcription factor responsible for regulating transcripts associated with human immunodeficiency virus type 1 (HIV-1) (Ou et al. 1995). Later in 2001, it was

shown to be a pre-messenger RNA (mRNA) splicing protein in relation to the cystic fibrosis transmembrane conductance regulator gene (CTFR) (Buratti et al. 2001). Additionally, it has been found to regulate the splicing of hundreds of other genes such as SMN which is later discussed (Lagier-Tourenne et al. 2010).

The *TARDBP* gene structurally consists of a total of six exons, the first of which is non-coding, with the remaining 5 exons responsible for encoding the protein. These regions show a high level of conservation of the amino sequence in many different species (Sreedharan et al. 2008). TDP-43 is part of the heterogeneous nuclear ribonucleoprotein family (hnRNP) (Krecic & Swanson 1999). It has an N-terminal domain which contains a nuclear localisation signal and a C-terminal domain consisting of a glycine rich region of the protein responsible for interactions with other proteins (Lukavsky et al. 2013). In between these regions exist the RRM1 and RRM2 domains responsible for binding RNA and DNA shown in Figure 1.3 (Warraich et al. 2010). Interestingly, the most homology was found across species in these regions suggesting that the binding of RNA and DNA between species is a highly specific process (Ayala et al. 2005). These RRM domains contain RNP1 and RNP2 regions which are required for the binding of TDP-43 to UG repeats specifically (Kuo et al. 2009). Additionally, TDP-43 contains both a nuclear localisation signal (NLS) and a nuclear export signal (NES) allowing it to be motile between the cytoplasmic and nuclear compartments (Warraich et al. 2010).

Figure 1.3

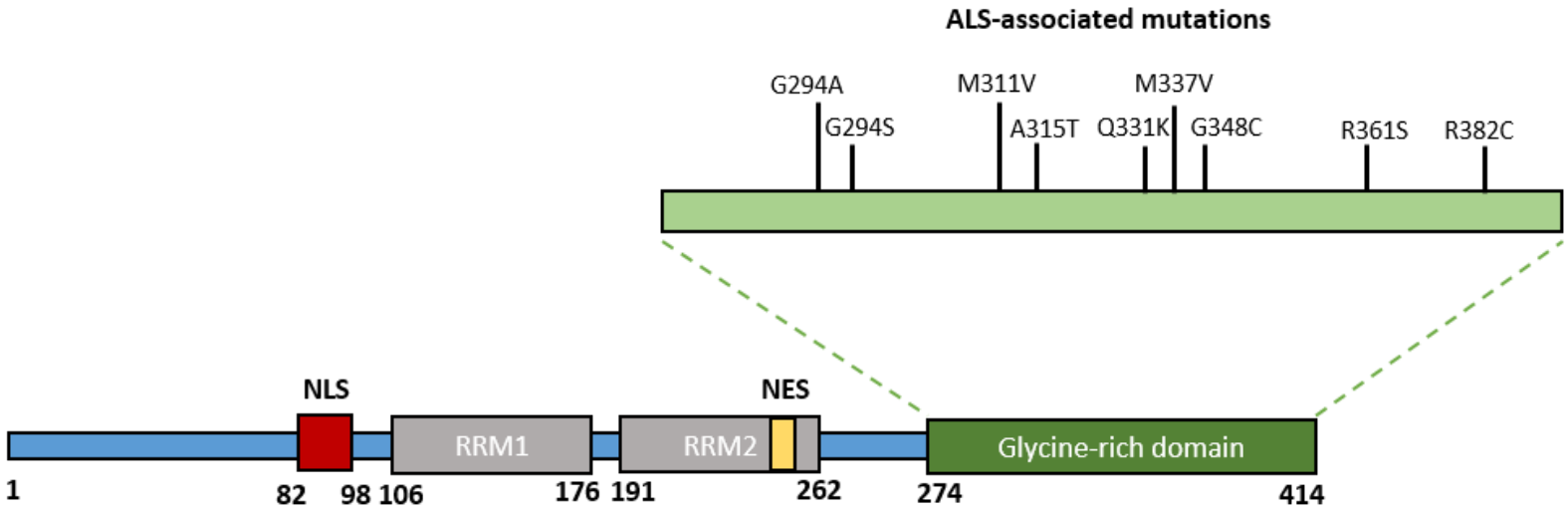

Figure 1.3- The functional regions of TDP-43. Importantly the glycine rich domain is a mutation 'hot-spot' in cases of familial ALS and is particularly important for protein-protein interactions. The nuclear localisation signal (NLS) and the nuclear export signal (NES) are the regions responsible for shuttling the protein between the nucleus and the cytoplasm. Figure adapted from (Lagier-Tourenne et al. 2010).

1.5.5 TDP-43 dependent transcription and its autoregulation

The functional roles of TDP-43 are diverse, as previously alluded to, TDP-43 has an important role in transcription. It has been found to bind regulatory DNA elements in both HIV-1 and a spermatogenesis-related gene in mice (SP-10) to negatively repress the production of transcripts (Ou et al. 1995; Acharya et al. 2006). Conversely, TDP-43 has also been found to localise to areas of transcriptionally active DNA (euchromatin) through immunofluorescence and *in situ* transcription assay techniques in mammalian neurons (Casafont et al. 2009). TDP-43 has many other direct targets highlighted by Ratti and Buratti with likely many more that will become apparent (Ratti & Buratti 2016). In addition to the ability of TDP-43 to target transcripts of other proteins, TDP-43 can also target its own. This type of *TARDBP* autoregulation enables the tight control of TDP-43 expression thus ensuring that the concentrations of the protein remain in a physiological range (Ayala et al. 2011). A recent study has shown that the depletion of TDP-43 results in altered expression across 273 proteins in SH-SY5Y cells, most of which were found to be involved in RNA processing (Štalekar et al. 2015).

1.5.6 TDP-43 and splicing of pre-mRNA

Another key role that TDP-43 plays in the processing of mRNA transcripts is splicing. This is a crucial process which removes introns (not in every case) from pre-RNA transcripts to facilitate the correct expression of genes. Short sequences that exist at intron-exon junctions enable a splicing code to be recognised by the spliceosome (Singh & Cooper 2012). This is a protein complex

comprised of small ribonucleoproteins (snRNPs) which interact with the introns whilst an orchestration of over 100 proteins facilitate the removal of the intron and joining of the exons (Singh & Cooper 2012). TDP-43 has been found to bind to many introns of pre-mRNAs and the knockdown of TDP-43 has been shown to cause splicing alterations in the striatum of mice as well as in the SH-SY5Y neuroblastoma cell line (Tollervey et al. 2011; Polymenidou et al. 2011)**.** Additionally, Tollervey indicates that many of the TDP-43 RNA binding targets are in fact non-coding RNA (ncRNA) which is becoming further implicated in neurological disease (Szafranski et al. 2015).

1.5.7 TDP-43 and micro RNA (miRNA) biogenesis

MiRNAs are short non-coding RNA molecules of around 20 nucleotides in length and play a vital role in the regulation of gene expression (Chekulaeva & Filipowicz 2009). These short sequences are generated from double stranded RNA containing a loop (pri-miRNAs) which are then processed by the Drosha complex (creating pre-miRNAs) in the nucleus and then the Dicer complex in the cytoplasm. This maturation then allows them to interact with the 3' untranslated region of their targets to prevent their translation (Kawahara & Mieda-Sato 2012). TDP-43 has been shown to be a component of the Drosha complex promoting its interaction with certain pri-miRNAs. In addition to this TDP-43 has also been shown to complex with Dicer to facilitate the processing of these specific pri-miRNAs (Kawahara & Mieda-Sato 2012). The altered expression of miRNAs has been identified in ALS, skeletal muscle from patients have been found to contain elevated levels of miR-23a (targets PGC1-α), miR-29b and miR-455 which have

been suggested to affect gene expression in mitochondria (Kye & Gonçalves 2014).

1.5.8Transport of mRNA granules via TDP-43

Granules refer to aggregates found in the cytoplasm comprised of RNA and RBP. These granules can contain multiple mRNA molecules as well as a diverse selection of RNA binding proteins and are trafficked in the cytoplasm (R. Smith et al. 2014). In neurons these granules can be trafficked in order to supply key transcripts to both dendrites and axons to be locally translated in these distal regions (R. Smith et al. 2014). TDP-43 was found to be associated with the 3' UTR's of many transcripts in human brain suggesting a role for transport or stability of mRNA (Tollervey et al. 2011). Further investigation has shown that TDP-43 is a main component of mRNA-RNP (mRNP) containing granules and is transported in an anterograde direction in neurons. The exact role that TDP-43 plays in this instance, however, is still unclear (Alami et al. 2014).

1.5.9 TDP-43 and the stress granule response

Stress granules are structures found in the cytoplasm comprised of mRNAs, the 40s subunit of ribosomes, and a myriad of more than thirty other proteins. As the name suggests they form under instances of environmental stressors such as hyperosmolarity or heat shock (Dewey et al. 2012). The stress granules are generated when the initiation step of translation is interrupted. TDP-43 has been found to be a main component of stress granules in many instances. The caveat here however, is that the localisation of TDP-43 to stress granules is dependent

upon the stressor as well as the cell (Dewey et al. 2012). Although the exact mechanisms of TDP-43 stress granule biology are unknown the RRM1 domain (residues 267-324) is thought to play a vital role in its localisation to stress granules (Dewey et al. 2011).

1.5.10 TDP-43 mouse models

There have been many murine models of TDP-43 that have attempted to model ALS with a spectrum of varied phenotypes (see Table 1.3). Mouse models of TDP-43 (like many other mouse models) and the generation of ALS phenotypes are dependent upon the promotor used for the expression of the transgene. The level of TDP-43 expression is likely to affect potential motor phenotypes. Many of the TDP-43 mouse models exhibit axonal phenotypes but only moderate loss of motor neurons is observed (McGoldrick et al. 2013). To analyse the phenotypic repercussions of the loss of function of TDP-43, knock-out mice have been developed. However, total loss of TDP-43 results in embryonic lethality indicating that it plays a crucial role in development (Sephton et al. 2010). Mice with one functional allele of the TARDBP gene do not show any reduction of protein level likely due to TDP-43 autoregulation (McGoldrick et al. 2013).

Promotor	Protein	Protein expression (fold)	Survival (weeks)	Motor phenotype	LMN degen.	UMN degen.	Cortex degen..	Axonal degen.	Gliosis path.	TDP-43 path.	CTFs	Reference
Hb9:Cre	MN depletion	0	40	Yes	60% loss	nd	nd	nd	Yes	nd	nd	(Wu et al. 2012)
mPrp	A315T	3	22	Yes	20% loss	Yes	nd	Yes	Yes	Yes	Yes	(Wegorzewska et al. 2009; Guo et al. 2012)
MPrp	WT	1.9	Not aff.	No	-	-	-	-	-	-	-	(Xu et al. 2010)
mPrp	WT	2.5	4-8	Yes	No	nd	nd	Yes	Yes	Yes	Yes	(Xu et al. 2010)
mPrp	M337V	1.9	Not aff.	No	-	-	-	-	-	-	-	(Wegorzewska et al. 2009)
mPrp	M337V	2.5	4	Yes	nd	nd	nd	Yes	Yes	Yes	Yes	(Y.-F. Xu et al. 2011)
mPrp	WT	3-4	nd	No	nd	nd	nd	nd	Yes	nd	nd	(Stallings et al. 2010)
mPrp	A315T	4	37.5	Yes	nd	nd	nd	nd	Yes	Yes	Yes	(Stallings et al. 2010)
Thy 1.2	WT	Males:3.6	nd	Yes	No	nd	nd	Yes	Yes	No	No	(Shan et al. 2010)
Thy 1.2	WT	Females:1.3	nd	Yes	No	nd	nd	nd	nd	No	No	(Shan et al. 2010)
Thy 1.2	WT	1.9	nd	Yes	nd	nd	nd	nd	nd	nd	nd	(Wils et al. 2010)
Thy 1.2	WT	3.8	27	Yes	10% loss	15% loss	nd	nd	Yes	Yes	nd	(Wils et al. 2010)
Thy 1.2	WT	5.1	4	Yes	25% loss	30% loss	nd	nd	Yes	Yes	Yes	(Wils et al. 2010)
CaMKII	WT	2	71	Yes	nd	nd	Yes	nd	Yes	Yes	Yes	(Tsai et al. 2010)
CaMKII	WT	0.8 (4 WKs)	nd	Yes	nd	Yes	Yes	nd	Yes	nd	nd	(Igaz et al. 2011)
CaMKII	ΔNLS	7.9 (4 WKs)	26	Yes	nd	Yes	Yes	Yes	Yes	Yes	nd	(Igaz et al. 2011)
CaMKIIα	WT	3	nd	nd	nd	nd	Yes	nd	Yes	Yes	nd	(Cannon et al. 2012)

Table 1.3- Mouse models of TDP-43

TDP-43 (BAC)	WT	3	nd	Yes	nd	nd	nd	No	Yes	nd	nd	(Swarup et al. 2011)
TDP-43 (BAC)	A315T	3	nd	Yes	nd	nd	nd	No	Yes	Yes	Yes	(Swarup et al. 2011)
TDP-43 (BAC)	G348C	3	nd	nd	nd	nd	nd	No	Yes	Yes	Yes	(Swarup et al. 2011)

Table 1.3 *cont*

Table 1.3- The above table outlines all known published TDP-43 mouse models and their respective lifetimes as well as observed phenotypes. Table adapted from (McGoldrick et al. 2013).

1.5.11 Fused in sarcoma (*FUS*)/Translocated in liposarcoma (*TLS*)

After mutations in TDP-43 were identified, ALS associated mutations in a gene known as Fused in sarcoma were identified in 2009 (Vance et al. 2009; Kwiatkowski et al. 2009). This gene encodes FUS which shares much functional homology with TDP-43 as it is similarly a RNA binding protein. Like TDP-43 many of the mutations reside in the RNA binding domain of the protein (Marangi & Traynor 2015). Mutations in *FUS* therefore, reinforced theories supporting aberrant RNA metabolism (see ALS pathology) although only accounting for around 4% of the cases of fALS and around 1% of sALS (Renton et al. 2014; Marangi & Traynor 2015). The phenotype often associated with FUS mutations relates to typical ALS symptoms (see table 1.1) but often presents at a juvenile stage with some patients exhibiting FTD (Marangi & Traynor 2015).

1.5.12 Structure and function of FUS

FUS is a 75 kDa protein comprising of 526 amino acids which are encoded by a total of 15 exons (Lagier-Tourenne et al. 2010). The protein can be divided into two main regions, firstly, the N-terminal (or 'prion-like') domain contains a high number of glutamine, glycine, serine and tyrosine residues known as a QGSY region spanning amino acids 1-165 (see Figure 1.4). Furthermore, the N-terminal segment of the protein contains a glycine rich region (amino acids 166-267) in which many of the ALS associated mutations are found (Lagier-Tourenne et al. 2010). Secondly, the C-terminal half of the protein comprises of a RRM (RNA recognition motif) domain (amino acids 285-371) as well as two RGG (Arg-Gly-Gly) regions that span from amino acids 371-422 and 453-501. In between these

regions (amino acids 422-453) exists a Cys_2-Cys_2 zinc-finger domain (ZNF) (Shang & Huang 2016). The C-terminal region of the protein is highly conserved and contains the nuclear localisation signal (NLS) in the most distal region of the protein which is also a hot-spot for ALS associated mutations (Shang & Huang 2016).

Figure 1.4

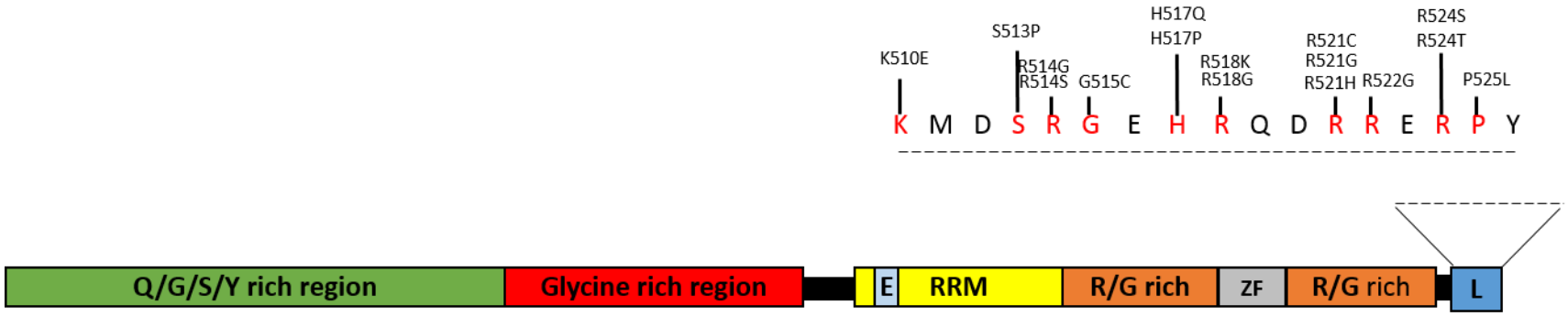

Figure 1.4- The illustration above depicts the structure of the FUS protein. The L segment of the protein represents the nuclear localisation signal for the protein. This region is a 'hot-spot' for ALS mutations and some of the common mutations observed in this region are depicted above. Figure adapted from (Lagier-Tourenne et al. 2010).

1.5.13 FUS dependent transcription and autoregulation

Originally *FUS/TLS* (hereafter *FUS*) was identified in instances of genomic translocation of its N terminal domain to fusion genes in both liposarcoma tumors and myeloid leukemia (Crozat et al. 1993; Ichikawa et al. 1994). This was found to increase the transcription of the associated chimeric genes in both cases (Ratti & Buratti 2016). Recently in 2014, the QGSY region of FUS has been found to be particularly important for binding with chromatin (Yang et al. 2014). Furthermore, it has been proposed that the interaction between FUS and chromatin occurs through a mediation with RNA polymerase II, although its interaction with this enzyme is not thought to be through the QGSY region (Yang et al. 2014). This data supports previous findings of FUS mediated transcription of manganese superoxide dismutase (MnSOD) in which FUS knockdown led to inhibition of MnSOD transcription (Dhar et al. 2013).

As with TDP-43, transcriptionally regulating the expression of other genes and its own protein levels, FUS can also regulate its own expression through binding of its own pre-mRNA (Zhou et al. 2013). This type of autoregulation mechanistically differs from the self-regulation of TDP-43 as it is driven by non-sense mediated decay of the transcript. FUS targets transcripts that have been subjected to exon 7 skipping through a splicing event and FUS knockdown prevents this repression (Zhou et al. 2013).

1.5.14 RNA binding properties of FUS

To elucidate if FUS specifically interact with RNA motifs, various studies have employed techniques to confirm that this is the case. Cross linking immunoprecipitation (CLIP) and in vitro selection assays have been used to show that FUS can bind to RNA containing a GUGGU motif (using mouse and brain tissue) (Lerga et al. 2001; Polymenidou et al. 2011). Interestingly it must be noted that other studies using similar techniques do not identify specific FUS-RNA binding sequences (Colombrita et al. 2012). Additionally, there have been reports of FUS binding to RNA exhibiting ternary structure, and also binding RNA in the absence of previously reported motifs (Takahama et al. 2013; Wang et al. 2015). Overall this evidence suggests that the interaction of FUS to RNA can be both specific and general not excluding higher order RNA structures.

1.5.15 FUS regulated splicing of pre-mRNA

The role of FUS in the splicing of pre-mRNA in accordance with the current literature can be segregated into direct and indirect mechanisms of splicing. The direct mechanism of FUS mediated splicing is closely related to transcription as FUS regulates the interaction between RNA pol II and U1 small nuclear ribonucleoprotein (U1 snRNP) which is a splicing factor and one of the initial factors to bind RNA during the assembly of the spliceosome (Yu & Reed 2015; Wahl et al. 2009). A comprehensive review of the make-up of the spliceosome is covered by Wahl et al. (2009). Secondly, FUS can interact with the survival motor neuron gene (SMN), deficiency in which is deemed pathogenic in spinal muscular atrophy. SMN is one of many important factors making up the SMN complex

which is involved in snRNP biogenesis (Battle et al. 2006). Despite FUS clearly integrating into the processes involving the splicing of pre-mRNA, the specific splicing targets are not clear due to mixed reports (Ratti & Buratti 2016).

1.5.16 The role of FUS in mRNA stability

As FUS can interact with the 3' UTR sequences of certain transcripts it is plausible that this may influence the degradation and over stability of these associated transcripts. A study by Colombrita et al. (2012) analysed the stability of certain transcripts after FUS depletion in motor neuron like cells in mice (Colombrita et al. 2012). The knockdown of FUS did not affect the stability of the mRNA in this case, another study indicated that FUS reduction can result in reduced AMPA receptor expression through reducing transcript stability of a GluA 1 subunit in cortical neurons (Udagawa et al. 2015). This indicates that FUS bound mRNA is likely altering inherent transcript stability, but could be transcript dependent and requires further investigation.

1.5.17 FUS regulation of miRNA processing

Similar to TDP-43, FUS has been associated with the Drosha complex. The ability of FUS to interact with nascent pre-mRNA molecules drives translocation of the Drosha complex to areas of active transcription enabling the processing of miRNA (Gregory et al. 2004; Morlando et al. 2012). FUS has been shown to regulate the biogenesis of a subset of miRNAs through knockdown experiments. The reduction of FUS primarily resulted in the reduction of miRNA (but not in all cases) expression including miRNAs important in neuronal function (miR-9, miR-

125b, and miR-132) (Morlando et al. 2012). Interestingly, the overexpression of FUS has been found to increase the production of two specific miRNAs (miR200a and miR141) which interact with the 3' untranslated region of the *FUS* transcript. This is another example of FUS expression regulation separable from interacting with its own mRNA in order to control the physiological concentrations of FUS (Dini Modigliani et al. 2014).

1.5.18 Long non-coding RNA (lncRNAs) and nuclear paraspeckles

Long non-coding RNA molecules are defined as any non-coding RNA molecule over 200 nucleotides in length and on a molecular level identical to mRNA (Szafranski et al. 2015). They have many emerging roles some of which include regulation of gene expression as well as regulation of neuronal function (Wu et al. 2013). One important role for lncRNAs is promotion of nuclear paraspeckle formation (otherwise known as nuclear bodies). Nuclear paraspeckles are nuclear sub structures that store edited RNA as well as RNPs to be released under stress conditions (Prasanth et al. 2005). FUS has been shown to be a component of these paraspeckles and knockdown of FUS has been shown to prevent paraspeckle formation in human cell lines (Shelkovnikova et al. 2014). Furthermore, FUS interacts with a lncRNA known as *NEAT1* which induces paraspeckle formation and has been found to be upregulated in motor neurons in ALS (Nishimoto et al. 2013).

1.5.19 FUS associated mRNA transport

The first evidence that FUS was involved in mRNA transport was in 2005 when investigations revealed FUS localisation to dendritic spines in hippocampal neurons. FUS was shown to co-localise with other RBPs as well as with NMDA receptors. Furthermore, FUS-depleted hippocampal neurons exhibited reduced spine density as well as abnormal morphologies (Belly et al. 2005; Fujii et al. 2005). Additionally, FUS has been found to localise with ribonucleoprotein complexes in distal cellular regions promoting local translation of a subset of mRNAs (Yasuda et al. 2013). The co-localisation of FUS with actin rich spines as well as neurofilament associated FUS localisation, suggests a dependency of FUS localisation on specific cytoskeletal elements (Belly et al. 2005; Muresan & Ladescu Muresan 2016). This evidence taken together suggests a role for FUS in synaptic metabolism and neuronal morphology.

1.5.20 Response to DNA damage

The first discovery that FUS was involved in DNA damage repair mechanisms was in 1995 when a protein known as POMp75 (FUS) promoted double strand break repair through homologous recombination (Baechtold et al. 1999). A year later in 2000 a study of B-lymphocytes and embryonic fibroblasts from neonatal mice indicated that the *Fus* protein was imperative for development. Additionally, the authors found that 67% of *Fus* knockout fibroblasts exhibited aneuploidy (Hicks et al. 2000). Further observations in *Fus* depleted fibroblasts included centromeric fusion as well as chromosomal breakage (Hicks et al. 2000). These studies indicated the importance of FUS in maintaining genomic stability.

Later in 2008 a study using DNA-chromatography was implemented to identify DNA binding proteins such as FUS, that were targets for ataxia-telangiectasia mutated (ATM) and ATM- and Rad3 related (ATR) (Gardiner et al. 2008). These proteins are kinases that belong to the phosphoinositide 3-kinase-like kinase (PIKK) family and are important in maintenance of genome stability (Gardiner et al. 2008). Interestingly, an overlap between FUS, ncRNAs, and DNA damage was also discovered in 2008. DNA damage was shown to promote FUS dependent inhibition of the *Cyclin D1* gene through inhibiting histone acetyltransferases induced by a conformational change in FUS when it bound certain ncRNAs (Wang et al. 2008).

More recently, research has shown that the localisation of FUS to DNA damage is dependent on poly ADP ribose polymerase 1 (PARP1). The recruitment of both endogenous and GFP- FUS to sites of UVA induced DNA damage was impaired in PARP1 null cells (Rulten et al. 2013). This finding was confirmed by Mastrocola et al (2013) and showed that FUS depletion affected homologous recombination (HR) and non-homologous end joining (NHEJ) (Mastrocola et al. 2013). The extent of the role that FUS plays in DNA damage events is still to be determined.

1.5.21 FUS mouse models

Compared to TDP-43 there are few FUS transgenic models (published) that aim to recapitulate the ALS motor phenotype (see Table 1.4). Firstly, there are transgenic mice which overexpress human FUS (tagged with HA) using a prion promotor. Secondly, there are transgenic models which express human FUS (V5 tagged) that have been generated using somatic viral techniques. Thirdly, a

mutant model expressing a R521C variant, and lastly, a Δ14 model in which the FUS protein is truncated and the nuclear localisation signal is no longer present (McGoldrick et al. 2013). FUS knockout mice are not viable similar to that of TDP-43 knockout mice and die within 16 hours (Hicks et al. 2000). The D520G mouse model (unpublished) which is subject to investigation in chapter 3 was generated through *N*-ethyl-*N*-nitrosourea (ENU) mutagenesis at Harwell laboratories. This model has no known motor phenotypes and has a normal life span.

Table 1.4- FUS mouse models

Promotor	Protein	Protein expression (fold)	Survival (weeks)	Motor phenotype	LMN degen.	UMN degen.	Cortex degen..	Axonal degen.	Gliosis path.	FUS path.	CTFs	Reference
mPrp	WT	1.4	Not aff.	-	-	-	-	-	-	-	-	(Mitchell et al. 2013)
mPrp	WT	1.7	12	Yes	60% loss	nd	nd	nd	Yes	Yes	nd	(Mitchell et al. 2013)
SBT-rAAV	WT	nd	nd	nd	nd	nd	nd	nd	nd	Yes	nd	(Verbeeck et al. 2012)
SBT-rAAV	R521C	nd	nd	nd	nd	nd	nd	nd	nd	Yes	nd	(Verbeeck et al. 2012)
SBT-rAAV	Δ14	nd	nd	nd	nd	nd	nd	nd	nd	Yes	nd	(Verbeeck et al. 2012)

Table 1.4 - FUS mouse models that have been published with the aim of recapitulating the ALS motor phenotype in mice. These models include transgenic, mutant, and truncated expression of the protein.

1.5.22 Hexanucleotide repeat expansion in *C9orf72*

A recent discovery in 2011 has provided perhaps one of the most important genetic signatures to date in the ALS field. This relates to a repeat expansion discovered at C9orf72 (chromosome 9 open reading frame 72) which has been strongly implicated in the cause of chromosome 9p21-linked ALS and FTD (Renton et al. 2011; DeJesus-Hernandez et al. 2011). This newly discovered expansion is found at an astounding percentage in both fALS and familial FTD (40% and 25%), respectively. This finding may help to explain the connection between these two seemingly different disorders (Majounie et al. 2012). In addition to this in ALS cases with European ancestry, the C9orf72 expansion accounts for 7% of sALS cases (Renton et al. 2014).

1.5.23 Structure and function of C9ORF72

The C9orf72 gene consists of 11 exons interconnected with introns illustrated in Figure 1.5. The expansion consists of a GGGGCC (G_4C_2) sequence that exists in intron 1 which is between exons 1a and 1b (both non-coding). The exons become differentially spliced in order to produce 3 variants. The ‘long’ isoform (isoform a) is generated from variants 2 and 3 and the ‘short’ isoform (isoform b) does not include the final 6 exons (Todd & Petrucelli 2016). In healthy individuals the repeat length of the G_4C_2 sequence is commonly between 5 and 10 but is mostly (in nearly all cases) below 23 (Gitler & Tsuiji 2016).

Figure 1.5

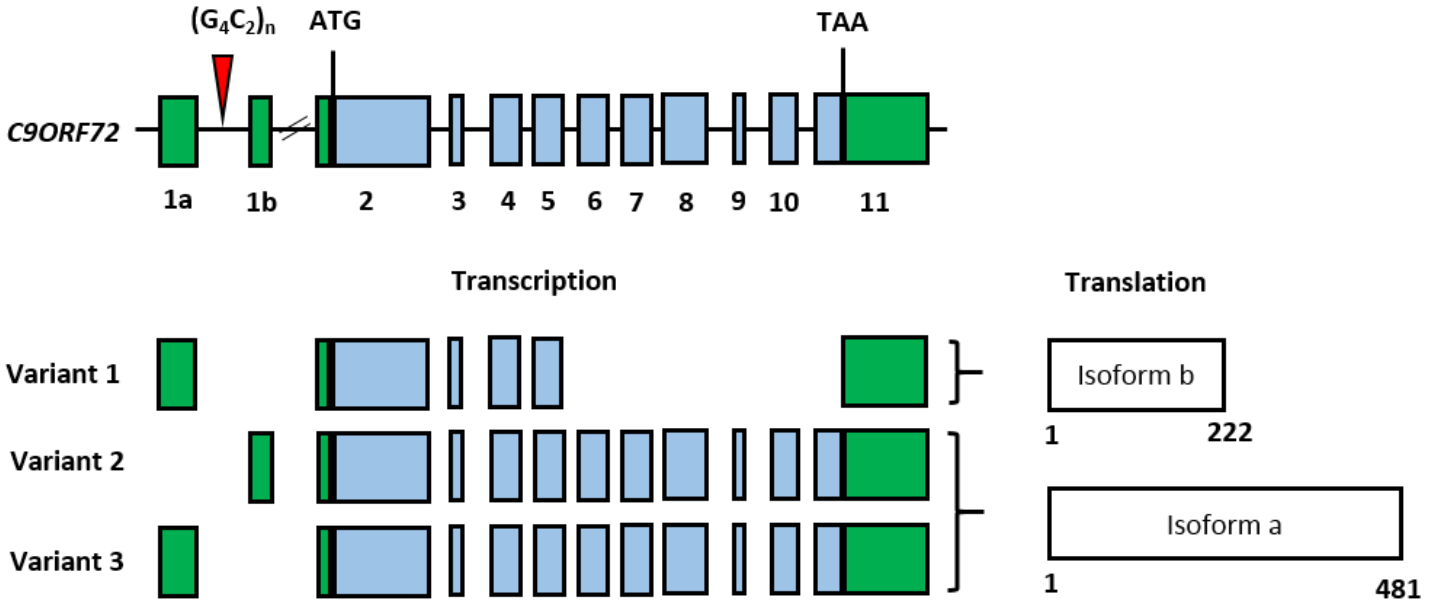

Figure 1.5 – The translation of the C9ORF72 isoforms are driven from 3 variant transcripts generated, variants 2 and 3 produce isoform a and variant 1 produces isoform b. The hexanucleotide repeat is marked by the red triangle in intron 1. The exons that are non-coding are coloured in green and coding exons are coloured blue. The amino acid lengths of each protein are annotated below each isoform produced. Figure adapted from Todd et al. 2016 (Todd & Petrucelli 2016).

Currently there is limited information on the function and structure of the protein translated from the *C9orf72* gene. Despite this some studies have reported the protein to have similar homology to that of the Differentially Expressed in Normal and Neoplasia (DENN) family of proteins. This family of proteins are Guanine nucleotide exchange factors (GEFs) which control the activity of Rab GTPase enzyme activity through enabling GDP-GTP exchange (Levine et al. 2013; Gitler & Tsuiji 2016; Bhuin & Roy 2014). Rab GTPase enzymes can regulate membrane trafficking at the Golgi and the trans-Golgi-network (TGN) (McDonold & Fromme 2014). C9ORF72 has been specifically found to co-localise with many Rab's including Rab7 and Rab5 in primary cortical neurons (Farg et al. 2014).

In addition to this, some evidence has suggested that the C9ORF72 protein has an important role in motor neurons. Zebrafish have an orthologue to the protein which exhibits 76% homology (Ciura et al. 2013). Experiments blocking the translation of this protein through antisense oligonucleotides resulted in perturbed neuronal arborisation and stunted axons in motor neurons (Ciura et al. 2013). However, it is important to mention that off-target effects of the oligonucleotides cannot be ruled out. Crucially, mammalian expression of *C9orf72* has been reported in neurons of mice with strong expression in the gray matter of the spinal cord and weaker expression detected in the cortex (Koppers et al. 2015). Importantly, there are also reports outlining the expression patterns of C9orf72 in human neocortex and spinal cord (Stewart et al. 2012).

The cellular localisation of C9ORF72 will at this current juncture somewhat be dictated by the availability and quality of the commercially available antibodies. The protein has been found to exhibit a diffuse nuclear localisation as well as display punctate cytoplasmic aggregates in SH-SY5Y and Neuro2a cell lines as well as primary cortical neurons. The cytoplasmic pattern of staining could support the role of C9ORF72 in membrane trafficking (Farg et al. 2014). Knockdown of C9ORF72 using siRNA led to impaired endocytic trafficking and the formation of autophagosomes (Farg et al. 2014).

Recently, a study using isoform specific antibodies found contrasting evidence to that of Farg et al. Antibodies against both the long and short isoforms of the C9ORF72 protein did not produce punctate staining in spinal motor neurons in either control or ALS patients (*C9orf72* associated or otherwise) (Xiao et al. 2015). The long isoform antibody did produce a punctate staining pattern in Purkinje cells but with no co-localisation to endosomes. The short isoform antibody contrastingly outlined the nucleus in all cells and was depleted from the nucleus in ALS cases, but instead stained the plasma membrane (Xiao et al. 2015).

Strikingly, C9ORF72 interacts with hnRNP-A1/A2/B1 which all have ALS associated mutations and could elucidate to a common mechanistic link in terms of disease pathogenicity (Farg et al. 2014). Overall, these data suggest that the *C9orf72* gene encodes a protein important for intracellular trafficking in both nuclear and cytoplasmic compartments perhaps associated with RNA binding proteins.

2.0 ALS pathology

2.1 Protein aggregation

Protein aggregation is a pathological feature of many neurodegenerative diseases including ALS, FTD, Alzheimer's disease and Huntington's disease. Although this is the case the underlying related mechanisms of aggregation are not well understood. In ALS, protein inclusions and aggregates are found in motor neurons as well as other brain regions such as the hippocampus (Blokhuis et al. 2013). The aggregates that are primarily found in ALS motor neurons are ubiquitinated and are termed skein-like or Lewy body-like inclusions. These exist as randomly arranged filaments associated with fine granules. Ubiquitin-negative inclusions termed Bunina bodies appear as tubular aggregates surround electron dense material (Blokhuis et al. 2013).

The aggregates in ALS neurons can be co-localised with many proteins in which mutations in are also deemed pathogenic in ALS (see Table 1.5). This is a striking pathogenic feature of the disease perhaps due to interrelated functions of ALS associated proteins. Recent investigations have indicated that some misfolded proteins in ALS (Such as TDP-43, FUS, and SOD1) have prion protein like properties. Misfolded prion proteins underlie prion disease which is a group of neurodegenerative diseases in which transmissible proteins misfold and create amyloid β-sheets which promote further misfolding by acting as a template. Although no other neurodegenerative diseases are transmissible, the spreading of the pathology (see motor neuron degeneration and associated clinical symptoms) and age-related onset is similar to that of ALS (Smethurst et al. 2015).

The presence of protein aggregates likely result in loss of function of aggregating proteins, impaired transcription and translation, perturbed transport and disrupted cytoskeletal integrity in motor neurons.

2.2 Defective RNA metabolism

Many ALS causing mutations reside in proteins important for multiple steps in the metabolism of RNA most notably FUS and TDP-43. Physiologically, FUS and TDP-43 localise predominantly to the nucleus where they perform multiple roles in RNA biogenesis. Mutations in both TDP-43 and FUS result in thier mislocalisation from the nucleus into the cytoplasm. This perhaps hints at a loss of function mechanism of toxicity, but accumulation of FUS and TDP-43 aggregates in the cytoplasm may lead to a toxic gain-of-function (Rossi et al. 2016). The exact mechanisms of how mutations in these RNA binding proteins cause death of motor neurons is still unclear. A summary of the effects of ALS mutations in both TDP-43 and FUS driven RNA metabolism are outlined in Figures 1.6 and 1.7.

Table 1.5- The immunoreactivity of protein aggregates in ALS

	Ub	p62	SOD1	TDP-43	FUS	OPTN	UBQLN2	ATXN2	C9ORF72
sALS	+	+	-	+	+-	+	+	+	-
ALS SOD1	+	+	+	-	-	+-	+	NR	+
ALS VCP	NR	NR	NR	+	NR	NR	NR	NR	NR
ALS VAPB	NR	NR	NR	NR	NR	NR	NR	NR	NR
ALS TDP-43	+	+	-	+	+	+	+	NR	-
ALS FUS	+	+	-	+ -	+	+-	+	+	-
ALS OPTN	+	+	-	+	NR	+-	NR	NR	NR
ALS UBQLN2	+	+	-	+	+	+	+	NR	NR
ALS ATXN2	+	+	-		NR	NR	NR	+	NR
ALS C9ORF72	+	+	-	+	NR	+	+	NR	-

Table 1.5 – The immunoreactivity of protein aggregations in ALS is outlined in the above table. Non-responsive (NR), positive (+), negative (-), and conflicting evidence (+-) is annotated in each case. Adapted from Blokhuis 2013 (Blokhuis et al. 2013).

Figure 1.6

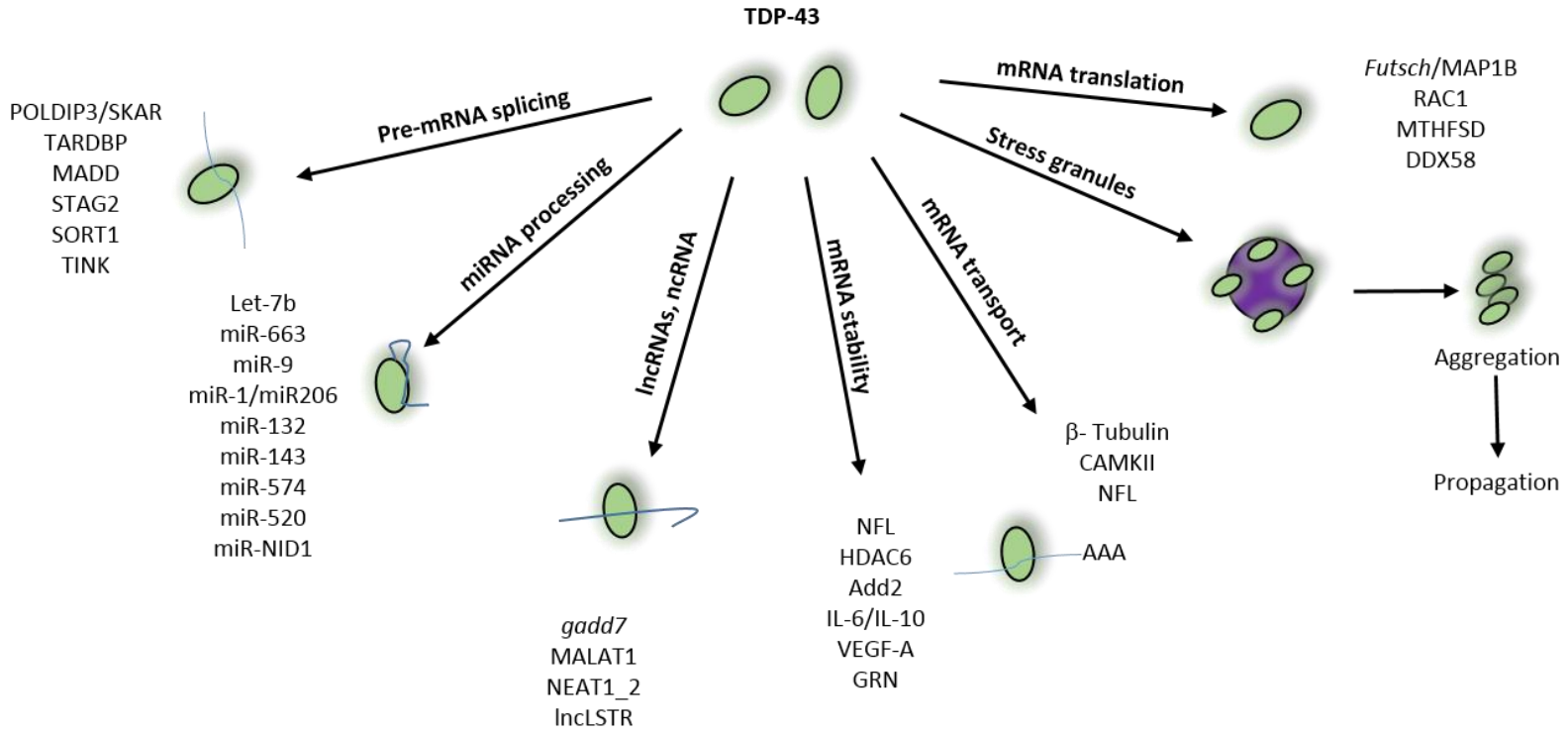

Figure 1.6 – The above diagram outlines the known roles for TDP-43 in RNA metabolism. The associated genes and proteins that have been validated experimentally are also included.

Figure 1.7

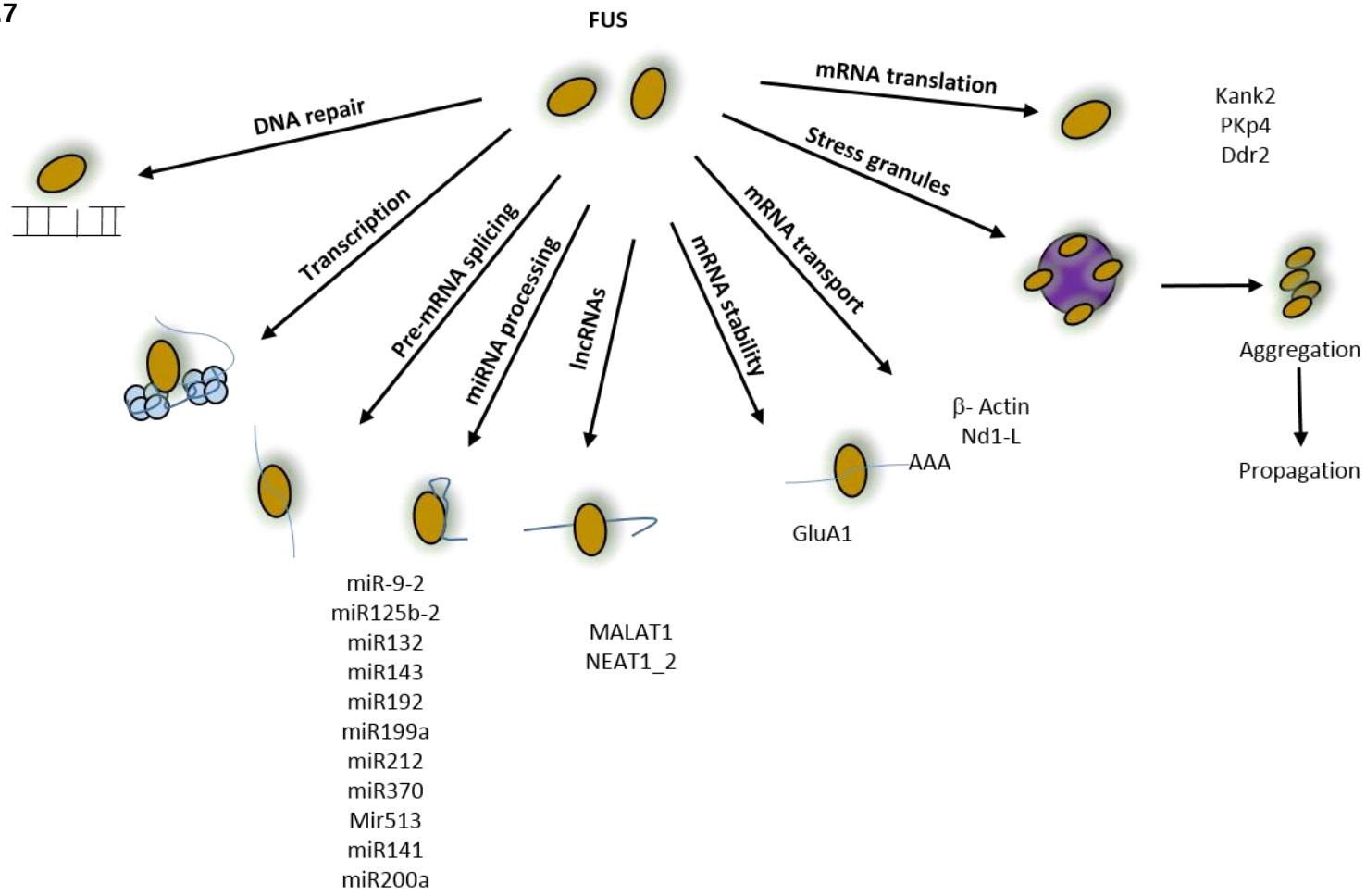

Figure 1.7– The above diagram outlines the known roles for FUS in RNA metabolism. The associated genes and proteins that have been experimentally validated are also included.

2.3 TDP-43 mutations and aberrant axonal transport

Axonal transport deficits have been reported in many neurodegenerative diseases including Alzheimer's disease, multiple sclerosis and ALS. Investigations into the transport of TDP-43 granules in axons has been extensively reported. Using *Drosophila* as a model, *TDP-43* ALS mutations A315T and M337V have been shown to impair anterograde and retrograde transport in motor neurons (Alami et al. 2014; Baldwin et al. 2016). This could be a compounding pathology and promote TDP-43 associated aggregation in the cytoplasm in motor neurons. Similarly, using similar *Drosophila* models a *FUS* ALS mutation P525L exhibited defective anterograde transport of vesicles in motor neurons, but not mitochondria. Interestingly, recent data from a C9orf72 expansion *Drosophila* model has indicated severe anterograde transport deficits caused by the hexanucleotide expansion (Baldwin et al. 2016). This indicates that disrupting multiple processes through different ALS related mutations can cause axonal transport discrepancies.

2.4 Gliosis and excitotoxicity of motor neurons

Glial cells are the predominant population of immune cells in the central nervous system. They interact with both T-cells and astrocytes in modifying the inflammatory response. Additionally, glial cells accomplish this modification by releasing cytokines that can promote or depress the inflammatory response. In patients with ALS, migration of microglia to areas of injury (known as microgliosis) occurs and is increased in the cortex, brainstem, corticospinal tract, and the ventral horn of the spinal cord. Aberrant glial function was first reported in ALS a

glutamate transporter EAAT2/GLT1 was found to be depleted in the spinal cord and motor cortex of sALS and fALS patients. This was also found in a mutant SOD1 mouse model G85R and further studies have shown that deletion of mutant SOD1 from both astrocytes and microglia improve motor neuron survival (Philips & Rothstein 2014; Bruijn et al. 1997). This indicates that some immune cells of the central nervous system contribute to motor neuron deterioration.

Even though glutamate is well known for presynaptic release from neurons, astrocytes release glutamate extracellularly and this concentration of glutamate is tightly regulated. Inhibition of glutamate uptake is toxic to cortical and spinal motor neurons shown in vitro (Rothstein et al. 1993). Therefore, the dysfunction of the EAAT2 transporter could play a crucial role in motor neuron death. This glutamate toxicity could be exacerbated by over excitability of neurons causing an increase of glutamate release from the presynaptic neuron. This could be primarily driven by mechanisms such as ER stress or changes in calcium influx in pre-synaptic neurons but the evidence for this induction of excitotoxicity is not well reported. However, data from the SOD1-G93A mouse model derived from synaptosomes suggested that the efflux of glutamate was increased in mutant mice compared to wild-type mice (Milanese et al. 2011). Although the mechanisms are not clear, mutant SOD1 likely plays a regulatory role in glutamate homeostasis.

2.5 Oxidative stress and its potential detriment in ALS

Oxidative stress refers to the generation of noxious free radical species known as reactive oxygen species (ROS). The generation of these free radicals could

be induced by environmental factors and biomarkers of oxidative stress have been found commonly in sALS patients (D'Amico et al. 2013). Oxidative stress may have an important role in non-SOD1 ALS as mutations in valosin-containing protein (VCP) have also shown susceptibility to ROS in SH-SY5Y cells (Hirano et al. 2015). Despite this, no single pro-ROS mechanism or factor has been found in ALS to date. However, there may be a pathogenic link between oxidative stress and protein aggregation. The SOD1 protein has been found to aggregate when oxidized which again could be another compounding factor in mutant SOD1 ALS (Guareschi et al. 2012).

2.6 Mitochondrial damage in ALS

Mitochondria are the main production site for both adenosine triphosphate (ATP) and consequently, ROS, and can be themselves damaged by toxic free radicals. Perturbed activity of the mitochondrial respiratory complex in ALS has been found in post-mortem spinal cord and brain tissue from ALS patients as well as in a SOD1 transgenic mouse model (Cozzolino & Carri 2012). It has been suggested that mitochondrial damage is a consequence of SOD1 aggregation and furthermore provides another possible pathological relationship (Carrì et al. 2015). The fALS associated protein VCP is crucial for mitochondrial function as *VCP* mutations result in abnormal mitochondrial function and reduced ATP production (Bartolome et al. 2013). Mutations in both TDP-43 and FUS have also been suggested to cause aberrant mitochondrial functions but the ways in which defective RNA metabolism may be detrimental to mitochondria are unclear (Carrì et al. 2015). The instability of mitochondrial DNA has also been implied in through

ALS associated mutations in a protein of unknown function encoded by *CHCHD10* resulting in mitochondrial DNA breakage (Bannwarth et al. 2014).

2.7 DNA damage and neurodegeneration

Macromolecules in biology are all susceptible to corruption, but DNA lesions are particularly detrimental to cells. DNA is the blueprint from which proteins are produced and cannot be resynthesized in a straightforward manner. These aberrations can lead to disruption of cellular mechanisms inducing cell death, senescence, or uncontrolled replication leading to cancer. Motor neurons have to last for a lifetime and so have to be able to cope with prolonged DNA damage. Many neurodegenerative diseases are caused by defects in DNA damage repair proteins although many of these diseases are congenital, DNA damage could also underlie age associated deterioration of neurons (Madabhushi et al. 2014). Neurons are postmitotic cells and rely on repair mechanisms which are summarised below.

2.7.1 Nucleotide excision repair (NER)

This is the repair process in which the aberrations in the DNA helix are detected rather than modifications of bases. These aberrations are diverse and can prevent the continuation of transcription and result in apoptosis. There are over 30 proteins which orchestrate to complete the NER process which can be segregated into two categories. The first is known as global genome NER (GG-NER) and is a process which is global. The second is transcription coupled NER

(TC-NER) which only targets the DNA strand transcribed in genes which are active (Madabhushi et al. 2014).

2.7.2 Base excision repair (BER)

BER is a process similar to that of the NER process but has evolved to specifically detect modified bases and excising them via the cleavage of a N-glycosidic bond. The BER pathway targets a large range of damage induced modifications which are subsequently converted into a small number of intermediates via DNA glycosylases of which there are at least 15 found in humans. These produced intermediates are then the primary substrates for the BER machinery including XRCC1, APE1, and polβ (Madabhushi et al. 2014).

2.7.3 Single strand break repair (SSBR)

Although ROS can lead to modifications of existing bases, damage can also lead to the induction of a single strand break (SSB). These type of lesions can also arise from the BER pathway or from topoisomerase I aborted reactions. In this type of repair pathway, the outcome generates DNA ends which are conducive to ligation. As the lesions produced can vary this requires a large number of processes that will produce compatible DNA ends, similarly SSBR uses molecular machinery found in the BER pathway.

2.7.4 Double strand break repair (DSBR)

Single strand breaks that occur in proximal regions of DNA can lead to double strand breaks of the double helix. This can also occur when translation machinery collides with a single strand break leading to abortive reactions. This type of lesions can be induced by environmental factors such as ionising radiation or other noxious drugs used in chemotherapy. For these reasons, double strand breaks are not as common as single strand breaks and can result in chromosome rearrangements which can lead to cell death or sometimes uncontrolled cell division. In neurons these types of lesions are repaired through non-homologous end joining (Madabhushi et al. 2014). This type of damage is recognised by KU70/80 which attaches itself to the broken DNA ends before recruiting other DNA repair machinery such as ARTEMIS and APLF to access the damage site (Madabhushi et al. 2014). This interaction prepares the strands to be ligated before the XRCC4/LIG4 complex completes the ligation. It is important to note that even though this process is integral for the resistance to DSB in neurons this repair pathway has not been extensively investigated in the mature brain (Madabhushi et al. 2014).

3.0 Childhood-onset motor neuron diseases

3.1 Spinal muscular atrophy (SMA)

Spinal muscular atrophy (OMIM#253300) is the largest genetic contributor to mortality in infants and is characterised by the loss of anterior horn lower motor neurons. The clinical features of the disease vary in severity through type I SMA

(where the disease is most lethal) to type III in which patients exhibit altered mobility (see Table 1.6). The molecular genetics of SMA are underpinned by the loss of telomeric survival motor neuron 1 (*SMN1*). This gene encodes SMN which is found in both the nucleus and the cytoplasm. SMN complexes with gemin proteins to form an assemblyosome which is key for the production of snRNPs (Arbab et al. 2014). This indicates that RNA metabolism may be defective in this disease although the available data is limited (Tisdale & Pellizzoni 2015).

The deficiency of *SMN1* is compensated for by *SMN2* which encodes a truncated form of the SMN protein which is quickly degraded. This only partially compensates for its functionality and the copy number associated with *SMN2* can dictate the severity of the disease. SMA mouse models have exhibited varying vulnerability of neurons, for example, neurons that innervate muscles proximal to lumbar level L1 seem to deteriorate quicker than neurons that innervate distal muscles from L5 (Tisdale & Pellizzoni 2015). The complete knock-out of *SMN1* is embryonically lethal and it is not known why mutations in SMN1 are so detrimental to motor neurons (Arbab et al. 2014).

Table 1.6-Childhood onset motor neuron diseases

Motor neuron disease	Disease characteristics and clinical features	References
Hereditary spastic paraplegia **(HSP)**	A subset of childhood neurodegenerative disorders affecting the spinal cord clinically characterised through progressive spasticity with a prevalence of 2-10:100,000. Pure HSP • Progressive spasticity and weakness. • Mild sensory abnormalities. • Urinary dysfunction. Complicated HSP (additional complications) • Cerebellar ataxia. • Epilespy. • Cognitive deficits. • Deafness.	(Lindig et al. 2015)
Brown-Vialetto-Van Laere syndrome **(BVVL)**	A progressive and sensory neuropathy with an early childhood onset of disease caused by mutations in the riboflavin transporter type 2. • Early onset hearing loss. • Sensory hearing loss. • Upper limb weakness. • Optic atrophy. • Bulbar weakness. • Respiratory failure.	(Menezes et al. 2016)
Spinal muscular atrophy. **(SMA)**	Neurodegenerative disorder affecting lower alpha motor neurons with onset spanning between childhood and early adulthood with an incidence of 1:10,000. Type I • Cessation of fetal movements in mothers. • Severe weakness at birth. • Respiratory failure within 2 years. Type II • Inability to stand but can sit unaided. • Prognosis between 5-25 years depending on respiratory muscle involvement. Type III • Varied ability to walk. • Life expectancy normal.	(Arbab et al. 2014; Scheffer 2004)

Table 1.6 ***cont.***

Motor neuron disease	Disease characteristics and clinical features	References
Spinal muscular atrophy with lower extremity pre-dominance. **(SMA-LED)**	Characterised by congenital or childhood onset of disease which is autosomal dominant and non-progressive with broad clinical features. • Lower limb weakness and atrophy • Waddling gait. • Reduced ability to climb stairs. • Incidences of ADHD. • Epilepsy. • Some incidences of severe mental retardation.	(Harms et al. 2012; Schiavo et al. 2013)

Table 1.6- Childhood motor neuron diseases with associated disease characteristics and clinical features.

3.3 Spinal muscular atrophy with lower extremity pre-dominance (SMA-LED)

SMA-LED (OMIM#158600) may have been clinically reported as early as 1917 by Timme who describes a family with a form of muscular dystrophy in which the onset of disease was noted at 3-4 years of age. Years later a follow-up on this family was conducted by Young in 1972 and indicated that the disease seemed to resemble an early childhood onset autosomal dominant spinal muscular atrophy (Timme 1917). Many years later Harms et al. (2010) reported a family of North American heritage in which 10 individuals exhibited onset of a mild or non-

progressive SMA with early age onset (Harms et al. 2010). These individuals presented with a lower extremity predominance and Harms coined the disease SMA-LED which marked the modern age of investigation into the disease.

3.2 Clinical characteristics of SMA-LED

The clinical presentation of SMA-LED can be very diverse and affect a range of mobility and cognitive related abilities (see Table 1.5). A study by Harms et al. in 2012 in which SMA-LED was confirmed in a 3 generation family described typical SMA-LED symptoms. Affected individuals all were described as having an abnormal gait with atrophy of lower limbs which did not progress into later life (see figure 1.8). This was coupled by reduced tendon reflexes in the knees and a disparity in strength between flexion and tension of the knees. Investigations into nerve conduction indicated that sensory nerve conduction was normal but motor neuron conduction was poor, this finding was coupled by chronic denervation (Harms et al. 2012). The cognitive deficits experienced by patients with SMA-LED can range from mild learning difficulties to severe mental retardation.

Figure 1.8

Figure 1.8- The above picture illustrates the severity of lower limb wasting in SMA-LED, picture adapted from Oates et al. 2013 (Oates et al. 2013).

3.4 Molecular genetics of SMA-LED

SMA-LED is a congenital autosomal dominant heritable disease which is characterised by lower limb atrophy of the muscles combined with motor deficits. Human mutations identified through linkage analysis were first identified on chromosome 14 (14q32) which was found to encode for DYNC1H1 a subunit component of the motor complex dynein (See dynein structure and function) (Harms et al. 2010; Harms et al. 2012; Vissers et al. 2010). Additionally, in 2013 linkage analysis identified mutations at another locus (9q22.3) which encodes BICD2 a protein which interacts directly with dynein (see Figure 2.1) (Neveling et al. 2013). These pathogenic mutations show complete penetrance and both result in very similar disease phenotypes typical of SMA-LED.

3.5 Molecular motors

Molecular motors are stunning examples of harmonious biological machinery in which protein complexes orchestrate to exert force on a cellular scale. There are three main types of molecular motors found in cells, firstly, there are dyneins which interact with microtubule tracks to produce motion in a retrograde direction. Secondly, there are kinesins which also interact with microtubules but travel in the opposite anterograde direction towards the cell periphery. Lastly, there are myosins which interact directly with actin filaments to influence contraction and torsion forces within cells. All of these motors hydrolyse ATP in order to produce conformational changes in subunits of the motor to evoke a stepping motion along its respective substrate. There is a large diversity observed in these molecular motors as various subunits can be utilised in their function. Furthermore, when

accounting for their post-translational modifications and respective binding partners, these motors are equipped to serve the highly diverse requirements of cellular dynamism.

3.5.1 Dynein families

There are two distinct families of dynein termed axonemal dynein and cytoplasmic dynein. Axonemal dynein is a molecular motor which is abundant in cilia and flagella protrusions associated with some cell types. The primary core structural component in these protrusions is known as the axoneme. This consists of nine pairs of microtubules that interact with axonemal dynein (Kuhns et al. 2013). The second family is known as cytoplasmic dynein which binds to cytoskeletal microtubules in eukaryotic cells to primarily provide retrograde transportation of cargoes such as endosomes or mitochondria. Two subdivisions of cytoplasmic dynein exist: Cytoplasmic dynein 1 and cytoplasmic dynein 2. Cytoplasmic dynein 1 (hereafter dynein) is the SMA-LED disease relevant complex that will be referred to in the subsequent sections.

3.5.2 The structure and function of the Dynein complex

Dynein is a large motor complex (~1.5MDa) comprised of multiple subunits which cohesively function to primarily transport cellular cargo towards the minus-end of microtubules (retrograde direction). The DYNC1H1 homodimer (dimerization region 302-1142) is the core of the complex and binds with the intermediate chains (DYNC1I1 and DYNC1I2) and light intermediate chains (DYNC1LI1 and DYNC1LI2). Additionally, light chains (DYNCLT1, DYNCLT2, DYNLL1, DYNCLL2, DYNLRB1 or DYNLRB2) interact with the complex through the intermediate chains (see Figure 1.9 A) (Chowdhury et al. 2015). The holoenzyme complex utilises ATP in the nervous system to provide transport over large distances especially in the case of motor neurons.

Cytoplasmic dynein heavy chain 1 encoded by DYNC1H1 (hereafter DHC) can be subdivided into the tail domain and the motor domain (see Figure 1.9 B). The motor domain includes six AAA ATPase domains (1868-4221 amino acids) which are responsible for ATP hydrolysis and the microtubule binding domain (MTBD). ATP hydrolysis is hypothesised to drive conformational changes in the linker and the tail domain of dynein to generate a ‘power stroke’ for dynein motility (Carter 2013).

Figure 1.9 A

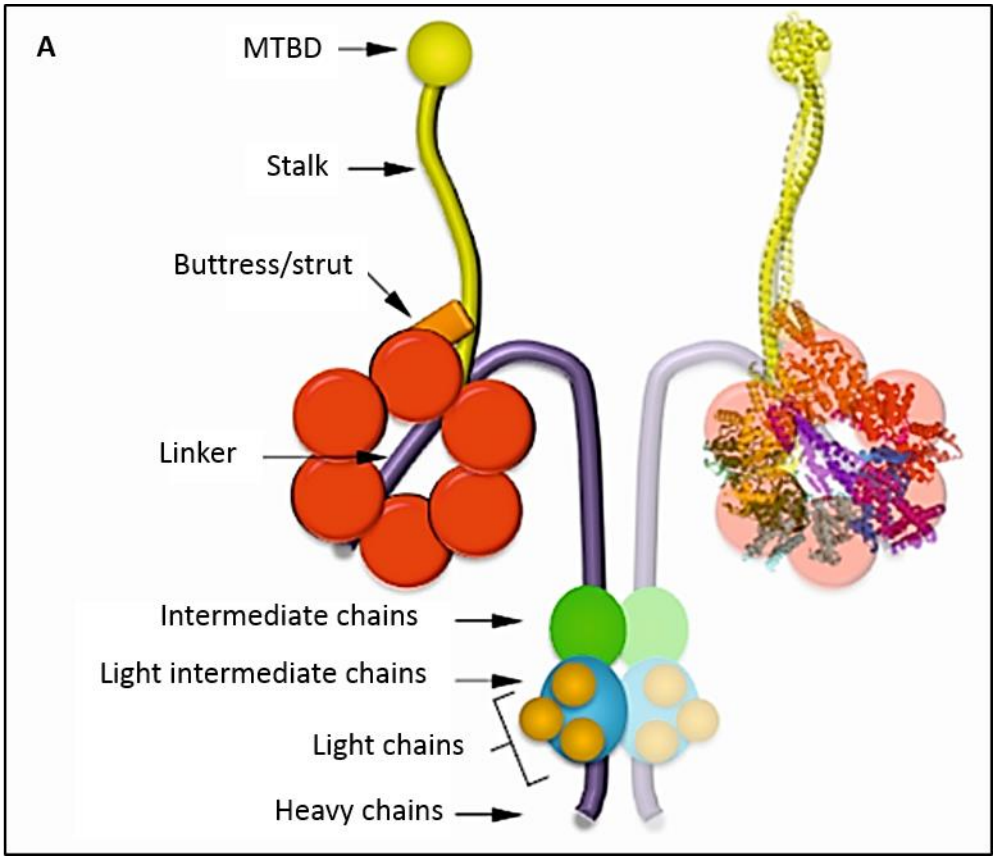

Figure 1.9 A- The above figure depicts a schematic of cytoplasmic dynein. The DHC (violet) is the core of the complex to which all the other subunits attach. The ATPase domains (orange) are a ring structure which hydrolyses ATP to ADP. The stalk domain of the complex includes the microtubule binding domain (yellow) responsible for the attachment of the complex to microtubules. This figure was adapted from (Schiavo et al. 2013).

Figure 1.9 B

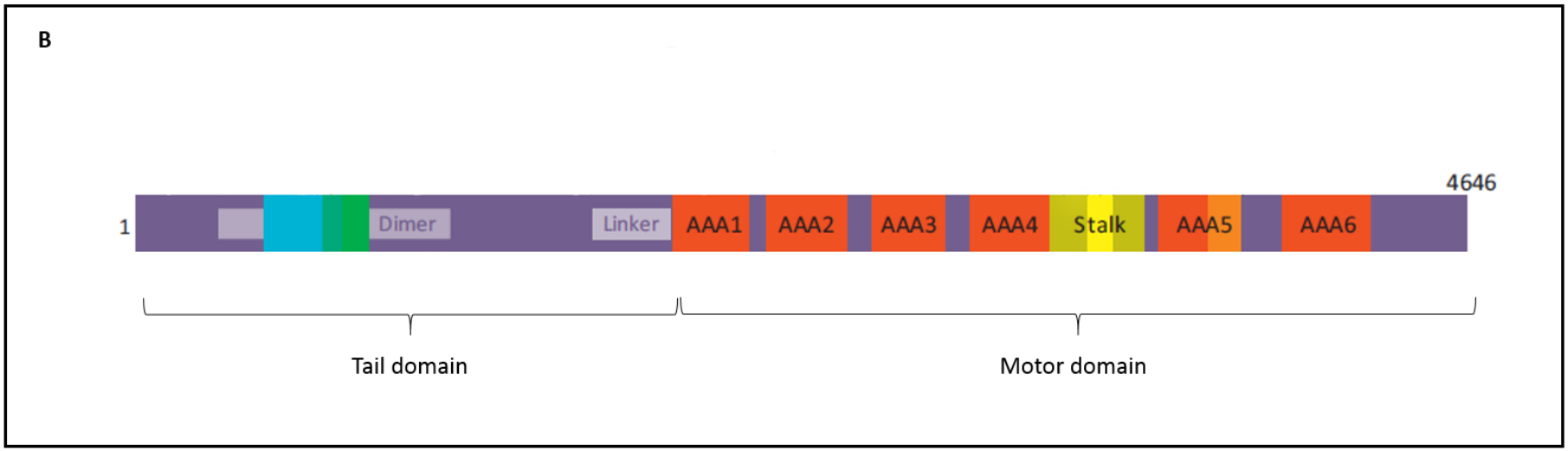

Figure 1.9 B- The above schematic depicts the organisation of the DYNC1H1 subunit of cytoplasmic dynein segregated into the tail and the motor domain. The intermediate (green) and light intermediate chain binding region (blue) reside in the homodimerisation domain which are located in the tail domain of the protein. The motor domain encompasses all AAA domains including the stalk domain. The light yellow highlighted box indicates the microtubule binding domain portion of the stalk domain.

3.5.3 The ATPase activity of Dynein

When there is absence of binding of a nucleotide at the AAA1 domain the dynein complex remains tightly associated with the microtubules, but interaction with ATP results in rapid dissociation between the MTBD and the microtubules. After ATP has been hydrolysed to ADP and an inorganic phosphate, the motor domain interacts with a new binding site on the microtubule. This interaction is thought to gradually become stronger straightening the linker representing the 'power stroke' and the inorganic phosphate is released from the AAA1 domain. Lastly, ADP dissociates from the AAA1 domain before the cycle restarts (Roberts et al. 2013). The AAA2-4 domains of the DHC are thought to also contain nucleotide binding pockets whereas the AAA5 and AAA6 domains do not have hydrolysing activities and their precise role is yet to be elucidated (Roberts et al. 2013).

The tail domain of dynein is towards the N-terminal region of the DYNC1H1 homodimer and regulates interaction between other adaptor proteins and cargoes (Schiavo et al. 2013). The association of adaptor proteins modulate the processivity of dynein along microtubules.

3.5.4 The dynein adaptor dynactin

Mammalian dynein on its own is non-processive and therefore, requires association with other proteins to facilitate movement of the complex, dynactin is the primary facilitator of dynein functionality. Dynactin is a large protein complex (~1.0MD) consisting of over 20 subunits that relate to 11 separate proteins (see Figure 2.0). The dynactin complex is constructed around a core filament of actin

related protein (ARP1). This protein has close structural similarities with actin and has both a pointed and a barbed end, both of which are capped by protein complexes.

This filamentous structure interacts with a p150^{Glued} (DCTN1) 'shoulder' which contains a dynein binding region and is the largest subunit of dynactin (Urnavicius et al. 2015). Additionally, the shoulder can consist of p135 which is a truncated isoform of p150^{Glued} and is deficient of a Cap-Gly domain which is a microtubule binding region (Mckenney et al. 2014).

Dynactin consists of two ARP1 protofilaments that intertwine, the lower of the two filaments also contains β-actin (see Figure 2.0). The pointed end of the complex consists of p25, p27 and p62 whereas the barbed end is comprised of CapZ$\alpha\beta$ (Urnavicius et al. 2015). The interaction between dynactin and dynein is stabilised by Bicaudal-D2 (BICD2). Dynactin is regarded as vital for all the functional roles that dynein is associated with and specifically is important for the attachment of cargo and to act as a processivity factor (Cianfrocco & Leschziner 2014).

Figure 2.0

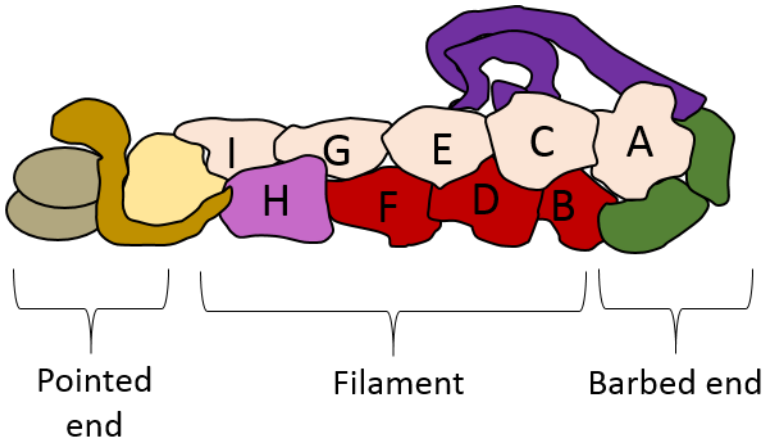

Figure 2.0 – The structural composition of dynactin is depicted above. The dark purple 'shoulder' region consists of p150^{Glued}/p135, p50 and p24. This interacts with the top protofilament (coloured beige) which is wrapped around the bottom filament (coloured red). Subunits A-I consist of ARP1 whereas subunit H represents β-actin. The pointed end of the complex consists of ARP11 (yellow), p62 (orange), and p25/p27 (brown) which caps the pointed end of the complex. The barbed end of the complex is capped by CapZαβ (green). Figure adapted from Urnavicius et al (Urnavicius et al. 2015).

3.5.5 Dynein-dynactin-microtubule structural organisation

Recent investigations through cryo-EM imaging has enabled visualisation of the interaction between dynein, dynactin, and microtubules at a resolution of 6.5 angstroms. Data from Chowdhury et al (2015) has indicated structural insights into the dynein complex. The dynein heavy chain appears to have a structural 'kink' which has not been previously observed (see Figure 2.1). It is positioned between the tail domain and the motor domain and has been suggested to act as a shock absorber or hinge during the cyclical ATP driven motion of dynein. Secondly, the authors show that a portion of the intermediate chain of dynein

extends behind the complex and does not interact with the heavy chain. This flexible domain of the intermediate chain interacts with the LC7 (DYNLRB2) dimer (see figure 2.1), this information refines the structural complexity of the tail domain of dynein (Chowdhury et al. 2015).

3.5.6 The dynein adaptor BICD2

The BICD protein was originally identified in *Drosophila* in which mutations caused defective mRNA transport during development leading to physical abnormalities. The BICD homologues in mammals are BICD1 and BICD2 and are comprised of three colied coil (cc) domains responsible for maintaining a homodimer of the protein (Rossor et al. 2015). BICD2 is a member of the golgin family which are proteins characterised by coiled coil domains that reside on the cis and trans regions of the Golgi. The N-terminal region (cc1 and cc2) of the protein is responsible for dynein and dynactin interactions (see figure 2.1) and can interact with the p50 dynactin subunit as well as the dynein intermediate chain (hereafter, DIC) (Neveling et al. 2013; Matanis et al. 2002; Hoogenraad et al. 2001). The third cc3 domain is crucial for interacting with cargo-associated proteins such as Rab6 which is located on Golgi derived vesicles (Matanis et al. 2002). It is through these interactions that BICD2 is likely important for regulating cargo interactions with molecular motors such as dynein. McKenney et al. has importantly shown that when BICD2 is removed from the dynein-dynactin complex, dynactin will dissociate away from dynein and the motor is no longer processive (McKenney et al. 2014).

Figure 2.1

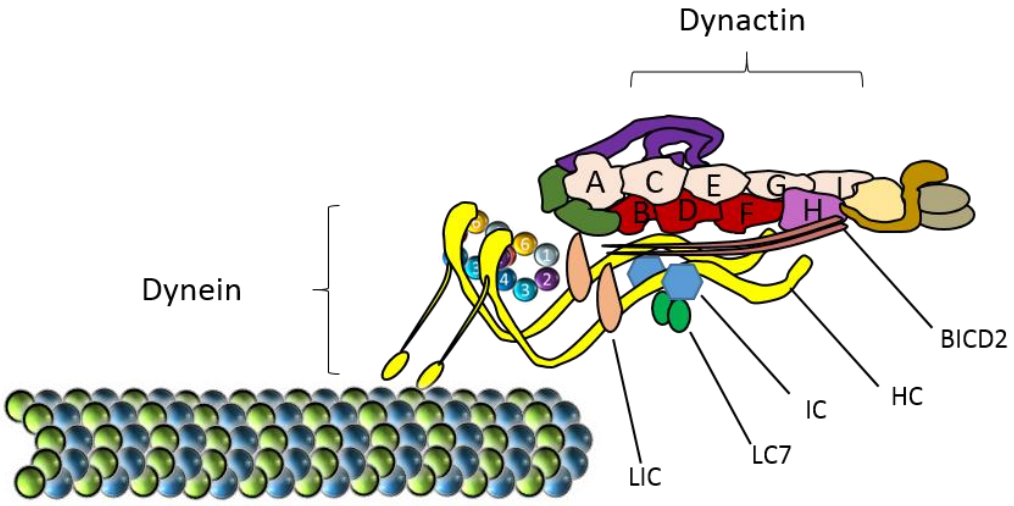

Figure 2.1- The interaction between dynein, dynactin, BICD2, and microtubules. The dynein complex interacts with the p150^{Glued} subunit of dynactin (purple) via a coiled-coiled domain obscured by the ARP1 filaments of dynactin (beige and red). BICD2 interacts with the complex via the intermediate chain of dynein and sits between both the dynein and dynactin complexes. The kink in the heavy chain of dynein can be pictured in this diagram close to the LIC binding region and is proposed to facilitate dynein motility. The above diagram was adapted from Chowdhury et al. (2015) (Chowdhury et al. 2015).

3.5.7 Other co-factors of cytoplasmic dynein

Even though both dynactin and BICD2 represent the primary adaptors of dynein there are other dynein co-factors that have evolved to regulate the activity of the motor complex. The first of which is LIS1 which interacts with the AAA1 domain of the DHC. Mutations in *LIS1* are associated with the disease lissencephaly in which malformation of the cortex and disruption of neuronal migration in the cortex occur during development. Even though the exact influence that LIS1 has on dynein is far from complete, recent evidence from yeast studies have suggested that it can block the mechanochemical cycle of dynein. This suggests that LIS1 can sterically inhibit dynein and promote a constant microtubule-bound state (Toropova et al. 2014). Data from the LIS1 homolog NUDF in fungi has also shown that LIS1 is closely associated with the plus-end microtubule tips. In summary, this indicates that LIS1 stalls cytoplasmic dynein and associates with the motor complex at the tips of microtubules (Han et al. 2001).

Other proteins known as Nudel/NudE have been found to interact with LIS1 in vitro and became linked with dynein regulation (Sasaki et al. 2000). Mutations in Nudel/NudE are related to abnormally developed brains and microcephaly (Bradshaw et al. 2013). Aside from their interactions with LIS1 these proteins also bind dynein directly through interaction with the dynein intermediate chain (Cianfrocco et al. 2015). It has been suggested that the role of Nudel/NudE is to directly tether LIS1 to dynein indicating a purely mechanistic contribution to the dynein complex (Cianfrocco et al. 2015). A summary of dynein co-factors can be seen in Table 1.7.

Table 1.7- Co-factors of cytoplasmic dynein

Co-factor	Subunit binding	Role	Reference
Dynactin	DIC	Processivity	(Holzbaur & Tokito 1996)
BICD2	DIC	Processivity/Dynein-dynactin complex integrity/cargo binding	(Hoogenraad et al. 2001)
LIS1	DHC	Mechanochemical clutch	(Huang et al. 2012)
Nudel/NudE	DIC	LIS1 tether	(Cianfrocco et al. 2015)
Spindly	nd	Kinetochore recruitment	(M. A. Cianfrocco & Leschziner 2014)
Hook	DHC/p25	Endocytosis/cargo binding	(Minton 2014)
Rab11-FIPS	LIC	Endosomal membrane association	(Horgan et al. 2010)

Table 1.7- The above table summarises dynein co-factors which modulate dynein-centric processes or dynein motility.

3.5.8 Dynein, axonal transport and microtubules

Cytoplasmic dynein 1 is crucial in the transport of cargos along microtubule tracks from the cell periphery. This retrograde stream of cargo is especially important in large polarised cells such as motor neurons in which the trafficking occurs between distal neuronal synaptic terminals and the cell soma.

Whilst the regulation of dynein and its specific cargoes can be modulated via various co-factors and adaptors, the activity of dynein is totally dependent on microtubules. Firstly, the posttranslational modifications of tubulin, the primary subunit of microtubules have been strongly implied in the interaction between dynein and their microtubule tracks. Increasing acetylation of tubulin at lysine 40 has been shown to increase retrograde transport through the recruitment of the dynein motor (Dompierre et al. 2007). Secondly, intracellular location of microtubules is vital as dynein can only act in cellular compartments in which microtubules are intact. The permutations of these mechanisms will be thoroughly discussed in chapter 6.

3.5.9Endocytic vesicle transport

Aside from transportation of cargo over large distances, dynein is also involved in shorter forms of transport between the cell soma membrane and the cytoplasmic compartment. Endosomal transport is a vital cellular process in which epidermal growth factor (EGF) receptors and G-protein coupled receptors (GPCRs) for example bind their respective ligands and become internalised before being transported to the peri-nuclear region (Sorkin & von Zastrow 2009).

This processes are integral for maintaining physiological concentrations and localisation of proteins. Endosomes in mammals are transported by dynein to perinuclear regions for degradation or to be recycled back to the cell membrane via kinesin motors (Soldati & Schliwa 2006). The disruption of the endocytic pathway has been suggested to play a role in neurodegenerative diseases such as Parkinson's Disease (Schreij et al. 2015).

3.6 Transport independent roles of dynein

3.6.1 Dynein at the Golgi apparatus

The Golgi apparatus is a highly dynamic organelle responsible for the post translational modifications of proteins. It is an organelle that is important for axon homeostasis and neuronal migration. Structurally, the Golgi apparatus (hereafter Golgi) is comprised of multiple stacks of interconnected cisternae, this forms a continuous membrane 'ribbon' which is closely localised to the centrosome (Klumperman 2011). The size of the Golgi is dictated by cell type as well as secretory pathway requirements (Yadav & Linstedt 2011).

The Golgi can be subdivided into three distinct segments known as *cis*, medial or *trans* Golgi where the cis side of the Golgi faces the nucleus and the trans side faces the cell membrane (see Figure 2.2). Each subdivision has its own subset of proteins that are associated with that particular region of the Golgi although some proteins reside in multiple segments (Yadav & Linstedt 2011). Table 1.8 outlines key proteins and their associated Golgi localisation including optineurin mutations in which cause ALS. In neurons small segments of Golgi membrane

reside in dendrites and distal regions of axons known as Golgi outposts that are crucial for local translation of proteins (Quassollo et al. 2015).

Cytoplasmic dynein is localised to the Golgi and DHC knockout mice exhibit fragmented Golgi in early embryonic cells (Harada et al. 1998). Furthermore, targeted knockdown of either the DHC, DIC, or dynein light chain (hereafter, DLC) resulted in perturbed Golgi structure (Palmer et al. 2009). A mouse model of SMA-LED which is discussed later (*Loa* mice) also shows a deficiency in Golgi reformation after washout of microtubule depolymerising agent nocodazole (Hafezparast 2008).This clearly indicates that cytoplasmic dynein has an important functional role at the Golgi apparatus.

Recent evidence from Yadav et al. has identified golgin 160 as a binding partner for dynein at the Golgi membranes (Yadav et al. 2012). The DIC subunit interacts with golgin 160 via Arf1 and is important for Golgi positioning. Golgi positioning is crucial in neurons as secretory pathways need to face the direction of polarisation in neurons in order to deliver proteins to distal compartments such as synapses. However, this only provides a very basic insight into the function of dynein at the Golgi apparatus. Golgi membrane trafficking is not well understood and the holistic role that dynein plays in this respect is likely to be complex.

Table 1.8- Key Golgi proteins

Protein	Localisation
Lava lamp	Golgi
Golgin 160	*cis* Golgi
GMAP210	*cis* Golgi
Golgin 245	*trans* Golgi
Dynein	Golgi
Dynactin	Centrosome
Huntingtin	*trans* Golgi
BICD2	*trans* Golgi
Golgin 97	*trans* Golgi
Golgin 84	*trans* Golgi
Myosin VI	Golgi
Optineurin	Golgi
Hook 3	Centrosome
Clasp 1/2	Golgi
GM130	*cis* Golgi
Spectrin	Endomembranes
Giantin	*cis*/medial

Figure 2.2

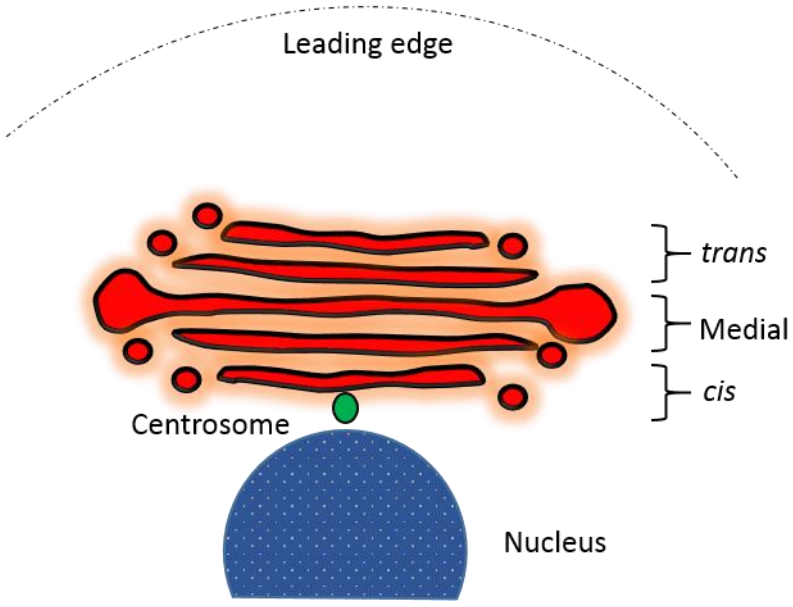

Table 1.8 and **Figure 2.2** – A list of key proteins and their respective Golgi localisations. The term Golgi refers to the entire organelle and endomrembranes refer to membranes from the endocytic pathway. Table adapted from (Yadav & Linstedt 2011).

3.6.2 Cortical and nuclear dynein

Microtubule organising centres (MTOCs) such as the centrosome are important for generation of microtubules and for imposing intracellular forces through molecular motors such as dynein. These forces control cell polarities as well as dictate aspects of cell division (Laan et al. 2012). The positioning of MTOCs are controlled by the interaction between microtubules and the cell cortex. Studies in yeast have identified that dynein is captured by a cortical anchor Mcp5 which subsequently activates dynein motility in order to position the mitotic spindle (Lammers & Markus 2015). The capture of dynein to the cell cortex involves dynein at the tips of microtubules in an 'off' state, recently Num1 was identified as the molecular 'on' switch that removes LIS1 motor inhibition (Lammers & Markus 2015). This indicates that dynein is an important cellular anchor between microtubules and the cell cortex. Furthermore, dynein has been reported to be found on nuclear pores along with dynactin and BICD2. This is thought be a mechanism to facilitate nuclear migration in dividing cells between G2 of the cell cycle and mitosis (Hu et al. 2013). In summary, these functions of dynein indicate that it has a crucial role to play in cell division.

3.7 SMA-LED DYNC1H1 mutations

3.7.1 R399G mutation

The p.Arg399Gly mutation was identified in a homozygous patient that had presented with floppiness and joint contractures at birth (the source of homozygous human fibroblasts in this study were obtained from a skin biopsy

from this patient). This patient also presented with thinning of the lower limbs (typical of SMA-LED) as well as learning and speech difficulties with attention deficit hyperactivity disorder (ADHD) at the age of 9.5 with malformations of cortical development (MCD). The father and mother were both heterozygous for the variant and the father presented with lower limb weakness in the fourth decade with no data available for cognitive ability (Scoto et al. 2015). In this study the heterozygous fibroblasts were obtained from a skin biopsy from the father.

The R399G mutation resides in the tail domain of dynein specifically in the homodimerisation domain of the DHC and is outside of the region in which the DIC interacts with the DHC subunit (see Figure 2.3). A comprehensive list of all known SMA-LED mutations in the DHC is shown in Table 1.9.

Ethical approval of the use of human fibroblasts from the MRC Centre for Muscular Diseases was obtained in an ethical committee on the 22nd December 2010. Please see the National Research Ethics Service document for full details (REC reference 09/H071661).

3.8 SMA-LED mouse models

3.8.1 *Loa* mouse model

The *Loa* (legs at odd angles) mouse model was developed at the MRC Mammalian Genetics Unit in Harwell in 1984. The original female mouse was generated by ENU mutagenesis of male C3H mice and was noticed for having a reptilian locomotion as well as holding her legs at unusual angles when suspended from the tail. This is an indicative phenotype that corresponds to a

motor system deficit. The mouse was subsequently bred with the 101 strain and the heterozygous mice were found to exhibit a slowly progressive locomotor phenotype (similar to that observed in SMA-LED) with grip strength deficiencies compared with wild-type littermates. The point mutation induced by the ENU led to a p.Phe580Tyr substitution in the DIC binding region of the *Dync1h1* gene (see Figure 2.3) in which homozygotes die shortly after birth (~24 hours).

Table 1.9- DYNC1H1 mutations in SMA-LED

Protein variation	Location	MCD
p.Ser3360Gly	Stalk	No
p.Glu3048Lys	AAA4	Yes
p.Glu2616Lys	AAA3	No
p.Arg1603Thr	Tail domain	No
p.Gln1194Arg	DHC HD	Yes
p.Tyr970Cys	DHC HD	Yes
p.Trp673Cys	DLIC BR DIC BR DHC HD	No
p.Lys671Glu	DLIC BR DIC BR DHC HD	No
p.Val612Met	DIC BR DHC HD	No
p.Glu603Val	DIC BR DHC HD	No
p.Arg598Cys	DIC BR DHC HD	No
p.Arg598Leu	DIC BR DHC HD	No
p.Ile584Leu	DIC BR DHC HD	No
p.Met581Leu	DIC BR DHC HD	No
p.Arg399Gly	DHC HD	Yes
p.Asp338Asn	DHC HD	No
p.His306Arg	DHC HD	No
p.Arg264Gly	Tail domain	Yes
p.Asn199Ser	Tail domain	No

Table 1.9- Table outlining all SMA-LED causing DYNC1H1 mutations outlining subunit binding regions (BR) and the homodimerisation domain (HD). Information regarding functional regions of the DHC protein was cross-referenced using Uniprot and Scoto et al. (2015). The table also outlines if the mutation causes malformation of cortical development (MCD). Table adapted from (Strickland et al. 2015; Scoto et al. 2015).

Figure 2.3

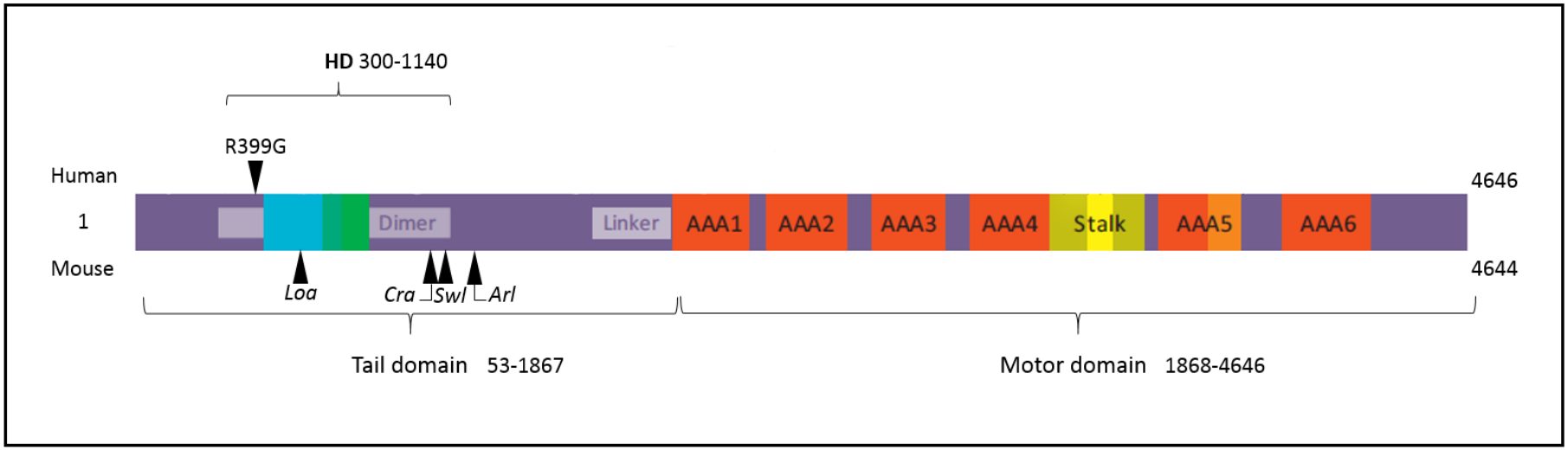

Figure 2.3- Schematic diagram with amino acid annotations of the DHC depicting the location of the R399G mutation as well as the locations of the *Loa*, *Cra*, *Swl*, and *Arl* mouse model mutations. The homodimerisation domain (HD), tail domain and motor domain all have amino acid annotations corresponding to the human protein.

Subsequently, research on the effect of this mutation on the dynein complex showed that the DIC binding affinity to the DHC is increased and subsequently LC binding (alternatively named Tctex-1) to the DIC (Garrett et al. 2014). This in turn causes a compromised binding of the $p150^{Glued}$ subunit of dynactin (Deng et al. 2010). Consistent with these findings further research has shown aberrant trafficking of endosomes through impaired velocity and run lengths in homozygous *Loa* mice (Garrett et al. 2014).

3.8.2 *Cra1* mouse model

In 2001 when the genomic region of the *Loa* mouse was presented at a conference Dr. Andreas Russ realised that the region and mutation was near identical to another mouse model, Cramping 1. This was a mouse model generated by a German ENU mutagenesis project and was found to have a p.Tyr1055Cys mutation over 400 amino acids away (see Figure 2.3) from the *Loa* mutation in the homodimerisation (HD) domain (Hrabé de Angelis et al. 2000). Similar to the *Loa* model the *Cra1* model exhibits an unusual twisting and hind-limb grasping phenotype when tail-suspended, and the homozygous mice die shortly after birth (~24 hours). At 16 months old significant loss of spinal α motor neurons is observed in heterozygous mice a phenotype which is mirrored by the heterozygous *Loa* mice (Hafezparast 2008).

3.8.3 *Swl* mouse model

The Sprawling (*Swl*) model was similarly developed at Harwell although this model was generated through irradiation rather than ENU. The *Swl* mouse was generated much earlier than other models in 1967, but it was only in 2007 that the mouse was genetically characterised. A deletion of 9-bp (Δ1040-3) was detected giving rise to a G-I-V-T to A amino acid change at position 1040 (see Figure 2.3) (Chen et al. 2007). The *Swl* mice show an abnormal clenching phenotype similar to that of the *Loa* and *Cra1* models and also show a reduction in hind-limb grip strength. These mice additionally have sensory deficiencies and exhibit dorsal root ganglion degeneration during development (Chen et al. 2007).

3.8.4 *Arl* mouse model

The *Arl* model coined 'Abnormal rear leg' was generated via an ENU mutagenesis project in Toronto at the Centre for Modelling Human Disease (CMHD). Characteristic of other *Dync1h1* mutations the *Arl* model exhibits a similar clenching of the hind limbs reflective of the previously discussed models. The autosomal dominant p.T3616C mutation leads to a more severe phenotype than the *Loa* mice resulting in a p.Trp1206Arg change in the protein sequence. Noticeably, the breeding of this model line is notoriously difficult to maintain through sporadic loss of new-born pups possibly due to parental behaviours or feeding difficulties. This is supported by a noticeable reduction in size in comparison to wild-type litter mates up to 2 weeks of age seen in heterozygous mice as homozygous mice are non-viable. A slow progressive motor phenotype exhibited by the *Arl* mice is supported by loss of muscle force in 1-year-old mice (data unpublished) although further experiments are required to characterise the severity of the *Arl* mutation.

3.9 Research aims and objectives

The basis of my research is concentrated on revealing the cellular and molecular basis underlying neurodegeneration in adult onset amyotrophic lateral sclerosis (ALS) and in the congenital disease spinal muscular atrophy with lower extremity predominance (SMA-LED).

Mutations in RNA binding proteins FUS and TDP-43 are pathogenic in motor neuron disease but the disease mechanisms of motor neuron degeneration are unknown. Although previous literature has suggested a role for FUS in DNA damage repair little information currently exists about the specific role it plays at DNA lesions. Additionally, as TDP-43 shares many functional similarities with FUS there has been no published research analysing the potential role that TDP-43 could also play in DNA repair. To investigate this, I have investigated what response both FUS and TDP-43 have to DNA damage, if mutations in FUS can perturb this response and what mechanisms may underlie the recruitment of FUS to DNA lesions.

Mutations in dynein cytoplasmic 1, heavy chain 1 (*DYNC1H1*) are associated with SMA-LED, an autosomal dominant congenital motor neuron disease. The holistic role that the retrograde dynein motor plays in cells is incomplete and the implications of mutations in its largest subunit are not clear. In order to analyse the repercussion of human DYNC1H1 mutations I studied human patient fibroblasts harbouring a p.R399G mutation. This work was firstly to elucidate if this mutation could impair the subunit composition of the complex. Secondly, to explore the potential impact this mutation could have on the Golgi apparatus as

dynein mutations are known to impair Golgi reformation after artificial fragmentation. Thirdly I set out to unveil potential underlying mechanisms that could relate dynein mutations and perturbed Golgi structure.

The *Arl* mouse model (see SMA-LED mouse models) is known to recapitulate the slow motor neuron disease progression of SMA-LED, but this model is yet to be fully characterised. One symptomatic feature sometimes seen in SMA-LED is malformations of cortical development (MCD). I set out to understand if this dynein mutation resulted in any malformation of cortical organisation in the brains of *Arl* mice. Additionally, I went on to investigate if any changes in cortical development were related to cell migration deficits caused by the *Arl* mutation by analysing mouse embryonic fibroblasts from this model.

Chapter 2- Materials and methods

4.0 Genotyping

4.1 DNA preparation

Approximately 0.1 cm^2 of tissue was obtained either from the ear or tail using a sterilised ear punch or scissors, respectively (unless stated otherwise). The tissue was subjected to a digest using 200 μl of lysis buffer containing 2 μl of proteinase K (20 mg/ml) at 55 ^oC overnight. The following day the digested tissue was subjected to centrifugation at 16 RCF for 5 minutes before diluted in double distilled water (1:50). To ensure homogeneity, diluted DNA samples were vortexed and unless otherwise stated 1μl of this diluted DNA was used in all PCR reactions.

4.2 *Arl* genotyping

A 10μl PCR reaction was conducted comprised of Qiagen Hot Start Taq (Qiagen, 203203) comprising of dNTPs (200 μM), $MgCl_2$ (4 mM), Qiagen Hot Start polymerase (2.5 units of activity), forward primer (0.1 μM), reverse primer (0.1μM), double distilled H_20, and DNA (0.1μg). The primer sequences used are as follows: Forward primer sequence 5'-CACTCCAGATGCACAGTGCTCTCCAACCAC -3'; Reverse primer sequence 5'-CCCACTCACCCTCGATGTTGTCAATGTAAACCC -3'.

The PCR parameters are outlined as: DNA denaturation (initial) 15 minutes at 95 ^oC, denaturation for 30 seconds at 94 ^oC, primer annealing for 30 seconds at 63 ^oC, extension for 1 minute at 72 ^oC, these steps were repeated 34 times before a

final extension for 10 minute at 72 ^{o}C. The subsequent PCR product was then digested with Ava I restriction enzyme (5 units per reaction). This will result in distinct signature bands as the *Arl* mutation creates a site that the Ava I enzyme can recognise (C'YCGR'G) this PCR protocol was designed by Amelia Philpott. The PCR product was subsequently run on a 3% agarose gel for 35 minutes in order to achieve adequate separation (Figure 2.4). Heterozygous mice will produce 3 bands (270bp, 235bp, and 35bp), homozygous mice would produce 2 bands (although these mice are not viable) of 235bp and 35bp, and wild-type mice will produce a single band (270bp) as shown in the figure below. The 270bp fragment represents the uncut product and the 235bp fragment and the 35bp fragments are the product of Ava I restriction (note the 35bp product will run off the gel during the separation of the 270bp and 235bp product).

Figure 2.4

A

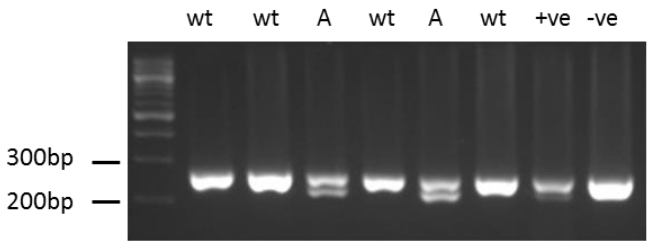

A= *Arl* heterozygote
wt= Wild type
+ve= Positive control
-ve= Negative control

B

Primer sequences 5' - 3'
F- CACTCCAGATGCACAGTGCTCTCCAACCAC
R- CTCACCCTCGATGTTGTCAATGTAAACCC

GTTTGTGTTGGTAGAGAAACTGACAGGCCACTCCAGATGCACAGTGCTCTCC
AACCACAACAGTCGTGAGGTAGACGGTTATAGAAGGCAGGTGCTTTGATCTG
TGTGTCCTTCTGTCCCAGGAGTCCTGCTTGTTGTCGAGAGGTTGGCAGTGAT
TTCTCCTATTGTTATAGGAAAAAAACCAATTTATCCTTTTATCTTTCAAAGCTCT
ACCGCAATGGTCAGCGTCTGCTGGAAAAACAAAGGTTCCAGTTCCCGCCTTC
TCGGGTTTACATTGACAACATCGAGGGTGAGTGGGGGGCCTTCAATGACAT
CATGCGGCGGAAGGACTCTGCCATTCAGCAACAGGTGGCAAACCTGCAAAT
GAAGATCGTACAGGAGGACAGAGCTGTGGAAAGCCGGACCACGGATCTGTT
GACAGACTGGGAGAAGACCAAACCTGTCACAGTGAGTGTCACTTAACCCTGC
CAGCCAGCAGCACATCATGGCTTCTTTCTGACAGACTTGGGAGGCCACTCCG
CGGCATAGCTTTTCAGATATGTCTGCCCTCCAGTAACTACAAGGCCGCATGG
TAGCCAGTCATTTAGGCTAAGGCAGAAGGGTTGCTTGGGTATGTGAGTGTGA
GGCAGCATGGCAAGATGCCACCAAAATAACAGTGAGGAGCTGGGAGCAGAG
CAGTAGGGACC

Figure 2.4- **(a)** The figure depicted above indicates an agarose 3% gel representative of PCR products after AvaI restriction in *Arl* mice in comparison to wild-type mice. **(b)** Additionally, the figure illustrates the primers employed and the subsequent sequence that is amplified during the PCR reaction. The reverse primer shows a mismatch shown in red this should be a 'G' but the mutation 'C' creates the Ava I site (highlighted in blue) in conjunction with the mutation. The *Arl* mutation is a 3616T>C substitution (larger font) resulting in a change from tryptophan to arginine.

4.3 TDP-43 ^{F210I} genotyping

A 10 μl PCR reaction comprised of Microzone (2MM-1) Taq (5 μl), forward primer (0.1 μM), reverse primer (0.1 μM), $MgCl_2$ (2.75 mM), double distilled H_20, and DNA (1 μg) per reaction was employed. This method of identification relies on two separate reactions per DNA sample. The PCR parameters used are as follows: DNA denaturation (initial) 5 minutes at 95 ^oC, denaturation for 30 seconds at 95 ^oC, primer annealing for 30 seconds at 63.5 ^oC, extension for 1 min at 72 ^oC, these steps were repeated 34 times before a final extension for 10 min at 72 ^oC.

One reaction uses two outer primers that produce a band of 225bp in addition a primer specific to the wild-type sequence was included producing a 143bp band in both the wild-type and the heterozygous mice (Figure 2.5). Similarly, the second reaction comprised of the same outer primers but the inner primer is specific to the F210I mutation (Figures 2.5, 2.6 and 2.7). The outer primers simply provide a control to asses if the PCR reaction has worked whereas the allele specific primer denotes the genotype.

Figure 2.5

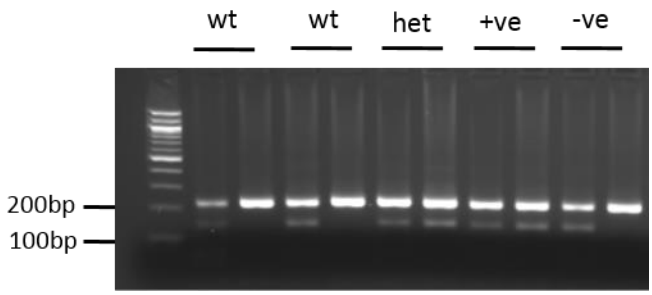

Reaction	+/+	TDP43^{F210I}/+	TDP43^{F210I}/TDP43^{F210I}
1			
2			

Figure 2.5- The above figure illustrates the band pattern produced by the products of the F210I genotyping in each of the cases for both reactions 1 & 2 for each of the genotypes. The PCR product was run on a 2% agarose gel for 20 minutes depicted at the top of the figure, along with the positive (+ve) and negative (-ve) controls.

Figure 2.6

GTCTTGTCAGTATACACCTTTAATTTCCATCTGGGGTGCGGGTGTGTGTACAGG
CCAGGCAGTAGTACACAGTTAGCCTCATCTTTAGAAACAAAAACACCCAAGACG
GGAAGGCACTTAAGTATGCATTGATGTGTTTACCATCTCCTGTTCTCTCTTGACC
AGCAAAGCCCAGACGAGCCTTTGAGAAGCAGAAAGGTGTTTGTTGGACGTTGT
ACAGAGGACATGACTGCTGAAGAGCTTCAGCAGATTTTCTGTCAGTATGGAGA
AGTGGTAGATGTCTTCATTCCCAAACCATTCAGAGCTTTTGCCTTCGTCACCTTT
GCAGATGATAAGGTATATTTGTTGGTCATTTGTCCCAGGGCTGGGAATGGATCT
GGTTTAGTGCTACTGTATGTGCCCAGCATGGTACACCAGGGGCTGCACTCAGT
CTCCAACACTGAAAATGATAAGT

Primer Type	Primer sequence
Wild-type allele specific primer	TACCACTTCTCCATACTGACAGAATAA
Mutant allele specific primer	TACCACTTCTCCATACTGACAGAATAT
Outer forward primer	GTGTTTACCATCTCCTGTTCTCTCTT
Outer reverse primer	GACAAATGACCAACAAATATACCTTATC

Figure 2.6- The above figure shows the sequence that is amplified surrounding the F210I mutation (A>T). The colour coded primers in the table correspond to the nucleotides they complement in the above sequence. The 'A' in larger font denotes the mutation whilst the nucleotide 'T' highlighted in purple corresponds to the introduced mismatch.

Figure 2.7

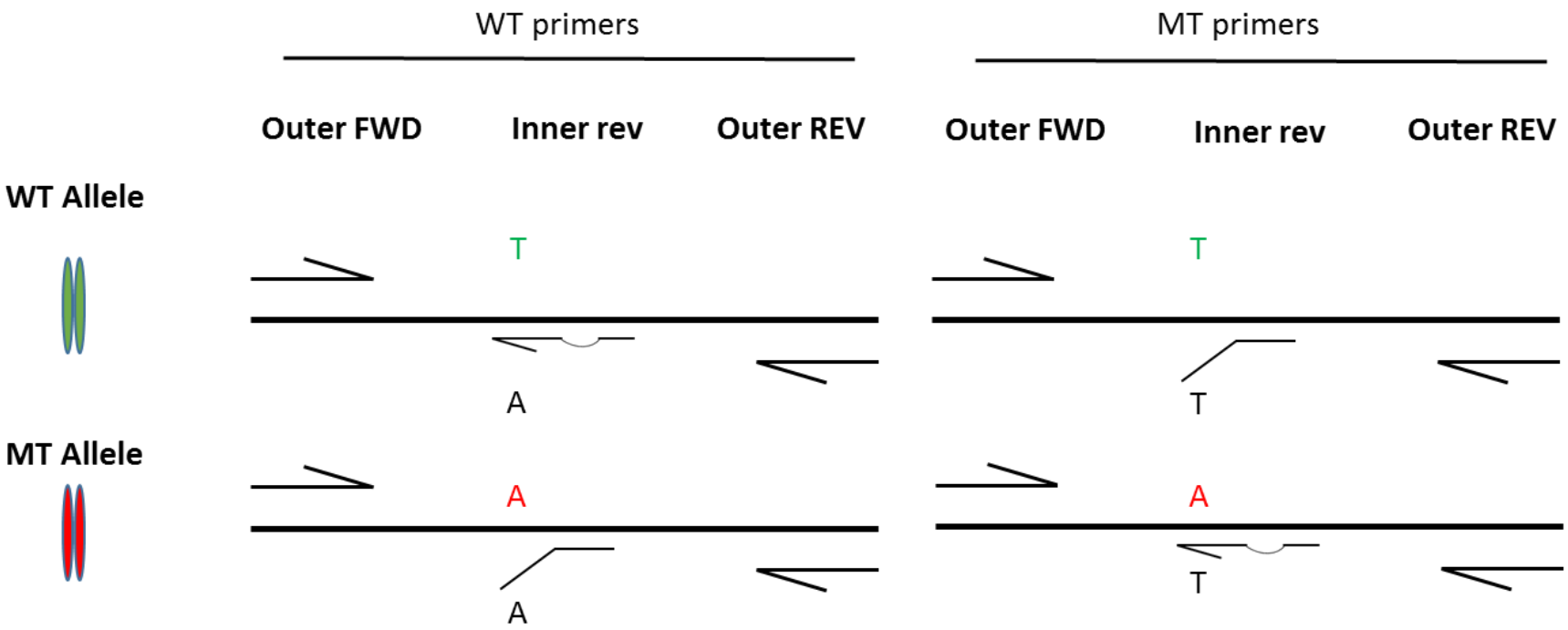

Figure 2.7- The above schematic diagram illustrates the methodology of genotyping TDP-43^{F210I} mice using three separate primers to generate PCR products. The red lettering denotes the mutation; the green lettering denotes the wild-type sequence.

4.4 *Fus* ^{D520G} genotyping

A 10 μl PCR reaction comprised of Microzone (2MM-1) Taq (5 μl), forward primer (0.1 μM), reverse primer (0.1 μM), $MgCl_2$ (2.75 mM), double distilled H_20, and DNA (1 μg) per reaction was employed. The reaction conditions for the PCR are as follows: denaturation (initial) 5 minutes at 95 ^oC; denaturation for 30 seconds at 95^oC; primer annealing for 30 seconds at 64.1^oC; extension for 1 minute at 72 ^oC; 34 cycles; final extension for 10 minutes at 72 ^oC. The subsequent PCR product is then digested with Alw I producing three separate segments of DNA as two restriction sites are present in the wild-type sequence. The D520G mutation removes one of the restriction sites producing only 2 bands (Figures 2.8 and 2.9).

Figure 2.8

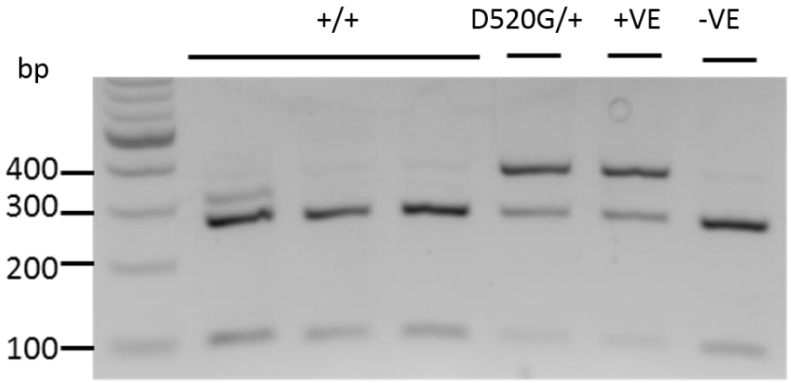

Primer Type	Primer sequence
Forward	**TTTTGGCCCTGGCAAGAT**
Reverse	**TAGTCTGACACACACACACAC**

AGAATTGAAGATGATAACATGACTTTTTTTCTAGGGGGAAACTATGGAGATGAT
CGACGTGGCAGAGGAGGATATGACCGGGGCGGCTACCGGGGCCGAGGAGG
GGACCGTGGGGGCTTCAGAGGGGGCCGGGGTGGTGGGGACAGAGGCGGTT
TTGGCCCTGGCAAGATGGACTCCAGGTGAGTAAGTCAAAACAAAAGTCAAGA
AAATTGGTCAGAGATCATGAGGAAATCAGGTTTCCCTGGGAAAGTCAGCTTAG
CTGGTTACATTTTTGGGAAGGAAGAAGAAAAGTTCAGAACCCAGTCTTTGAGG
CTGTTTTGCTTTAAAGTCATTTGTTGGGTAGCAGAGACTTGAAGGGTGTGCAT
GGGTAGGGTAGTTCAGTAACACGTAATCTAACATAACTTTTTCTTTCAGGGGC
GAGCACAGACAGGATCGCAGGGAGAGGCCATATTAGCCTGGCTCCTGAAGTT
CTGGAACTCTTCCTGTACCCAGTGTTACCCTTGTTATTTTGTAAACTTACAATT
CAGGATCGCTCATGGATATTTTTTTTTGGGGGGGGTGGGGCGGTTGTGTGTG
TATGTGTGTGTGTGTGTCAGACTACCCTAATTGTAACCATATCTCTGGTTCC
CATTAAAAAACATCATTTTAGTTAAATTCTGTTTCCCCCAGTTTACTTTCTGAAG
AATGGGTCCATGTTATTAATGTGGGGCAGTATTAT

Figure 2.8- The above illustrates the agarose gel run for both wild-type and FUS D520G sequences after a 1.5-hour digestion at 37 ^{o}C with the AlwI restriction enzyme. Additionally, the sequence amplified is encompassed by the forward (yellow) and reverse (blue) primers shown above.

Figure 2.9

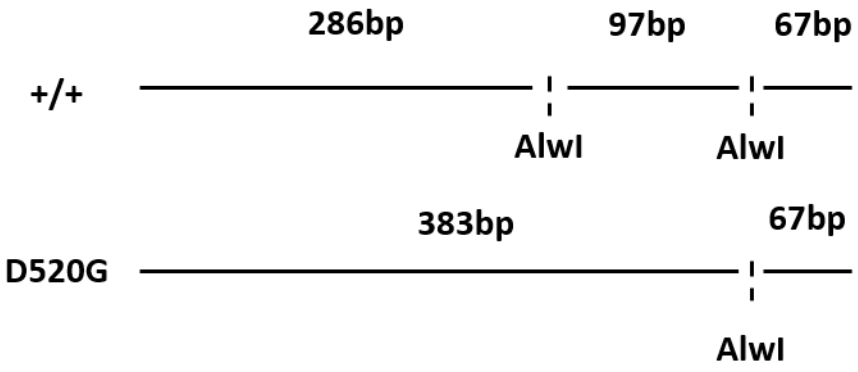

Figure 2.9- The above figure illustrates the locations of the restriction sites that the Alw I restriction enzyme can recognise in the PCR products for both wild-type and mutant D520G sequences.

4.5 DYNC1H1 ^{R399G} genotyping

DNA was obtained from collecting human fibroblasts from a T25 tissue culture flask before lysing the cells using the same protocol employed for DNA extraction when using tissue biopsies.

A 10 μl PCR reaction comprised of Microzone (2MM-1) Taq (5 μl), forward primer (0.1 μM), reverse primer (0.1 μM), $MgCl_2$ (2.75 mM), double distilled H_20, and DNA (1 μg) per reaction was employed. The reaction conditions for the PCR were as follows: denaturation (initial) 5 minutes at 95 ^oC; denaturation for 30 seconds at 95 ^oC; primer annealing for 30 seconds at 64.1 ^oC; extension for 1 minute at 72 ^oC; 34 cycles; final extension for 10 min at 72 ^oC. Two reactions are set up in parallel for each cell sample. The first reaction (reaction 1) comprised of two outer primers (which will anneal to both wild-type and mutant sequences) and one inner

reverse primer specific to the wild-type sequence. Reaction 2 had the same outer primers but the inner reverse primer had specificity to the mutant sequence. When the allele specific primer can adequately anneal to the corresponding sequence a product of 188bp is produced which out-competes the outer primers during the PCR reaction (normally producing a product of 515bp). Conversely, if the inner allele specific primer cannot anneal to the template the outer primers will successfully amplify the 515bp product (Figure 3.0).

Figure 3.0

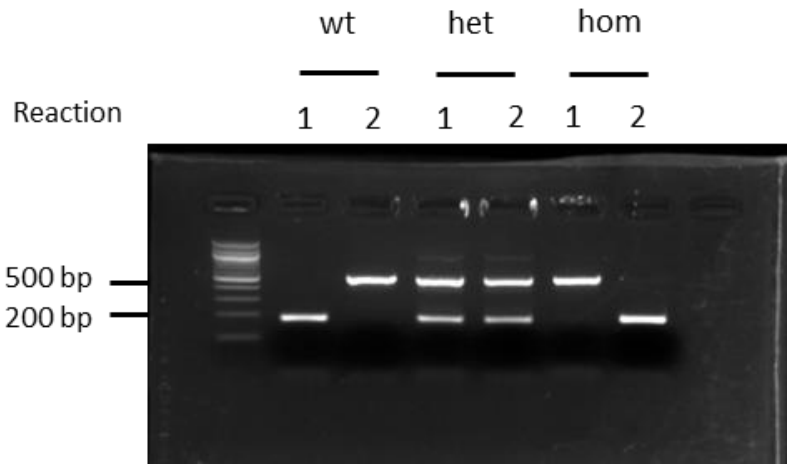

Primer Type	Primer sequence
Wild-type allele specific primer	GCAACATGCATCAATTTCCT
Mutant allele specific primer	GCAACATGCATCAATTTCCC
Outer forward primer	GATTTGCTGTCTGCCACGGA
Outer reverse primer	AGGACCCTGACGATAACAGC

GTCTAAAACAGGCTTTGGAAACTGTGAATGACTACAATCCTCTGATGAAAGATTT
CCCTCTGAATGATTTGCTGTCTGCCACGGAGCTGGACAAAATAAGACAGGCGC
TTGTTGCCATTTTCACACATTTGAGAAAGATCCGAAACACAAAATATCCTATTCA
GAGGGCACTGCGTTTGGTGGAGGCAATTTCAAGAGACTTGAGTTCTCAATTACT
CAAAGTATTGGGCACTAGGAAATTGATGCATGTTGCTTATGAAGAATTTGAAAAA
GTAAGTTTGAATATATAAGACAACCAACCTCAAGACATTGAGATGAAAATATGTC
TTAATAATAAGCCTCACTTTTGAAATTATATCCTAGGTTATGGTAGCATGCTTTGA
AGTTTTTCAGACTTGGGATGATGAGTATGAGAAACTTCAGGTATTGTTGAGAGA
CATCGTCAAAAGAAAAAGGGAAGAAAATCTGAAGATGGTGTGGCGTATCAACCC
TGCCCACAGGAAGCTGCAGGCCCGCCTTGACCAGATGAGAAAATTTAGACGCC
AGCATGAACAGCTAAGAGCTGTTATCGTCAGGGTCCTGAGGCCACAG

Figure 3.0- The above figure illustrates the substitution at position 1195 from an A to a G (base highlighted in red). The yellow portion of the sequence denotes an intron whereas the black font represents coding sequences (all primers here were designed against coding sequences).

5.0 Cell culture and tissue dissection

5.1 Dissection and culture of murine embryonic fibroblasts

A female pregnant mouse was sacrificed through cervical dislocation at 13 days post-coitum. The mouse was then position using pins on a cork dissection board in order to access the ventral side of the mouse. Sterile autoclaved and ethanol (80%) washed dissection tools were used to open the abdomen of the mouse and carefully remove the embryos. Subsequently the embryos were placed in a 10 cm diameter sterile petri dish in DPBS (Thermofisher,14040133) supplemented with penicillin and streptomycin (Sigma, P4333) at 4 ^{o}C on ice.

Each embryo was removed from its respective amniotic sac and placed in a black dissection dish under a dissection microscope. The amniotic sac from each embryo was kept aside in a 1.5 ml tube on ice for genotyping purposes. For each embryo the head was then removed using a sterile scalpel as well as any remaining red coloured tissue. Subsequently, this dissected tissue was then washed with DPBS supplemented with P/S before dicing the body tissue with a razor blade in 100 μl of DPBS until homogenous. The tissue was transferred into a 15 ml falcon tube before allowing the tissue to settle in the bottom of the tube through gravity in a laminar flow cabinet. The DPBS was carefully aspirated before adding 0.05% Trypsin (Gibco, 25200056) supplemented with DNase (Sigma, D5025) at an activity of 100 u/ml and incubating in a water bath at 37 ^{o}C for 15 minutes inverting the tube every 5 minutes. The tube was removed from the water bath and any undigested pieces of tissue were allowed to sink to the bottom of the tube. The supernatant was then carful removed and added to 2 ml

of MEF media in a universal tube before centrifuging the cells for 5 minutes at 390 g. The resultant cell pellet was then resuspended in 5 ml of MEF media before transferring the suspension to a T25 tissue culture flask for subsequent culturing of fibroblasts.

5.2 Dissection and culture of cerebral cortex neurons

A female CD1 mouse was sacrificed at 18 dpc by cervical dislocation. Subsequently, embryos were removed from the abdomen followed by quick removal of the heads. When required tail tissue was removed in order to genotype the mice. Carefully, the brains were removed from the cranial cavity and placed in HBSS -/- (Invitrogen, 10594243) containing 1% P/S. Using a dissection microscope and forceps the meninges covering the cortical surface of the brain were carefully removed and the hemispheres were then separated. Both hemispheres were then moved into fresh HBSS -/- (without Ca^{2+}or Mg^{2+}) in order to avoid debris accumulation. One at a time, both hemispheres were sliced as finely as permitted by anchoring the hemisphere with forceps whist slicing sections using a scalpel producing around 5 slices per hemisphere. These slices were then placed flat and then using 18-gauge hypodermic needles the cortical tract was targeted and carefully the cortical tissue was removed away from the rest of the brain for each slice concurrently. After the slices were obtained each was sliced into cubes, collected and placed into 10 ml of HBSS -/- in a 15 ml tube. The cortical tissue was then washed once in HBSS -/- before being exposed to pre-warmed HBSS-/- containing 0.04 % trypsin for 15 minutes (inverting the tube every 5 minutes) at 37 ^{o}C. Subsequently 5 ml of DNAase solution (0.2 mg/ml)

was added and then aspirated after which 1 ml of triturating solution was added to the re-suspend the cortical tissue. Pasteur pipettes were then fire polished by flaming the opening of each pipette using a blue flamed Bunsen burner to obtain three sizes of opening each getting gradually smaller. Starting with the pipette with the largest opening the pipette was attached to a pipet aid and the cortical tissue was pipetted up and down 15 times. This procedure was then repeated for the other two pipettes with smaller openings at which point all of the cortical tissue had dissociated and the solution had become cloudy. Neuro-basal media (3 ml) was added to the dissociated cortical neurons and were then counted using a haemocytometer. Subsequently 50,000 cells were plated onto coverslips coated with poly-D-lysine (Sigma, P6407) (overnight at room temperature) in a 24 well plate. Cultured neurons were left for 48hr before any experiments were conducted.

Culture media

Table 2.0- Human fibroblast / Mouse embryonic fibroblast medium

Reagent	Concentration
DMEM (Gibco 12491015)	-
L-Glutamine (Gibco 11500626)	1%
Penicillin/Streptomycin (Gibco 11528876)	1%
Bovine growth serum (HYC001-06B)	10%

Table 2.1- Neuro-basal medium

Reagent	Concentration
Neurobasal media (Gibco 11570556)	-
L-Glutamine (Gibco 11500626)	1%
Penicillin/Streptomycin (Gibco 11528876)	1%
B27 50x supplement (17504-044)	1x

Table 2.2 Triturating solution (50 ml)

Reagent	Concentration
Albumax (Gibco 11020-013)	1%
Trypsin inhibitor (Sigma T9003)	0.5 mg/ml
DNAse (Sigma D5025)	0.2 mg/ml
HBSS +/+ (Thermo scientific SH30268.02)	-

Tables 2.0 - 2.2 - Above tables indicate composition of cell culture media and solutions.

Laboratory consumables

Table 2.3-Tissue culture and lab plastics

Product	Company	Catalogue number
Microplate 6 well polystyrene 9.5cm^2 growth area	(VWR)	734-1599
Microplate 24 well polystyrene 1.9cm^2 growth area	(VWR)	734-1605
Art filter tips 10μl sterile	(VWR)	732-2219
Art filter tips 100μl sterile	(VWR)	732-2204
Art filter tips 200μl sterile	(VWR)	732-2207
Art filter tips 1000μl sterile	(VWR)	732-2355
Pipettes 1ml individually wrapped	(VWR)	612-3707
Pipettes 2ml individually wrapped	(VWR)	612-3704
Pipettes 5ml individually wrapped	(VWR)	612-3702
Pipettes 10ml individually wrapped	(VWR)	612-3700
Pipettes 25ml individually wrapped	(VWR)	612-3698
Falcon Tubes 50ml sterile	(VWR)	525-0158
Universal tubes 30ml	(Greiner Bio One)	201171
Cell scraper small sterile 18mm	(VWR)	734-1527
Tissue culture flask 25cm^2 vented cap	(Corning)	430639
Tissue culture flask 75cm^2 vented cap	(Corning)	430725u
Tissue culture flask 175cm^2 vented cap	(Corning)	431080
Gel tips 1-200 μl	(Alpha laboratories)	LW1100
Microcentrifuge tube polypropelene 1.5 ml	(Fisher Scientific)	11706467

Table 2.3- The above table indicates tissue culture and lab plastics used throughout experimental procedures.

Table 2.4- Tissue culture and lab glassware

Product	Company	Catalogue number
Cover slip Best circular 13mm diameter 0.08 to 0.12 mm thick	Fisher Scientific	12392128
Chambered cover glass Lab-Tek II two well sterile	Fisher Scientific	10654602
Chambered cover glass Lab-Tek II one well sterile	Fisher Scientific	177372
Glass microscope slides 76 x 26 mm	Menzel-Glaser	BS7011
Pasteur Pipettes 230 mm	Fisher Brand	FB50253
35 mm dish No.1.5 0.16-0.19 mm	Corning	p35GC-0-10-C

Table 2.4- The above table indicates tissue culture and lab glassware used throughout experimental procedures.

Table 2.5- Primary Antibodies

Antibody	Source	Western blot dilution	Immunofluorescence dilution	Host
Acetylated Tubulin	Sigma T7451	3:6000	1:400	Mouse
β–Actin	Sigma A5316	1:5000	-	Mouse
B23	Life technologies FC61991	-	1:1000	Mouse
Cofilin	Abcam ab11062	1:10000	-	Rabbit
Calnexin	Santa Cruz sc-6465	1:1000	-	Rabbit
De-tyrosinated tubulin	Abcam ab48389	1:500	-	Mouse
Dynactin (p150/135)	Santa Cruz 47711	1:200	-	Rabbit
Dynein heavy chain	Santa Cruz SC-9115	1:100	-	Rabbit
Dynein intermediate chain	Kevin pfister ab6304	1:1000	1:200	Mouse
Dynein light intermediate chain	Kevin pfister	1:1000	-	Rabbit
FUS	Novus NB100-565	1:1000	1:400	Rabbit
Giantin	Santa Cruz SC-6465	-	1:1000	Rabbit
Golgin 160	Santa Cruz sc-27680	1:1000	-	Goat
TDP-43	Proteintech 10782-2	-	1:200	Rabbit
α-Tubulin (DM1A)	05-829	1:5000	-	Mouse

Table 2.5- The above table indicates which primary antibodies have been employed throughout experimental procedures.

Table 2.6- Secondary Antibodies

Antibody	Source	Western blot dilution	Immunofluorescence dilution	Host
Anti-rabbit IgG HRP	GE Healthcare NA934	1:30,000	-	Donkey
Anti-goat IgG HRP	Santa Cruz sc2020	1:10,000	-	Donkey
Anti-mouse AP	Sigma A3562	1:10,000	-	Goat
Anti-mouse HRP	Dako P0260	1:10,000	-	Rabbit
Anti-rabbit Alexa fluor 546	Invitrogen A11035	-	1:400	Goat
Anti-rabbit Alexa fluor 488	Invitrogen A11029	-	1:400	Goat
Anti-mouse Alexa fluor 546	Invitrogen A11030	-	1:400	Goat
Anti-mouse Alexa fluor 488	Invitrogen A11030	-	1:400	Goat
Anti-rabbit Alexa fluor 633	Invitrogen A21072	-	1:400	Goat

Table 2.6- The above table indicates which secondary antibodies have been employed throughout experimental procedures.

5.3 Preparation of cell lysates

All following reagents and tools for cell lysate preparation were kept at 4 ^{o}C and centrifugation steps were conducted at 390 x g unless otherwise stated. Firstly, cells (95% confluent) were trypsinised from T175 tissue culture flasks at 37^{o}C for 5 minutes, centrifuged, and washed once with DPBS -/-. The cells were then centrifuged and the DPBS -/- was aspirated before adding an appropriate volume of RIPA lysis buffer (25mM Tris HCl pH 7.6, 150mM NaCl, 1% NP-40, 1% sodium deoxycholate, 0.1% SDS) to the cells supplemented with phosphatase cocktail inhibitor 2&3 (Sigma, P0044) and protease inhibitor (Roche, 11836170001). The suspension was then pipetted into a glass dounce homogeniser and the cells were then manually homogenised with 20 strokes and left on ice for 20 minutes. Cells that were cultured in 6 well plates were not trypsinised, but washed and lysed in the plate and manually removed using a cell scraper, transferred into an Eppendorf tube before leaving the homogenate on ice for 20 minutes to ensure complete lysis of cells.

5.3 Measuring protein concentration of lysates

The protein concentration of cell lysates were measured using a BSA assay as per the manufacturers protocol (Thermo scientific, 23227) utilising a standard curve using a nanodrop 2000 (Thermo scientific).

5.4 SDS-PAGE

Homogenates were either run on 10% laboratory prepared gels or pre-cast 12% /4-12% gels (NuPAGE, NP0341/NP0322). Higher percentage gels were used when probing for smaller molecular weight proteins and laboratory prepared gels were generally employed when protein concentration of the homogenate was reduced (more protein can be loaded in laboratory produced gels). Gradient gels were used when probing constituents for multiple proteins (Table 2.5). The transfer of protein between the gel and PVDF (Amersham, 10600021) membrane was conducted at either 100 v for 75 minutes or 20 v for 16 hours.

5.5 Immunoblotting of membranes and quantification

All PVDF membranes were blocked in 5% powdered skimmed milk dissolved in PBS containing 0.05% Tween-20 (Sigma, P9416) (PBST) for 30 minutes unless specified with agitation on a rocker. The membranes were then exposed to three quick rinses with PBST to ensure all undissolved powder was cleaned from the membrane. Primary antibody raised against the target protein was then diluted at an optimised dilution in PBST (see Table 2.5) before applying to the membrane with agitation for a duration of either one hour or overnight. Subsequently, the membrane was washed with PBST twice for a duration of 10 minutes each and then twice again for a duration of 5 minutes each. Secondary antibody with immunoreactivity to the host species of the primary antibody was then applied to the membrane for one hour. The secondary antibodies applied were diluted in PBST (see Table 2.6) and were conjugated with alkaline phosphatase or horse radish peroxidase enzymes. The membrane was then exposed to further washing

steps as outlined above before applying either CDP-STAR (Sigma, C0712) or ECL substrate (Amersham, RPN2232) to the side of the membrane containing the protein for a total of 1 minute. Subsequently the excess of the substrate was blotted onto tissue before placing between two plastic transparencies (to avoid drying out of membranes) in a developing cassette. Developing film (Thermofisher, 34089) was then placed in the cassette to ensure a tight sandwich between the film and the transparency sheets typically for a duration of 5-60 seconds before placing in a developer.

5.6 Co-immunoprecipitation

All centrifugation steps in the following protocol were performed at 0.4 x g at a temperature of 4 ^{o}C for a total of 2 minutes unless otherwise stated.

Protein A sepharose beads (Life Technologies, 101041) were washed with DPBS (W/O Ca^{2+}/Mg^{2+}) and centrifuged three times before being conjugated with either antibody raised against DYNC1I1 or golgin 160 for 2 hours at 4 ^{o}C. Simultaneously homogenates obtained from human fibroblasts were exposed to pre-washed beads to account for any non-specific interactions between the beads and homogenate.

Subsequently, pre cleared homogenates from human fibroblasts were incubated with the beads overnight at 4 ^{o}C. The beads were then subjected to five washes in DPBS each followed by centrifugation (Sigma) before one final wash in double distilled H_2O at 4 ^{o}C. The beads were then centrifuged at 16 x g and exposed to 1 x SDS sample buffer and boiled 95 ^{o}C for 5 minutes to release any protein from

the beads. The sample buffer was then removed using a gel loading tip to prevent uptake of beads and utilised for SDS-PAGE analysis.

5.7 Sucrose density gradient analysis of dynein in DYNC1H1$^{R399G/R399G}$ mutants

Linear sucrose gradients were made by the technique of freeze thawing outlined by Luthe (Luthe 1983). The gradients were formed by freeze-thawing (three times) 4.75 ml of 12.5% sucrose in DPBS -/- supplemented with the protease inhibitors and phosphatase inhibitor cocktails 2 & 3 (Roche).

For both DYNC1H1$^{+/+}$ and DYNC1H1$^{R399G/R399G}$ mutants, four T175 flasks were used to grow enough fibroblasts to achieve 10 mg/ml final protein concentration. Fibroblasts were washed once in PBS before being trypsinised and spun at 400 g to a single pellet. Subsequently, cells were lysed in 200 μl of RIPA lysis buffer. The cells and lysate were transferred to a glass dounce homogeniser before applying 20 strokes to lyse any remaining cells in the suspension. The protein concentration of the lysate was then measured against a BSA curve normalised to RIPA buffer using a nanodrop 2000 (Thermo scientific). The sucrose gradients were thawed for 2 hours at 4 ^{o}C and carefully a total of 2 mg of protein was then loaded on top of the gradients slowly as to not disturb the linear sucrose distribution. The gradients were weighed and carefully placed into a swing-bucket Sw55 Ti Beckman rotor and spun at 237,000 x g for a total of four hours at 4 ^{o}C. The gradients were carefully removed from the rotor and fixed in place using a clamp stand at eye level before 11 fractions (450 μl) were slowly removed with a

shortened p1000 filter tip. Collected fractions were kept on ice at 4 ^{o}C before being transferred to -80 ^{o}C for storage before SDS-PAGE analysis.

5.8 Immunocytochemistry of primary cells

All cells used in immunofluorescent experiments were cultured onto 13 mm glass coverslips in 24 well plates which were either coated with collagen type I (BD biosciences, 354236) or poly-D-lysine. For collagen coating of coverslips 200 μl (10 μg/ml) was used to cover the coverslips before allowing to air dry in a laminar flow tissue culture hood. Similarly, for coating with poly-D-lysine (Sigma, p7280), 200 μl was applied to the coverslips and left at room temperature overnight before washing them with 1 ml of double distilled water.

Unless otherwise stated cells were fixed at 4% FA (Thermofisher, 28906) for 5 minutes at room temperature after washing the cells once with PBS. After fixation of the cells, the PFA was aspirated before washing the cells three times in PBS before permeabilising the cells with PBS containing 0.1% Triton X-100. Cells were then subsequently blocked with 5% BSA (Sigma, A9056) in PBS for 30 minutes with agitation on a rocker. The blocking solution was then aspirated from the wells before applying 200 μl of primary antibody diluted into 1% BSA in PBS (see Table 2.5 for dilutions). The primary antibody was applied overnight unless otherwise stated at 4 ^{o}C with agitation on a rocker in a humidified box. Subsequently, the primary antibody was aspirated from the wells before washing once with 1 ml of PBS with 0.1% tween 20 and 0.02% SDS (PBSTS) for 5 minutes with agitation. The PBSTS was then aspirated before applying a fluorescent

secondary antibody raised against the host animal the primary antibody was produced from at a dilution of 1:400 with agitation. This step and subsequent steps were shielded from any light using a foil wrapped box to prevent any bleaching of the conjugated fluorophore. Lastly three final washing steps with 1 ml of PBSTS were performed to remove any unbound secondary antibody. In order to mount the coverslips onto glass microscope slides a small volume of anti-fade mounting medium containing DAPI was applied to a glass microscope slide before carefully removing the coverslip from the (Invitrogen, p36931) 24 well plate and placing it on top of the medium (cell-side down). The coverslip was then subsequently sealed with quick dry nail varnish before imaging.

5.9 Dynein and Golgi apparatus co-localisation

Human fibroblasts were cultured on glass 13mm coverslips in a 24 well plate at a density of $5x10^4$. Cells were washed once in PBS and subsequently fixed in 4% PFA for immunoflurorescent staining with antibody against DYNC1I1 and giantin.

The IC and Golgi co-localisation quantification was performed by Dr. Carlos Reyes-Aldasoro Constantino in the following way using Matlab: Both channels were thresholded with Otsu levels resulting in one red region and several green objects. The red channel was processed with closing and dilation of morphological operators and used to discard all elements of the green channel outside the resulting red region. Several measurements were obtained from the segmented results.

5.10 Golgi polarisation assay in DYNC1H1^{R399G} mutants

Monolayers of human fibroblasts were cultured on 13 mm glass coverslips before introducing a wound across the fibroblast culture from the top to the bottom of the coverslip using a sterile 10 μl pipette tip. To prevent reattachment of any removed cells the cultures were washed three times with MEF medium before being allowed to migrate into the wound for 8 hours. Subsequently the monolayers were washed once with PBS before fixation with 4% PFA for 5 minutes. Immunofluorescent staining was then conducted using a combination of giantin and phalloidin in order to determine the location of the Golgi and the direction of cell migration through actin visualisation. The quantification of the Golgi localisation during migration is outlined below.

5.11 The Azimuthal average quantification of Golgi polarisation

The polarity of the Golgi in migrating fibroblasts was quantified using the ImageJ plug-in 'Azimuthal average' by plotting normalised fluorescence over each degree radian within quadrants of the cell with reference to the direction of migration.

The images were opened in ImageJ and the pictures were split into their respective channels. A Gaussian blur filter was then applied to the DAPI image depicting the nuclei. Subsequently, a threshold was then set to detect the nuclei only in the image. The centre of the nuclei was then obtained by enabling the centre of mass option in the measurement settings. This coordinate was recorded for each cell analysed. ImageJ was then closed and reopened before opening the 'Azimuthal average' plugin in ImageJ. The X and Y coordinates were then

typed into the values window before setting the inner radius, starting angle, and setting bins to 360 to measure each degree of fluorescence. The starting angle was determined by measuring the half way point across the leading edge for each cell.

The Azimuthal average was then run and each fluorescence value for each degree for each cell was recorded. These values were then averaged across all cells measured in each genotype after subtracting a background reading of fluorescence from each Image. The final fluorescence values were allocated positive values if they were facing the scratch and negative values if they were facing away from the scratch (see results).

5.12 Endosomal trafficking in DYNC1H1 ^{R399G} human fibroblasts

Human fibroblasts were plated onto 13 mm glass coverslips in 24-well plates at a density of $5x10^4$ and left to culture overnight. Subsequently the fibroblasts were serum starved for 2 hours at 37 ^oC before being placed on ice at 4 ^oC in serum-free media to prevent any endocytosis for a period of ten minutes. Directly after the cells were taken off ice, the cold medium was aspirated and then the cells were reintroduced to 37 ^oC MEF of medium. Immediately 2 μg/ml of conjugated EGF-555 was added to fibroblasts for ten minutes. The fibroblasts were then washed with MEF medium to remove any unbound antibody to the EGF receptor before re-introducing the fibroblasts to normal MEF media. Subsequently, the cells were then washed once with PBS before fixing the cells in 4% PFA at time points 0, 10, 30 and 60 minutes. Coverslips were then mounted and used for immunofluorescent imaging.

5.13 Wound healing assay

Wild-type and *Arl/+* murine fibroblasts were cultured in a six well plate at a confluency of $3X10^5$ cells in each well. The fibroblasts were then treated with mitomycin C at a concentration of 10 μg/ml for 2 hours to arrest cell proliferation. The medium was then subsequently aspirated and washed with MEF media once before returning to the incubator for a further 2 hours to allow the fibroblasts to recover. A sterile 10 μl pipette tip was then used to introduce a monolayer wound in each well of cultured fibroblasts before changing the media in each well to ensure debris and unattached cells are removed from suspension. The cells were then incubated at 37 ^oC for a duration of 12 hours to monitor cell motility after capturing a picture of the cells at time point 0.

In order to accurately capture a picture of cell migration at 12 hours to ensure the same position of the wound was imaged, tape was used to mark plate positions on a Zeiss Axiovert 25 microscope (Figure 3.1). This ensured that the exact location could be imaged at both 0 and 12-hour time points for each genotype. The images were captured with a canon G3 camera using an eye-piece adaptor (Carl Zeiss, 426126) at three separate positions from each scratch from each well at 20x magnification. To ensure the images were calibrated adequately for analysis, a picture of a haemocytometer was taken after each set of images to ensure that each picture was correctly calibrated (pixels/μm).

The acquired images were analysed in ImageJ by deducting the final area at the 12-hour time point away from the initial area of the wound at the 0-time point, this

value was then divided by 12 to provide a rate with the unit of μm^2/hr. For statistical analysis the data was first tested with a Shapiro-Wilk test to confirm normal distribution of data before performing an independent samples t-test.

Figure 3.1

Figure 3.1- The above image depicts the microscope was marked in order to find exact positions of fibroblasts wounds in a 6-well plate.

5.14 Single strand break assays with topoisomerase I inhibitor camptothecin (CPT)

Cells were counted and plated onto glass coverslips at a density of $5x10^4$ in a 24 well plate in either fibroblast media or in neurobasal media. After 24 hours, the medium was subsequently changed and the cells were exposed to 4 μM of CPT

(Sigma, C9911) for a total of 1 hour. When caffeine (Sigma, C0750) was employed as in inhibitor in relation to preventing CPT related foci the caffeine was used at either 10 μm or 20 μm and added to the cell culture 1 hour before treatment with CPT. After the treatment, cells were washed once in PBS before being fixed in 1% PFA, cells were stored at 4 ^{o}C until stained for immunofluorescent confocal microscopy.

5.15 Transfection and UVA microirradiation assays

In order to detect GFP-FUS, A549 cells were plated onto glass bottom plates (MatTek) 2 days before the start of the transfection. Subsequently the lipofectamine (GeneJuice) was diluted into optimem at room temperature for 5 minutes at a ratio of 3:100 μl (as per the manufacturer's protocol). The solution was well mixed before adding 1 μg of plasmid for a further 30 minutes at room temperature.

The transfection solution was then added to the seeded cells to a volume of 2 ml of fibroblast media. The cells were then left for 72 hours at 37 ^{o}C before being sensitised to 10 mg/ml of Hoescht dye (Sigma, 861405) for 30 minutes. Cells which were positive for GFP were then subjected to irradiation with UVA laser at 351-nm wavelength using a 40x /1.2-W objective mounted on a Zeiss Axiovert. Images were taken using a LSM 520 Meta camera. For analysing endogenous protein cells were treated as above before being fixed with 4% PFA before immunofluorescent staining.

5.16 RNA polymerase I and II inhibition

Cortical neurons were cultured as previously described and 24 hours after culture were exposed to DRB (Sigma, D1916) at a concentration of 300 μM for 1 hour and α-amanitin (Sigma, A2263) at a concentration of 4 μg/ml for 18 hours. They are both inhibitors of RNA polymerase II. In order to inhibit RNA polymerase II cortical neurons were treated with CX5461 (Selleckchem, 2S684) at a concentration of 10 μM for 1 hour. Neurons were subsequently washed three times in PBS before fixing in 1% PFA before immunofluorescent staining.

5.17 Preparation and cryo-sectioning of murine brains

Adult mice were terminally sedated before exposing the heart and subsequently an 18-gauge needle was inserted into the left atrium. An incision was made in the right atrium in order for PBS and PFA to drain after it had passed through the circulatory system of the mouse. The circulatory systems of adult mice were initially washed through with PBS for 5 minutes using a masterflex L/S 77202 at a flow rate of 5 ml/min before being perfused with 4% PFA. A last wash –through of PBS for 5 minutes was conducted before removing the brain and storing in PFA 4% overnight. For P4 mice the brains are substantially smaller and can be dissected and placed directly in 4% PFA as in the previous step without the need for perfusion. The brains were then transferred into 30% sucrose for 48 hours before being frozen in crushed dry ice and stored for sectioning at -80 ^{o}C.

Prior to sectioning the brains were transferred to a Leica cryostat set at -18 ^{o}C for 1 hour in order for the brains to equilibrate to temperature. The brains were then secured using a hard setting glue via the posterior of the brain to a stage that

then is subsequently secured into a chuck. Sections of the brain were then taken at 30μm thick and stored in a 24 well plate containing PBS. The sections were washed twice in PBS and once in PBS supplemented with 0.2% triton X-100 for 5 minutes each.

5.18 Cresyl violet staining

The sections were then carefully selected and removed from the 24 well plate into a larger 10 cm dish filled with PBS using a fine paint brush to manipulate the sections of tissue. Subsequently, the sections were gently moved and secured onto glass slides specific for mounting tissue sections (VWR superfrost plus, 631-0108). The slides were then left to dry for 16 hours on a drying rack before beginning the staining procedure. To stain the tissue sections with cresyl violet the glass slides were secured into a slide rack to enable quick transition of slides between solutions. Glass dishes were filled with 300 ml of each solution and placed in a fume hood. The slides were transferred into histoclear (national diagnostics) for 5 minutes; 95% ethanol for 3 minutes; 70% ethanol for 3 minutes; H_2O for 3 minutes; cresyl violet (Sigma, C5042) stain for 9 minutes (60 ^oC); H_2O for 3 minutes; 70% ethanol for 3 minutes; 95% ethanol for 3 minutes; and one quick dip in 100% ethanol before returning to a solution of Histo-Clear (National Diagnostics, 12358637). Glass rectangular cover-slides were then used to protect the mounted sections after application with Histomount (National Diagnostics, HS-103).

5.19 Propagation and preparation of plasmid DNA

5.19.1 Transformation of competent DH5-α E.coli

Aliquots of competent DH5-α E.coli (ThermoFisher, 18265017) were thawed (50 μl) on ice at 4 °C with occasional agitation before 2 μl of the DYNC1H1-halotag plasmid DNA was added and carefully mixed by pipetting and incubated at 4 °C for 30 minutes. The mixture was then carefully mixed again before being heat-shocked at 42 °C in a water bath for exactly 40 seconds without disturbing the mixture. The mixture was then transferred to ice for 2 minutes before SOC medium (Invitrogen, 15544034) was added to the mixture (100 μl for ampicillin selection or 400 μl for kanamycin selection, also see Table 2.7). Subsequently the mixture was then placed in a shaker for 1 hour at 37 °C before being plated onto LB agar plates containing the appropriate antibiotic (at least 100 μl of the transformed E.coli can be added to the plates) before being carefully distributed with a spreader. The plates were then left to dry at room temperature before being placed inverted in an incubator at 37 °C overnight. The following morning the plates are then checked for colonies.

Table 2.7- Antibiotics used for transformation

Antibiotic	Working concentration (High copy)	Working concentration (Low copy)
Ampicillin	50 μg/ml	20 μg/ml
Kanamycin	50 μg/ml	10 μg/ml

Table 2.7- Concentrations of antibiotic employed during transformation.

5.19.2 Midiprep of plasmid DNA

The isolation of plasmid DNA was prepared using the Purelink HiPure Plasmid Filter Purification Kit (Invitrogen k2100-04) using the manufacturers instructions. A bacterial culture was prepared by initially inoculating a starter culture comprising of 5 ml of LB broth with an inoculating loop for 8 hours at 37 ^{o}C with shaking. Subsequently this culture was then introduced into 100-500ml of LB at 37 ^{o}C for 16 hours at a dilution factor of 1:000 at 37 ^{o}C with shaking (200 rpm) ensuring that the LB medium had turned cloudy. Either 25 ml (for a high copy plasmid) or 75 ml (low copy plasmid) was centrifuged for 30 minutes at 4 ^{o}C (3760 x g). A series of resuspension steps and washing steps were then performed as instructed by the manufacturer's protocol. Finally, the plasmid DNA was pelleted by adding 100% isopropanol (Sigma, 278475), this was carefully removed before washing with 70% ethanol with minimal disturbance to the pellet. The pellet was centrifuged again for 10 minutes at 3760 g before carefully removing the ethanol and allowing the pellet to air-dry for 10 minutes. Subsequently, the DNA pellet was resuspended in an adequate volume of double distilled water (usually 100-200 μl). The obtained concentration was then calculated using a nanodrop spectrophotometer before freezing at 80 ^{o}C for further downstream applications.

5.19.3 Maxiprep of plasmid DNA

The isolation of plasmid DNA was prepared using the Purelink HiPure Plasmid Filter Purification Kit (Invitrogen, k2100-16) using the manufacturers provided instructions. A bacterial culture was prepared by initially inoculating a starter culture comprising of 5 ml of LB broth with an inoculating loop for 8 hours at 37

°C with shaking. Subsequently, this culture was then introduced into 100/500 ml of LB at 37 °C for 16 hours at a dilution factor of 1:000 at 37 °C with shaking (200 rpm) ensuring that the LB medium had turned cloudy. Either 100 ml (for a high copy plasmid) or 500 ml (low copy plasmid) was centrifuged for 30 minutes at 4 °C (3760 x g). A series of resuspension steps and washing steps were then performed as instructed by the manufacturer's protocol. Finally, the plasmid DNA was pelleted by adding 100% isopropanol, this was carefully removed before washing with 70% ethanol with minimal disturbance to the pellet. The pellet was centrifuged again for 10 minutes at 3760 x g before carefully removing the ethanol and allowing the pellet to air dry for 10 minutes. Subsequently the DNA pellet was then resuspended in an adequate volume of double distilled water (usually 100-400 μl). The obtained concentration was then calculated using a nanodrop spectrophotometer before freezing at 80 °C for further downstream applications.

5.20 Transfection of primary and immortalised cells

5.20.1 Electroporation of primary human fibroblasts

The electroporation protocol was carried out using a neon transfection system (Invitrogen MPK10025) as per the manufacturer's instructions. Cultured fibroblasts were trypsinised from T175 tissue culture flasks and spun at 400 x g before being re-suspended in PBS before being re-centrifuged. The cell pellet was then re-suspended in 115 μl of buffer 'R' before being transferred into an Eppendorf tube containing 5 μg of plasmid DNA. The electroporation module was then filled with buffer 'E' and changed after every genotype electroporated. The buffer 'R' plasmid mix was then pipetted up and down to ensure it was mixed and carefully inserted into the electroporation module ensuring that there are no

bubbles in the tip (bubbles will result in arcing and cell death). The fibroblasts were then subsequently electroporated at 1650 mV using a pulse width of 20 ms for 1 pulse only. The electroporated fibroblasts were then removed from the electroporation module and the electroporated cells were reintroduced into recovery media (MEF media lacking antibiotics penicillin or streptomycin). The fibroblasts were then plated into a 24 well plate and left to recover for 18 hours before being reintroduced to fibroblast media containing antibiotics.

5.20.2 Transfection of cells using lipofection

A549 cells were seeded into 35mm glass bottom dishes at a density of 2 x 10^5 and left overnight to culture. To make up the transfection solution 100μl of Optimem was combined with 4 μl of GeneJuice® for 5 minutes at room temperature as per the manufacturer's instructions. Subsequently 1 μg of the plasmid was then added and carefully pipetted up and down several times before being incubated at room temperature for 30 minutes. The mixture was then added to a total of 2 ml of warmed medium and added to the cells for 24 hours. The medium was then changed before further down-stream applications.

5.21 Image acquisition and analysis

Fixed cell image acquisition was conducted using either a spinning disc Olympus-3I microscope using a 63x oil objective mounted with an EMCCD Evolve camera (confocal), an Olympus BX55 with QI click camera (for morphological brain differences in mice) or a Leica TSC SP8 confocal microscope (Leica Microsystems) utilising PMT and HyD GsAsp hybrid point detectors (confocal). Image analysis was conducted using ImageJ or by Constantino Reyes-Aldosoro

using Matlab for quantifying Golgi-DIC co-localisation, Golgi fragmentation in p.R399G mutant fibroblasts and peri-nuclear acetylated tubulin.

5.22 Matlab Image analysis

All the images unless otherwise stated were processed automatically with in-house algorithms developed in Matlab ® (Natick, MA, USA). First, to quantify the fragments of Golgi per cell, individual fragments on the red and blue channels were identified separately using an intensity-based segmentation based on Otsu's algorithm for optimal thresholds (Otsu 1979). Initially, the green channel was segmented to identify a general background and foreground, which contained red and green regions by thresholding and a morphological closing with a circular structural element of 8-pixel radius. The red channel was segmented with an Otsu threshold calculated from the overlap of the foreground region with the red channel. The segmentation was applied a labelling and all regions with area lower than 10 pixels were discarded. The remaining regions were again labelled, counted and their areas and intensities calculated.

Second, to quantify the peri-nuclear acetylated tubulin, a combined intensity and distance analysis of the cells was performed similar to the analysis of focal adhesions previously described (Reyes-aldasoro et al. 2015). Briefly, the blue channel (nucleus) and green channels (whole cell) were segmented through intensity thresholding and a series of morphological operators. The distance transform from the nucleus of the cell towards the edge of the cell was calculated (Kimmel et al. 1996). For each distance from the nucleus, which appeared as an irregular concentric region, the mean intensity was calculated. This resulted in an intensity profile of the fluorescence as a function of distance from the nucleus

from which the average intensity of the profile were calculated.

5.23 Quantification of western blots

All western blot bands quantified used ImageJ densitometry analysis. Breifly, lanes were marked using the rectangular selections tool and select ‘first lane’ in the ‘analyse’ section of the tool bar. After selecting multiple lanes ‘plot lanes’ was then selected from the ‘analyse’ section of the tool bar. After generation of the peaks the background was then subtracted by drawing a straight line under each peak. The ‘magic wand’ option is selected and then clicking on each curve generated an arbitrary figure for an area under each curve representing the protein quantity for each band.

5.23 Statistical analysis

All data sets obtained from experimental findings were evaluated with tests of normality such as the Kolmogorov-Smirnov and the Shapiro Willks. This was conducted in SPSS and Q-Q plots were used in order to visualise normally or non-normally distributed data. Tests were also used to determine the Skewness and Kurtosis of the data obtained to highlight outliers in the data. The correct parametric (student T-test or ANOVA) or non-parametric (Mann-Whitney U) statistical analysis was then employed to determine significant differences between ($P<0.005$) various sets of data obtained. All graphs plotted from these data sets were constructed in GraphPad Prism with the standard error of the mean.

Chapter 3- Investigating the roles of FUS and TDP-43 in DNA damage repair

6.0 Introduction

Mutations in both *FUS* and *TDP-43* are known to be pathogenic in familial and sporadic ALS. The core reasons for why mutations in these RNA/DNA binding proteins result in the disease of motor neurons are not clear as they have diverse functions, some of which are shared.

The role of FUS in DNA damage repair has been previously eluded to through research conducted by Hicks et al. and Wang et al (Hicks et al. 2000; Wang et al. 2008). Firstly, *Fus* knockout murine fibroblasts were shown to exhibit cases of aneuploidy and chromosomal breakage implicating the importance of *Fus* in chromosomal stability (Hicks et al. 2000). Secondly, DNA damage has been shown to induce binding of FUS to ncRNAs leading to inhibition of the *Cyclin D1* gene indicating that FUS has an active response to DNA damage (Wang et al. 2008). However, the exact mechanistic role of FUS when responding to DNA damage is unknown and could prove vital in understanding motor neuron pathology in ALS.

The way in which TDP-43 responds to instances of DNA damage is even more uncertain than the FUS response due to a lack of data. However, importantly TDP-43 has been shown to have a close association with transcription. Recent literature has suggested that the stalling of transcription at a site of DNA damage can initiate a repair mechanism known as transcription-coupled nucleotide excision repair (TCR) (Haines et al. 2014). This indicates that transcription and lesion repair are perhaps intertwined, but the role (if any) that TDP-43 plays is unknown.

To investigate these responses to DNA damage I have employed several techniques to analyse this in A549 cells, primary human fibroblasts and cortical neurons. Cortical neurons were chosen to be studied due to high numbers of neurons produced from a single cultured brain.

I have explored the response to oxidative damage induced by the microirradiation of nuclei as well as single strand break induction via topoisomerase I inhibition. Furthermore, with a specific focus on FUS, I have attempted to explore its mechanisms of recruitment through various cell assays.

6.1 Results

6.1.1 Endogenous FUS re-localises to DNA lesions induced by UVA laser-induced oxidative damage.

There is limited knowledge on the recruitment of FUS to DNA lesions induced by oxidative damage. Preliminary investigations in the Hafezparast laboratory with collaboration with investigators at the Genome Damage and Stability Centre (GDSC) at the University of Sussex began by highlighting the recruitment of GFP tagged FUS to UVA-induced DNA damage in A549 cells (Rulten et al. 2013).

In order to establish if the recruitment of FUS to UVA-induced lesions was not an artefact of the GFP-tagged protein, untransfected A549 cells were plated onto 35mm dishes, exposed to Hoechst stain and microirradiated. Subsequently, the cells were fixed in 1% PFA 2 minutes later in order to capture the re-localisation of FUS and labelled with an anti-FUS antibody for immunofluorescent staining.

As seen in Figure 3.2 (panel a) FUS re-localised to the site of microirradiation indicated by the dashed inset across the nucleus (also see publication). To confirm the specificity of the recruitment of FUS to these sites of damage, A549 cells were transfected with siRNA against FUS over a 48-hour period before microirradiation. The siRNA prevented adequate translation of the FUS protein leading to a reduction of re-localised FUS after microirradiation (see Figure 3.2). The siRNA efficiency was additionally confirmed by western blot analysis of lysates from cells transfected with the siRNA (panel b). In Summary FUS is recruited to oxidative damage induced by UVA microirradiation in A549 cells.

Figure 3.2

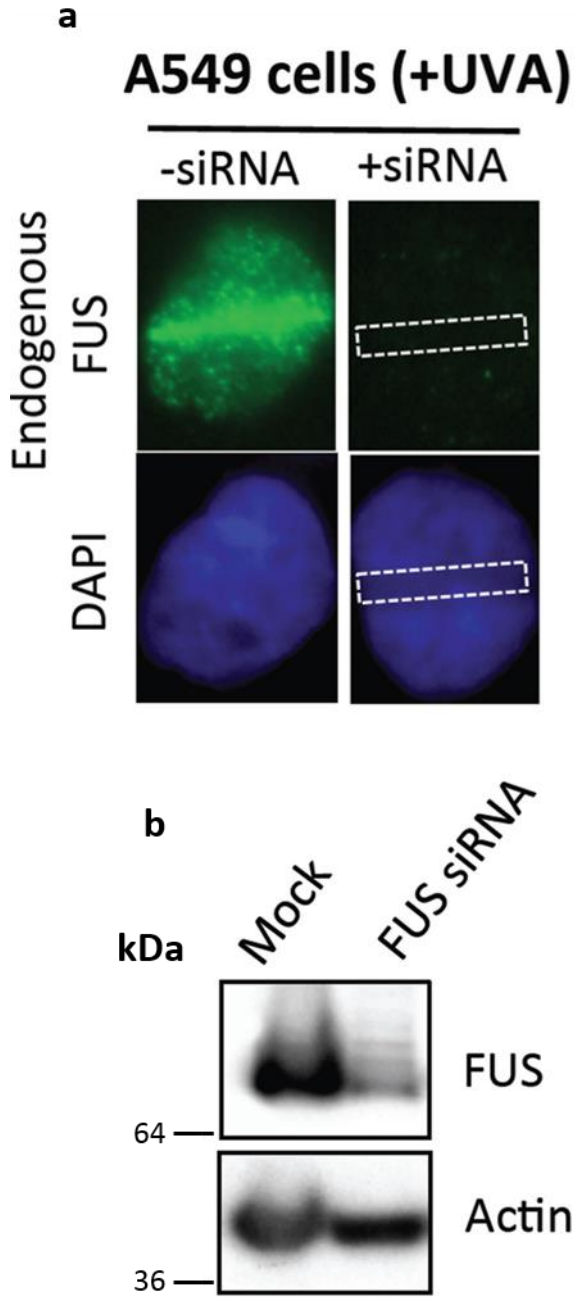

Figure 3.2- **(a)** Endogenous nuclear FUS after microirradiation of A459 nuclei and immunofluorescent staining using an anti-FUS antibody **(b)** SDS-PAGE analysis of A549 cell total homogenate after 48-hour transfection with siRNA against FUS with β-actin implemented as a loading control. Image acquisition was conducted using a spinning disc Olympus-3I microscope using a 63x oil objective mounted with an EMCCD Evolve camera.

6.1.2 TDP-43-GFP re-localises away from DNA lesions induced by UVA laser-induced oxidative damage

TDP-43 shares many functional roles with FUS such as the splicing of pre-mRNA and the regulation of transcription. Importantly, both proteins bind to DNA elements in order to regulate the production of transcripts. As FUS is clearly recruited to UVA-induced DNA damage it is feasible to hypothesise that TDP-43 may play a similar role and become recruited to DNA strand breaks. In order to investigate this A549 cells ($3x10^5$) were transfected with TDP-43 tagged with GFP in glass bottom 35 mm dishes over a period of 48 hours. The cells were then exposed to Hoechst fluorescent stain before being microirradiated for the same duration as used when analysing endogenous FUS re-localisation. Nuclear TDP-43 was then monitored using live cell imaging over a period of 20 seconds (see Figure 3.3). After microirradiation of the A549 nuclei the TDP-43-GFP began to vacate the area of damage after 2 seconds indicated by the dashed white line (panel a).

This experiment was repeated and A549 cells with comparable levels of TDP-43-GFP transfection were chosen (n=8) in order to quantify this expulsion of TDP-43. The graph in Figure 3.3 (panel b) indicates that the TDP-43 reduces in the area of DNA damage to a level of ~60% over a period of 10 seconds and remained at that level thereafter (panel b). This gradual reduction of TDP-43 localisation to the microirradiated area also rules out the possibility of bleaching of the GFP signal as in this case the signal would reduce almost instantly after the point of irradiation. This datum indicates that conversely to FUS the TDP-43

protein vacates areas of DNA damage evoked by oxidative damage through UVA microirradiation.

Figure 3.3

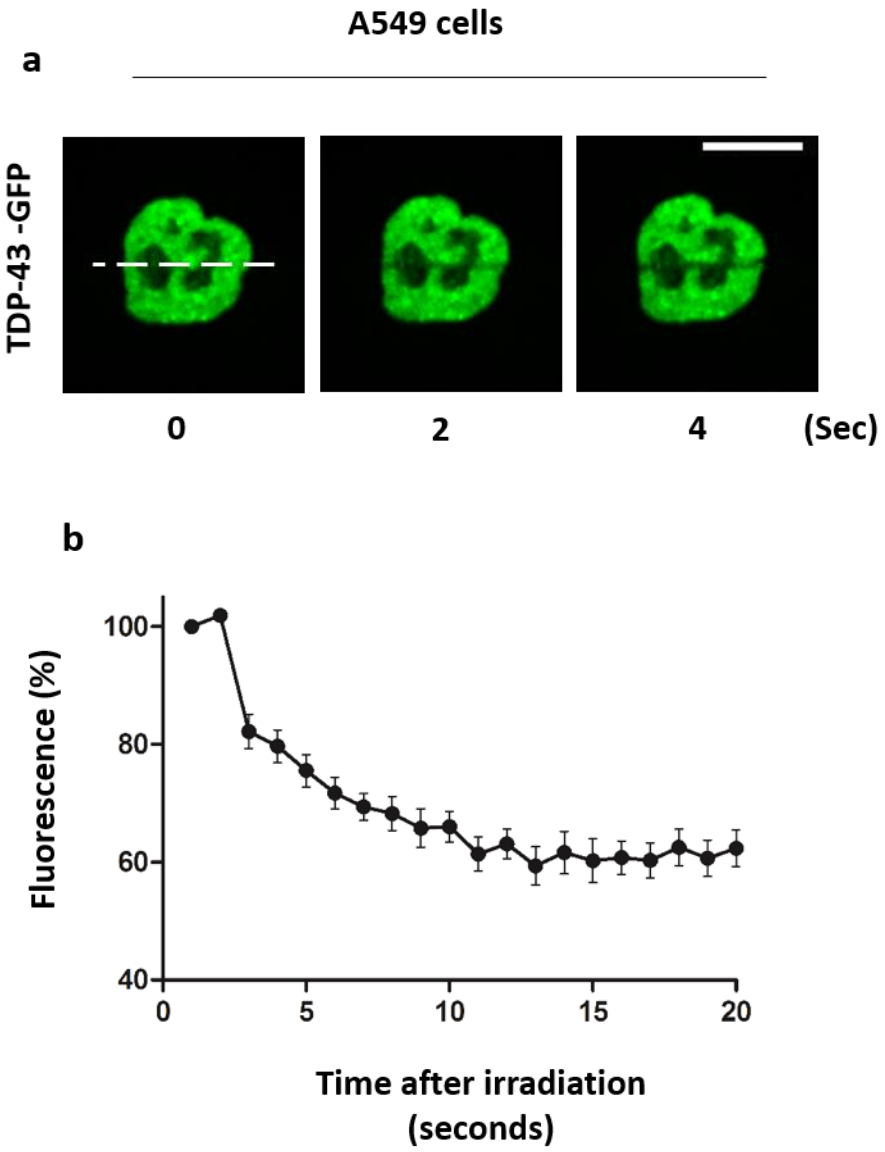

Figure 3.3- **(a)** A549 cells (n=8) transfected with TDP-43-GFP after a 48-hour period. Nuclei were microirradiated (indicated by the dashed line) and imaged for 20 seconds (scale bar 10 μm). **(b)** Quantification of the fluorescence of the microirradiated region (minus background) over a 20-second period. Image acquisition was conducted using a spinning disc Olympus-3I microscope using a 63x oil objective mounted with an EMCCD Evolve camera.

6.1.3 FUS re-localises to nuclear foci after camptothecin exposure in human fibroblasts

The re-localisation of FUS after UVA microirradiation was discovered by our collaborating group at the GDSC to be dependent on poly (ADP-ribose) polymerase 1 (PARP-1). Although this provides insight into how FUS responds to this type of DNA damage, the use of UVA microirradiation is not comparable to actual physiological DNA damage, furthermore, the laser energy could damage proteins or protein-DNA/RNA complexes.

To induce a more physiologically relevant type of damage a topoisomerase I inhibitor was employed in human fibroblasts. Topoisomerases are enzymes that modulate DNA supercoiling and are important for processes such as transcription. These enzymes 'relax' supercoiled DNA by introducing DNA breaks (single strand or double strand breaks) to allow the passing of another strand through the lesion (Uday Bhanu & Kondapi 2010). These enzymes then re-join the lesions, however, the use of camptothecin (a potent topoisomerase inhibitor) prevents this re-joining of the strands and the damage remains.

To investigate the response of FUS to camptothecin (hereafter CPT) exposure, human wild-type fibroblasts were cultured and exposed to either CPT or DMSO (control) for a duration of 1 hour. The cells were subsequently fixed and labelled with an anti-FUS antibody for immunofluorescence analysis (see Figure 3.4). As expected the DMSO control shown in the bottom panel did not result in any re-localisation of FUS. In contrast, after CPT exposure FUS appeared to re-localise to foci in the nucleus (indicated by arrows in the top panel of Figure 3.4). These

foci were found to correlate with a co-stain of fibrillarin which is a component of nucleoli (see Figure 3.4). In summary, FUS foci associated with the nucleoli form as a response to topoisomerase I inhibition after CPT exposure.

Figure 3.4

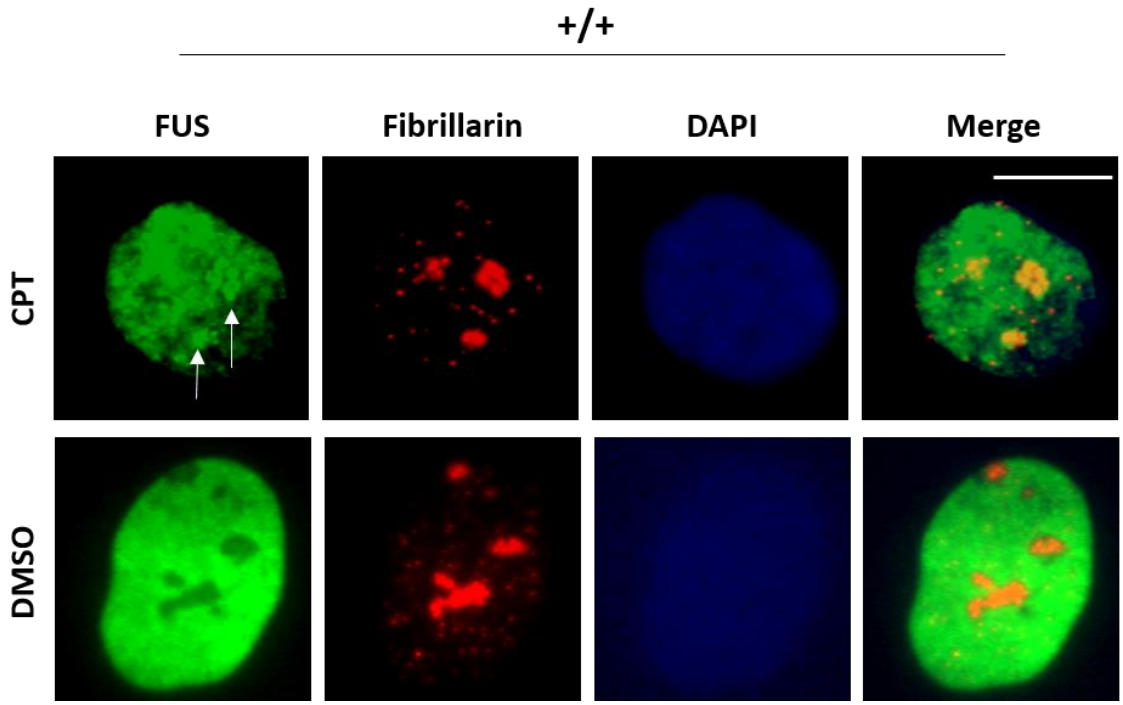

Figure 3.4- Wild-type human fibroblasts treated with 4 μM CPT and DMSO. Cells were fixed and probed using antibodies for the nucleoli marker fibrillarin and FUS and (imaged at 100x magnification, scale bar represents 10 μm). Image acquisition was conducted using a Zeiss Axiovert equipped with LSM 520 Meta.

6.1.4 Camptothecin does not induce TDP-43 nuclear foci formation in human fibroblasts

The formation of FUS foci in response to the inhibition of topoisomerase I through CPT exposure prompted the possibility that TDP-43 could also undergo nuclear re-localisation. As TDP-43 re-localised away from UVA induced DNA damage in A549 cells it was hypothesised that CPT could result in a re-organisation of sub-nuclear TDP-43.

Wild-type human fibroblasts were cultured onto 13mm glass coverslips in a 24 well plate overnight before a 1-hour exposure to CPT. Cells were fixed as before and labelled with an anti-TDP-43 antibody for immunofluorescent analysis. The exposure to CPT resulted in no clear re-organisation of sub-nuclear TDP-43 (Figure 3.5 top panel). Instead the TDP-43 formed ring-like structures that appeared in all nuclei treated with CPT. This was not the case in DMSO treated cells and no re-localisation of TDP-43 was observed. In summary, TDP-43 did not re-localise to foci in wild-type fibroblasts after CPT treatment but instead re-organised to ring-like structures within the nucleus (see discussion).

Figure 3.5

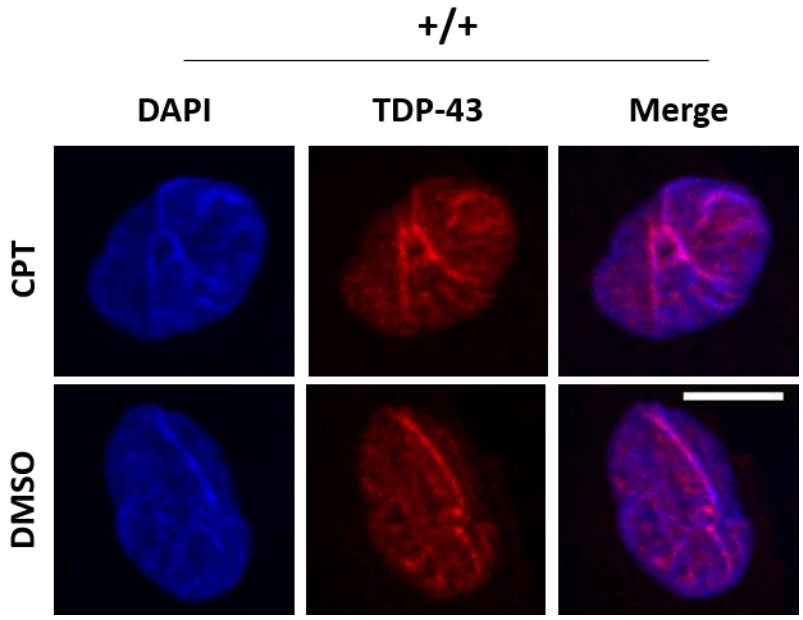

Figure 3.5- Wild-type representative human fibroblast nuclei after treatment with 4 μM CPT or DMSO (control). Cells were fixed and labelled with an antibody against TDP-43 for immunofluorescent imaging at 100x magnification (scale bar represents 10 μm). Image acquisition was conducted using a spinning disc Olympus-3I microscope using a 63x oil objective mounted with an EMCCD Evolve camera.

6.1.5 Nuclear re-localisation of FUS after camptothecin treatment in murine wild-type and p.D520G mutant cortical neurons

ALS is a disease of neurons in which the synapses between motor neurons and the musculature degenerate due to a 'dying back' phenomena preventing the innervation of muscle and in some cases causing cognitive aberrations (Dadon-Nachum et al. 2011). The DNA repair process in neurons has to be robust and heavily relies on the BER pathway in order to repair oxidative damage-induced lesions. Thus in order to analyse the neuronal response of FUS under conditions of DNA damage it is imperative to investigate this response in post mitotic neurons.

To investigate the FUS response to DNA damage in neurons both wild-type and p.D520G cortical neurons were cultured from E18 mice. The neuronal cultures were then exposed to CPT treatment or DMSO (control) before being fixed and immunostained for FUS. Analysis of the FUS sub-nuclear re-localisation in wild-type cortical neurons in response to CPT elicited FUS foci similar to that observed in wild-type human fibroblasts (Figure 3.6). In contrast, the DMSO treated control neurons rarely presented with FUS foci (Figure 3.6). Both the heterozygous and homozygous p.D520G neuronal cultures also presented with FUS foci after treatment with CPT and similar to wild-type fibroblasts, rarely presented with FUS foci after DMSO exposure.

In order to quantify if any difference in foci number could be detected in p.D520G cortical neurons compared to wild-type neurons, cultures were repeated and FUS foci were quantified in order to determine any significant differences (see figure

b). The graph depicts a trend of increased mean foci in heterozygous and homozygous p.D520G mutants compared to wild-type cells (n = 68, n = 70 and n = 85 respectively) although no significant difference could be detected. Similarly no significant differences were identified in DMSO treated cells between wild-type and p.D520G heterozygous and homozygous (n = 74, n = 104 and n = 98 respectively) mutant cortical neurons.

Overall these data indicate FUS foci formation in cortical neurons in response to topoisomerase I inhibition and no significant alteration in foci formation caused by the p.D520G mutation.

Figure 3.6

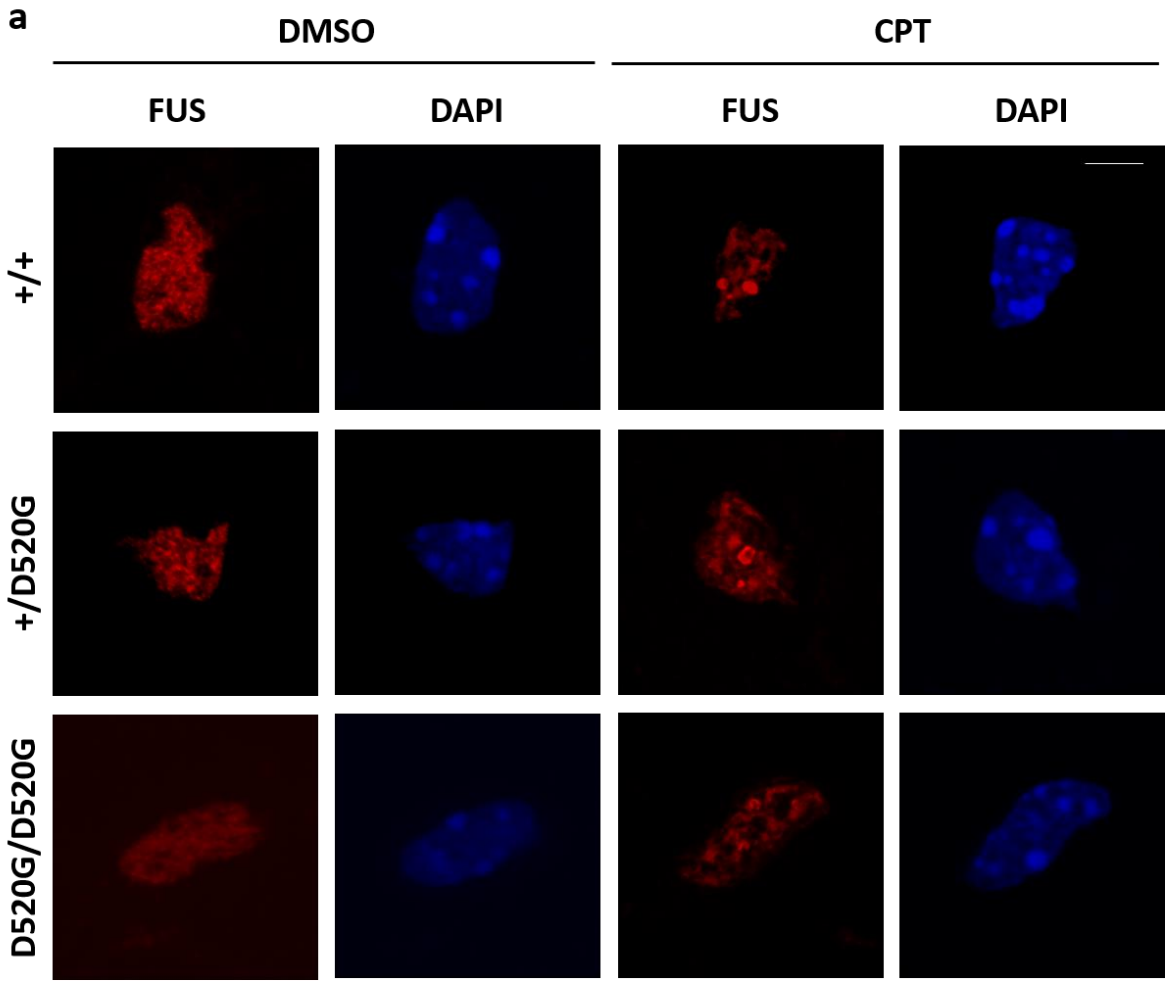

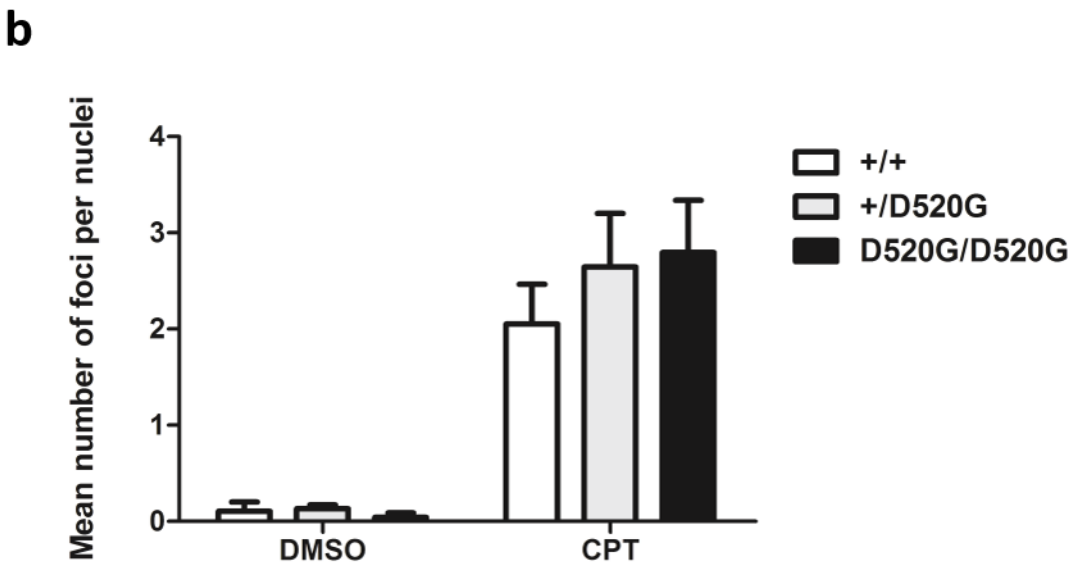

Figure 3.6- **(a)** Wild-type and p.D520G mutant murine cortical neuron nuclei treated with either 4 μM CPT or DMSO (control) 24-hours after culture. Neurons were fixed with PFA before being probed with an antibody against FUS for immunofluorescent analysis and imaged at 63x magnification (scale bar represents 5 μm). **(b)** Quantification of the mean number of foci per-nuclei in wild-type neurons and p.D520G mutants. Image acquisition was conducted using a Leica TSC SP8 confocal microscope with a 63x objective.

6.1.6 TDP-43 forms nuclear foci localised with FUS after camptothecin exposure in wild-type murine cortical neurons

To further explore the role of TDP-43 in the DNA damage response, cortical neurons were implemented to visualise the response to damage. This was in order to test the hypothesis that perhaps even though there was no similar response in fibroblasts (as seen with FUS) there could be neuronal specific responses of TDP-43 to DNA damage.

To analyse possibility of TDP-43 undergoing sub-nuclear localisation cortical neurons were cultured and treated with CPT or DMSO for 1 hour the following day and subsequently fixed and labelled with an antibody for TDP-43. Images taken at 100x magnification were used to detect any re-localisation of TDP-43. Cortical neurons treated with DMSO did not indicate any TDP-43 re-localisation in the nucleus as expected (Figure 3.7). Interestingly, wild-type cortical neurons treated with CPT indicated small foci that are indicated with white arrows (Figure 3.7). These foci were less obvious in comparison to the FUS foci previously observed in both fibroblasts and cortical neurons.

To further explore the possibility that TDP-43 and FUS were indeed occupying similar sub-nuclear areas, further cortical neurons were cultured and stained for both FUS (green) and TDP-43 (red) as shown in the bottom panel b of Figure 3.7. The co-staining of these interrelated proteins indicated that they both seem to occupy the same sub-nuclear region of the nucleus (FUS was previously shown to be associated with nucleoli under CPT conditions). In summary this indicates that the inhibition of topoisomerase I in cortical neurons is conducive to the formation of FUS and TDP-43 co-localised foci in sub-nuclear compartments.

Figure 3.7

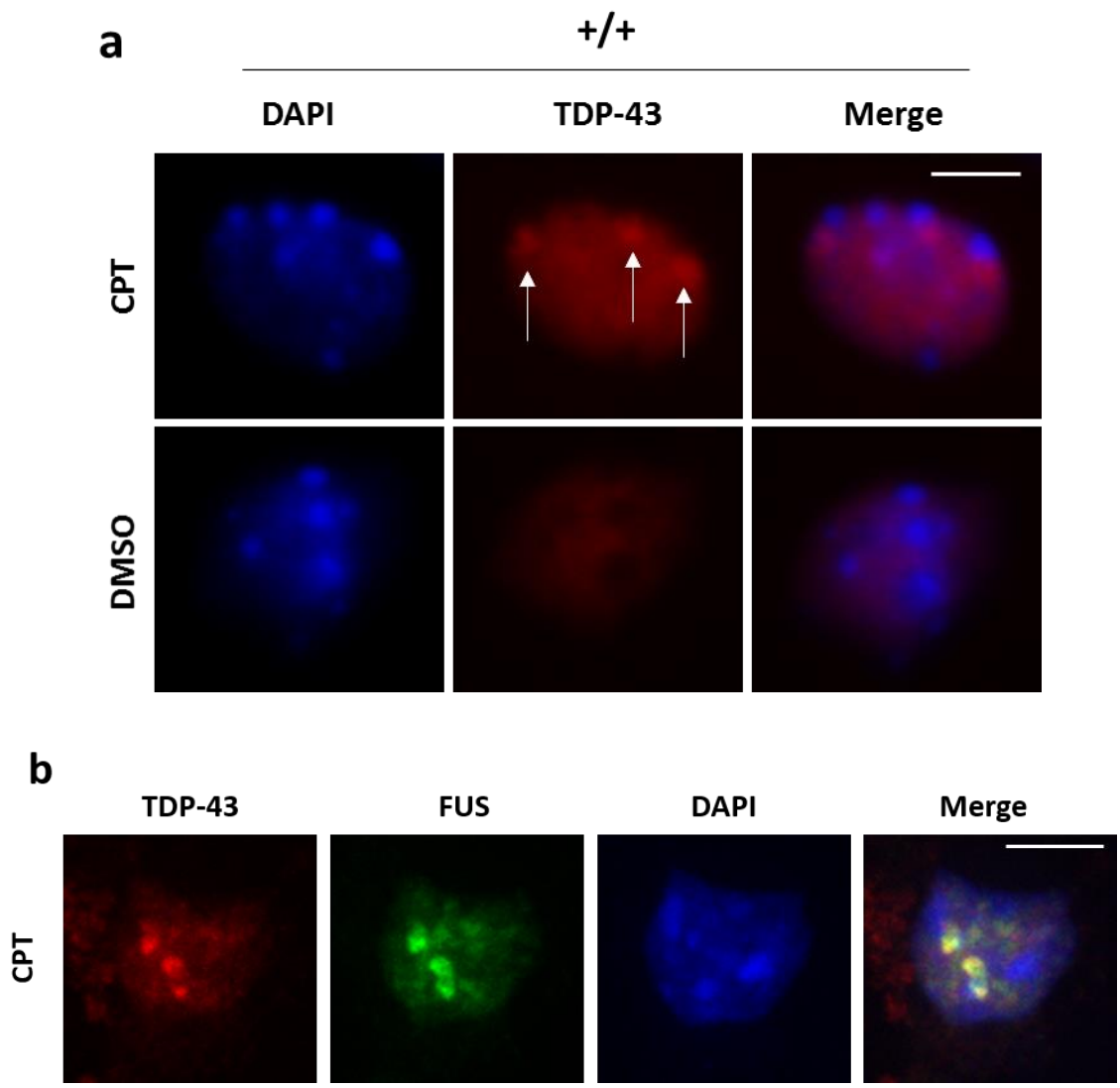

Figure 3.7- **(a)** Wild-type cortical neuron nuclei treated with either 4 μM CPT or DMSO (control) 24-hours after culture. Nuclei were labelled with antibody against TDP-43 for immunofluorescent analysis and imaged at 63x magnification. TDP-43 foci are indicated by white arrows. **(b)** Wild-type cortical neuron nuclei treated with CPT co-labelled for both TDP-43 and FUS at 63x magnification (all scale bars represent 5 μm). Image acquisition was conducted using a spinning disc Olympus-3I microscope using a 63x oil objective mounted with an EMCCD Evolve camera.

6.1.7 The FUS recruitment to nucleoli associated foci is inhibited by caffeine in murine wild-type cortical neurons

In order to further extrapolate the mechanism by which FUS is recruited to nucleolar sub-nuclear compartments, it is important to attempt to intersect cellular pathways by employing inhibitors for example. The DNA damage response is largely mediated by members of the PIKK family of enzymes, which have previously been shown to interact with FUS (Gardiner et al. 2008). The use of caffeine has been previously shown to inhibit both ATM and ATR kinases (Stępnik et al. 2015). To elucidate if these kinases are involved in the recruitment of FUS to nucleoli associated foci, cortical neurons were cultured and exposed to 10 mM and 20 mM concentrations of caffeine before being treated with CPT to induce DNA damage (Figure 3.8).

Analysis of nuclear FUS distribution after immunofluorescent staining indicated as expected that CPT induced the formation of FUS foci whilst the DMSO control did not evoke any response in the nuclei (more than 50 cortical neuron nuclei were analysed for every condition) (see Figure 3.8). The foci observed with CPT treatment co-localised with B23, a nucleolar associated protein (see discussion). In contrast, wild-type cortical neurons treated with 10 mM caffeine exhibited a significant (P = 0.0002) reduction in B23 associated FUS foci (see Figure 3.8 panel b). Furthermore, treatment with 20 mM caffeine significantly (P< 0.001) abolished FUS foci in wild-type cortical neurons treated with CPT (Figure 3.8). To confirm that the sub-nuclear organisation of FUS was not influenced by caffeine, cortical neurons were exposed to caffeine without CPT treatment. These neurons indicated normal homogenous nuclear distribution of FUS (see figure panel c).

In summary, the treatment of cortical neurons with the PIKK inhibitor caffeine resulted in the reduced formation of nucleoli associated FUS foci after topoisomerase I inhibition.

Figure 3.8

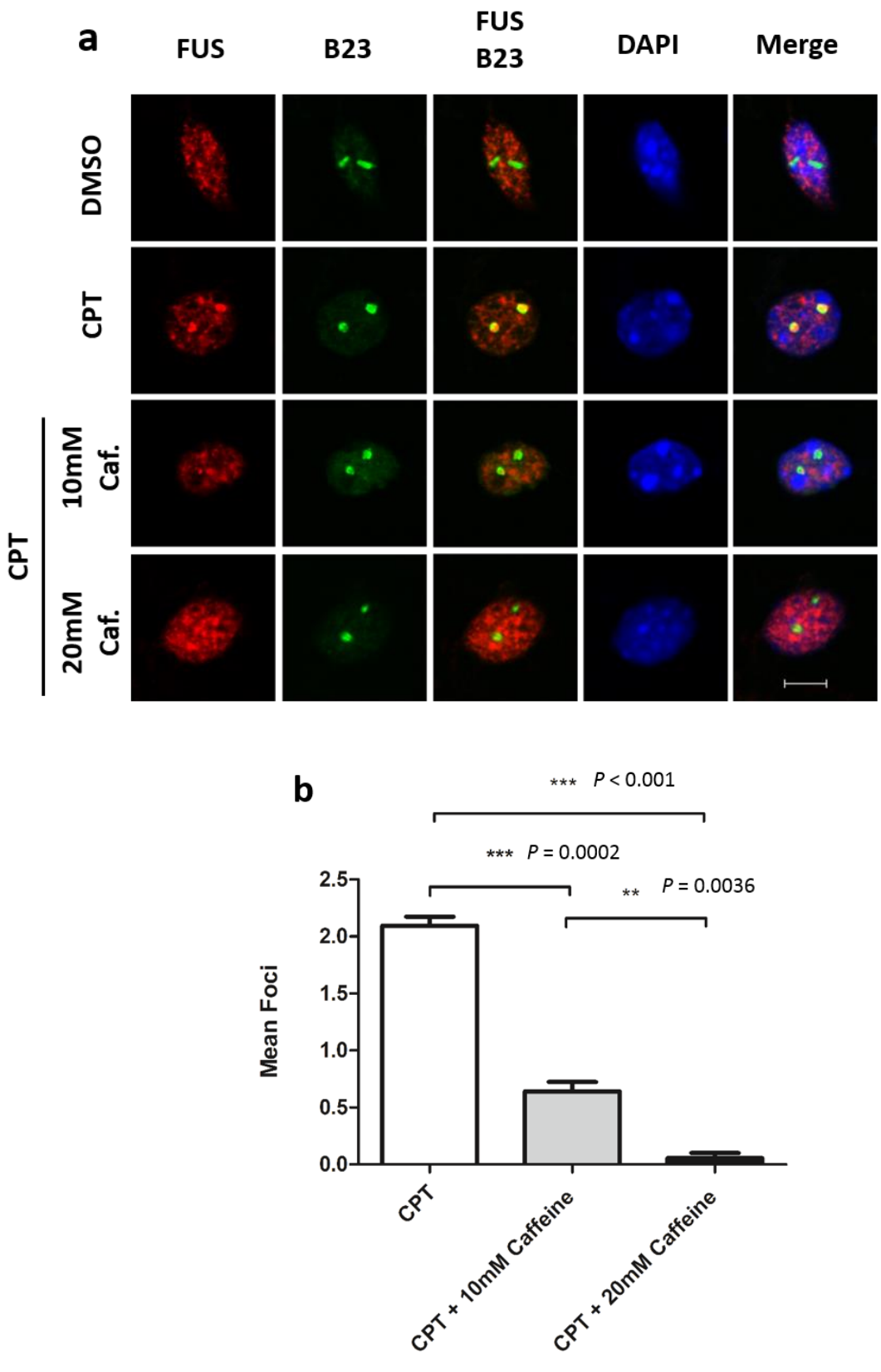
a
FUS
B23
FUS
B23
DAPI
Merge
DMSO
CPT
CPT
10mM Caf.
20mM Caf.
b
*** P < 0.001
*** P = 0.0002
** P = 0.0036
Mean Foci
2.5
2.0
1.5
1.0
0.5
0.0
CPT
CPT + 10mM Caffeine
CPT + 20mM Caffeine

Figure 3.8 *Cont.*

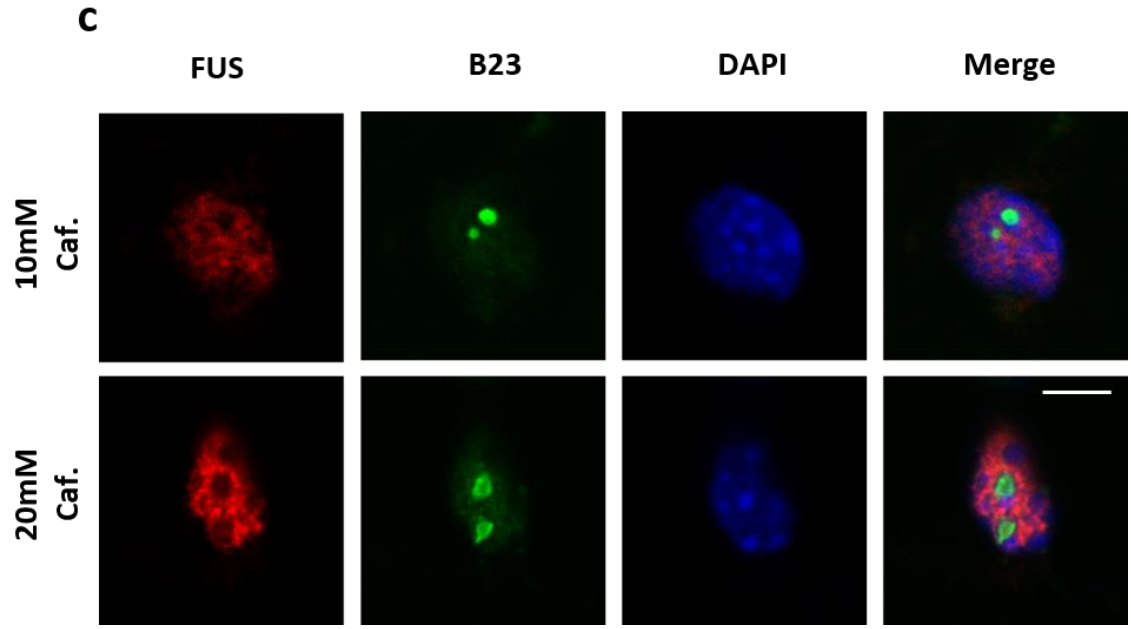

Figure 3.8 (a) Wild-type cortical neurons treated with either CPT, CPT and caffeine or DMSO (control) 24-hours after culture. Nuclei and nucleoli were labelled with antibody against FUS and B23, respectively, for immunofluorescent microscopy. **(b)** Quantification of the mean number of FUS foci per cortical neuron nuclei when treated with CPT and CPT with 10 or 20 mM caffeine pre-treatment. **(c)** Wild-type cortical neurons treated with caffeine alone to demonstrate that caffeine has no adverse effect on FUS nuclear localisation (all scale bars represent 5 μm). Image acquisition was conducted using a Leica TSC SP8 confocal microscope with a 63x objective.

6.1.8 Nucleoli associated FUS foci are induced by polymerase II inhibition but not polymerase I inhibition

Although caffeine is a known inhibitor of the PIKK family of enzymes the off target effects of caffeine have to be considered. In order to narrow down the pathway of FUS recruitment specific inhibitors were employed by Duncan Moore in the GDSC in U2OS cells in order to for a high-through put experimental design before attempting any inhibition in neurons. U20S cells were treated with ATM, ATR and DNA-PK inhibitors before exposure to CPT. The cells were then fixed for immunofluorescent analysis to determine if any of the specific inhibitors prevented the recruitment of FUS nucleolar foci. Surprisingly, these inhibitors had no effect on the recruitment of FUS to foci leading to the hypothesis that perhaps FUS was not responding to DNA damage per-se, but perhaps to the interruption of transcription which occurs whilst DNA lesions are repaired.

In order to investigate this, cortical neurons were cultured from E18 wild-type mice and subjected to inhibitors of both RNA polymerases I and II (Figure 3.9). The latter is the enzyme responsible for transcribing globally whilst RNA polymerase I is responsible for transcribing ribosomal RNA (RNA polymerase III transcribes non-coding RNA important for processes such as RNA processing) (Canella et al. 2010).

Cortical neurons were fixed for immunofluorescent staining of FUS after DRB (300 μM for 1 hour) and α-amanitin (4 μg/ml for 18 hours) exposure, which are both inhibitors of RNA polymerase II. Wild-type nuclei from cortical neurons presented with foci after both treatments that indicated FUS co-localisation with

B23 in all neurons (Figure 3.9). In the case of DRB treatment multiple foci were observed that were not always associated with the nucleoli, this could be due to the mechanism of inhibition (see discussion and Figure 3.9). In contrast when the polymerase I inhibitor CX4561 (10 μM for 1 hour) was applied to the wild-type cortical neurons no FUS foci were observed after immunofluorescent staining (Figure 3.9 panel b).

In summary, inhibition of polymerase II in cortical neurons with α-amanitin leads to nucleoli associated FUS foci formation. The use of DRB to inhibit polymerase II leads to multiple foci formation that are not always associated with nucleoli. Lastly, the inhibition of polymerase I does not lead to FUS foci formation.

Figure 3.9

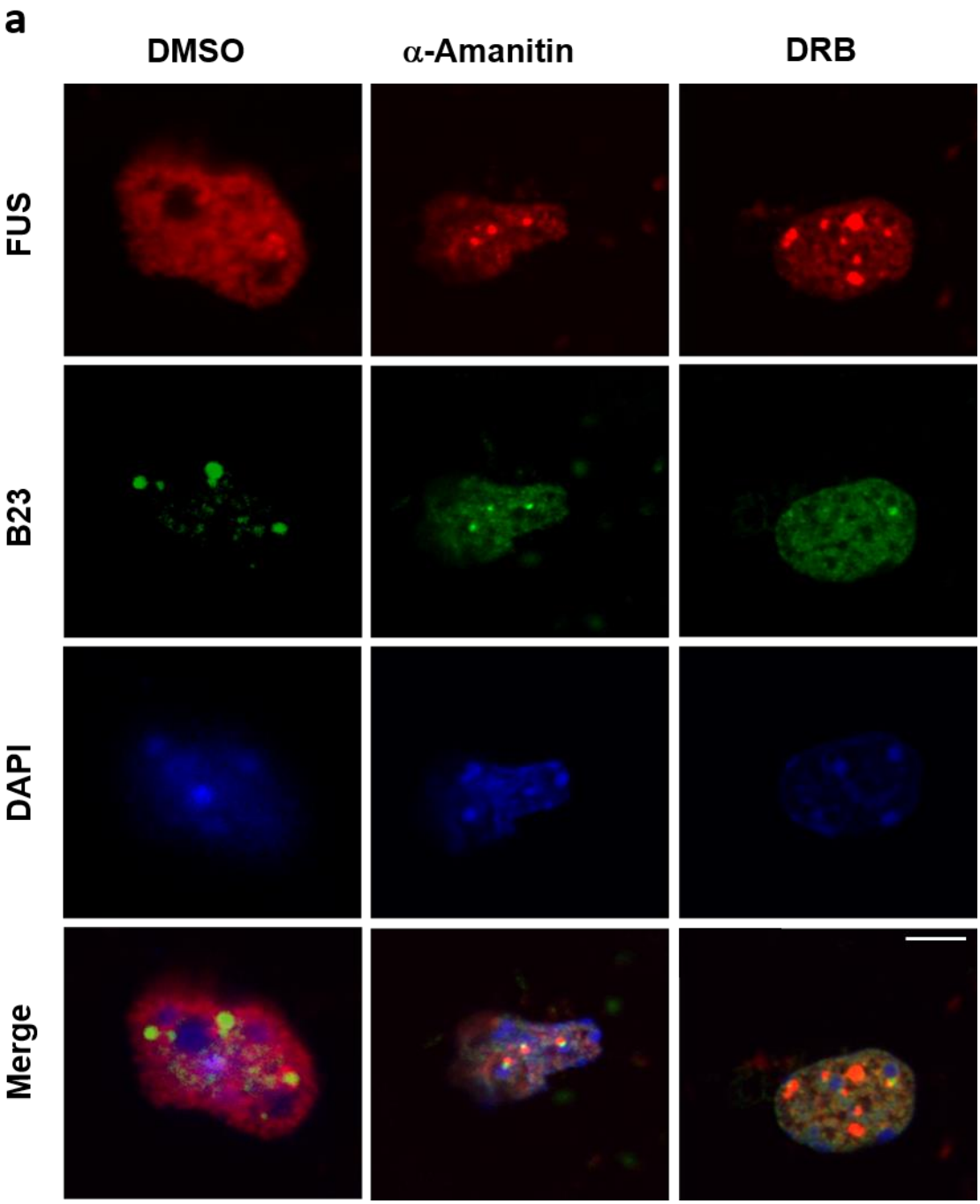

Figure 3.9 ***Cont.***

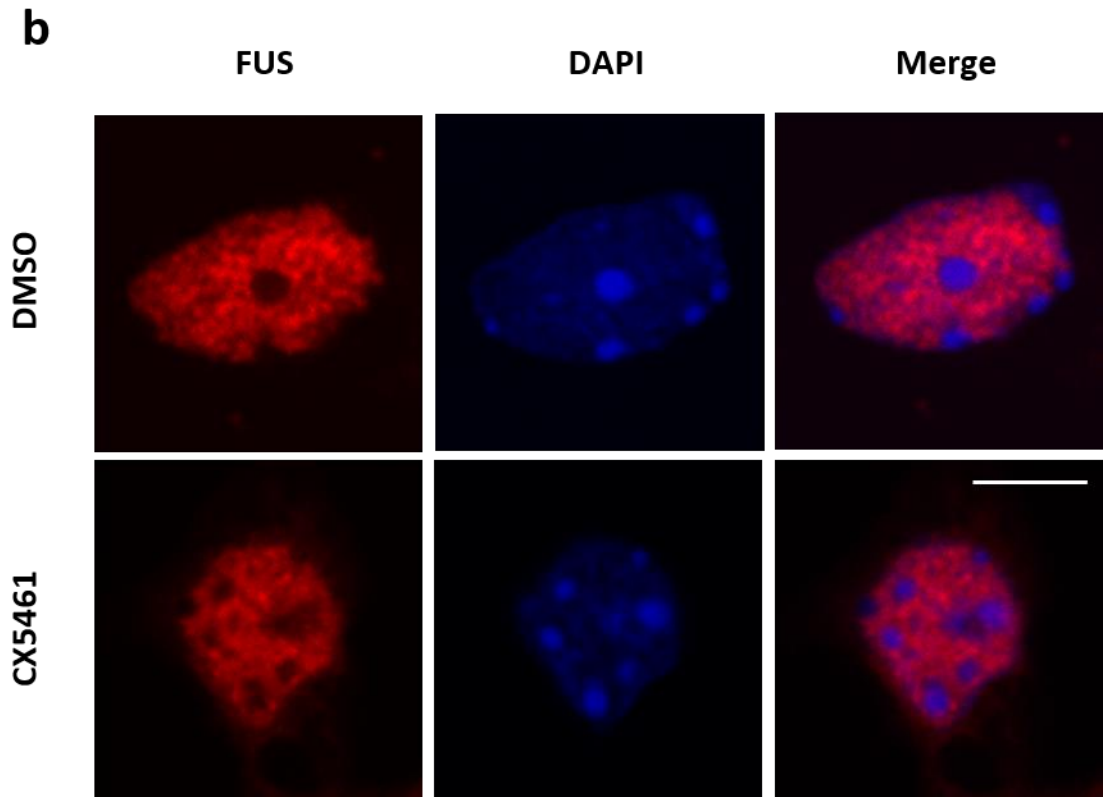

Figure 3.9- **(a)** Wild-type cortical neurons 24-hours after culture treated with DNA polymerase II inhibitors α-amanitin and DRB for 18 and 1-hour respectively or DMSO (control) immunostained for FUS and B23. **(b)** Wild-type cortical neurons treated with DMSO or the DNA polymerase I inhibitor CX5461 immunostained for FUS (all scale bars represent 5 μm). Image acquisition was conducted using a Leica TSC SP8 confocal microscope with a 63x objective.

6.1.9 FUS foci formation is inhibited by dipyridamole in murine wild-type cortical neurons

To further elucidate the mechanism of FUS recruitment to nucleoli after CPT treatment, other targets of caffeine other than the PIKK enzymes were considered potential recruiters of FUS. Caffeine is known to inhibit phosphodiesterases (PDEs) that represented a possible chaperone of FUS to CPT induced foci (Chavez-Valdez et al. 2016). PDEs in mammals are responsible for the regulation of intracellular signalling through degradation of cyclic AMP (cAMP) and cyclic GMP (cGMP) (Umar & Hoda 2015). A paper by Jackson et al. outlines that dipyridamole can be implemented in a concentration dependent manner to inhibit PDEs. A lower concentration of dipyridamole was observed to have an inhibitory effect of PDE 9,10 and 11 whereas high concentrations were shown to inhibit PDE 8 (Jackson et al. 2007).

To investigate if FUS was being recruited by any members of the PDE family cortical neurons were cultured from wild-type mice and exposed to 10 μM and 300 μM dipyridamole for 1 hour before being exposed to CPT treatment (Figure 4.0). Cortical neuron cultures that were initially exposed to 10 μM dipyridamole followed by CPT exposure remained to show FUS foci associated with the nucleolus (indicated by B23 in Figure 4.0). In contrast, when a higher concentration of 300 μM dipyridamole was applied to wild-type neurons before CPT exposure a significant (P<0.0001) reduction in nuclear FUS foci observed (Figure 4.0).

In summary, the treatment of wild-type cortical neurons with 300 μM dipyridamole abolishes the recruitment of FUS to nucleolar associated foci; thus implicating PDEs in the recruitment of FUS to nucleoli after inhibition of topoisomerase I through CPT treatment (see discussion).

Figure 4.0

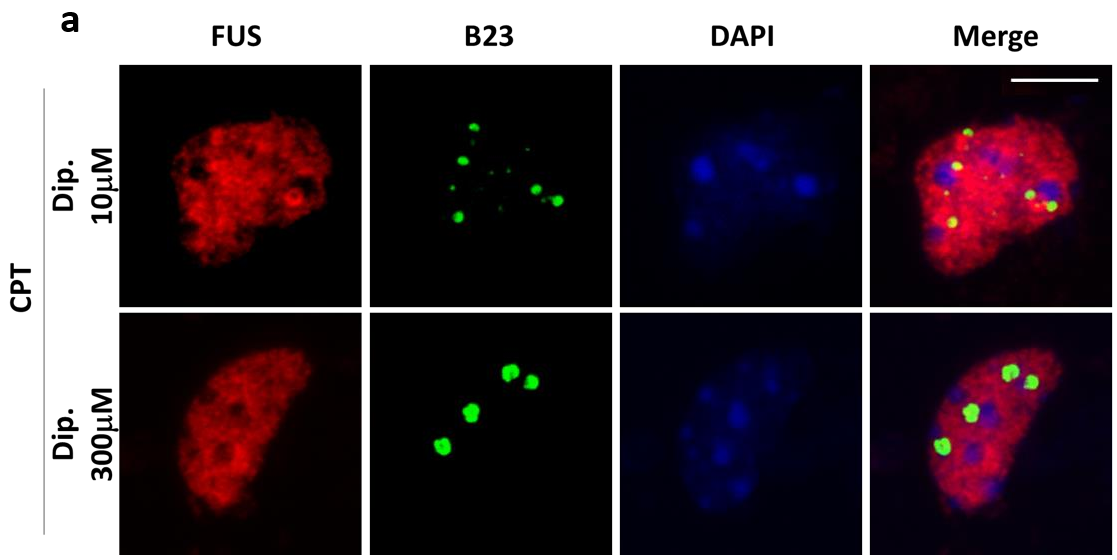

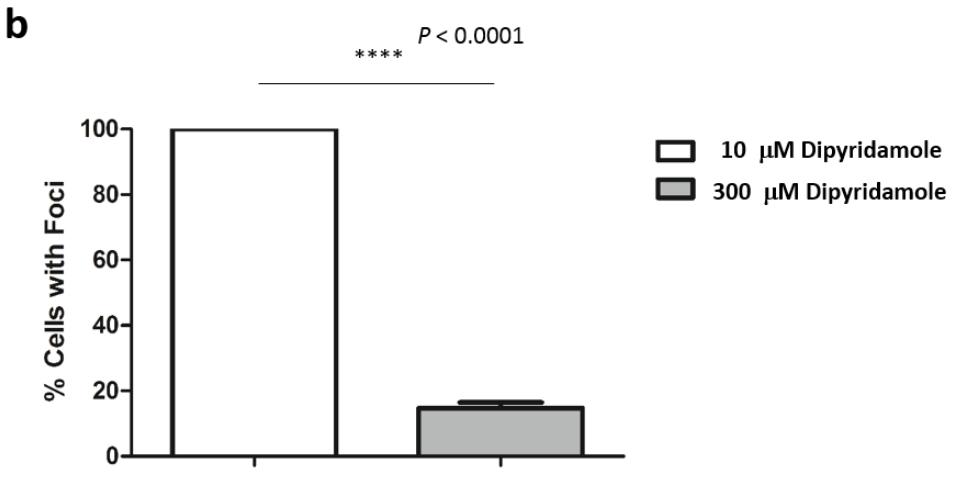

Figure 4.0- **(a)** Wild-type cortical neurons pre-treated with 10 μM and 300 μM dipyridamole before CPT application. Cortical neuron nuclei were then subjected to immunofluorescent staining using antibodies against FUS and B23 (scale bar represents 5 μm). **(b)** Quantification of the percentage of neurons with FUS nuclear foci when pre-treated with 10 μM and 300 μM dipyridamole (scale bar represents 5 μm). Image acquisition was conducted using a Leica TSC SP8 confocal microscope with a 63x objective.

6.10 Chapter 3 Summary

The data presented in this chapter shows that both FUS and TDP-43 respond to DNA damage. Firstly, FUS is recruited to damage evoked by oxidative damage caused by UVA microirradiation and to foci by topoisomerase I inhibition via CPT. However, the p. D520G mutation in murine cortical neurons did not alter the response of FUS when treated with CPT. The FUS foci formed are co-localised with nucleoli and these foci are replicated when DNA polymerase II inhibitors are employed. This recruitment was prevented by caffeine treatment in cortical neurons but not individual targeting of the PIKK family members (shown by colleagues). As caffeine also targets PDE's, dipyridamole was used as a specific inhibitor of PDE's showing that a high concentration of dipyridamole prevents FUS foci formation; indicating that PDE's are likely responsible for the recruitment of FUS to nucleoli after CPT treatment.

Secondly, the response of TDP-43 in contrast indicated that oxidative damage via UVA microirradiation resulted in the expulsion of TDP-43 from DNA lesions. Furthermore, no observable foci could be detected in human fibroblasts (unlike FUS) after CPT treatment. However, foci were detected in cortical neurons after CPT treatment that co-localised with FUS indicating that perhaps TDP-43 has a slightly different role in neurons under conditions of DNA damage. However, time restrictions prevented further exploration of the role that TDP-43 plays in the DNA damage response.

6.11 Chapter 3 discussion

6.11.1 FUS and TDP-43 re-localise after UVA microirradiation in A549 cells

The aim of this study in Chapter 3 was to characterise the response of FUS and TDP-43 to DNA lesions. Mutations in both coding genes are pathogenic in ALS and could be responsible for crucial DNA repair processes. This is particularly imperative for motor neurons as they produce high levels of ROS and are post-mitotic. To initially examine the response of FUS to oxidative DNA damage A549 nuclei were micro-irradiated and the re-localisation of FUS was analysed through fluorescence microscopy.

After microirradiation of nuclei the endogenous FUS protein localised to the damaged region indicating a clear response to the damage. The recruitment of FUS was found by colleagues at Sussex University to be inhibited on application of a PARP1 inhibitor (KU58948). This PARP1 dependency was further confirmed by demonstrating that FUS directly interacted with PARP1 to enable its re-localisation (Rulten et al. 2013). The microirradiation energy the nuclei were exposed to initiated both double and single strand breaks of the DNA double helix.

In the instance of SSBs, PARP1 promotes poly(ADP-ribos)ylation of repair proteins XRCC1 and polβ to induce ligase III repair (Ghosh et al. 2016). PARP1 knockout mice importantly also show delayed repair of SSBs (Schreiber et al. 2002). Interestingly, Mastrocola et al. demonstrated that PARP1 dependent FUS recruitment was initiated through DSB repair and additionally showed that FUS

depletion resulted in reduced DSB repair via non-homologous end-joining and homologous recombination (Mastrocola et al. 2013). Taken together, it is possible that the PARP1 response to both single and double strand breaks promotes the recruitment of FUS to DNA damage.

What is the role of FUS at the sites of these DNA lesions? One prospect is that it is stabilising pre-mRNA or perhaps processing pre-mRNA at the site of damage as FUS is well known for interacting with large numbers of pre-mRNAs. Alternatively, it may be the case that FUS is directly involved with the repair of DNA lesions as the DNA damage signalling kinase ATM is known to phosphorylate FUS perhaps promoting its recruitment (Gardiner et al. 2008). Lastly it is possible that FUS is regulating gene expression at the sites of DNA damage, as FUS dependent inhibition of the *Cyclin D1* gene was observed after DNA damage mediated by the binding of FUS to ncRNAs (Wang et al. 2008).

After microirradiation of GFP-TDP-43 transfected A549 nuclei TDP-43 responded to the oxidative damage by vacating the microirradiated region of the nucleus. This response indicates that in A549 cells the role of TDP-43 may differ from that of FUS despite many shared functions between these two proteins (see Chapter 1). TDP-43 has been identified as a regulator of transcription and depletion of TDP-43 results in changes of expression of over 200 proteins in SH-SY5Y cells (Štalekar et al. 2015). Transcription-coupled nucleotide excision repair has recently been highlighted as a mechanism in which the cessation of transcription can initiate repair (Haines et al. 2014). It therefore could be hypothesised that TDP-43 is sequestered away from transcriptionally active DNA to facilitate this repair mechanism. Although further time and investigation would be needed to

confirm the players involved in this active repression of TDP-43 from DNA lesions induced by oxidative damage.

6.11.2 FUS, but not TDP-43 form nuclear foci in human fibroblasts after topoisomerase I inhibition with CPT

To elicit a more physiologically relevant type of DNA damage, topoisomerase I was inhibited with CPT in human fibroblasts in order to produce SSBs and consequently monitor re-localisation of FUS and TDP-43. On the application of CPT, the FUS protein accumulates into foci in sub-nuclear compartments. When co-stained with nucleoli marker fibrillarin, it was clear that the FUS foci were forming in associated with the nucleoli within the nucleus.

Upon the global inhibition of topoisomerase I, (and consequently induction of single strand breaks) perhaps it would have been expected to visualise many FUS foci spread across the whole nucleus. This is because FUS would have been recruited to multiple sites of DNA damage, although this was not visually seen. However, it is possible that perhaps the low level of damage inflicted by CPT may not cause such a dramatic response in comparison to microirradiation of the nuclei, and thus be harder to visualise.

Even though this may be the case, a substantial FUS association with the nucleolus was observed after CPT exposure. The reason for this could be the close association between topoisomerase I and the transcription of ribosomal DNA (rDNA). The majority of topoisomerase I is found in the nucleolus as it is important for rDNA transcription creating single strand breaks in DNA to relieve

torsional forces (Christensen et al. 2004). Due to the association between topoisomerase I and rDNA transcription it can be hypothesised that perhaps FUS plays a protective role interacting with ribosomal pre-mRNA. As nucleoli are transcriptional 'hot spots' this could explain the accumulation of FUS in these sub-nuclear regions.

In contrast, TDP-43 did not appear to form foci in human fibroblast nuclei after inhibition of topoisomerase I. This is perhaps in accordance to previous data showing its vacation of regions of the nuclei that have been microirradiated (see Figure 3.3). However, inhibition of topoisomerase I led to the formation of ring like structures observed in the nucleus rather than foci per-se. The TDP-43 staining appeared to co-localise with the brighter DAPI staining, these regions are associated with heterochromatin. Upon topoisomerase I inhibition the ability of heterochromatin to become relaxed into transcriptionally active DNA (euchromatin) through SSBs is reduced. The ring-like structures are the outer regions of nucleoli as heterochromatin typically surrounds nucleoli (Padeken & Heun 2014). This likely explains why more ring like structures were observed in human fibroblasts treated with CPT.

However, the association of TDP-43 with heterochromatic regions is harder to explain as TDP-43 is well known for the association with transcriptionally active regions of DNA. Recent data suggests that TDP-43 has a role in regulating chromatin assembly perhaps providing a tentative explanation, though time restrictions prevented further investigation of this finding (Amlie-Wolf et al. 2015).

6.11.3 FUS and TDP-43 form nuclear foci after CPT treatment in neurons

The incidence of FUS foci in human fibroblasts after the inhibition of topoisomerase I prompted investigation into cortical neurons. Cortical neurons have an experimental advantage in terms of number of neurons that can be isolated from a single murine brain. When wild-type neurons were exposed to CPT FUS foci were observed as previously detected in human fibroblasts. This indicates that the role that FUS plays during topoisomerase I inhibition is active in both mitotic and post mitotic cells, suggesting that ALS mutations in FUS may impair this function of FUS.

Importantly, collaborative efforts showed that an ALS R521G FUS mutation showed reduced localisation to oxidative damage (Rulten et al. 2013). However, the murine D520G mutation did not show a similar impairment in recruitment after CPT exposure (Figure 3.6). The D520G mutation is akin to D512G in the human sequence and mutations at neighbouring residues such as 513 and 514 are thought to be pathogenic in ALS (Lagier-Tourenne et al. 2010). The D520G mouse model has no currently identified phenotype or pathology (perhaps surprisingly) associated with it, suggesting the amino acid substitution is somewhat silent.

Although no nucleoli associated TDP-43 foci were observed in human fibroblasts, cortical neurons showed distinct TDP-43 foci in cortical neurons. These foci were found to co-localise with FUS and indicates that perhaps TDP-43 may have a post-mitotic role after the inhibition of topoisomerase I.

In accordance with this observation, electron microscopy data of motor neurons have indicated co-localisation of TDP-43 and the nucleolus. Interestingly, a lack of TDP-43 in the nucleolus of sporadic ALS patients has been detected, even in motor neurons that appeared healthy (Sasaki et al. 2010). This suggests that TDP-43 has an important role in nucleoli in post-mitotic cells. However, this does not explain why the inhibition of topoisomerase I induces the re-localisation of TDP-43 in neurons. It is possible that TDP-43 has a neuroprotective role under conditions of DNA damage or cessation of transcription. This is supported through evidence from a neuroblastoma cell line indicating a significant reduction in cell viability when topoisomerase I was inhibited in parallel with TDP-43 knock down (Yu et al. 2012). Overall, this suggests that TDP-43 has a functional role at the nucleolus that could be increased under nucleolus stress in neurons, but time limitations have prevented further investigation.

6.11.4 The recruitment of FUS to the nucleolus is inhibited by caffeine

To further explore the mechanism of FUS recruitment to the nucleolus initially the PIKK family of enzymes were targeted as they are responsible for recruiting proteins in the DNA damage response. Caffeine (a known inhibitor of PIKK enzymes: ATM, ATR and DNA-PK) was added to cortical neuron cultures followed by the addition of CPT. Neurons were then fixed and immuno-labelled for FUS. Initially a concentration of 10 mM of caffeine was employed as used by Tresini et al in order to inhibit the PIKK enzymes (Tresini et al. 2015). This concentration produced a reduction of FUS foci associated with the nucleoli (marked by B23) by over 50% although, many nuclei still contained observable FUS foci. Colleague Duncan Moore in the GDSC at Sussex University also

reported variable effects of the inhibitor caffeine in U2OS cells that could have been related to poor solubility in cell culture media. Aside from this, a higher concentration of 20 mM was attempted which abolished all FUS foci in cortical neurons indicating that 10 mM was not enough to prevent FUS recruitment to nucleoli.

This observation led to the hypothesis that one of either ATM, ATR or DNA-PK was responsible for recruiting FUS after topoisomerase inhibition by CPT. A high throughput screening of specific inhibitors were employed in U2OS by colleagues in the GDSC was conducted in order to save time. This was in order to identify the specific PIKK member that was responsible for recruiting FUS, although surprisingly specific inhibitors of ATM, ATR or DNA-PK did not influence FUS recruitment.

6.11.5 RNA polymerase II inhibition produces nucleoli associated FUS foci

This evidence led to the hypothesis that perhaps the PIKK enzymes were not responsible for recruiting FUS to the nucleolus and consequently, may not be responding to DNA damage, but to the specific cessation of transcription. In order to analyse this, cortical neurons were treated with polymerase II inhibitors α-amanitin and DRB before detecting FUS re-localisation with immunofluorescent microscopy. The inhibition of RNA polymerase II evoked the formation of FUS foci similarly to that of CPT. Although this was the case DRB inhibition of polymerase II led to multiple global FUS foci that were not always associated with

the nucleolus. The inhibition of RNA polymerase I (control) did not evoke a re-localisation of nuclear FUS.

DRB is known for inhibiting RNA polymerase II by interfering with the elongation step of transcription by inhibiting CDK7 and CDK9 which are responsible for phosphorylating one of the subunits of RNA polymerase II (Turinetto et al. 2009). The action of α-amanitin is more direct by interacting with polymerase II and preventing its translocation to DNA (Bushnell et al. 2002). These differences in the mode of inhibition could explain the difference in FUS foci localisations. FUS may be required for an intermediary stage binding to certain molecular weight transcripts upon stalling of the elongation step in the case of DRB inhibition in comparison to α-amanitin inhibition although this is only a hypothesis.

Cortical neurons that were treated with CPT or α-amanitin produced FUS foci only related to the nucleoli. Both treatments have been found to structurally fragment the nucleolus which could potentially evoke a FUS response (Wachtler & Stahl 1993). A shortage of gene products through inhibition of RNA polymerase II could compromise the integrity of the nucleolus (Olson et al. 2000).

Nucleolar structure is dictated by chromatin and it has been proposed that the association between FUS and chromatin is dependent on RNA polymerase II (McKeown & Shaw 2009; Yang et al. 2014). FUS may be required for the production of ribosomal transcripts and it is possible that RNA polymerase II is regulating FUS in this manner therefore; when it is inhibited it can no longer sequester FUS away from these regions. Interestingly, FUS has been previously

found to inhibit transcription by RNA polymerase III clearly indicating an important role at the nucleolus (Tan & Manley 2010). Furthermore, it is possible that FUS is involved with the processing of nascent ribosomal RNA transcripts. The global inhibition of RNA polymerase II could be evoking a cellular response in which ribosome production is increased requiring more FUS to process these transcripts. Alternatively, FUS could be binding to these transcripts to prevent any further ribosome production in order to conserve cellular energy, further research is required to determine this mechanism.

6.11.6 Formation of nucleoli associated FUS foci is inhibited by dipyridamole

To further investigate the mechanism of recruitment of FUS to CPT induced foci other targets of caffeine had to be considered as specific inhibitors of the main members of the PIKK family, did not prevent FUS recruitment. Aside from the PIKK family caffeine is known to inhibit PDEs which regulate intracellular signalling (Umar & Hoda 2015). Dipyridamole has been previously used in a concentration dependent manner in order to selectively inhibit different PDEs. Cortical neurons were exposed to 10 μM and 300 μM dipyridamole for 1 hour before being exposed to CPT in an attempt to inhibit FUS recruitment. FUS foci were not abolished at the lower concentration of 10 μM but could not be detected in neuronal nuclei exposed to 300 μM dipyridamole before CPT treatment (Figure 4.0). Although FUS foci were still observable at 10 μM they were often not as bright as previously observed FUS foci, making them difficult to image and were not always completely co-localised with nucleoli. This could perhaps be due to

minor impairment of FUS recruitment caused by effects of the lower concentration of dipyridamole.

Jackson et al had shown that lower concentrations of dipyridamole had an inhibitory effect of PDE 9, 10 and 11 whereas higher concentrations specifically inhibited PDE 8 (Jackson et al. 2007). Therefore, this indicates that the recruitment of FUS could be attributed to PDE 8. Despite this being the case off-target effects cannot be ruled out and a more specific approach using siRNA specifically against certain PDEs needs to be employed although this was not viable in the time available.

Interestingly, recent evidence has indicated a link between FUS and PDEs, a study showing the importance of FUS in cell proliferation indicated that cell proliferation was rescued in cells knocked down with FUS when treated with a PDE 4 inhibitor (Ward et al. 2014). PDEs have specific substrates and PDE 8 specifically hydrolyses cAMP, this could represent an indirect mechanism that could influence FUS recruitment due to the broad influence of cAMP on intracellular signalling. Inhibition of PDEs will increase PKA signalling and lead to CREB activation and increased gene expression (see Figure 4.1). The CREB co-activator CREBBP may be down regulated as a consequence resulting in reduction of nucleolar chromatin remodelling and therefore reduced FUS recruitment (Lee et al. 2014; Cardinaux et al. 2000). However, there are over 100 proteins that are produced from the PDE genes generated from splice variants and alternative translation start sites furthermore; it is possible that more than one of these species can influence FUS recruitment to nucleoli (Y. Xu et al. 2011).

Figure 4.2 summarises the proposed mechanisms and localisation of both FUS and TDP-43 during oxidative DNA damage and topoisomerase I inhibition.

Figure 4.1

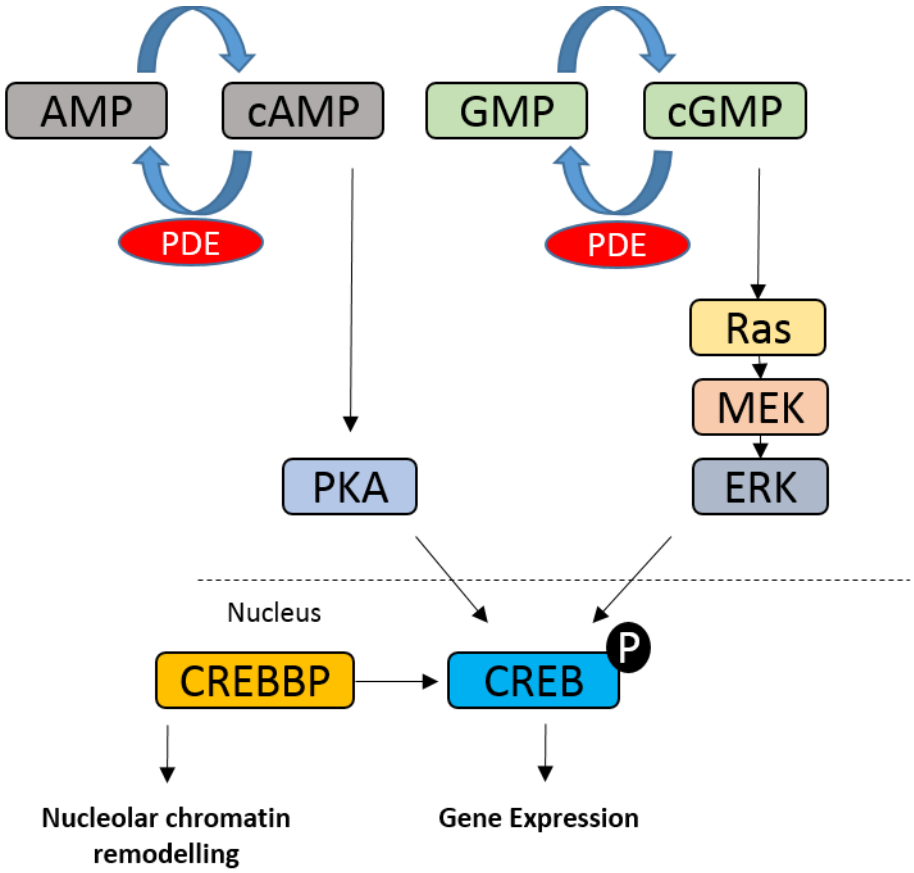

Figure 4.1- The above schematic depicts the signalling pathway influenced by PDEs. Inhibition of PDEs would lead to increased gene expression through CREB activation. This in turn could down regulate CREBPB which could decrease nucleolar chromatin remodelling and prevent FUS recruitment.

Figure 4.2

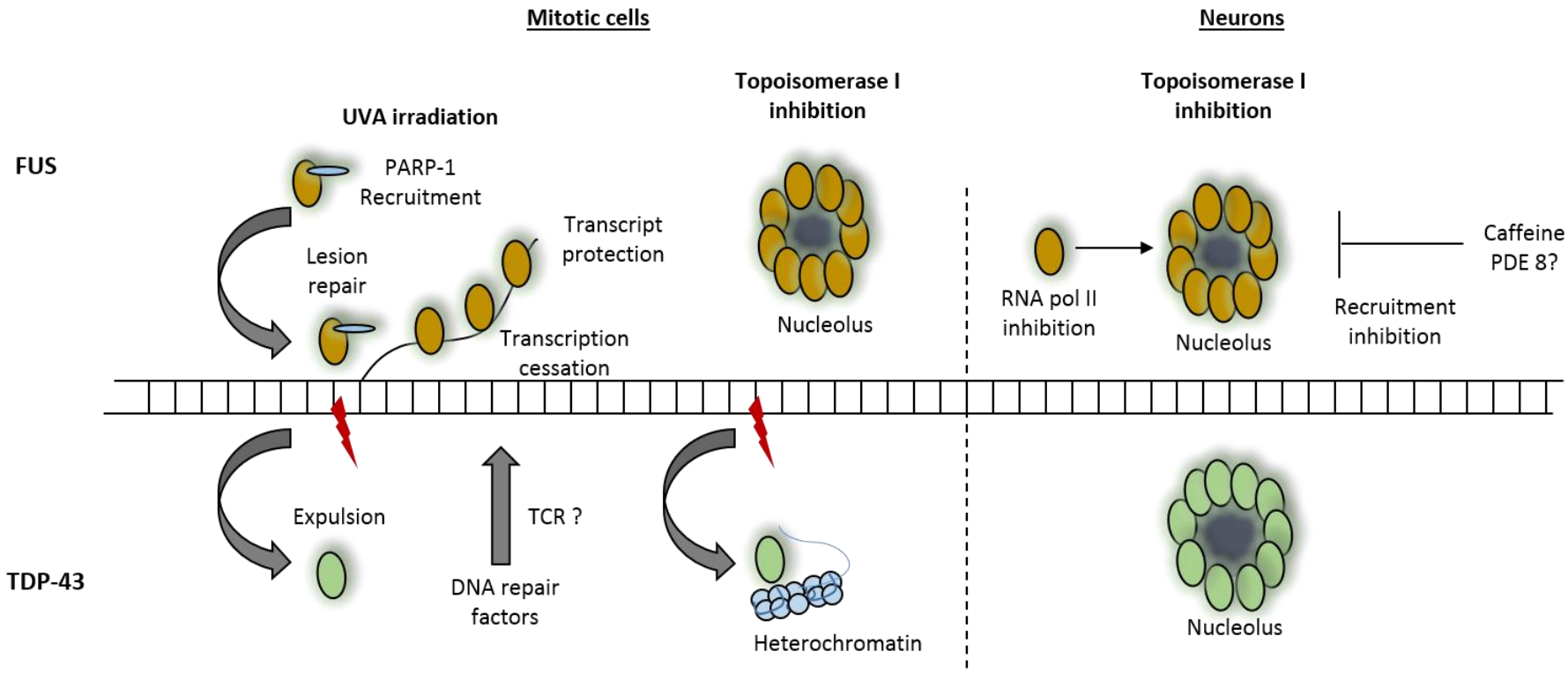

Figure 4.2- A summary of proposed responses of both FUS and TDP-43 to microirradiation of DNA and the inhibition of topoisomerase I.

Chapter 4- The DYNC1H1 ^{R399G} mutation in SMA-LED

7.0 Introduction

Mutations in the *DYNC1H1* gene are pathogenic in SMA-LED, a congenital condition characterised by motor neuron loss and muscle atrophy of lower limbs. The key aberrant molecular mechanisms that underpin this condition are not known and the varied association of other signs such as cognitive impairment likely reflect the complexity of the disease.

DYNC1H1 is the heavy chain component of cytoplasmic dynein, a protein complex which is known for dictating retrograde transport of cargo along microtubules. Aside from its connection to microtubules, dynein can be localised to many other cellular organelles such as the Golgi apparatus of which its associated function is not well understood.

Recent data from Yadav et al. has shown that dynein interacts with a Golgi bound protein golgin 160 to tether microtubules to Golgi membranes (Yadav et al. 2012). Additionally, mutations in *DYNC1H1* have been shown to cause a delay in the reformation of the Golgi after induced fragmentation with microtubule depolymerising agent nocodazole (Fiorillo et al. 2014; Hafezparast et al. 2003). Importantly, Golgi fragmentation has been identified in fibroblasts from SMA-LED patients with mutations in BICD2 another Golgin protein. Together, this implicates Golgi fragmentation as a potential common mechanism of disease that could contribute to the loss of motor neurons in SMA-LED.

To address this, I have employed several biochemical techniques to investigate human fibroblasts with a *DYNC1H1* mutation p.R399G. Firstly, this was to determine if the mutation causes a disruption of the dynein complex. Secondly, to determine if there is disruption of the Golgi apparatus caused by this mutation and if so to reveal mechanisms that potentially underlie this pathology.

7.1 Results

7.1.1 Analysis of the dynein complex in p.R399G homozygous fibroblasts

In order to elucidate if the R399G mutation has any adverse effects on the formation of the dynein complex, a sucrose density analysis was performed. Previous data from the Hafezparast lab has shown that mutations in the dynein heavy chain can have adverse effects on the complex formation of dynein. When homogenates from the *Loa/Loa* mouse model were subjected to sucrose density gradient analysis it was discovered that the DIC and the DLIC exhibited increased binding affinity to the DHC (Deng et al. 2010). This could have detrimental effects in terms of further binding of other subunits, adaptor proteins, and importantly cargo.

The formation of linear sucrose gradients from 5% to 20% was achieved through a method of freeze-thawing. Homogenates from wild-type and homozygous fibroblasts were loaded onto these gradients and were subjected to high speed centrifugation. A total of 11 fractions were collected from the gradients and were analysed through SDS-PAGE.

When analysing the wild-type gradient profile of the DHC it can be seen that the DHC occupies fractions 7 through to 11. In comparison the homozygous profile was detected through fractions 6-11. To determine if this was a repeatable observation this experiment was duplicated and the wild-type gradient was probed yet again for the DHC. Figure 4.3 highlights that after the second attempt (exp 2) the DHC western blot profile obtained in the wild-type fibroblasts matches

the homozygous profile. The repeated attempt importantly correlated with previous wild-type DHC profiles of murine origin (Deng et al. 2010).

Both subunits of dynactin (p150 and p135) were then analysed in terms of their distribution throughout the gradients between both genotypes. Figure 4.3 highlights that the dynactin subunits can be found in both genotypes between fractions 4 and 11 with a very faint signal barely detectable in fraction 3.

Similarly, when probing for the DIC (DYNC1I2) in both wild-type and homozygous fractions the protein was detectable in fractions 7 through to 11 in both genotypes (Figure 4.3). Interestingly a DIC signal was detectable in fraction 3 for both genotypes.

Lastly both DLIC1 and DLIC2 were analysed by western blot to indicate which fractions they occupied in the 5-20% gradients (Figure 4.1). Unsurprisingly the fractions occupied by the DLIC were reflective of the DIC (from fractions 7-11). In addition to this a signal was also detected in fraction 3 similarly to the DIC again perhaps eluding to incomplete dynein complexes. In summary, this data indicates that the p.R399G mutation does not appear to influence the subunit organisation of cytoplasmic dynein.

As the p.R399G mutation resides close to the DIC-DHC binding (see introduction) region a co-immunoprecipitation assay was conducted to further confirm that the p.R399G mutation was not impeding complex formation. An antibody against the DIC subunit of dynein was used to pull down the ~500 kDa DHC subunit in wild-type, heterozygous and homozygous human fibroblasts. The western blot analysis of the co-immunoprecipitation indicated no visual difference between the

genotypes in the immunoprecipitation of the DHC when targeting the DIC. This further confirms that the p. R399G mutation does not affect the subunit composition of the dynein complex.

Figure 4.3

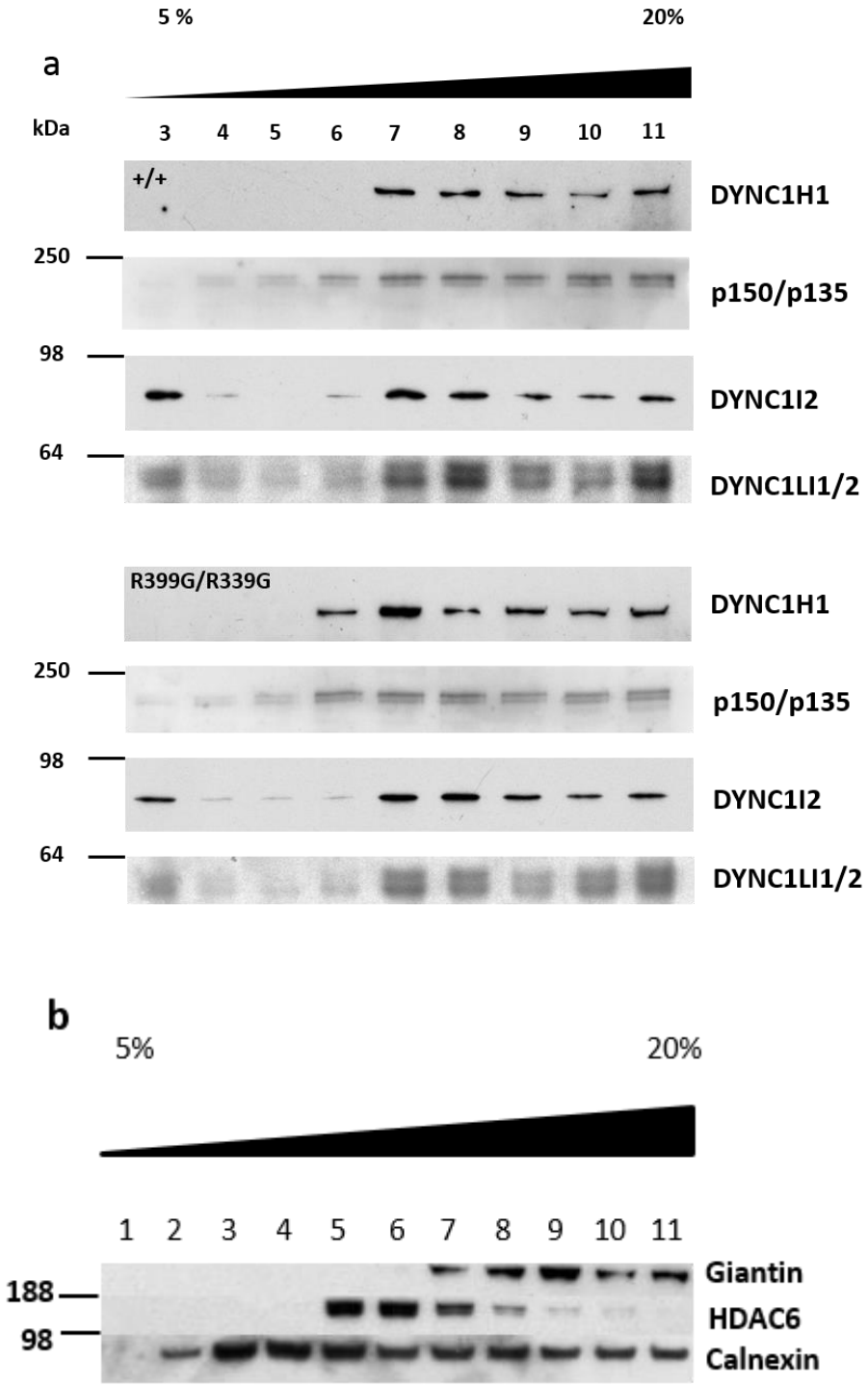

Figure 4.3 ***cont.***

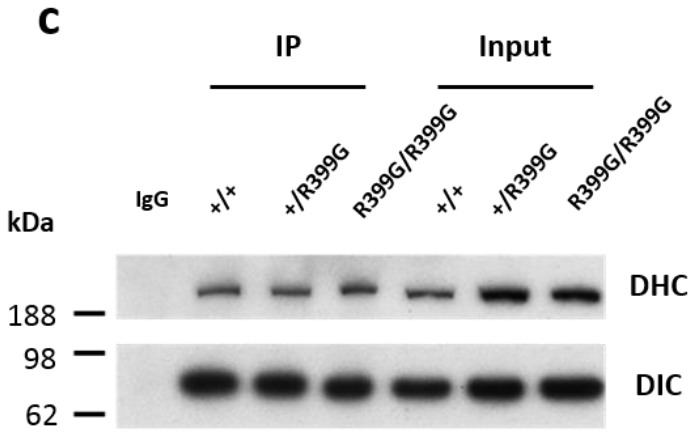

Figure 4.3- **(a)** SDS-PAGE analysis of sucrose density fractionation of cellular homogenates from wild-type and p.R399G fibroblasts probed for cytoplasmic dynein subunits. Antibodies specific to the DHC, DIC, p150/p135, and DLIC subunits of dynein implemented to analyse the complex integrity of dynein. Sucrose gradient 5-20%. **(b)** Sucrose density gradient indicating gradient separation of Golgi (Giantin), cytoplasmic (HDAC6), and endoplasmic reticulum fractions (calnexin). **(c)** Co-immunoprecipitation of the DHC subunit using an antibody against DIC subunit of dynein in wildtype and p.R399G mutant fibroblasts conducted in two experiments (n= 2).

7.1.2 The p.R399G mutation causes Golgi fragmentation in human fibroblasts

Dynein has an important role in Golgi homeostasis, previously mutations have elicited delayed Golgi reformation after nocodazole treatment. To establish if the p.R399G mutation effects Golgi integrity, initially live cell imaging of the Golgi was conducted using a Cell Light BacMam 2.0 viral labelling system (labels Golgi resident enzyme N-acetylgalactosaminyltransferase 2). When visualised for the first time the Golgi appeared to have a fragmented phenotype in the heterozygous and homozygous mutants with less frequently observed interconnection between cisternae (Figure 4.4 panel a). This phenotype was further investigated during live cell imaging by taking Z-stack images of the entire Golgi structure indicating that the mutation was resulting in fragmentation in the X, Y and the Z plane (Figure 4.4 panel b).

To understand the extent of this phenotype and for high –throughput quantification purposes, mutant fibroblasts were cultured and fixed to coverslips in a 24-well plate for immunofluorescent imaging. The cells were then labelled with the *cis*/medial marker giantin to visualise the Golgi. Low magnification images (20x, n = 6 from 2 experiments) were taken in order to visualise many cells in a large field of view in order to improve the accuracy of any Golgi phenotypes the mutation could be causing (Figure 4.4 panel c). An algorithm was then employed to accurately calculate the extent of the fragmentation in the mutants. High throughput quantification revealed that both heterozygous and homozygous fibroblasts had significantly fragmented Golgi with increasing zygosity compared to wild-type cells (P = 0.0061 and P <0.0001, respectively)

(Figure 4.4 panel d). This data shows that the p. R399G DYNC1H1 mutation compromises the structural integrity of the Golgi.

Figure 4.4

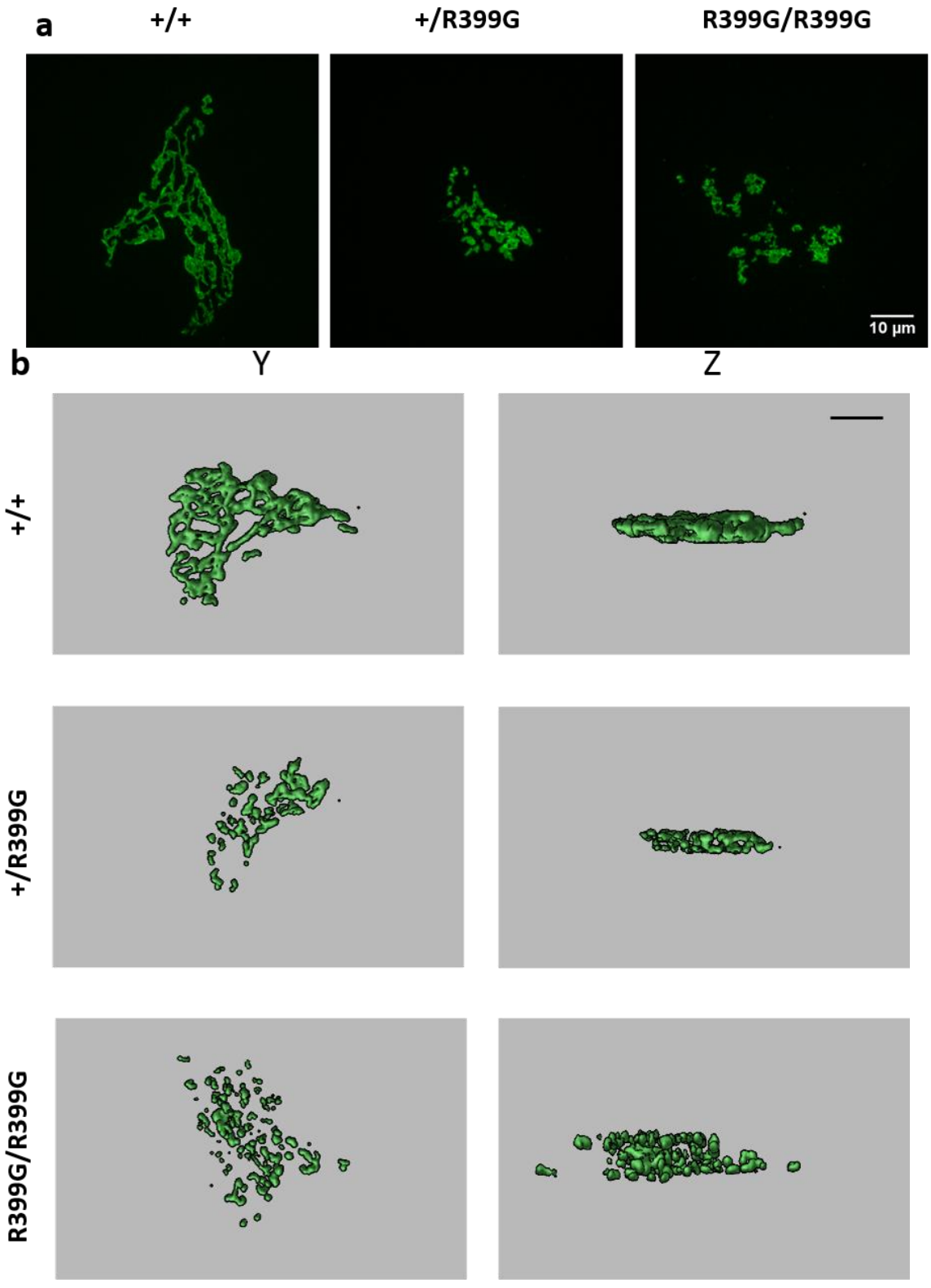

Figure *Cont.*

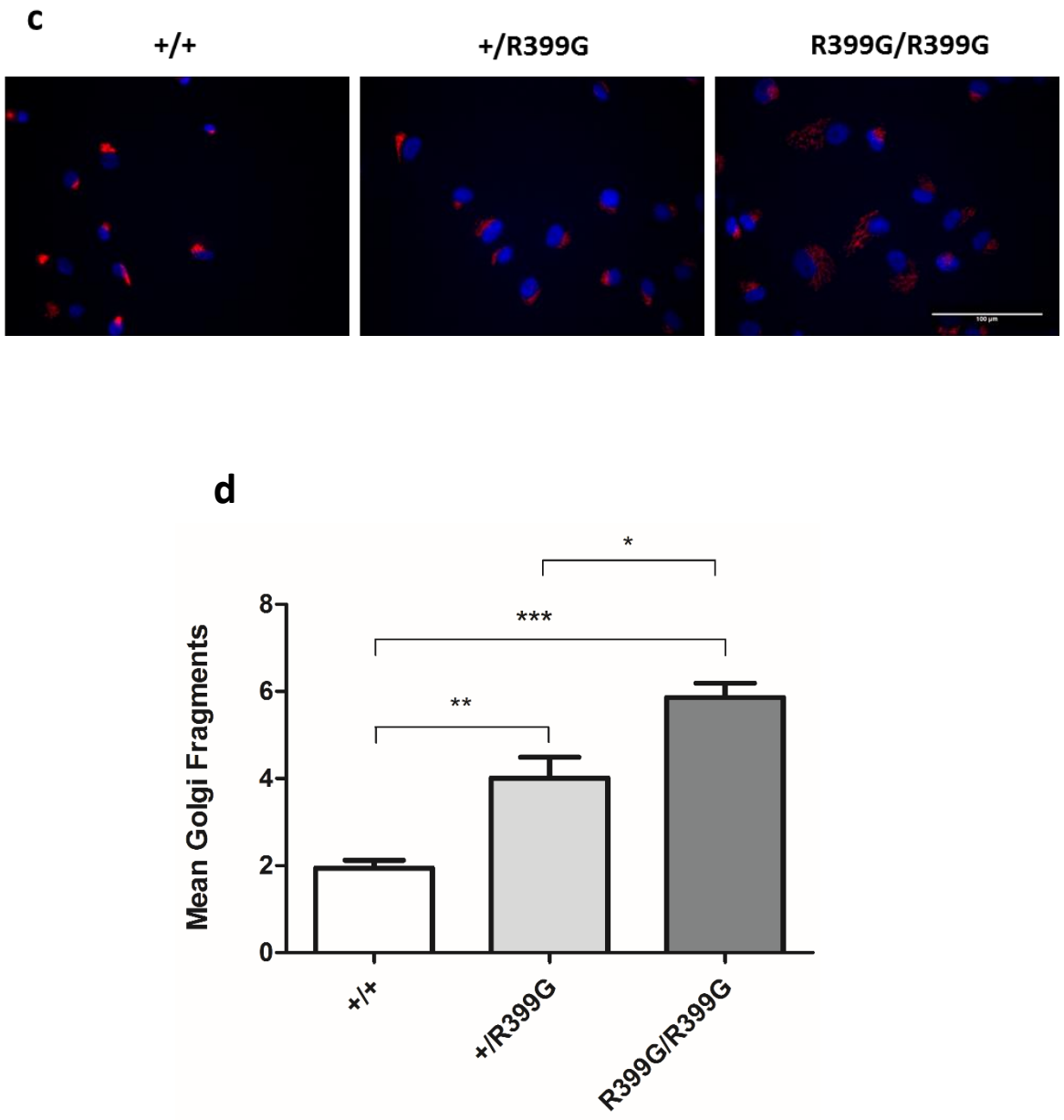

Figure 4.4- **(a)** Live cell imaging of the Golgi complex in fibroblasts at 63x magnification using the BacMam 2.0 cell light Golgi reagent. **(b)** 3D rendering of the Golgi complex from live cell imaging in the Y and Z axis to visualise Golgi fragmentation in both dimensions. Imaged with a spinning disc Olympus-3I microscope using a 63x oil objective mounted with an EMCCD Evolve camera **(c)** High through-put quantification images of the Golgi apparatus (20x) from wild-type and p.R399G mutant fibroblasts. **(d)** Quantification of Golgi fragmentation from images in **(c)**.

7.1.3 DYNC1H1-Halotag transfection restores a compact Golgi morphology in p. R399G homozygous fibroblasts

To elucidate if the R399G mutation in the dynein heavy chain was the direct cause of the Golgi fragmentation, homozygous fibroblasts were transfected with the wild-type DYNC1H1-halotag construct. Fibroblasts were electroporated and left to recover for 48 hours before being fixed and then immunostained with giantin in order to assess Golgi integrity.

Analysis of the wild-type human fibroblasts that when transfected with the Halotag construct displayed an unusual Golgi phenotype in comparison to the mutant fibroblasts (Figure 4.5); Overexpression of the wild-type dynein heavy chain in wild-type fibroblasts resulted in severe fragmentation of the Golgi in all cases where electroporation of the Halotag construct had been successful. Golgi mini-stacks were observed in the peri-nuclear region of the fibroblasts with multiple smaller Golgi objects distributed in the cellular periphery.

In surprising contrast, the +/R399G and the R399G/R399G mutant fibroblasts displayed intact Golgi cisternae in comparison. The +/R399G fibroblasts indicated some partial fragmentation whereas the homozygous genotype displayed remarkable condensation and compaction of the Golgi cisternae (Figure 4.5). This clearly highlights that the R399G mutation in the dynein heavy chain seems to be directly responsible for the fragmentation of the Golgi cisternae in human fibroblasts.

Figure 4.5

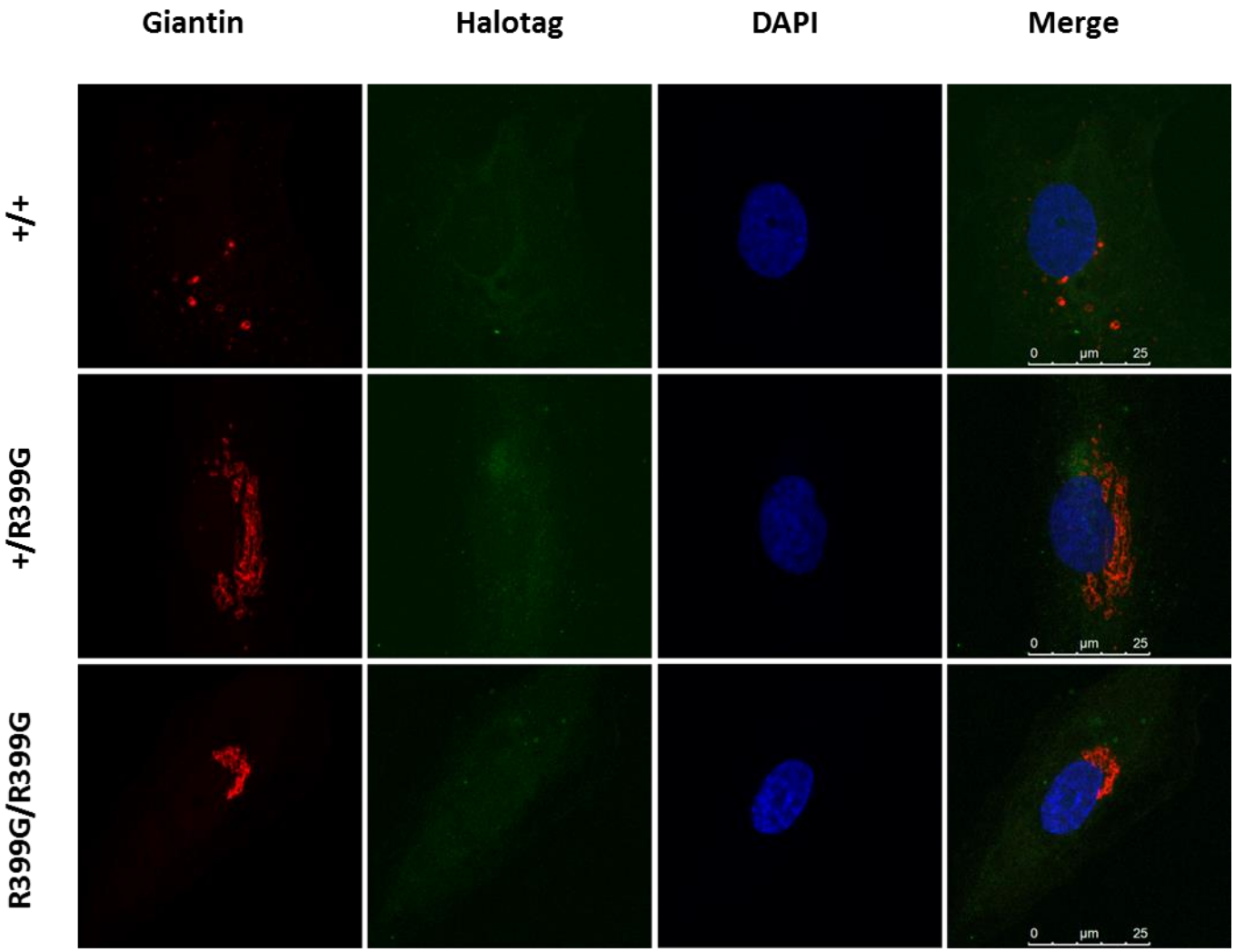
Giantin
Halotag
DAPI
Merge
+/+
+/R399G
R399G/R399G
0 µm 25
0 µm 25
0 µm 25

Figure 4.5- Wild-type and p.R399G mutant fibroblasts transfected with a wild-type DYNC1H1-Halotag construct. Giantin labelled Golgi is represented in the red channel; the Halotag plasmid is illustrated in the green channel and the cell nuclei are represented with DAPI in the blue channel. Wild-type cells efficiently transfected with the DYNC1H1 plasmid present with a severely fragmented Golgi phenotype. Heterozygous mutants appeared with a partially fragmented phenotype after transfection with the Halotag plasmid. Lastly the homozygous fibroblasts that had been transfected with the Halotag plasmid all illustrated Golgi's with intact, compact morphologies. Image acquisition was conducted using a spinning disc Olympus-3I microscope using a 63x oil objective mounted with an EMCCD Evolve camera.

7.1.4 Investigating Golgi orientation and morphology in p.R399G mutants in migrating fibroblasts

The Golgi apparatus has a pivotal role in the migration and arborisation of neurons, both of which are fundamental during development. In particular, these processes are reliant on the ability of the Golgi to re-orientate in a unipolar fashion towards the growth cone, site of arborisation, or leading edge (Yadav et al. 2009; Horton et al. 2005; Hanus & Ehlers 2008).

To elucidate if the fragmentation of the Golgi apparatus in human fibroblasts with the R399G mutation resulted in disruption of Golgi polarisation a wound healing assay was performed. This process involved growing cells in a monolayer on a coverslip and then introducing a monolayer wound and leaving the cells for 6 hours. After which, fibroblasts would begin to migrate and could be fixed and immuno-stained for F-actin (phalloidin) and the Golgi (giantin antibody). Cells imaged were chosen by the classical shape of a migrating fibroblast exhibiting a wide leading edge and a thinner trailing edge using β-actin as a guide (Figure 4.6 panel a).

To determine distribution of the Golgi apparatus across all genotypes during migration the azimuthal average of all migrating cells were analysed across 15 cells of each genotype (see materials and methods). The distribution of the fluorescence of the Golgi was then averaged and plotted as an average distribution of Golgi during migration over 360 degrees (Figure 4.6 panels b and c). In wild-type fibroblasts the distribution of the Golgi apparatus was as expected,

polarised towards the direction of migration with an elongated cisternae appearance outstretched towards the leading edge of the cell.

Surprisingly, when the Golgi from the R399G mutant fibroblasts were analysed both the heterozygous and homozygous genotypes also had re-orientated in a polarised manner towards the leading edge. However, the R399G mutants displayed a condensation phenotype which increased in severity with increasing zygosity (Figure 4.6 panels a and b). There was a significant increase in Golgi condensation in the homozygous mutants compared to wild-type fibroblasts (P = 0.016). Although an increase in Golgi condensation was observed in the heterozygous fibroblasts, no significant difference was found in comparison to wild-type cells.

In summary these data show that the p.R399G mutation is correlated with the loss of the elongated, expanded cisternae observed in wild-type migrating fibroblasts.

Figure 4.6

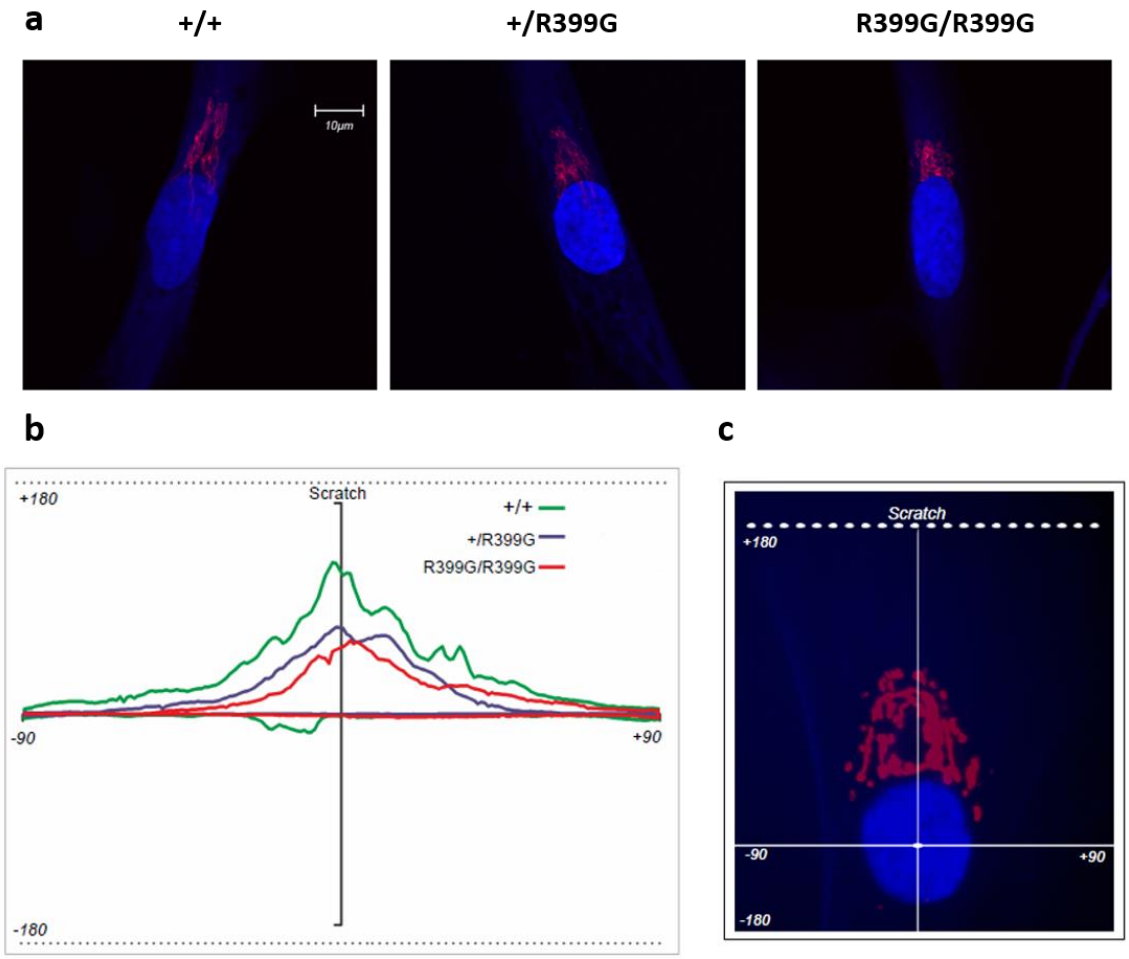

Figure 4.6- (a) p.R399G mutant fibroblasts during migration six hours post monolayer wound exhibit a condensed Golgi phenotype in comparison to wild-type cells. The direction of cell migration was determined using F-actin stain phalloidin (cell edges seen in blue). The Golgi was visualised using an antibody against giantin (shown in red). **(b)** Quantification of the distribution of the Golgi apparatus during migration post scratch (n=15) using the Azimuthal average plugin in ImageJ. **(c)** Representative schematic of the quantification of Golgi distribution during cell migration; the fluorescence from the Golgi was measured across 360 degrees (see methods). Image acquisition was conducted using a spinning disc Olympus-3I microscope using a 63x oil objective mounted with an EMCCD Evolve camera.

7.1.5 The p.R399G mutation results in an increased interaction between dynein and Golgin 160 recapitulated with nocodazole treatment in wild-type fibroblasts

Recent evidence from Yadav et al. (2012) has shown that the DIC subunit of the dynein complex directly interacts with golgin160 complex. The knock-down of golgin 160 results in Golgi fragmentation and may lend to the hypothesis that perturbed interaction between the DIC and golgin 160 is affected in p.R399G mutant fibroblasts. This was investigated through co-immunoprecipitation of golgin 160 using an antibody against the DIC subunit.

Golgin 160 associated with the DIC subunit of dynein was assessed with SDS-PAGE (Figure 4.5 panel a). The 'IP' section of the panel indicates the amount of golgin160 pulled down with the corresponding amount of the DIC subunit of dynein directly below. As the blot indicates the first Golgin160 band observed above the 98 kDa ladder marker appears stronger with incidence of the p.R399G mutation. This band is likely the 155 kDa isoform of golgin 160.

Similarly, in panel b the co-immunoprecipitation has been performed using antibody against golgin 160 to assess the amount of associated DIC (Figure 4.7 panel b). As in the previous co-immunoprecipitation, it can be observed that the quantity of the DIC protein that has been co-immunoprecipitated with golgin 160 increases with incidence of the R399G mutation. The input panels for both co-immunoprecipitations reflect quantity of protein present in cell homogenates prior to the assays. In summary the p.R399G mutation causes an increased interaction between the DIC subunit of dynein and golgin 160.

To assess if this was a cause or consequence of the fragmentation, a similar co-immunoprecipitation was performed using homogenate from cells treated with nocodazole for different periods of time. Nocodazole causes microtubule depolymerisation and consequently causes fragmentation of the Golgi.

The DIC IP panel (Figure 4.7 panel c) shows DIC associated golgin 160 after the co-immunoprecipitation using an antibody against the DIC subunit of the dynein. In wild-type fibroblasts the quantity of DIC- associated golgin 160 increases after increased exposure to nocodazole up to 4 hours. The increased intensity of this golgin 160 isoform was not observed in p.R399G mutants after increasing exposure to nocodazole. Importantly, it must be noted that the band that appears above the proposed 155 kDa isoform is assumed to be the 167 kDa isoform and is extremely variable in appearance during SDS-PAGE analysis (see discussion). To conclude the increased association between golgin 160 and dynein appears as a consequence of Golgi fragmentation indicated by the increased association of golgin 160 and dynein in wild-type cells after nocodazole treatment.

Figure 4.7

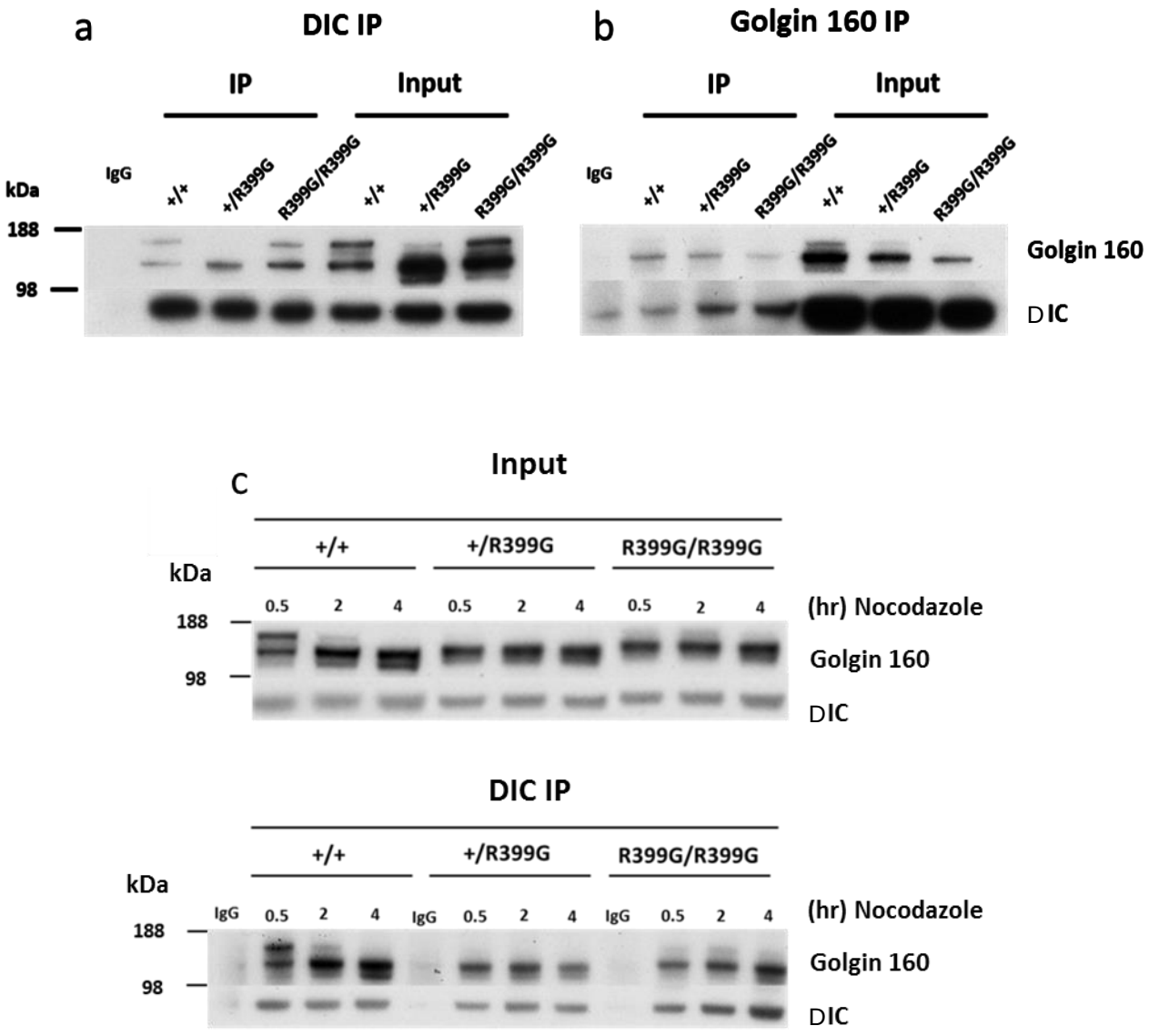

Figure 4.7- **(a)** SDS-PAGE analysis of a co-immunoprecipitation of golgin 160 using an antibody against the DIC in wild-type and in p.R399G mutant fibroblasts. **(b)** Co-immunoprecipitation of the DIC using an antibody against golgin 160. **(c)** Input loading of total cellular homogenates harvested post fibroblast treatment of nocodazole for 0.5, 2, and 4 hours (top panel). The bottom panel illustrates a co-immunoprecipitation of golgin 160 using an anti-DIC antibody from fibroblasts treated with nocodazole (as above).

7.1.6 The p.R399G mutation in human fibroblasts results in a depletion of acetylated tubulin at Lysine 40

The increased association between golgin 160 and DIC with concurrent Golgi fragmentation is paradoxical as Yadav et al showed that siRNA against golgin 160 causes Golgi fragmentation (Yadav et al. 2012). This leaves open the possibility that altered microtubule stability or associated modifications may underlie the fragmentation. As stated in the introduction, microtubule modifications such as acetylation are important for both the association of dynein with microtubules as well as Golgi cohesion.

To investigate if the Golgi fragmentation in the p.R399G fibroblasts was due to depleted acetylated tubulin, western blot analysis was used to compare total acetylated tubulin between wild-type and homozygous mutants (Figure 4.8 panel a). A clear depletion of acetylated tubulin was detected in the homozygous mutants (*P<0.05) compared to wild-type fibroblasts (Figure 4.8 panel b). Simultaneously, fellow lab member Fabio Simoes analysed the levels of detyrosinated tubulin (detyrosinated microtubules are proposed to have increased stability) elucidating that no statistical difference was detected between wild-type and mutant fibroblasts (Figure 4.8).

To further confirm and establish this phenotype both wild-type and p.R339G heterozygous and homozygous fibroblasts were labelled with anti-acetylated tubulin antibody for immunofluorescent imaging. The majority of acetylated tubulin is found in the peri-nuclear region of cells and high resolution microscopy was employed to accurately resolve the microtubules in a 40 μm radius around

the nucleus (Figure 4.8 c). Quantification of the mean intensity of acetylated tubulin was conducted through Matlab by Constantino Reyes Aldosoro and indicated that both heterozygous and homozygous fibroblasts elicited depleted acetylated tubulin in this region compared with wild-type cells ($P = 0.0141$ and $P = 0.0001$ respectively). In summary the DHC p.R399G mutation causes a specific reduction of lysine 40 acetylation of tubulin in human fibroblasts.

Figure 4.8

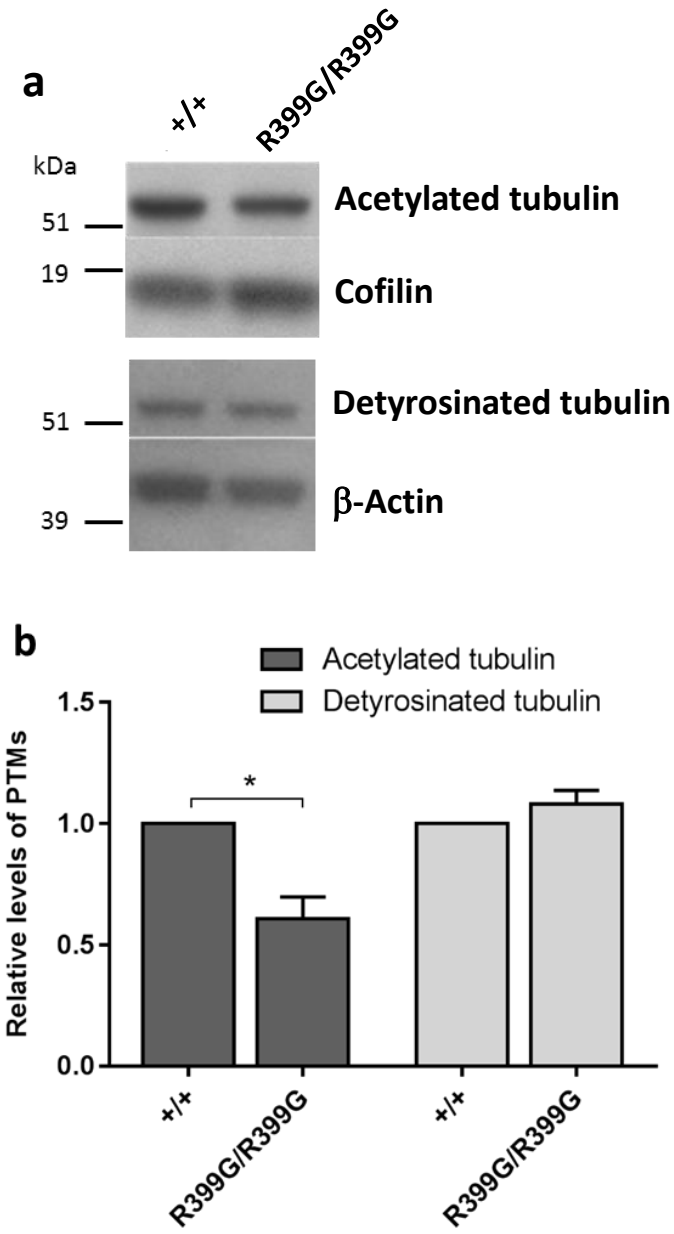
a
+/+
R399G/R399G
kDa
51
19
Acetylated tubulin
Cofilin
51
39
Detyrosinated tubulin
β-Actin
b
Acetylated tubulin
Detyrosinated tubulin
Relative levels of PTMs
1.5
1.0
0.5
0.0
*
+/+
R399G/R399G
+/+
R399G/R399G

Figure 4.8 *Cont.*

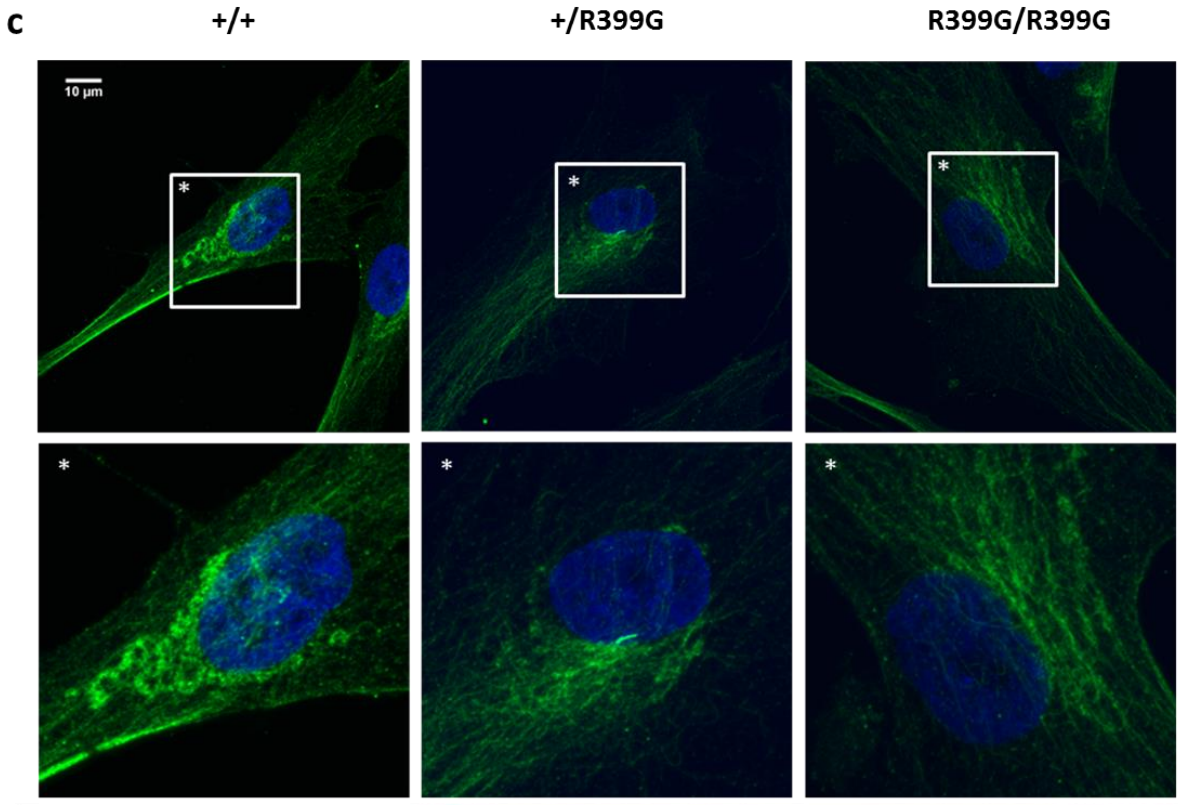

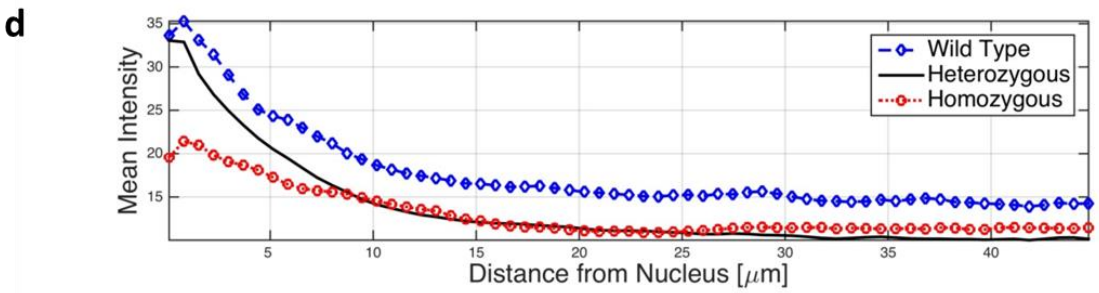

Figure 4.8- **(a)** SDS-PAGE western blot of acetylated tubulin and detyrosinated tubulin in wild-type and p.R399G homozygous fibroblasts. Both cofilin and β-actin are presented as loading controls respective to their adjacent bands. **(b)** Quantification of acetylated tubulin and detyrosinated tubulin in wild-type and homozygous fibroblasts. **(c)** Immunofluorescent high resolution 63x images of peri-nuclear acetylated tubulin (shown in green) in fixed wild-type and p.R399G mutant fibroblasts (asterisks highlight zoomed in regions). **(d)** Quantification of peri-nuclear (40µm) acetylated tubulin in wild-type and mutant fibroblasts. Image acquisition was conducted using a Leica TSC SP8 confocal microscope with a 63x objective.

7.1.7 Elucidating the rate of α-tubulin deacetylation at Lysine 40 in p.R399G homozygous fibroblasts

HDAC6 is the primary deacetylase enzyme in cells that can remove the acetyl group present on tubulin at the Lysine 40 residue. As a depletion of acetylated tubulin has been detected in p.R399G mutants it is important to measure the rate of deacetylation. This was achieved by treating cells with tubacin, a potent HDAC6 inhibitor in order to increase the amount of acetylated tubulin. The drug was then washed away from the cells in order to measure the rate of deacetylation. The subsequent homogenates obtained from these cells were then subjected to SDS-PAGE analysis (Figure 4.9 panel a).

The western blot indicates that at the 2-hour time point in homozygous mutant fibroblasts after tubacin wash-out there was a substantial decrease in acetylated tubulin in comparison to the wild-type cells. This is not due to changes in total tubulin as no differences in the control blot could be detected and levels of acetylated tubulin are comparable at the 0-time point for both wild-type and mutant fibroblasts (Figure 4.9 panel a). The quantification of three separate experiments did not yield a significant difference between the genotypes although a clear trend of increased deacetylation can be seen in the homozygous mutant fibroblasts (Figure 4.9 panel b).

Figure 4.9

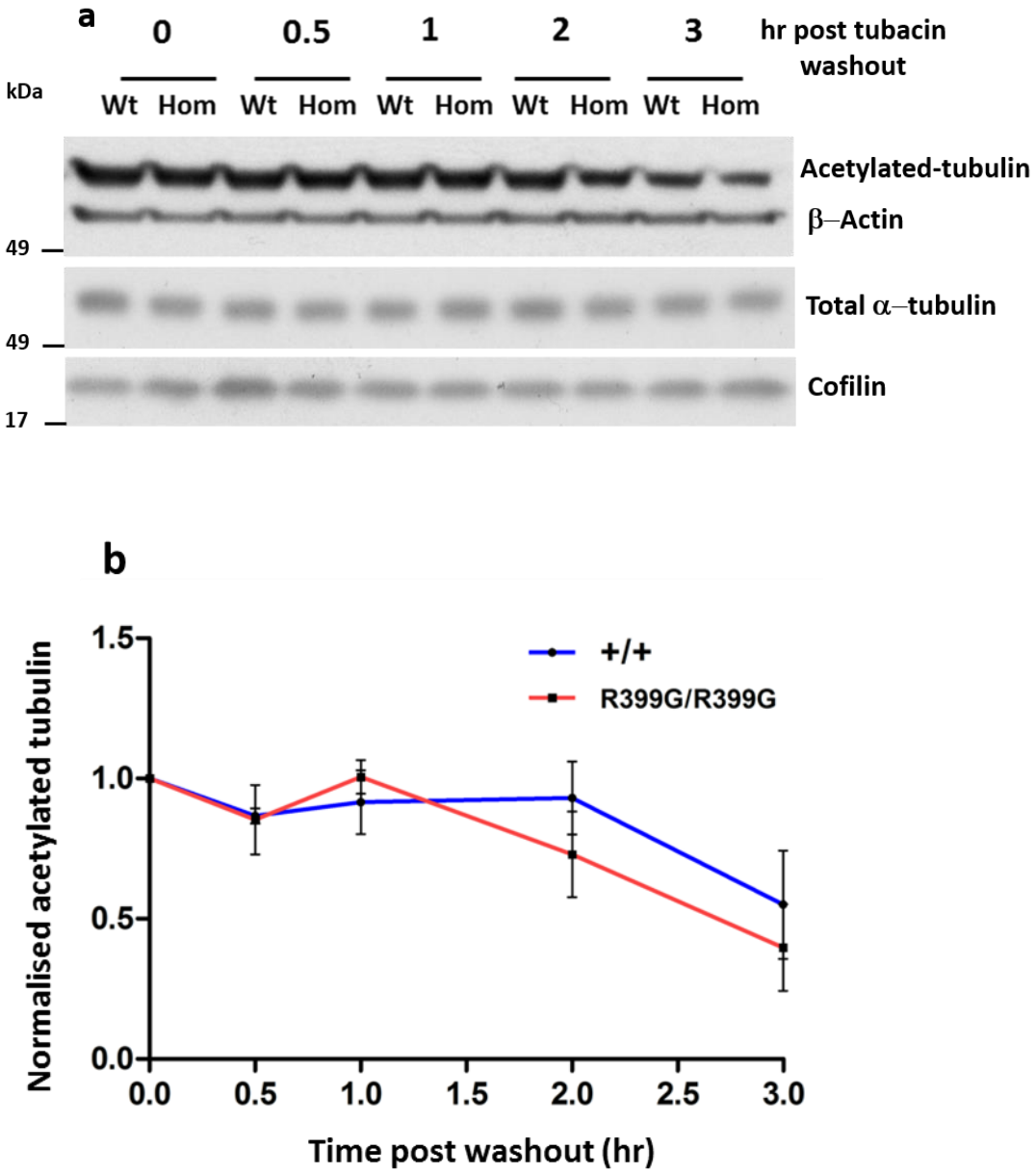

Figure 4.9- **(a)** SDS-PAGE analysis of total cell homogenates harvested from wild-type and mutant p.R399G fibroblasts after post 20 μM tubacin washout. The response to the tubacin washout was monitored using an antibody against acetylated tubulin at 0,0.5, 1,2 and 3-hour time points. **(b)** Quantification of acetylated tubulin normalised to either β–actin or cofilin, total α-tubulin was also probed for to demonstrate no change in protein levels.

7.1.8 Dynein depletion on the Golgi apparatus in p.R399G fibroblasts is not rescued by increasing acetylated tubulin

Dynein preferentially interacts with microtubules that are acetylated at Lysine 40 and furthermore, the population of microtubules that are associated with the Golgi are rich with post-translational modifications. Therefore, it could be hypothesised that the recruitment of dynein to Golgi membranes is possibly promoted by microtubule acetylation.

To test this hypothesis p.R399G fibroblasts were cultured on glass coverslips and labelled with antibodies against the DIC as well as giantin to visualise the Golgi. High resolution images of the Golgi in wild-type and p. R399G homozygous mutants were taken to assess the extent of DIC associated with the Golgi membranes. In this analysis, the total intensity of the DIC signal present on the Golgi was divided by the area of the Golgi apparatus in both genotypes (Figure 5.0 panel a). Visually, a striking reduction of DIC signal associated with the Golgi apparatus was apparent in the p.R399G homozygous fibroblasts compared to the wild-type cells. Quantification of the reduction indicated a significant difference between wild-type (N = 21) and homozygous (N = 20) fibroblasts (P <0.05 see Figure 5.0 panel b) from three experiments. To establish if this depletion of dynein from the Golgi membranes could be improved by increasing acetylated tubulin via inhibition of HDAC6, fibroblasts were treated with tubacin (Figure 5.0 panel a). Upon visualisation of dynein in these treated cells no obvious improvement of dynein associated with the Golgi was detected. The reduction of dynein at the Golgi in p.R399G human fibroblasts in comparison to wild-type cells was statistically maintained (P = 0.0052).

In summary, the p.R399G mutation results in a striking depletion of dynein associated with the Golgi apparatus. However, this depletion seems independent of the reduced acetylation at Lysine 40 of α-tubulin.

Figure 5.0

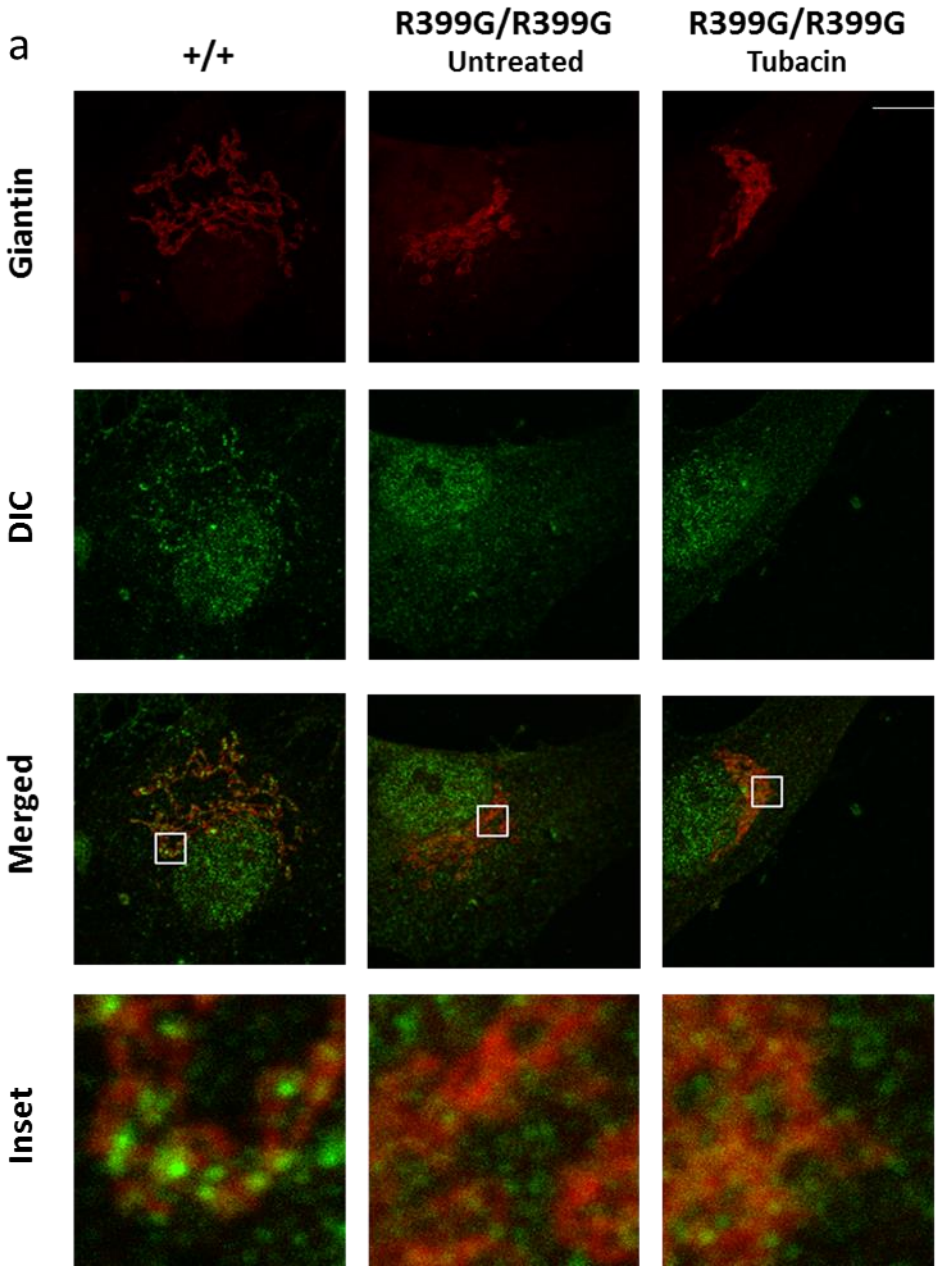
a
+/+
R399G/R399G
Untreated
R399G/R399G
Tubacin
Giantin
DIC
Merged
Inset

Figure 5.0 ***Cont.***

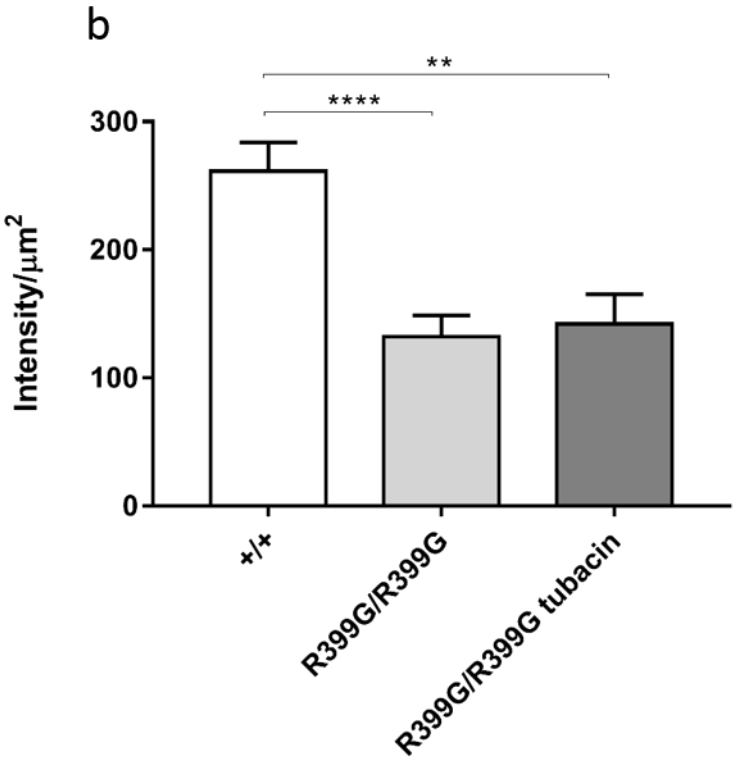

Figure 5.0- **(a)** Immunofluorescent images taken at 63x magnification (1.2 factor zoom) of wild-type and homozygous p.R399G fixed fibroblasts stained with antibodies against the DIC (green) and giantin Golgi marker (red). Wild- type fibroblasts show visual association between the DIC and giantin signals whereas the homozygous mutants do not. Tubacin treated homozygous mutants do not show recovery of DIC –Golgi localisation. **(b)** Quantification of the DIC total intensity associated with the Golgi divided by Golgi area in wild-type and homozygous mutants (see materials and methods). Image acquisition was conducted using a Leica TSC SP8 confocal microscope with a 63x objective.

7.1.9 Increasing acetylated tubulin in p.R399G homozygous mutants rescues Golgi fragmentation

Simultaneously whilst investigating the association between dynein and the Golgi apparatus (see above) the extent of Golgi fragmentation was also examined. This was to determine if increasing acetylation through tubacin had any impact on Golgi fragmentation in the p.R399G mutant fibroblasts and three independent experiments were subsequently conducted (Wild type N=30, p.R399G homozygous N=33, wild type tubacin N=33, p.R399G homozygous tubacin N=32).

As expected in DMSO treated cells a clear increase in Golgi fragmentation in the p.R399G mutants remained both visually and quantitatively compared to wild-type fibroblasts (***P<0.001, Figure 5.1 panels a and b). When treated with tubacin, wild-type human fibroblasts did not show any significant change in mean Golgi fragments. In contrast when p.R399G homozygous fibroblasts were treated with tubacin the fragmentation of the Golgi apparatus significantly decreased to wild-type levels (**** P<0.0001).

These results indicate that the HDAC6 inhibitor tubacin can rescue Golgi fragmentation inflicted by the p.R399G mutation although the lack of dynein present on the Golgi apparatus cannot be rescued through this mechanism.

Figure 5.1

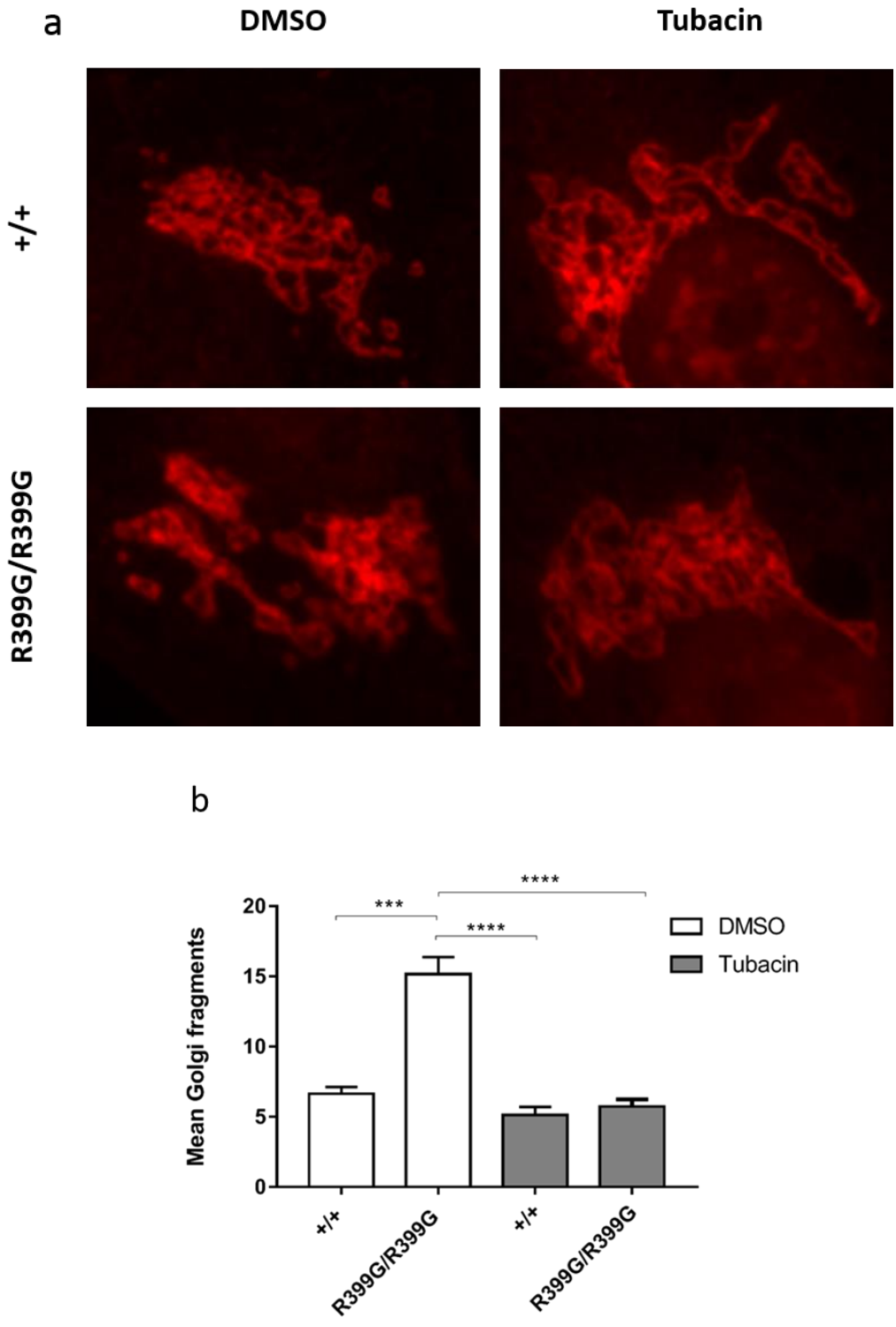

Figure 5.1- **(a)** Immunofluorescent images of fixed wild-type and p.R399G mutant fibroblasts stained with giantin (Golgi) treated with either DMSO or 20 μM tubacin. **(b)** Quantification of Golgi fragments from wild-type or homozygous p.R399G fibroblasts after treatment with tubacin or DMSO (control). Image acquisition was conducted using a Leica TSC SP8 confocal microscope with a 63x objective.

7.1.10 Increasing acetylated tubulin at Lysine 40 results in a down-regulation of golgin 160

As golgin 160 is part of a tether that couples microtubules to the Golgi membrane through dynein it was hypothesised that changes in acetylation may affect golgin 160 expression. Yadav et al. had previously shown that the siRNA knock-down of golgin 160 had no impact on microtubule acetylation however, the response of golgin 160 to changes in α-tubulin have not been reported.

Both wild-type and p.R399G fibroblasts were cultured in a 6-well plate and treated with tubacin before harvesting the homogenates for SDS-PAGE analysis. Both wild-type and mutant fibroblasts illustrated a dramatic increase in acetylated tubulin as expected (Figure 5.2 panel a). In contrast, the amount of golgin 160 detected in both genotypes fell dramatically after tubacin treatment. Quantification of wild-type fibroblasts from separate experiments experiments (N = 3) indicated a significant decrease (*P<0.05) of golgin 160 after exposure to tuabcin (Figure 5.2 panel b). This result indicates that the level of golgin 160 is responsive and downstream to changes in acetylated tubulin at Lysine 40.

Figure 5.2

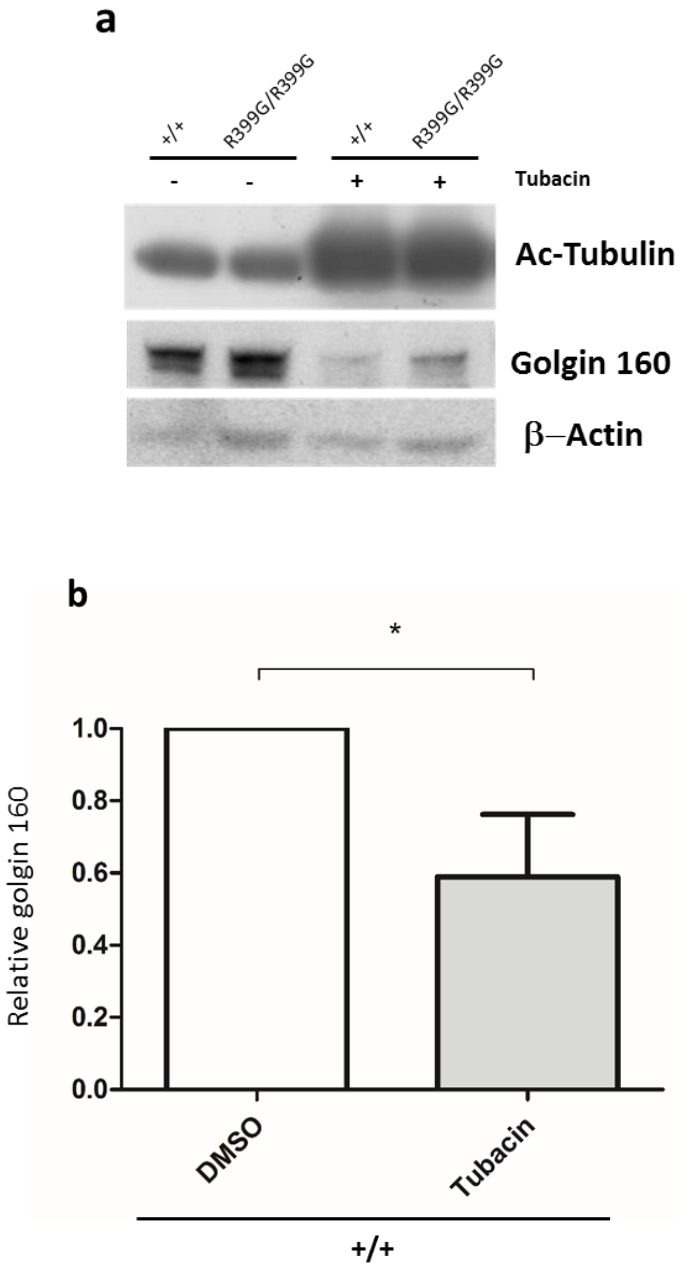

Figure 5.2- **(a)** SDS-PAGE analysis of total cell homogenates from wild-type and homozygous p.R399G mutants using antibodies against acetylated tubulin and golgin 160 with and without tubacin treatment of cells. The loading control employed in this blot was β-actin. **(b)** Quantification of golgin 160 in wild-type fibroblasts after treatment with 20 μM tubacin or DMSO (control).

7.1.11 The maturation of endosomes is impaired in p. R399G mutant fibroblasts

Dynein is important for the retrograde motility of endosomes within the endocytic pathway. Dynein contributes to the short-range mobilisation of endosomes but importantly, is responsible for driving the long-range transport of endosomes in which dynactin is highly essential and integral for neuronal function (Flores-Rodriguez et al. 2011). Furthermore, mutations in the tail or motor domains of the DHC have been found to perturb early endosome trafficking (Xiang et al. 2015; Garrett et al. 2014). It is critical therefore to establish if the p.R399G mutation could be causing endosomal pathology in human fibroblasts as it provides insight into dynein motility in these mutants.

Initially, as the number of endosomes produced during endocytosis is likely affected by cell size, the area of wild-type and heterozygous and homozygous mutants were measured (N = 15, respectively). Statistical analysis indicated no difference in cell size between the different genotypes (Figure 5.3 panel b).

Next, to determine if the p.R399G mutation was detrimental to endocytosis; fibroblasts were exposed to EGF-Alexa Fluor ® 555 after serum starvation and fixed at 0, 10, 30, and 60 minute time points. The number of endosomes from each cell (N >10 for each genotype at every time point) were then counted using the particle analysis tool on ImageJ (see Figure 5.3 panel a, c,).

Statistical analysis indicated that there were no differences in number of endosomes between genotypes at any time point (Figure 5.3 panel c). Despite

this a trend can be observed of increased number of endosomes in p.R399G homozygous cells at the 0 and 10 minute time points compared to wild-type and heterozygous fibroblasts.

As endosomes mature through the early to late stages of the endocytic pathway they become larger in size. To elucidate if the p.R399G mutation was indeed effecting this process the area of all detected endosomes were quantified (Figure 5.3 panel d). Statistical analysis indicated significant differences between all three genotypes at both 0 and 10-minute time points (***P<0.001). Noticeably endosomes from the heterozygous fibroblasts were much larger than both the wild-type and homozygous cells (Figure 5.3 panels a and d). No differences in endosome size were noted at the 30-minute time point. However, at the 60-minute time point, endosome sizes in the heterozygous and homozygous fibroblasts were statistically smaller than wild-type cells (***P<0.001 and ***P<0.001 respectively).

In summary, these results indicate that the p.R399G mutation in the DHC does not affect the ability of cells to endocytose the EGF receptor. Despite this the mutation alters the size of endosomes observed suggesting that maturation is impaired. The increase in endosome size in the heterozygous fibroblasts at earlier time points could suggest an affect caused by mixed dynein populations of wild-type and mutant DYNC1H1.

Figure 5.3

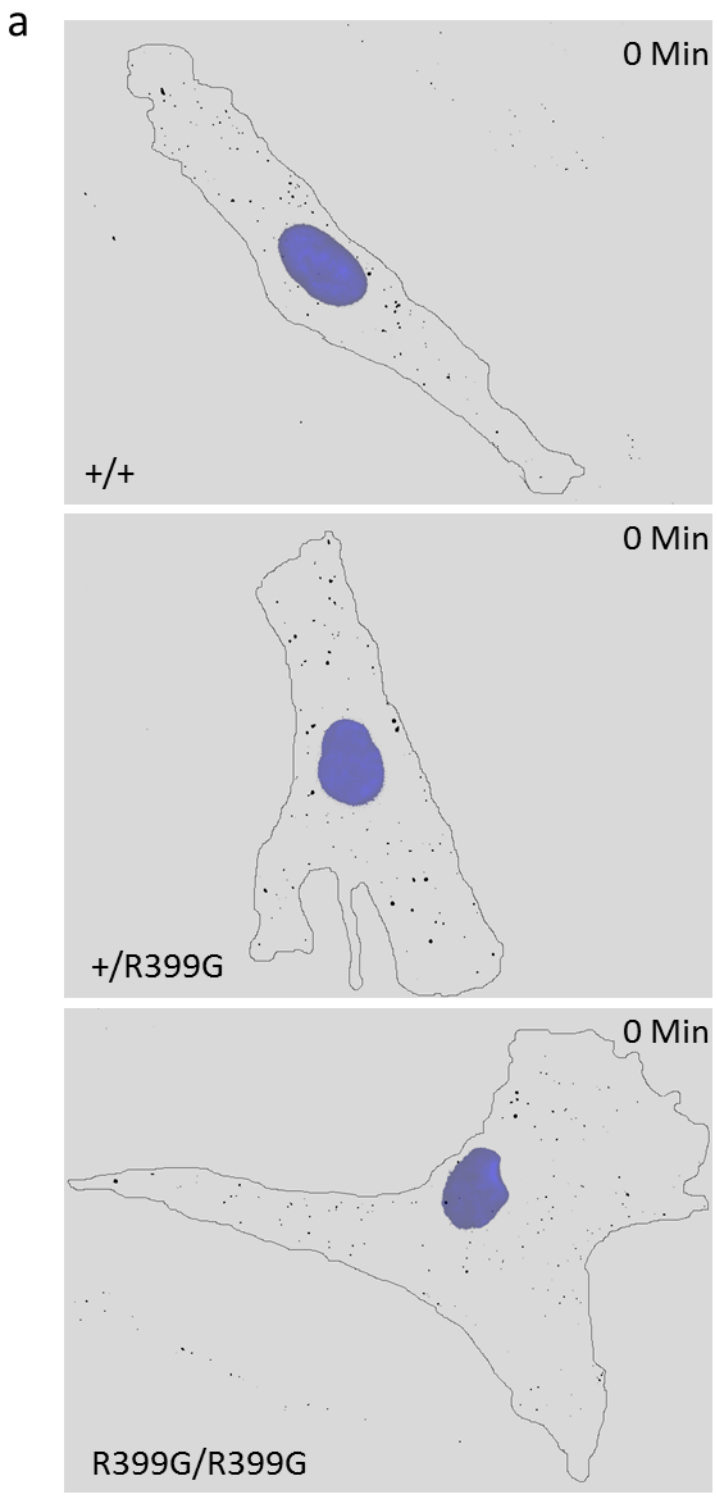

Figure 5.3 ***Cont.***

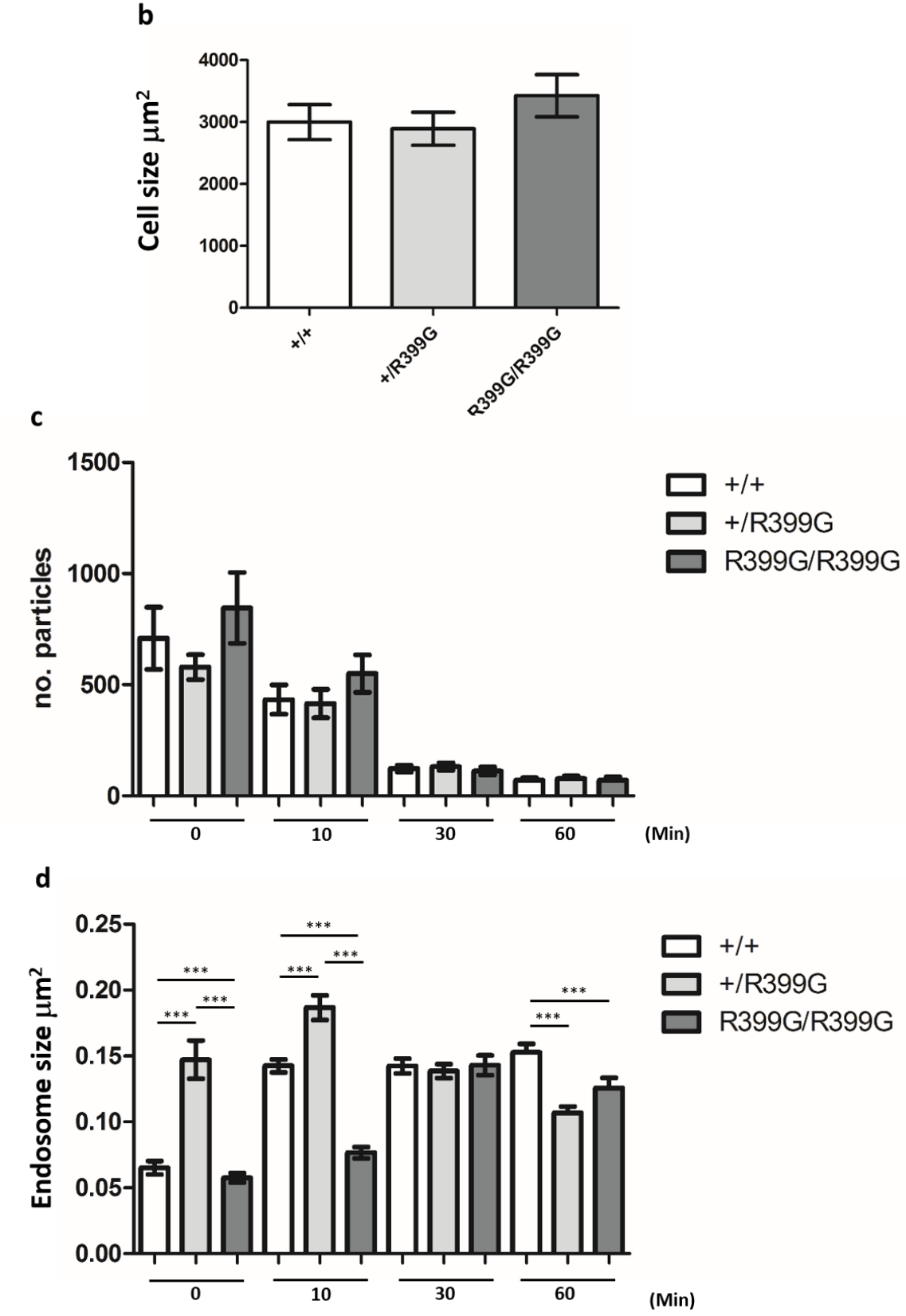

Figure 5.3- (**a**) Images of wild-type and p.R399G mutant fibroblasts indicating endosomes (black punctate signals) detected by thresholding in ImageJ with cell-edge traced and the nuclei (blue) super-imposed at time point 0 after addition of EGF-Alexa Fluor ® 555. (**b**) Quantification of cell area in wild-type and mutant fibroblasts showing no significant differences between genotypes. (**c**) Quantification of mean number of particles (endosomes) per cell in each genotype after serum starvation and addition of EGF-Alexa Fluor ® 555 at 0, 10, 30, and 60-minute time points (no significant differences were found). (**d**) Quantification of endosome sizes for each genotype measured at each time point to measure endosome maturation significant differences are indicated by *** (P<0.0001). Image acquisition was conducted using a spinning disc Olympus-3I microscope using a 63x oil objective mounted with an EMCCD Evolve camera.

7.12 Chapter 4 summary

The data from this chapter has shown that the p.R399G mutation does not affect the subunit assembly of the dynein complex suggesting that disruption of the complex is not the underlying pathogenic mechanism caused by this mutation. Additionally, this chapter has indicated for the first time that dynein mutations in human cells can cause inherent fragmentation of the Golgi apparatus which also effects Golgi morphology during migration. Additionally, this fragmentation is coupled with an increased interaction between golgin 160 and dynein and a decrease in acetylated α-tubulin at Lysine 40. This indicates for the first time that mutations in *DYNC1H1* can influence the acetylation of microtubules at Lysine 40. Importantly, the Golgi fragmentation can be rescued with HDAC6 inhibition, but a lack of association between dynein and the Golgi was not rescued suggesting a segregation of mechanisms. Lastly, endocytosis was not affected by the p.R399G mutation although a significant delay in endosome enlargement was observed indicating the mutation is affecting maturation of endosomes.

7.13 Chapter 4 Discussion

7.13.1The p.R399G mutation does not affect the dynein complex

Previous evidence from the Hafezparast lab has shown that mutations in the DHC subunit of dynein can impair dynein complex formation. Specifically, the *Loa* mutation was found to cause an increase in binding in the DIC and the DLIC subunits of dynein. To determine if the p.R399G mutation influences subunit binding of the dynein complex a sucrose density gradient was performed with subsequent SDS-PAGE analysis of wild-type and homozygous fibroblasts. It is

worthy to note that much optimisation was needed to accurately perform this type of analysis due to the sensitivity of the technique. Analysis of the Western blots indicated a possible dissociation of DYNC1H1 from the complex as indicated by a signal in fraction 6. However, duplication of this experiment identified this signal also in wild-type fibroblasts. This led to the conclusion that the difference from the first experiment was likely due to a Western blot discrepancy with the DYNC1H1 protein due to its large size (>500kDa) and not a disruption caused by the p.R399G mutation.

Interestingly, a signal from the DYNC1I2 was repeatedly observed in both genotypes in fraction 3 indicating a possible dissociation away from the complex. This was coupled with matching signals in fraction 3 from DYNC1LI1/2 in both genotypes. The DIC and DLIC complex with the DHC in the dynein complex but have not been found to be functionally active outside of the dynein complex thus far. However, the dynein light chains such as LC8 has multiple binding partners that are dynein independent (Asthana et al. 2012). Therefore, the DIC and DLIC observed in fraction 3 could represent partially dissociated dynein through the homogenisation process.

In order to confirm that the p.R399G mutation was not disrupting any subunit interaction, an IP was performed between DIC and DYNC1H1 as the mutation lies closest to the DIC binding region. Investigation of the subsequent blot, however, indicated no differences in the binding affinity between DYNC1H1 and the DIC and furthermore, indicated no DYNC1H1 homodimerisation defect.

7.13.2 The p.R399G mutation causes Golgi fragmentation and perturbed morphology during migration in human fibroblasts

Dynein has a key role in Golgi homeostasis and previous data from the Hafezparast lab has shown that *Arl* and *Loa* mutations in the DHC can inflict impaired Golgi recovery after nocodazole treatment. To study the structure of the Golgi, both live cell imaging and fixed cell imaging techniques were employed. Results from these investigations showed that the p.R399G mutation caused fragmentation of the Golgi apparatus. This is further confirmed by the electroporation of the mutant fibroblasts with a wild-type dynein construct which rescued the fragmentation of the Golgi apparatus.

It has been shown that DHC human mutations can result in impaired Golgi recovery after nocodazole treatment (Fiorillo et al. 2014). But my data for the first time show that inherent fragmentation is present in patient cell harbouring the p. R399G mutation.

The reasons for why this fragmentation is observed is less clear however, it is likely due to an interruption of a dynein specific interaction or perhaps an impact upon microtubule dynamics or stability which prompted further investigation.

To further explore this phenotype, the Golgi of migrating fibroblasts harbouring the p.R399G mutation were studied and compared to wild-type migrating cells. The ability of cells to migrate and neurons to undertake arborisation is partly dependent on the Golgi, thus, it was hypothesised that this dysregulation could underlie SMA-LED. Dynein is crucial for Golgi re-orientation, these results from

this experiment however, did not indicate an impairment of the Golgi to orientate towards the direction of migration in p.R399G mutants (Yadav et al. 2012). Rather, a condensation phenotype is observed in the mutants in comparison to the wild-type fibroblasts.

This could perhaps indicate that the mechanism of Golgi re-orientation is not affected by this mutation, but instead segregated sections of Golgi membrane collapse into a peri-nuclear region. My data could suggest another function of dynein that maintains the Golgi in an expanded morphology perhaps to ensure adequate secretion and delivery of proteins to their target sites.

7.13.3 The p.R399G mutation results in an increased interaction between golgin 160 and dynein.

These morphological results prompted investigation into the interaction between dynein and a protein known as golgin 160 which represents the only known binding partner of dynein at the Golgi membrane. Golgin 160 resides in the membrane of the Golgi apparatus and consequently, dynein acts as the tether between microtubules and the Golgi (Yadav et al. 2012). Immunoprecipitation of golgin 160 with its binding partner DIC, however, indicated that the p.R399G mutation resulted in an increased interaction with golgin 160. This was a surprising result as Yadav et al. demonstrated that knock-down of golgin 160 causes extensive Golgi fragmentation (Yadav et al. 2012). Additionally, the authors had previously shown that siRNA against golgin 160 resulted in an inability for the Golgi to orientate during migration (Yadav et al. 2009).

As results show that re-orientation is not impaired by the mutation and that an increase in golgin 160 binding is observed in mutants, this strongly suggests that the interaction between dynein and golgin160 is unaffected. Rather, this indicates a compensatory response to ameliorate the Golgi fragmentation. This is supported by the fact that when the Golgi was artificially fragmented using nocodazole in wild-type cells, the quantity of golgin 160 pulled down with dynein increased. There was little or no response to this artificial fragmentation in mutants suggesting that this compensatory mechanism may already be active. Despite this, increased affinity between golgin 160 and dynein due to the p.R399G mutation cannot be completely ruled out.

7.13.4 The p.R399G mutation causes depletion of acetylation at Lys40

The data indicating that the interaction between dynein and golgin 160 was increased prompted the hypothesis that another faulty mechanism may be the cause of the observed Golgi fragmentation. Microtubules have long known to be important in the structural maintenance of the Golgi apparatus. Additionally, these Golgi associated microtubules are rich in post translational modifications (PTMs) such as acetylation at Lys40 are thought to contribute to Golgi coherence (Rios 2014; Thyberg & Moskalewski 1993).

Initially, p.R399G homozygous mutant fibroblasts were analysed by SDS-PAGE in order to quantify the amount of acetylated tubulin at Lys40 (acetylated tubulin hereafter) in comparison to wild-type cells. This indicated a significant reduction of acetylated tubulin in homozygous mutants. This difference was not observed when detyrosinated tubulin (another Golgi PTM) was analysed suggesting that

the p.R399G mutation was specifically affecting acetylated tubulin. This was further confirmed with high resolution immunofluorescent images of peri-nuclear acetylated tubulin indicating a significant reduction in the p.R399G mutants.

The question as to why a mutation in dynein is affecting PTMs of microtubules is not clear. Currently there is conflicting evidence as to the stabilising implications of PTMs upon microtubules. The acetylation of microtubules occurs when they are stable, the p.R399G mutation could be effecting the stability of microtubules as dynein travels along them. However, reduced stability would have also led to a decrease in detyrosinated tubulin which was not observed.

This therefore indicates a specific mechanism that dynein influences for the acetylation of microtubules, this might not be surprising as dynein preferentially interacts with acetylated microtubules. A potential mechanism could be through a protein known as GEF-H1, a nucleotide exchange factor associated with microtubules. It is known to increase microtubule stability and acetylation but importantly interacts with dynein through Tctex-1 (Yoshimura & Miki 2011; Meiri et al. 2014). This is currently under investigation by the Hafezparast lab as it could be the link between dynein and acetylation of microtubules. Interestingly, further data from this lab has shown that fibroblasts from the *Loa* mouse model also show depletion of acetylated tubulin.

7.13.5 Evaluating the rate of α-tubulin deacetylation in p.R399G homozygous fibroblasts

The lack of acetylated tubulin at Lysine 40 in p.R399G mutants prompted the hypothesis that the deacetylation rate in p.R399G mutant fibroblasts may be different to that of wild-type cells. To test this a HDAC6 inhibitor tubacin was employed to maximise the acetylation of the microtubules, tubacin was then washed out and the amount of acetylation at Lysine 40 was monitored over a 3-hour period.

The quantification of the rate of deacetylation in homozygous mutants indicates a trend of increased deacetylation in comparison to wild-type cells. Although this was not measured to be a significant result, comparing total α-tubulin between the two genotypes clearly indicates that it is not simply a general reduction in total α-tubulin. There are multiple reasons for why an increased deacetylation rate is observed in the homozygous mutants.

Firstly, as aforementioned, this could be related to microtubule stability but this is unlikely. Secondly, the active availability of HDAC6 in p.R399G homozygous mutants could be impaired. HDAC6 interacts with dynein as an adaptor for cargo that has been tagged with ubiquitin for clearance of misfolded or aggregating proteins (Kawaguchi et al. 2003). If the p.R399G mutation somehow causes increased aberrant binding of HDAC6 to dynein it may promote deacetylation of microtubules due to more available HDAC6. Despite this the impact of HDAC6 and dynein interaction upon the rate of deacetylation is currently unknown.

Lastly, an increase in actual HDAC6 activity could be possible, Rho-associated coiled-coil kinase (ROCK) activity increases the activity of HDAC6 through TPPP1 phosphorylation (Schofield et al. 2012). ROCK is a target of Rho which can be activated by GEF-H1 release from microtubules (an aforementioned binding partner of dynein) (Takesono et al. 2010). In summary, this means that a binding deficiency between dynein and GEF-H1 caused by the p.R399G mutation could underlie the observed acetylated tubulin phenotype. The intricacies of this pathway would have to be carefully considered in future research.

7.13.6 Homozygous p.R399G mutant fibroblasts show dynein depletion on the Golgi apparatus which cannot be rescued through increasing acetylated tubulin

It is possible that the acetylation of microtubules could be important in recruiting dynein to the Golgi. This is due to the fact that dynein preferentially binds acetylated microtubules and the Golgi has a large proportion of acetylated microtubules associated with it. To analyse this the DIC co-localised with the Golgi was evaluated in homozygous p.R399G mutants and wild-type fibroblasts. A reduction in associated DIC with the Golgi was detected in the mutants compared to the wild-type cells however, this was not rescued with tubacin treatment.

These results show that a reduced acetylated tubulin phenotype and a reduced DIC-Golgi association phenotype exist due to the p.R399G mutation, but they are likely unrelated. Although a link between Golgi-dynein localisation and the acetylation status of microtubules cannot be ruled out. The increase in acetylation

through HDAC6 inhibition did not promote the association of dynein with the Golgi. This suggests that the recruitment of dynein to Golgi membranes is impaired. Interestingly, it has been shown that cells lacking Golgin 160 cause dynein associated with the Golgi to be depleted more than 90% (Yadav et al. 2012). In the case of the p.R399G mutants there is an increase in Golgin 160 and dynein interaction but less dynein associated with the Golgi. This could perhaps suggest that dynein could be interacting with Golgin 160 away from Golgi membranes but remains to be determined. Poor immunofluorescent staining with the Golgin 160 antibody prevented any analysis of Golgin 160 localisation in p.R399G mutant fibroblasts.

7.13.7 Increasing microtubule acetylation through HDAC6 inhibition in p.R399G homozygous mutants rescues Golgi fragmentation

Even though increasing microtubule acetylation did not influence the association between dynein and the Golgi, it was important to determine if the Golgi fragmentation phenotype could be rescued. Wild-type and homozygous mutants were treated with tubacin to determine if HDAC6 inhibition could rescue Golgi fragmentation. The results showed that the fragmentation in the p.R399G homozygous mutants significantly reduced when treated with tubacin. This indicates that increasing acetylation at Lysine 40 of microtubules in mutants may rescue the phenotype through a mechanism that maybe unrelated to lack of dynein on the Golgi membranes that may actually cause the fragmentation. Conversely the tubacin treatment maybe bypassing an aberrant mechanism of acetylation related to the localisation of dynein to the Golgi. This data further

indicates that the lack of co-localisation between dynein and the Golgi may not be solely imperative to Golgi cohesion.

Interestingly, recent evidence gathered in the Hafezparast lab has shown that another human dynein mutation p.D338N results in depletion of acetylated tubulin. Despite this there is no lack of co-localisation of dynein with the Golgi but no inherent Golgi fragmentation suggesting that both deficiencies are required for Golgi fragmentation. This is summarised in a diagram depicted in Figure 5.4.

Figure 5.4

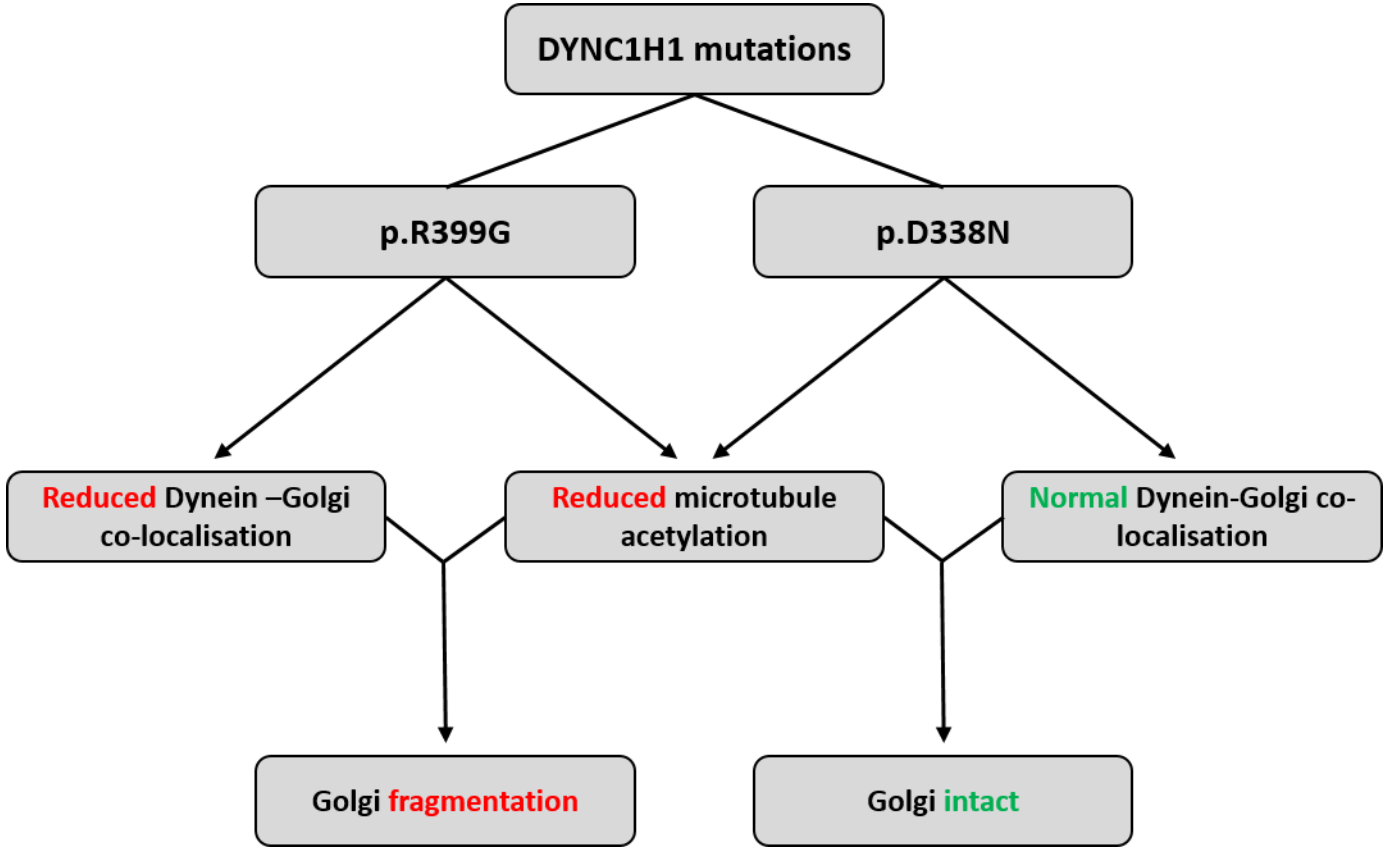

Figure 5.4- The above diagram depicts the impact of human dynein mutations upon the acetylation status of microtubules as well the co-localisation of dynein to the Golgi. The summation of the MT acetylation and dynein recruitment to the Golgi dictate the structural integrity of the Golgi in human fibroblasts.

Increasing acetylation at Lysine 40 results in a down-regulation of golgin 160

The concomitant reduction in acetylated microtubules coupled with an increased interaction between dynein and golgin 160 in p.R399G mutant fibroblasts prompted the idea that these phenotypes may be interrelated. To test this hypothesis both wild-type and homozygous mutant p.R399G fibroblasts were treated with HDAC6 inhibitor tubacin, before analysing golgin 160 through SDS-PAGE analysis (Figure 5.0).

Data obtained from this experiment indicated that the golgin 160 seems to be down regulated when the acetylation at Lysine 40 is increased in both wild-type and mutant cells. Previous (unpublished) data from Yadav et al. has shown that golgin 160 knockdown did not affect acetylated tubulin (Yadav et al. 2009). Together, this suggests that golgin 160 is regulated down-stream of acetylated tubulin. Furthermore, it is possible that the decrease in acetylated tubulin in the p.R399G mutants is causative of the increased interaction between golgin 160 and dynein previously shown. This proposes a potential regulation of golgin 160 through PTMs of microtubules although time restrictions have prevented further investigation.

The maturation of endosomes is impaired in p.R399G mutant fibroblasts

Dynein is integral for the retrograde motility of endosomes during the endocytic pathway. Other mutations in the DHC such as in the *Loa* mouse model have indicated deficiencies in endocytic trafficking (Garrett et al. 2014). Wild-type and

p.R399G mutant fibroblasts were serum-starved before exposure to EGF-Alexa Fluor ® 555 and fixed at several time points in order to monitor endocytosis (Figure 5.1).

The number of endosomes did not significantly differ between genotypes at any of the time points (0, 10, 30 and 60 minutes). This indicated that the process of endocytosis was not affected by the p.R399G mutation. This was a distinct possibility as dynein has been implicated in the tubular internalisation of vesicles (Day et al. 2015). Upon analysing the size of the endosomes in order to measure endosome maturation the p.R399G mutation caused a delay in endosome maturation in the homozygous fibroblasts (particularly at the 10 minute time point). Previous data from Garrett et al. showed that the *Loa* homozygous fibroblasts also show a reduction in size of EGF containing vesicles at the ten-minute time point (Garrett et al. 2014).

This indicates a dynein dependent step of endosome maturation that is affected by mutations in the DHC. Interestingly, the endosomes observed in the heterozygous mutants at the 0 and 10-minute time points seem to be much larger than the other genotypes. These larger endosomes could actually represent small clusters of endosomes in which the clusters are periodically brought together for maturation but the DHC mutation causes disruption of the endosomal fusion. This may be due to mixed populations of dynein imparting counteractive effects on endosomal maturation in the heterozygous fibroblasts but this requires further investigation.

Chapter 5- Analysing the impact of the *Arl* mutation on cell migration and brain morphology

8.0 Introduction

The *Arl* mouse model was generated through ENU mutagenesis and exhibits an autosomal dominant p.Trp1206Arg mutation in the tail domain of Dync1h1. This model effectively recapitulates the slow motor neuron degenerative progression of SMA-LED, therefore representing a valuable model for understanding aspects of disease progression in SMA-LED.

A common condition compounding SMA-LED in patients is MCD in which the aberrant organisation of neurons in the cortex can result in cognitive deficits. Not all patients with DYNC1H1 mutations present with MCD and it is currently unknown why this disparity exists. Previous data from the Hafezparast lab at Sussex University have shown that the *Loa* mutation (another tail domain mutation) causes a deficit in fibroblast migration. Importantly, the *Loa* mutation has been found to impair cortical lamination in mice although it is unclear if this has any relationship to aberrant cell migration (Ori-McKenney & Vallee 2011).

Currently, there is no information outlining the effects of the *Arl* mutation on both cell migration and its impact on cortical organisation of the brain. As both the *Loa* and *Arl* mutations have been found to impair Golgi recovery after fragmentation with nocodazole, it was hypothesized that they share common insufficiencies of cellular function. This could potentially also translate to shared abnormalities in the organisation of the cortex.

To investigate this, I have employed a fibroblast migration assay to investigate the impact of the *Arl* mutation on the speed of cell migration. Secondly I have

used perfusion and cryosectioning techniques in order to study gross anatomical differences in the brain between wild-type and *Arl*/+ adult mice. Lastly, the impact of the *Arl* mutation on cortical organisation was studied in p4 littermates.

8.1 Results

8.1.1 The *Arl*/+ mutation results in delayed cell migration in mouse embryonic fibroblasts.

Previous data from the Hafezparast lab has implicated mutations in *Dync1h1* in causing a defect in cell migration. Mouse embryonic fibroblasts cultured from the homozygous *Loa* mouse model indicated significant impairment in fibroblast migration. The p.Trp1206Arg *Arl* mutation is over 500 amino acids further towards the C-terminal in comparison to the *Loa* mutation. Although this is the case, both mutations still reside in the tail domain of the DHC and raises the hypothesis that mutations in the tail domain impair cell migration.

To investigate if the *Arl* mutation can result in perturbed cell migration, both wild-type and heterozygous fibroblasts were cultured in 6 well plates at the same density of 3×10^5. After 24 hours, monolayers of fibroblasts were observed at the same density for both genotypes. Cells were treated with 10 μg of mitomycin C to prevent cell division before introducing a monolayer wound across all wells using a 10 μl pipette tip. Pictures were taken at the time of introducing the wound and 12 hours later in order to derive comparisons (see Figure 5.5). Visually after 12 hours, *Arl*/+ fibroblasts had not closed the wound as quickly in comparison to the wild-type fibroblasts used as a control (Figure 5.5). In order to quantify this

difference, images were taken from three wound healing experiments for wild-type and *Arl*/+ fibroblasts furthermore, for each wound three images were taken in three separate positions (n = 9). The rate of gap closure was quantified in each case and a significant (P<0.05) delay in fibroblast migration was calculated in the case of the *Arl*/+ fibroblasts in comparison to the wild-type cells (Figure 5.5).

Figure 5.5

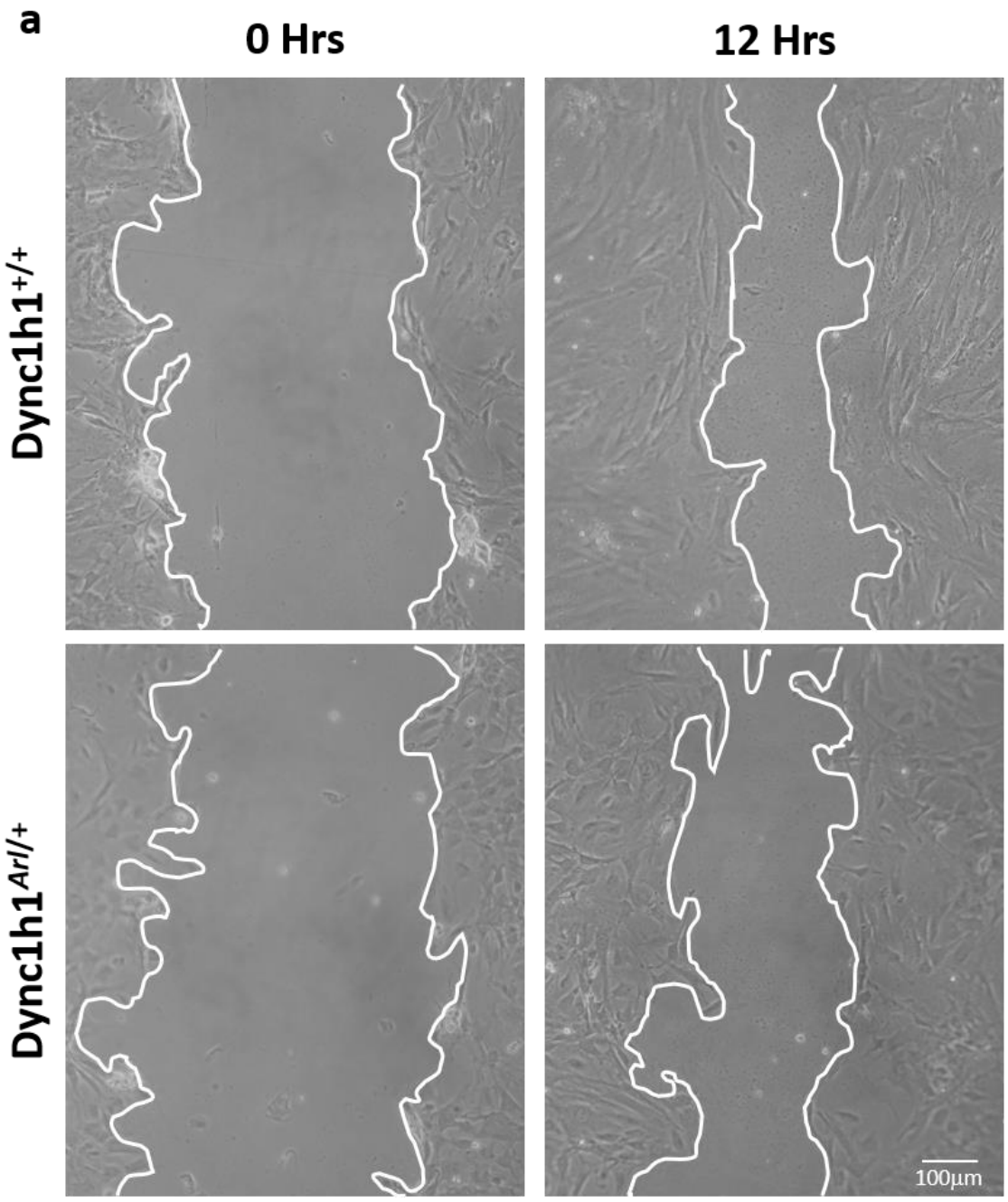

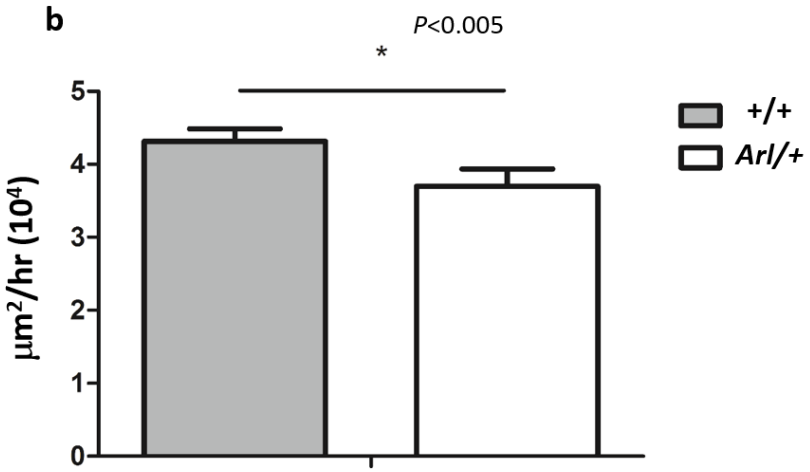

Figure 5.5- **(a)** Images (20x) of fibroblasts monolayer wound for both *Arl*/+ and wild-type cells indicating 0 and 12 hours post wound imaged on Zeiss Axiovert 25 (scale bar 100 μm). **(b)** Quantification of the rate of fibroblast migration for both wild-type and *Arl*/+ fibroblasts.

8.1.2 The organisation of cortical layers is impaired in *Arl*/+ adult mice

In accordance with the impaired *Loa/Loa* fibroblast migration data obtained by Dr Muruj Barri others have reported neuronal migration defects in the same genotype. Vallee et al. shows neuronal migration and cortical lamination deficits in the homozygous *Loa* mouse in comparison to wild-type mice (Ori-McKenney & Vallee 2011).

Similarly, as both the *Loa* and *Arl* mutations seem to result in a delay in fibroblast migration after a wound healing assay it was hypothesised that gross structural brain aberrations may be detected in *Arl*/+ mice. In order to test this hypothesis two adult *Arl*/+ (169 and 251 days old) and wild-type mice (115 and 122 days old) were perfused with 1% PFA to structurally preserve the brain. Subsequently, the

brains were cryopreserved, sectioned and then stained with cresyl violet in order to visualise the cell bodies of neurons in the coronal slices (see materials and methods).

Cortical slices were imaged at 4x and a murine brain atlas (Allen brain atlas available from: http://developingmouse.brain-map.org) was used in order to correctly match anatomical positions of every slice in both genotypes for definitive accuracy.

Cortical layers were determined through cross referencing images from Vallee et al (Ori-McKenney & Vallee 2011). Analysis of the coronal section of wild-type mice indicated a clear banding pattern of neurons in sections from both anterior and posterior regions of the brain (Figure 5.6). In comparison the *Arl*/+ mice exhibited a disorganised appearance of neurons in both layers II/III (white arrow) and prominently in layer IV (orange arrow). This abnormal neuronal phenotype was observed in both anterior and posterior regions of the brain (see Figure 5.6). In summary, this indicates that the *Arl* mutation perturbs neuronal organisation in the murine brain.

Figure 5.6

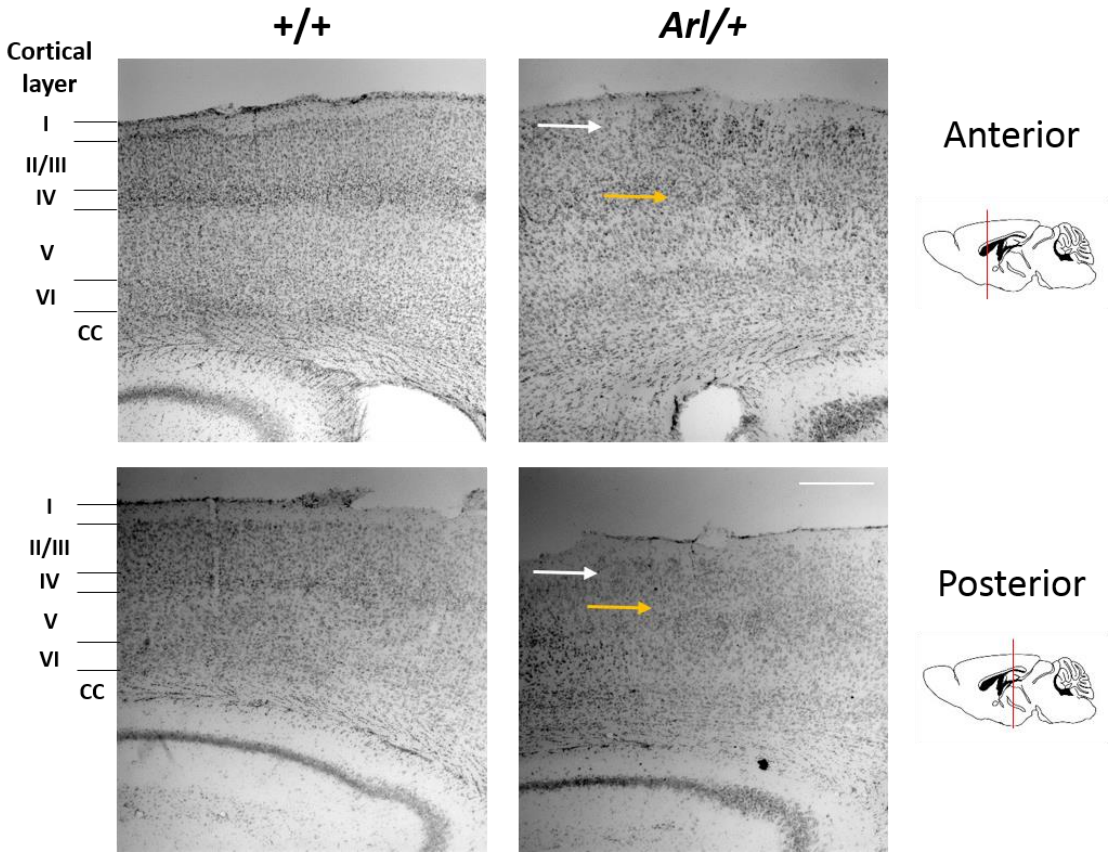

Figure 5.6- Images (4x) of coronal brain sections in anterior and posterior positions taken from both wild-type and *Arl*/+ mice stained with cresyl violet. Cortical layers are indicated on the left hand side of the figure as well as the corpus callosum (cc). White and orange arrows indicate observed structural differences. Cartoon brain images by Richard Osgood (scale bar represents 500 μm). Image acquisition was conducted using an Olympus BX55 with QI click camera.

8.1.3 The *Arl*/+ mutation causes a collapse of the third ventricle and condensation of the dentate gyrus.

After analysis of the disparity between *Arl*/+ and wild-type cortical neuron banding patterns observed in matched brain sections, other brain regions were examined for gross anatomical differences. Examination of the ventral regions of the brain in the *Arl*/+ mice, a striking observation regarding the third ventricle was highlighted. In all wild-type brain sections, the third ventricle appears to have an expanded phenotype with a clearly defined edge and a larger area polarised towards the dorsal region of the ventricle (Figure 5.7 panel a). Contrastingly, the third ventricle observed in *Arl*/+ brain sections exhibit a remarkable collapsed appearance with no polarity in area observed (Figure 5.7 panel a). In order to measure this difference, the area of the third ventricle was quantified in both *Arl* and wild-type genotypes with ImageJ (n = 4 respectively). The third ventricle size in *Arl* mice was measured to be significantly reduced in comparison to the third ventricles from the wild-type mice (Figure 5.7 panel b).

The examination of the dorsal area of the brain was prompted by the discovery by Vallee et al. that the size of the dentate gyrus was diminished in the *Loa/Loa* brain (Ori-McKenney & Vallee 2011). Upon observation of the dentate gyrus in the *Arl*/+ mice a clear condensed phenotype can be observed eliciting a distinctive shape. In comparison all sections from wild-type mice indicated a much narrower and protracted appearance in (Figure 5.7 panel c). In order to quantify any differences, the length of the dentate gyrus was measured from the most distal tips of the region in both genotypes (n = 4 in both cases). Although a clear trend of a reduced size of dentate gyrus can be seen in the *Arl*/+ genotype in

comparison to the wild-type brain, no statistical difference was found (Figure 5.7 panel d).

In summary the *Arl* mutation causes collapse of the third ventricle of the brain and an alteration of the shape of the dentate gyrus but without statistically affecting its length.

Figure 5.7

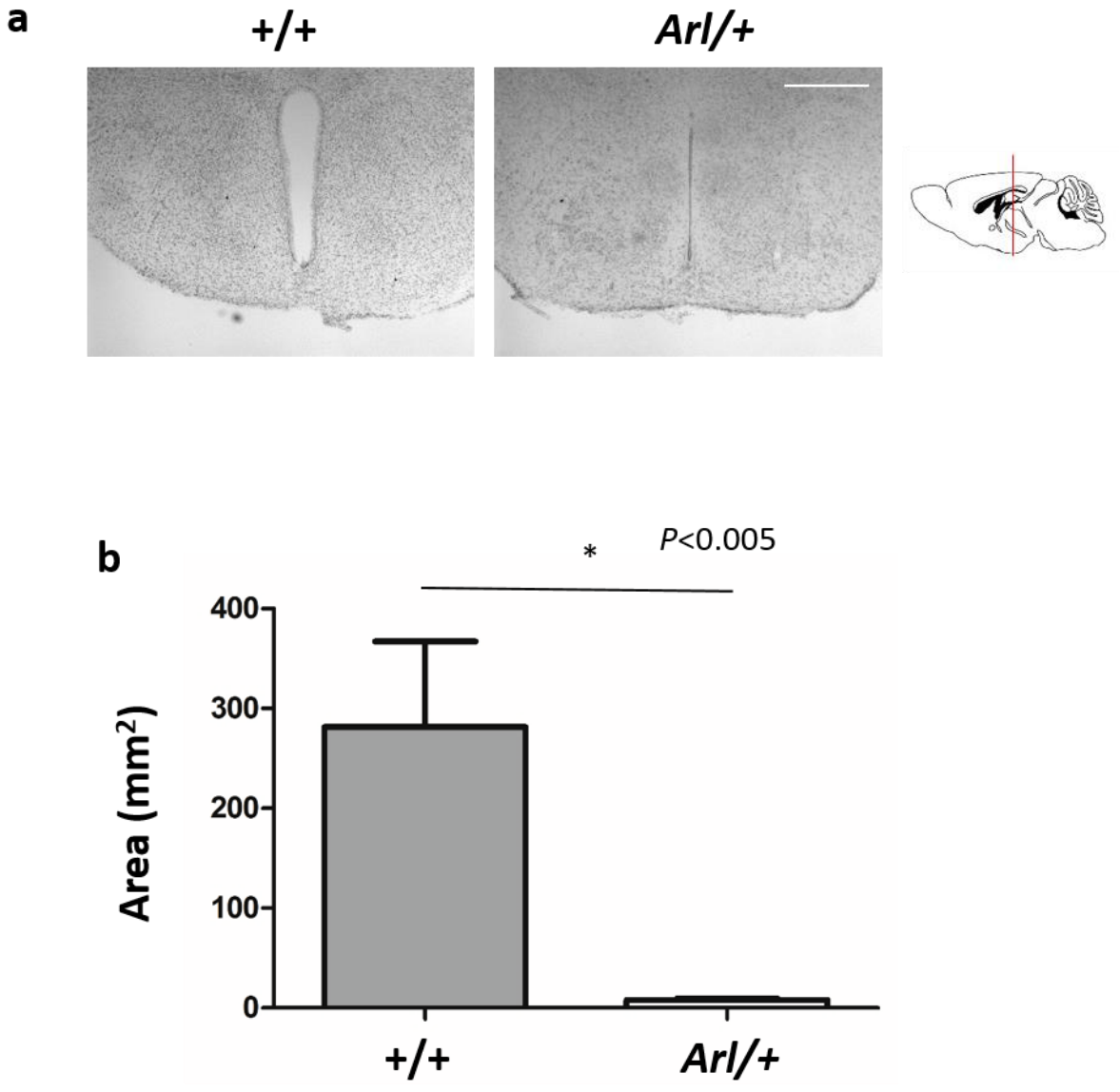

Figure 5.7 ***cont.***

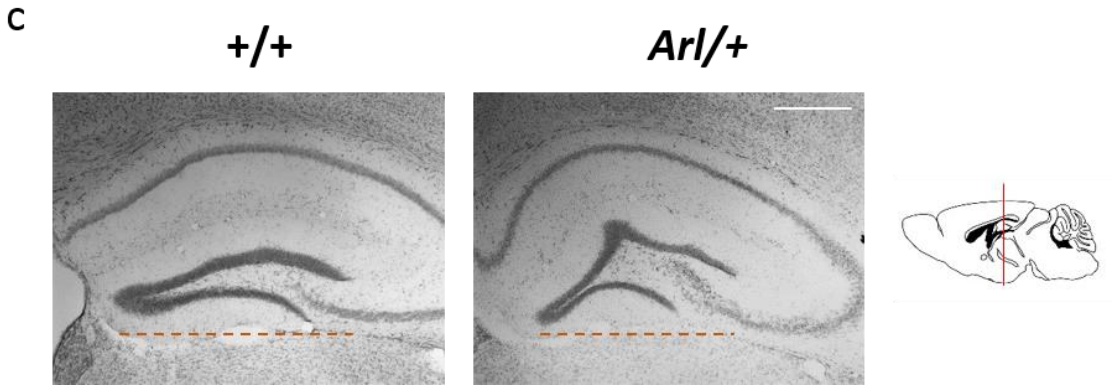

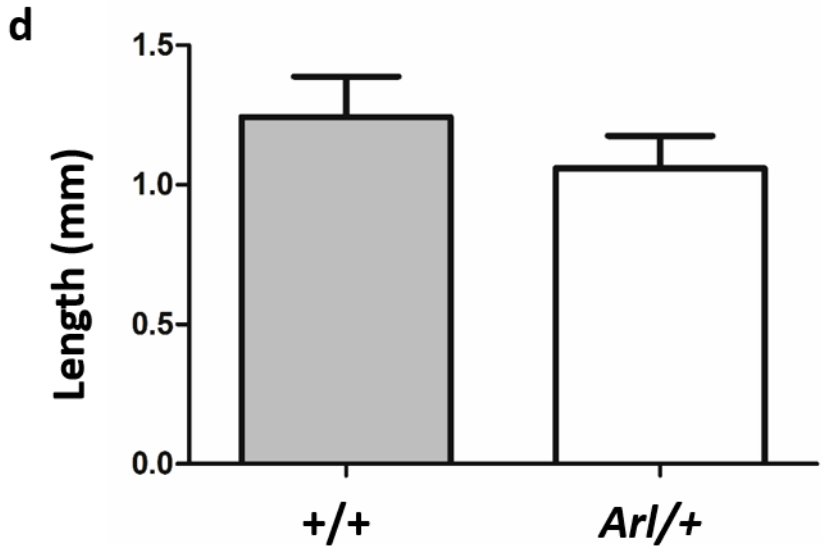

Figure 5.7- **(a)** Images (4x) of the third ventricle wild-type and *Arl*/+ matched coronal sections stained with cresyl violet. **(b)** Quantification of the area of the third ventricle in wild-type and *Arl*/+ mice. **(c)** Images (4x) of the dentate gyrus stained with cresyl violet in wild-type and *Arl*/+ matched coronal brain sections. Cartoon brain indicates position of coronal sections, dotted line represents measured region **(d)** Quantification of the length of the dentate gyrus in both wild-type and *Arl*/+ brain sections (scale bars represent 500 μm). Image acquisition was conducted using an Olympus BX55 with QI click camera.

8.1.4 The corpus callosum and dentate fascia brain regions are condensed in *Arl*/+ mice

The corpus callosum and dentate fascia (CC and DF) are situated dorsally above the dentate gyrus and functionally represent the fibre tract that connects both hemispheres of the brain (Paul et al. 2014). Visual analysis of this area of the brain in the *Arl*/+ coronal sections indicated that the size of this tract in the *Arl*/+ mice was much smaller in comparison to the wild-type brain sections (see Figure 5.8). In order to quantify the size of this brain region the CC & DF region was measured using ImageJ in 14 separate brain sections (Figure 5.7 panel a) for each genotype (sections derived from 2 different mice for each genotype). Quantification of this distance indicated a significant decrease (P<0.001) in the size of the CC & DF region in *Arl*/+ mice in comparison to wild-type mice (Figure 5.8 panel b).

The neighbouring brain region termed the retrosplenial area (indicated by the orange asterisk) additionally indicated a visually discernible phenotype in the *Arl*/+ brain sections in comparison to wild-type. This region in *Arl*/+ mice has a very granular and disorganised appearance, whereas in the wild-type brain regions, the retrosplenial area represents a distinct, defined band of cell bodies (Figure 5.8 panel a).

In summary, the *Arl* mutation results in condensation of the CC and DF brain region as well as a disordered and granular appearance of the retrosplenial area in comparison to wild-type mice.

Figure 5.8

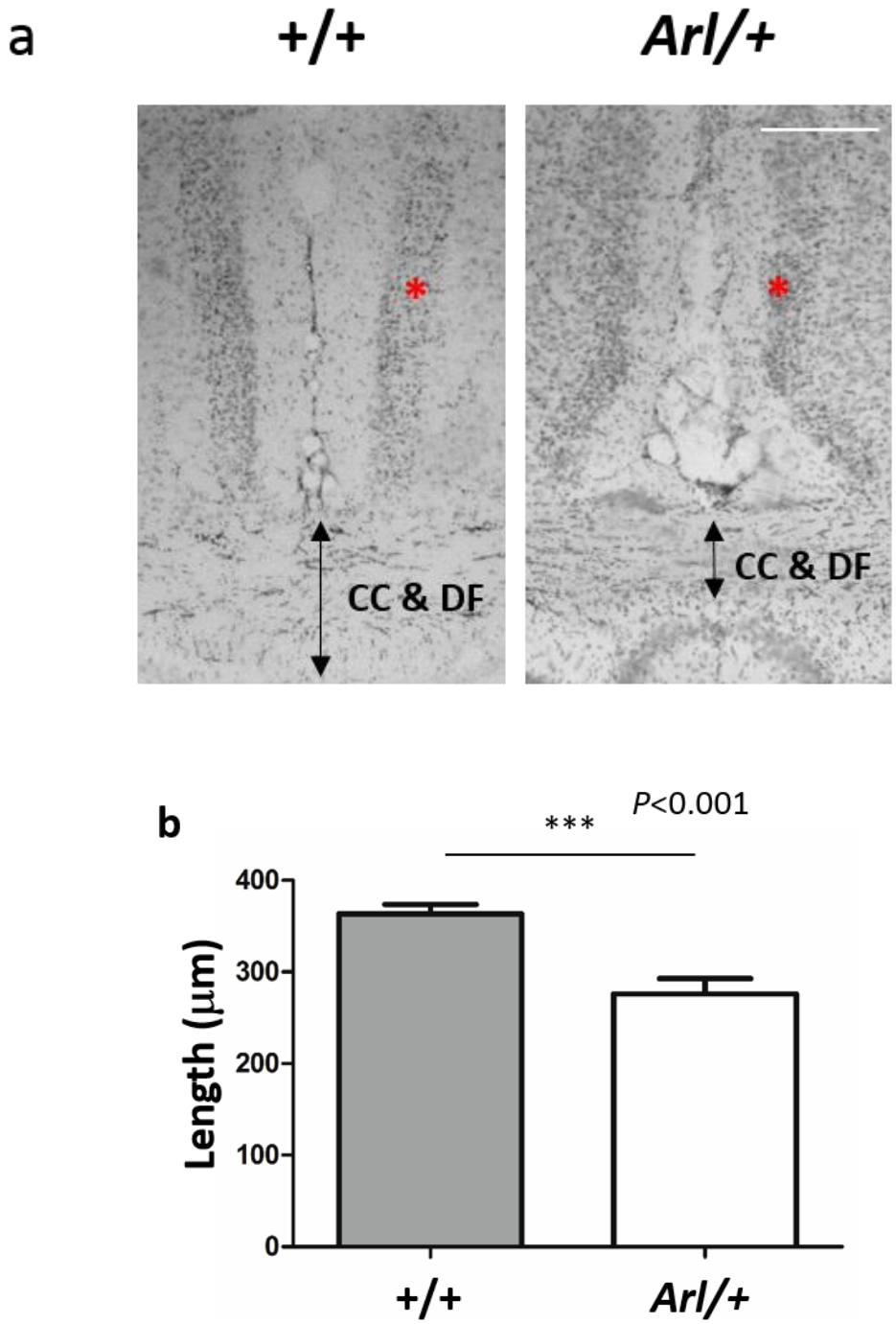

Figure 5.8- (a) Images (4x) of the corpus callosum (CC) and dentate fascia (DF) as well as the retrosplenial area (indicated by an orange asterisk) stained with cresyl violet in wild-type and *Arl*/+ coronal brain sections (scale bar represents 250 μm). **(b)** Quantification of the combined length of the corpus callosum and the dentate fascia in wild-type and *Arl*/+ brain sections. Image acquisition was conducted using an Olympus BX55 with QI click camera.

8.1.5 Cortical organisation is disrupted in p4 *Arl*/+ mice in comparison with littermates

Previous investigation into structural organisation of the cortical layers in *Arl*/+ mice were conducted in adult mice that were not age-matched. This presents the possibility that loss of neurons in the cortex (even though this may be unlikely in mice ~200 days old) in older mice could portray a similar phenotype to that of disorganisation of the cortical layers.

In order to investigate differences in younger litter mates p4 mice were culled before removal of the brain. Due to the small size of the brains in comparison to adult mice, the brains were placed directly into 1% PFA for fixation. The brains were then imaged (Figure 5.9) and both wild-type and *Arl*/+brains were weighed (0.19 g and 0.2 g, respectively). The brains were cryopreserved before cryosectioning and cresyl violet staining.

Upon Imaging the *Arl*/+ sections indicated a clear phenotype of regular regions of missing neuronal cell bodies in layer II/III indicated by the white arrow (see Figure 5.9). In comparison brain atlas matched sections in wild-type mice did not show this phenotype. Additionally, *Arl/*+ mice indicated a clear band of neurons at layer V (indicated by the orange arrow). This banding pattern was not apparent in any of the sections observed in wild-type mice, but instead a more granular phenotype is observed with a denser population of cell bodies seen just above the orange arrow (Figure 5.9). Interestingly observation of the corpus callosum tract (labelled cc) clearly shows that this tract is much larger in the wild-type mice

in comparison to the *Arl*/+ mice. This runs in accordance with the previous quantification of this region in adult mice.

In summary, the *Arl* mutation clearly affects cortical organisation in p4 *Arl*/+ mice in comparison to their wild-type littermates and furthermore a reduced size in the corpus callosum is also observed in the *Arl* heterozygous mice.

Figure 5.9

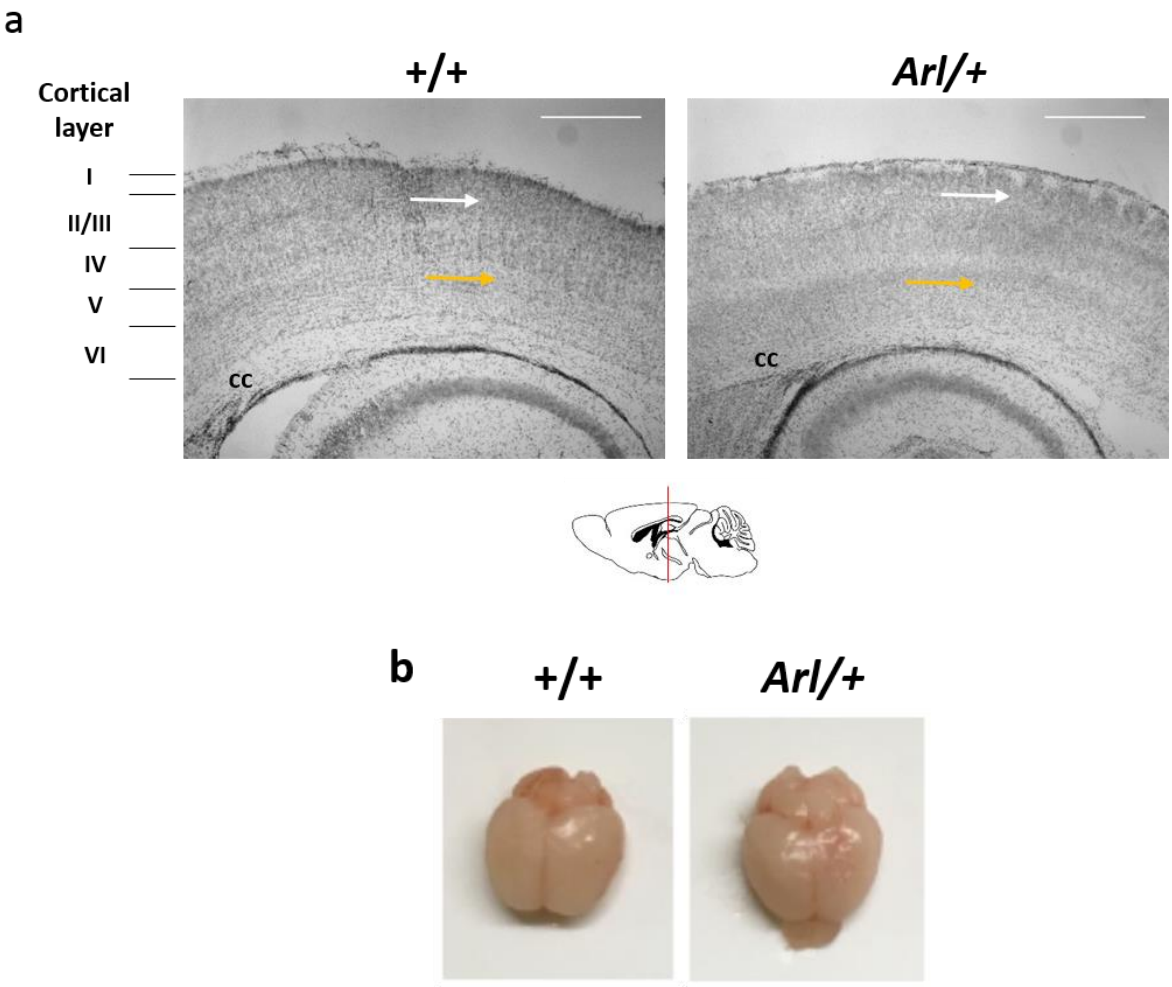

Figure 5.9- **(a)** Images (4x) of matched coronal brain sections from p4 wild-type and *Arl*/+ littermates stained with cresyl violet. Cortical layers are indicated on the left of the figure, the corpus callosum is represented by cc. White and Orange arrows indicate gross differences in the banding pattern of neurons between genotypes (scale bar represents 500 μm). **(b)** Pictures of both wild-type and *Arl*/+ brains prior to cryopreservation and sections. Image acquisition was conducted using an Olympus BX55 with QI click camera.

8.6 Chapter 5 summary

The data presented in this chapter indicates that mutations in *Dync1h1* have a negative effect on the speed of cell migration, shown by a deficit in rate of wound closure in heterozygous *Arl* fibroblasts. Furthermore, cortical organisation or lamination appears to be effected by the *Arl* mutation from observations in *Arl*/+ adult mice. This is further supported by data from p4 littermates further indicating that a distinct disorganisation of layers II/III was apparent at this stage of brain development. Finally, other gross anatomical differences were observed in *Arl*/+ adult mice. This included the dramatic collapse of the third ventricle, alteration of the dentate gyrus morphology, condensation of the CC and DF (which could also be observed in p4 mice) and disorganisation of the retrospenial area. Overall, this clearly indicates that the *Arl* mutation results in striking anatomical differences in the brain, but importantly highlights disrupted cortical lamination which shows deficits in brain development caused by this mutation.

8.7 Chapter 5 discussion

8.7.1 The *Arl* mutation causes delayed cell migration in mouse embryonic fibroblasts

Previous data from Dr Muruj Barri in the Hafezparast lab has shown that the *Loa* homozygous mouse model elicits a deficit in cell migration. This initiated the investigation into the *Arl* mutation to examine if this mutation resulted in aberrant cell migration. This was conducted by culturing *Arl* heterozygous fibroblasts and subjecting them to a monolayer wound before measuring the rate of migration

over a 12-hour time period. The results obtained indicated that there was a significant decrease in the rate of cell migration in the heterozygous fibroblasts in comparison to the wild-type cells. Coupled with the observed deficit in cell migration shown by the *Loa* homozygous fibroblasts, this indicates that mutations in the DHC tail domain of dynein can result in disrupted cellular migration.

There are several reasons as to why mutations in dynein could interfere with the process of cellular migration. Firstly, as shown in chapter 4 mutations in dynein can disrupt the Golgi complex. Both *Arl* (unpublished) and *Loa* mutations result in delayed recovery of the Golgi after nocodazole treatment (Hafezparast et al. 2003). The Golgi is important for delivering new proteins to leading edge of cells, disruption of which could have a negative impact upon cell migration (Bergmann et al. 1983). Secondly, similarly to the Golgi, the MTOC reorientation is dependent on dynein which is imperative to polarize microtubules towards the direction of migration (Palazzo et al. 2001). Additionally, migrating fibroblasts have microtubules which are rich in PTMs and regarded as stable, inhibition of dynein reduces acetylated tubulin levels indicating that dynein activity alone has an influence on the stability of microtubules (Sainath & Gallo 2014; Palazzo et al. 2003). Interestingly, a very recently discovered mutation in *NEK1* has been shown to be associated with fALS risk. *NEK1* is thought to be important for microtubule stability and axonal polarity perhaps leading to similar aberrant functions that DYNC1H1 mutations may cause in SMA-LED (Kenna et al. 2016).

8.7.2 The organisation of cortical layers is impaired in *Arl*/+ mice

The aberrant fibroblast migration observed in the *Arl*/+ fibroblasts further provoked the idea that perhaps neuronal organisation in the cortical layers of the murine brain could be affected. To explore this hypothesis initially two *Arl* adult mice were perfused in order to look at morphological brain differences. Upon investigation, clear disorganisation and reduced neuronal banding was observed in cortical layers II/III. This then prompted further investigation of p4 *Arl*/+ mice for comparison against a wild-type litter mate. Similarly, obvious disorganisation of cortical layers II/III were observed as well as in cortical layer V. This represents evidence that the *Arl*/+ mutation is having a dramatic effect upon cortical lamination in these mice. It must be noted that these investigations were very time consuming due to the infamous difficulty in breeding of the *Arl*/+ mice.

This data then correlates with evidence from Ori-Mckenney showing that *Loa* homozygous mice indicated neuronal migration defects seen in cortical layers II and III (Ori-McKenney & Vallee 2011). Furthermore, this type of cortical lamination is characteristic of disrupted organisation observed in heterozygous *Lis1* mice (Hirotsune et al. 1998). LIS1 promotes microtubule bound states of dynein towards the tips of microtubules, importantly it interacts with another dynein adaptor Nudel/Nude, mutations in which cause abnormally developed brains (Han et al. 2001; Bradshaw et al. 2013). Furthermore, LIS1 is known to attenuate the force production of dynein (McKenney et al. 2010).

This could affect the role that dynein has in apical motility of the nucleus in G2 of migrating neuronal progenitors (Dantas et al. 2016). Interestingly, Nudel and Lis1

null murine fibroblasts have also been shown to have microtubule organisation defects (Sasaki et al. 2005). Aside from migration deficits, this could result in defective neuronal arborisation or axonal pathfinding. Taken together these migratory processes could clearly be disrupted by aberrant dynein.

It is not yet determined if the *Arl* mutation could cause disruption between the complex and interaction with adaptors or if the *Arl* mutation causes a general impairment of dynein force production or perhaps causes microtubule destabilisation. Either way thus far both *Loa* and *Arl* mutations produce similar cortical lamination phenotypes due to *Dync1h1* tail domain mutations.

8.7.3 The *Arl*/+ mutation causes a collapse of the third ventricle and condensation of the dentate gyrus

Investigation into other differences in morphology in the *Arl*/+ mice led to the observation of the collapse of the third ventricle in comparison to wild-type mice. This was a strikingly significant observation detected in the *Arl*/+ mice which again could be related to LIS1. Mutations in *PAFAH1B1*, the gene encoding LIS1 have been shown to cause aberrant ependymal lining of the third ventricle (Assadi et al. 2003). Additionally, *Pafah1b1* $^{+/-}$ mice have been seen to exhibit large morphological differences (similar to that of the *Arl*/+ mice) of the third ventricle suggested to be due to a reduction in ependymal cells (Assadi et al. 2003). Ependymal cells are a type of epithelial cell that comprise the lining of the ventricles. They represent the barrier between the brain and cerebral spinal fluid (Kishimoto & Sawamoto 2012). This type of polarised cell is very dependent on

microtubule integrity and it is very likely that *Dync1h1* and *Lis1* mutations result in similar microtubule defects potentially causing this phenotype.

Similarly, the *Arl*/+ mice indicated morphological condensation of the dentate gyrus although this was not found to be significantly different. Importantly, in the *Loa* homozygous mouse a compaction of the dentate gyrus was also observed, this supports the evidence for Dync1h1 mutations resulting in defects in dentate gyrus morphology. These morphological differences in the *Loa* homozygous mouse were attributed to the distribution of granule cells which again could be an outcome of impaired cell migration (Ori-McKenney & Vallee 2011).

8.7.4 The corpus callosum and the dentate fascia brain regions are condensed in *Arl*/+ mice

Further analysis of brain abnormalities in the *Arl*/+ mice highlighted a reduced size in the corpus callosum and the dentate fascia in comparison to the wild-type equivalent region of the brain (Figure 5.5). Interestingly, MRI data from a patient with a p.Tyr970Cys DYNC1H1 mutation indicated thinning of the corpus callosum brain region (Scoto et al. 2015). Considering the large size of the DHC the p. Trp1206Arg *Arl* mutation exists close by in a similar region of the tail domain of dynein. The similarity in reduced size of the corpus callosum between the aforementioned patient and the *Arl*/+ mouse further highlights the important value of this SMA-LED mouse model. Furthermore, patients with DYCN1H1 mutations in the homodimerisation domain have been reported to exhibit irregular corpus callosum morphology; suggesting that this could represent a general morphological consequence of DYNC1H1 mutations (Jamuar et al. 2014). There

is limited information on the impact of DYNC1H1 mutations upon the morphology of the dentate fascia. However, the proximal nature of the corpus callosum and the dentate fascia suggests that perhaps migration defects in dynein mutants influences the morphologies of both sub-structures.

Chapter 6- Conclusion and general discussion

9.0 Conclusion

The data presented in this thesis has firstly advanced our knowledge of proteins FUS and TDP-43 and potential pathogenic mechanisms in adult onset ALS. Secondly, this thesis has explored the cellular impact of dynein heavy chain mutations related to the childhood onset condition SMA-LED by analysing patient p.R399G fibroblasts and the *Arl*/+ mouse model.

My data has shown that both FUS and TDP-43 respond to oxidative DNA damage as well as indicating a FUS specific nucleoli recruitment after topoisomerase I inhibition in mitotic cells. Importantly, I have also shown that both proteins are recruited to the nucleoli in cortical neurons after topoisomerase I inhibition. Focussing on FUS recruitment led to the finding that RNA polymerase II inhibition resulted in nucleoli FUS foci in neurons, indicating that the cessation of transcription initiates this recruitment. Both caffeine and high concentrations of dipyridamole inhibited FUS recruitment suggesting that PDEs may be responsible for this FUS response.

Furthermore, for the first time, my data has shown inherent Golgi fragmentation in fibroblasts from a SMA-LED patient with a p.R399G DYNC1H1 mutation. This led to the discovery of increased interaction between dynein and golgin 160, irregular Golgi morphology during migration and decreased acetylated α-tubulin at Lysine 40 in p.R399G mutants. Further investigations indicated aberrant Golgi-dynein localisation and increasing microtubule acetylation did not rescue this

phenotype but crucially rescued Golgi fragmentation. This suggests that HDAC6 inhibitors may have a future role to play in SMA-LED treatment.

Lastly in correlation with this data I have for the first time shown that the murine *Dync1h1 Arl*/+ mutation results in impaired rate of migration in fibroblasts. This led to the discovery of gross disorganisation of cortical lamination in these mice. Additionally, reduced size of the third ventricle as well as compaction of the corpus callosum and the dentate fascia was detected in *Arl*/+ mice. These findings broaden the phenotypes associated with the *Arl* mutation and highlights the importance of this model in future research of SMA-LED.

9.1 General discussion

Motor neuron disease is a collective-term for a group of neurological conditions in which motor neurons degenerate leading to loss of muscle innervation which can be fatal. Both ALS and SMA-LED are contrasting diseases despite the parallel connection of neurodegeneration of motor neurons. ALS is a disease in which multiple mechanisms of disease pathogenesis have been put forward in the field over many years suggesting that perhaps there may be further subdivisions of this disease in the future. The complexity of potential disease mechanisms also arises from mutations in proteins in which have many diverse complex functions. Both FUS and TDP-43 fall into this category and have been extensively researched in the context of ALS for many years without a single disease mechanism arising as a definitive leading contributor to ALS pathogenesis. This raises the possibility that mutations in both FUS and TDP-43 could result in a syndrome of collective aberrant processes that are specific to

motor neurons leading to their degeneration. A leading theory in motor neuron degeneration is the protein aggregation hypothesis in which mutant or misfolded protein such as FUS aggregates in the cytoplasm leading to terminal cellular disruption. This type of pathology is shared across different neurodegenerative disorders such as Parkinson's disease, Alzheimer's disease and prion diseases. This theory suits the progression of these diseases of older age as the delicate preservation of protein folding mechanisms are perturbed over time leading to accumulation of unfolded protein. This coupled with a reduced efficacy of the proteasome degradation system provides an attractive potential overall leading mechanism of age related neuron deterioration.

In the context of this thesis, investigation into both FUS and TDP-43 has been focussed on understanding the role they play the DNA damage response. Although not a leading theory in the pathogenesis of ALS the importance of understanding differences in DNA damage repair between mitotic and non-mitotic cells could clarify the importance of genome stability in motor neurons. In symmetry with the age related accumulation of the mis-folded protein theory, accumulation of DNA lesions in motor neurons over time could equally be the root cause of motor neuron death in ALS. Other neurological disorders support this theory such as Cockayne syndrome in which the genetic stability is thought to be impaired through mutations in a NER associated protein. Additionally, Parkinson's disease and Huntington's disease have also been linked with defective DNA repair processes such as BER and NER (Jeppesen et al. 2011).

Importantly in sALS, evidence of aberrant mitochondrial DNA repair has been reported which could be another parallel mechanism in which defective mitochondria contribute to the degenerative process. Furthermore, a rare infantile ALS can be caused by a mutation in the ALS2 protein which is suggested to protective under conditions of oxidative damage (Jeppesen et al. 2011). It is possible that other proteins in ALS have direct roles to play in the management of oxidative damage in motor neurons including at the DNA repair level. It is highly likely that the FUS protein is critical in DNA repair management in motor neurons and further investigations will unravel its holistic importance in this respect.

In contrast, SMA-LED is a neurodegenerative disorder which exhibits mutations in proteins such as DYNC1H1 and BICD2 which are associated with the dynein retrograde motor. The challenge in investigating defective dynein functionality arises when the full extent of the roles it plays are not well understood. Dynein is well known for its role in axonal transport and shares structural similarity with other similar motors such as myosin. However, dynein is found in very many different cellular compartments and is not only always associated with microtubules. In this thesis, dynein is found to be closely associated with the Golgi apparatus, but why this close association exists and how it is regulated is currently unknown. A regulation between acetylated microtubules, Golgi membranes, golgin 160 and dynein likely only forms a small snapshot of how many proteins regulate the Golgi apparatus. The bigger question is which element of dynein dysfunction is the most important/causative in SMA-LED? One would assume that aberrant retrograde transport is the main candidate. However, if retrograde transport was this severely impaired by DYNC1H1 mutations it could be expected perhaps in other cell types. The retrograde functionality of dynein

may not be the most crucial factor during axonal growth and pathfinding but its role at the Golgi apparatus for example could be much more critical for early neuronal development.

SMA-LED is a congenital condition which suggests that defective wiring of neurons during development could be a likely root cause. This would potentially explain cases in which some patients with DYNC1H1 mutations also show cognitive impairment. This is supported by data in this thesis in which the *Arl* mouse model clearly shows a disruption in cortical organisation. Potentially, this indicates that even though motor neurons in SMA-LED predominantly deteriorate, other types of neurons and perhaps supporting cells may also be effected in some cases. The variety of symptoms experienced by SMA-LED patients with DYNC1H1 mutations indicates that perhaps small modulations in the dynein complex can have diverse and contrasting repercussions. This is not surprising for a complex with a high number of functioning components with many potential functional roles.

The future challenge of determining the underlying cause of both ALS and SMA-LED will to some extent be governed by the ever growing knowledge about neuroscience and cell biology in general. Additionally, understanding common genetic aberrations between patients through sequencing has been a powerful tool to this date and is likely to continue to yield further informative data. Increasing our current understanding through these mechanisms is somewhat limited by current technology but recent advances in gene editing platforms have created further tools that also could serve as a therapeutic starting point in the near future. The use of pharmaceutical drugs such as riluzole in the case of ALS

has only had limited benefit for patients. The advancement of therapeutic strategies will undoubtedly improve the lives of patients suffering with neurodegenerative disorders.

References

Acharya, K.K. et al., 2006. cis-Requirement for the maintenance of round spermatid-specific transcription. *Developmental Biology*, 295(2), pp.781–790.

Agosta, F. et al., 2014. Resting state functional connectivity alterations in primary lateral sclerosis. *Neurobiology of Aging*, 35(4), pp.916–925.

Alami, N.H. et al., 2014. Axonal Transport of TDP-43 mRNA Granules Is Impaired by ALS-Causing Mutations. *Neuron*, 81(3), pp.536–543.

Amlie-Wolf, A. et al., 2015. Transcriptomic changes due to cytoplasmic TDP-43 expression reveal dysregulation of histone transcripts and nuclear chromatin. *PLoS ONE*, 10(10), pp.1–20.

Andersen, P.M., 2006. Amyotrophic lateral sclerosis associated with mutations in the CuZn superoxide dismutase gene. *Current Neurology and Neuroscience Reports*, 6(1), pp.37–46.

Andersen, P.M. et al., 1996. Autosomal recessive adult-onset amyotrophic lateral sclerosis associated with homozygosity for Asp90Ala CuZn-superoxide dismutase mutation. A clinical and genealogical study of 36 patients. *Brain : a journal of neurology*, 119 (Pt 4, pp.1153–1172.

Arbab, M., Baars, S. & Geijsen, N., 2014. Modeling motor neuron disease: the matter of time. *Trends in neurosciences*, pp.1–11.

Assadi, A.H. et al., 2003. Interaction of reelin signaling and Lis1 in brain development. *Nature genetics*, 35(3), pp.270–276.

Asthana, J. et al., 2012. Dynein light chain 1 (LC8) association enhances microtubule stability and promotes microtubule bundling. *The Journal of biological chemistry*, 287(48), pp.40793–805.

Ayala, Y.M. et al., 2005. Human, Drosophila, and C. elegans TDP43: Nucleic acid binding properties and splicing regulatory function. *Journal of Molecular Biology*, 348(3), pp.575–588.

Ayala, Y.M. et al., 2011. TDP-43 regulates its mRNA levels through a negative feedback loop. *The EMBO journal*, 30(2), pp.277–288.

Baechtold, H. et al., 1999. Human 75-kDa DNA-pairing protein is identical to the pro-oncoprotein TLS/FUS and is able to promote D-loop formation. *Journal of Biological Chemistry*, 274(48), pp.34337–34342.

Bak, T.H. & Hodges, J.R., 2001. Motor neurone disease, dementia and aphasia: Coincidence, co-occurrence or continuum? *Journal of Neurology*, 248(4), pp.260–270.

Baldwin, K.R. et al., 2016. Axonal transport defects are a common phenotype in Drosophila models of ALS.

Banks, G.T. et al., 2008. TDP-43 is a culprit in human neurodegeneration, and not just an innocent bystander. *Mammalian Genome*, 19(5), pp.299–305.

Bannwarth, S. et al., 2014. A mitochondrial origin for frontotemporal dementia and amyotrophic lateral sclerosis through CHCHD10 involvement. *Brain*, 137(8), pp.2329–2345.

Bartolome, F. et al., 2013. Pathogenic VCP Mutations Induce Mitochondrial Uncoupling and Reduced ATP Levels. *Neuron*, 78(1), pp.57–64.

Battle, D.J. et al., 2006. The SMN complex: An assembly machine for RNPs. *Cold Spring Harbor Symposia on Quantitative Biology*, 71, pp.313–320.

Bellingham, M.C., 2011. A Review of the Neural Mechanisms of Action and Clinical Efficiency of Riluzole in Treating Amyotrophic Lateral Sclerosis: What have we Learned in the Last Decade? *CNS Neuroscience and*

Therapeutics, 17(1), pp.4–31.
Belly, A. et al., 2005. Delocalization of the multifunctional RNA splicing factor TLS/FUS in hippocampal neurones: Exclusion from the nucleus and accumulation in dendritic granules and spine heads. *Neuroscience Letters*, 379(3), pp.152–157.
Bergmann, J.E., Kupfer, a & Singer, S.J., 1983. Membrane insertion at the leading edge of motile fibroblasts. *Proceedings of the National Academy of Sciences of the United States of America*, 80(5), pp.1367–71.
Bhuin, T. & Roy, J.K., 2014. Rab proteins: The key regulators of intracellular vesicle transport. *Experimental Cell Research*, 328(1), pp.1–19.
Blokhuis, A.M. et al., 2013. Protein aggregation in amyotrophic lateral sclerosis. *Acta Neuropathologica*, 125(6), pp.777–794.
Bogucki, A. et al., 2016. Unilateral progressive muscular atrophy with fast symptoms progression. *Neurologia i Neurochirurgia Polska*, 50(1), pp.52–54.
Bradshaw, N.J., Hennah, W. & Soares, D.C., 2013. NDE1 and NDEL1: Twin neurodevelopmental proteins with similar “nature” but different “nurture.” *Biomolecular Concepts*, 4(5), pp.447–464.
Briese, M., Esmaeili, B. & Sattelle, D.B., 2005. Is spinal muscular atrophy the result of defects in motor neuron processes? *BioEssays*, 27(9), pp.946–957.
Bruijn, L.I. et al., 1997. ALS-linked SOD1 mutant G85R mediates damage to astrocytes and promotes rapidly progressive disease with SOD1-containing inclusions. *Neuron*, 18(2), pp.327–338.
Bunton-Stasyshyn, R.K.A. et al., 2014. SOD1 Function and Its Implications for Amyotrophic Lateral Sclerosis Pathology: New and Renascent Themes. *The Neuroscientist : a review journal bringing neurobiology, neurology and psychiatry*, 21(5), pp.1–11.
Buratti, E. et al., 2001. Nuclear factor TDP-43 and SR proteins promote in vitro and in vivo CFTR exon 9 skipping. *EMBO Journal*, 20(7), pp.1774–1784.
Bushnell, D.A., Cramer, P. & Kornberg, R.D., 2002. Structural basis of transcription: α-amanitin–RNA polymerase II cocrystal at 2.8 Å resolution. *Proceedings of the National Academy of Sciences of the United States of America*, 99(3), pp.1218–1222.
Canella, D. et al., 2010. Defining the RNA polymerase III transcriptome: Genome-wide localization of the RNA polymerase III transcription machinery in human cells. *Genome Research*, 20(6), pp.710–721.
Cannon, A. et al., 2012. Neuronal sensitivity to TDP-43 overexpression is dependent on timing of induction. *Acta Neuropathologica*, 123(6), pp.807–823.
Cardinaux, J.R. et al., 2000. Recruitment of CREB binding protein is sufficient for CREB-mediated gene activation. *Molecular and cellular biology*, 20(5), pp.1546–52.
Carrì, M.T. et al., 2015. Oxidative stress and mitochondrial damage: importance in non-SOD1 ALS. *Frontiers in cellular neuroscience*, 9(February), p.41.
Casafont, I. et al., 2009. TDP-43 localizes in mRNA transcription and processing sites in mammalian neurons. *Journal of Structural Biology*, 167(3), pp.235–241.
Chavez-Valdez, R. et al., 2016. Mechanisms of modulation of cytokine release by human cord blood monocytes exposed to high concentrations of caffeine. *Pediatr Res*, pp.101–109.

Chekulaeva, M. & Filipowicz, W., 2009. Mechanisms of miRNA-mediated post-transcriptional regulation in animal cells. *Current Opinion in Cell Biology*, 21(3), pp.452–460.
Chen, X.-J. et al., 2007. Proprioceptive sensory neuropathy in mice with a mutation in the cytoplasmic Dynein heavy chain 1 gene. *The Journal of neuroscience : the official journal of the Society for Neuroscience*, 27(52), pp.14515–14524.
Chio, A. et al., 2012. Extensive genetics of ALS. *Neurology*, 78(Meeting Abstracts 1), pp.IN9–1.007–IN9–1.007.
Chiò, A. et al., 2010. Amyotrophic lateral sclerosis-frontotemporal lobar dementia in 3 families with p.Ala382Thr TARDBP mutations. *Archives of neurology*, 67(8), pp.1002–1009.
Chiò, A. et al., 2011. Large proportion of amyotrophic lateral sclerosis cases in Sardinia due to a single founder mutation of the TARDBP gene. *Archives of neurology*, 68(5), pp.594–598.
Chiò, A. et al., 2008. Prevalence of SOD1 mutations in the Italian ALS population. *Neurology*, 70(7), pp.533–537.
Chowdhury, S. et al., 2015. Structural organization of the dynein–dynactin complex bound to microtubules. *Nature Structural & Molecular Biology*, 22(March), pp.345–347.
Christensen, M.O. et al., 2004. Distinct effects of topoisomerase I and RNA polymerase I inhibitors suggest a dual mechanism of nucleolar/nucleoplasmic partitioning of topoisomerase I. *Journal of Biological Chemistry*, 279(21), pp.21873–21882.
Cianfrocco, M. a & Leschziner, A.E., 2014. Traffic control: adaptor proteins guide dynein-cargo takeoff. *The EMBO journal*, 33(17), pp.1845–6.
Cianfrocco, M. a. et al., 2015. Mechanism and Regulation of Cytoplasmic Dynein. *Annual Review of Cell and Developmental Biology*, 31(1), pp.annurev–cellbio–100814–125438
Cianfrocco, M.A. & Leschziner, A.E., 2014. Traffic control: adaptor proteins guide dynein-cargo takeoff. *The EMBO journal*, 33(17), pp.1845–6.
Ciura, S. et al., 2013. Loss of function of C9orf72 causes motor deficits in a zebrafish model of amyotrophic lateral sclerosis. *Annals of Neurology*, 74(2), pp.180–187.
Colombrita, C. et al., 2012. TDP-43 and FUS RNA-binding proteins bind distinct sets of cytoplasmic messenger RNAs and differently regulate their post-transcriptional fate in motoneuron-like cells. *Journal of Biological Chemistry*, 287(19), pp.15635–15647.
Cozzolino, M. & Carri, M.T., 2012. Mitochondrial dysfunction in ALS. *Progress in Neurobiology*, 97(2), pp.54–66.
Crozat, A. et al., 1993. Fusion of CHOP to a novel RNA-binding protein in human myxoid liposarcoma. *Nature*, 363(6430), pp.640–644.
Cudkowicz, M.E. et al., 1997. Intrathecal administration of recombinant human superoxide dismutase 1 in amyotrophic lateral sclerosis: A preliminary safety and pharmacokinetic study. *Neurology*, 49(1), pp.213–222.
D'Amico, E. et al., 2013. Clinical perspective on oxidative stress in sporadic amyotrophic lateral sclerosis. *Free Radical Biology and Medicine*, 65, pp.509–527.
Dadon-Nachum, M., Melamed, E. & Offen, D., 2011. The "dying-back" phenomenon of motor neurons in ALS. *Journal of Molecular Neuroscience*, 43(3), pp.470–477.

Dantas, T.J. et al., 2016. Emerging Roles for Motor Proteins in Progenitor Cell Behavior and Neuronal Migration during Brain Development. *Cytoskeleton*, pp. 566-576.
Day, C.A. et al., 2015. Microtubule Motors Power Plasma Membrane Tubulation in Clathrin-Independent Endocytosis. *Traffic*, 16(6), pp.572–590.
DeJesus-Hernandez, M. et al., 2011. Expanded GGGGCC hexanucleotide repeat in noncoding region of C9ORF72 causes chromosome 9p-linked FTD and ALS. *Neuron*, 72(2), pp.245–56.
Deng, W. et al., 2010. Neurodegenerative mutation in cytoplasmic dynein alters its organization and dynein-dynactin and dynein-kinesin interactions. *The Journal of biological chemistry*, 285(51), pp.39922–39934
Devic, P., Petiot, P. & Mauguière, F., 2012. Spinal charcot-marie-tooth disease: A reappraisal. *Muscle and Nerve*, 46(4), pp.604–609.
Dewey, C.M. et al., 2012. TDP-43 aggregation in neurodegeneration: Are stress granules the key? *Brain Research*, 1462, pp.16–25.
Dewey, C.M. et al., 2011. TDP-43 is directed to stress granules by sorbitol, a novel physiological osmotic and oxidative stressor. *Molecular and cellular biology*, 31(5), pp.1098–108.
Dhar, S.K. et al., 2013. FUsed in Sarcoma Is a Novel Regulator of Manganese Superoxide Dismutase Gene Transcription. *Antioxidants & redox signaling*, 00(00), pp.1550–1566.
Dini Modigliani, S. et al., 2014. An ALS-associated mutation in the FUS 3′-UTR disrupts a microRNA–FUS regulatory circuitry. *Nat Commun*, pp. 4335.
Dompierre, J.P. et al., 2007. Histone deacetylase 6 inhibition compensates for the transport deficit in Huntington's disease by increasing tubulin acetylation. *The Journal of neuroscience : the official journal of the Society for Neuroscience*, 27(13), pp.3571–3583.
Farg, M.A. et al., 2014. C9ORF72, implicated in amytrophic lateral sclerosis and frontotemporal dementia, regulates endosomal trafficking. *Human Molecular Genetics*, 23(13), pp.3579–3595.
Finsterer, J. & Burgunder, J.-M., 2014. Recent progress in the genetics of motor neuron disease. *European journal of medical genetics*, 57(2-3), pp.103–12.
Fiorillo, C. et al., 2014. Novel Dynein *DYNC1H1* Neck and Motor Domain Mutations Link Distal Spinal Muscular Atrophy and Abnormal Cortical Development. *Human Mutation*, 35(3), pp.298–302.
Flores-Rodriguez, N. et al., 2011. Roles of dynein and dynactin in early endosome dynamics revealed using automated tracking and global analysis. *PloS one*, 6(9), p.e24479.
Fujii, R. et al., 2005. The RNA binding protein TLS is translocated to dendritic spines by mGluR5 activation and regulates spine morphology. *Current Biology*, 15(6), pp.587–593.
Gardiner, M. et al., 2008. Identification and characterization of FUS/TLS as a new target of ATM. *The Biochemical journal*, 415(2), pp.297–307
Garrett, C. a et al., 2014. DYNC1H1 mutation alters transport kinetics and ERK1/2-cFos signalling in a mouse model of distal spinal muscular atrophy. *Brain : a journal of neurology*, pp.1–11.
Ghosh, R. et al., 2016. Common and unique genetic interactions of the poly(ADP-ribose) polymerases PARP1 and PARP2 with DNA double-strand break repair pathways. *DNA repair*, pp.1–7.
Gitler, A.D. & Tsuiji, H., 2016. There has been an awakening: Emerging mechanisms of C9orf72 mutations in FTD/ALS. *Brain Research*, pp.19-29

Gregory, R.I. et al., 2004. The Microprocessor complex mediates the genesis of microRNAs. *Nature*, 432(7014), pp.235–240.
Guareschi, S. et al., 2012. An over-oxidized form of superoxide dismutase found in sporadic amyotrophic lateral sclerosis with bulbar onset shares a toxic mechanism with mutant SOD1. *Proceedings of the National Academy of Sciences*, 109(13), pp.5074–5079.
Guo, Y. et al., 2012. HO-1 induction in motor cortex and intestinal dysfunction in TDP-43 A315T transgenic mice. *Brain Research*, 1460, pp.88–95.
Hafezparast, M., 2008. Mutations in Dynein Link Motor Neuron Degeneration to Defects in Retrograde Transport. *Science*, 300(5620), pp.808–812.
Hafezparast, M. et al., 2003. Mutations in dynein link motor neuron degeneration to defects in retrograde transport. *Science (New York, N.Y.)*, 300(2003), pp.808–812.
Haines, N.M. et al., 2014. Stalled transcription complexes promote DNA repair at a distance. *Proceedings of the National Academy of Sciences of the United States of America*, 111(11), pp.4037–42.
Han, G. et al., 2001. The aspergillus cytoplasmic dynein heavy chain and nudf localize to microtubule ends and affect microtubule dynamics. *Current Biology*, 11(9), pp.719–724.
Hanagasi, H. a. et al., 2016. A novel homozygous DJ1 mutation causes parkinsonism and ALS in a Turkish family. *Parkinsonism & Related Disorders*, pp.3–6.
Hanus, C. & Ehlers, M.D., 2008. Secretory outposts for the local processing of membrane cargo in neuronal dendrites. *Traffic*, 9(9), pp.1437–1445.
Harada, a. et al., 1998. Golgi vesiculation and lysosome dispersion in cells lacking cytoplasmic dynein. *Journal of Cell Biology*, 141(1), pp.51–59.
Harms, M.B. et al., 2010. Dominant spinal muscular atrophy with lower extremity predominance: Linkage to 14q32. *Neurology*, 75, pp.539–546.
Harms, M.B. et al., 2012. Mutations in the tail domain of DYNC1H1 cause dominant spinal muscular atrophy. *Neurology*, 78(22), pp.1714–20.
Hicks, G.G. et al., 2000. Fus deficiency in mice results in defective B-lymphocyte development and activation, high levels of chromosomal instability and perinatal death. *Nature genetics*, 24(2), pp.175–9.
Hirano, M. et al., 2015. VCP gene analyses in Japanese patients with sporadic amyotrophic lateral sclerosis identify a new mutation. *Neurobiology of Aging*, 36(3), pp.1604.e1–e6.
Hirotsune, S. et al., 1998. Graded reduction of Pafah1b1 (Lis1) activity results in neuronal migration defects and early embryonic lethality. *Nature genetics*, 19(4), pp.333–339.
Holzbaur, E.L. & Tokito, M.K., 1996. Localization of the DCTN1 gene encoding p150Glued to human chromosome 2p13 by fluorescence in situ hybridization. *Genomics*, 31(3), pp.398–399.
Hoogenraad, C.C. et al., 2001. Mammalian golgi-associated Bicaudal-D2 functions in the dynein-dynactin pathway by interacting with these complexes. *EMBO Journal*, 20(15), pp.4041–4054.
Horgan, C.P. et al., 2010. Rab11-FIP3 binds dynein light intermediate chain 2 and its overexpression fragments the Golgi complex. *Biochemical and Biophysical Research Communications*, 394(2), pp.387–392.
Horton, A.C. et al., 2005. Polarized secretory trafficking directs cargo for asymmetric dendrite growth and morphogenesis. *Neuron*, 48(5), pp.757–771.

Hrabé de Angelis, M.H. et al., 2000. Genome-wide, large-scale production of mutant mice by ENU mutagenesis. *Nature genetics*, 25(august), pp.444–447.
Hu, D.J.-K. et al., 2013. Dynein recruitment to nuclear pores activates apical nuclear migration and mitotic entry in brain progenitor cells. *Cell*, 154(6), pp.1300–13.
Huang, J. et al., 2012. Lis1 acts as a “clutch” between the ATPase and microtubule-binding domains of the dynein motor. *Cell*, 150(5), pp.975–986.
Ichikawa, H., Shimizu, K. & Hayashi, Y., 1994. An RNA-binding Protein Gene , TLS / FUS , Is Fused to ERG in Human Myeloid Leukemia with t (16 ; 21) Chromosomal Translocation. , pp.2865–2868.
Igaz, L.M. et al., 2011. Dysregulation of the ALS-associated gene TDP-43 leads to neuronal death and degeneration in mice. *Journal of Clinical Investigation*, 121(2), pp.726–738.
Jackson, E.K. et al., 2007. Characterization of renal ecto-phosphodiesterase. *The Journal of pharmacology and experimental therapeutics*, 321(2), pp.810–5.
Jamuar, S.S. et al., 2014. Somatic Mutations in Cerebral Cortical Malformations. *New England Journal of Medicine*, 371(8), pp.733–743.
Kawaguchi, Y. et al., 2003. The deacetylase HDAC6 regulates aggresome formation and cell viability in response to misfolded protein stress. *Cell*, 115(6), pp.727–38.
Kawahara, Y. & Mieda-Sato, A., 2012. TDP-43 promotes microRNA biogenesis as a component of the Drosha and Dicer complexes. *Proceedings of the National Academy of Sciences of the United States of America*, 109(9), pp.3347–52.
Keller, M.F. et al., 2014. Genome-wide analysis of the heritability of amyotrophic lateral sclerosis. *JAMA neurology*, 71(9), pp.1123–34..
Kenna, K.P. et al., 2016. NEK1 variants confer susceptibility to amyotrophic lateral sclerosis. *Nat Genet*, advance on.
Kimmel, R., Kiryati, N. & Bruckstein, A.M., 1996. Sub-pixel distance maps and weighted distance transforms. *Journal of Mathematical Imaging and Vision*, 6, pp.223–233.
Kirkman, H.N. & Gaetani, G.F., 2007. Mammalian catalase: a venerable enzyme with new mysteries. *Trends in Biochemical Sciences*, 32(1), pp.44–50.
Kishimoto, N. & Sawamoto, K., 2012. Planar polarity of ependymal cilia. *Differentiation*, 83(2), pp.S86–S90.
Klumperman, J., 2011. Architecture of the mammalian Golgi. *Cold Spring Harbor Perspectives in Biology*, 3(7), pp.1–19.
Koppers, M. et al., 2015. C9orf72 ablation in mice does not cause motor neuron degeneration or motor deficits. *Annals of Neurology*, 78(3), pp.426–438.
Krecic, A.M. & Swanson, M.S., 1999. hnRNP complexes: Composition, structure, and function. *Current Opinion in Cell Biology*, 11(3), pp.363–371.
Kuhns, S. et al., 2013. The microtubule affinity regulating kinase MARK4 promotes axoneme extension during early ciliogenesis. *Journal of Cell Biology*, 200(4), pp.505–522.
Kuo, P.H. et al., 2009. Structural insights into TDP-43 in nucleic-acid binding and domain interactions. *Nucleic Acids Research*, 37(6), pp.1799–1808.
Kurland, L.T. & Mulder, D.W., 1955. Epidemiologic investigations of

amyotrophic lateral sclerosis. 2. Familial aggregations indicative of dominant inheritance. I. *Neurology*, 5(3), pp.182–96..
Kwiatkowski, T.J. et al., 2009. Mutations in the FUS/TLS gene on chromosome 16 cause familial amyotrophic lateral sclerosis. *Science (New York, N.Y.)*, 323(5918), pp.1205–1208.
Kye, M.J. & Gonçalves, I.D.C.G., 2014. The role of miRNA in motor neuron disease. *Frontiers in cellular neuroscience*, 8(January), p.15.
Laan, L. et al., 2012. Cortical dynein controls microtubule dynamics to generate pulling forces that position microtubule asters. *Cell*, 148(3), pp.502–14.
Laferriere, F. & Polymenidou, M., 2015. Advances and challenges in understanding the multifaceted pathogenesis of amyotrophic lateral sclerosis. *Swiss Medical Weekly*, 145(January), pp.1–13.
Lagier-Tourenne, C., Polymenidou, M. & Cleveland, D.W., 2010. TDP-43 and FUS/TLS: Emerging roles in RNA processing and neurodegeneration. *Human Molecular Genetics*, 19(R1), pp.46–64.
Lammers, L.G. & Markus, S.M., 2015. The dynein cortical anchor Num1 activates dynein motility by relieving Pac1/LIS1-mediated inhibition. *The Journal of cell biology*, 211(2), pp.309–22.
Van Langenhove, T., van der Zee, J. & Van Broeckhoven, C., 2012. The molecular basis of the frontotemporal lobar degeneration-amyotrophic lateral sclerosis spectrum. *Annals of medicine*, 44(8), pp.817–28.
Lattante, S. et al., 2015. Defining the genetic connection linking amyotrophic lateral sclerosis (ALS) with frontotemporal dementia (FTD). *Trends in Genetics*, 31(5), pp.263–273.
Lattante, S., Rouleau, G.A. & Kabashi, E., 2013. TARDBP and FUS Mutations Associated with Amyotrophic Lateral Sclerosis: Summary and Update. *Human Mutation*, 34(6), pp.812–826.
Lee, J. et al., 2014. Nucleolar dysfunction in Huntington's disease. *Biochimica et Biophysica Acta - Molecular Basis of Disease*, 1842(6), pp.785–790.
Lerga, A. et al., 2001. Identification of an RNA Binding Specificity for the Potential Splicing Factor TLS. *Journal of Biological Chemistry*, 276(9), pp.6807–6816.
Levine, T.P. et al., 2013. The product of C9orf72, a gene strongly implicated in neurodegeneration, is structurally related to DENN Rab-GEFs. *Bioinformatics*, 29(4), pp.499–503.
Lindig, T. et al., 2015. Gray and white matter alterations in hereditary spastic paraplegia type SPG4 and clinical correlations. *Journal of Neurology*, 262(8), pp.1961–1971.
Ling, S.C., Polymenidou, M. & Cleveland, D.W., 2013. Converging mechanisms in als and FTD: Disrupted RNA and protein homeostasis. *Neuron*, 79(3), pp.416–438.
Luigetti, M. et al., 2016. Charcot-Marie-Tooth type 2 and distal hereditary motor neuropathy: Clinical, neurophysiological and genetic findings from a single-centre experience. *Clinical Neurology and Neurosurgery*, 144, pp.67–71.
Lukavsky, P.J. et al., 2013. Molecular basis of UG-rich RNA recognition by the human splicing factor TDP-43. *Nature Publishing Group*, 20(12), pp.1443–1449.
Luthe, D.S., 1983. A simple technique for the preparation and storage of sucrose gradients. *Analytical Biochemistry*, 135(1), pp.230–232.
Madabhushi, R., Pan, L. & Tsai, L.-H., 2014. DNA Damage and Its Links to Neurodegeneration. *Neuron*, 83(2), pp.266–282.

Majounie, E. et al., 2012. Frequency of the C9orf72 hexanucleotide repeat expansion in patients with amyotrophic lateral sclerosis and frontotemporal dementia: A cross-sectional study. *The Lancet Neurology*, 11(4), pp.323–330.
Marangi, G. & Traynor, B.J., 2015. Genetic causes of amyotrophic lateral sclerosis: New genetic analysis methodologies entailing new opportunities and challenges. *Brain Research*, 1607, pp.75–93.
Mastrocola, A.S. et al., 2013. The RNA-binding protein fused in sarcoma (FUS) functions downstream of poly(ADP-ribose) polymerase (PARP) in response to DNA damage. *Journal of Biological Chemistry*, 288(34), pp.24731–24741.
Matanis, T. et al., 2002. Bicaudal-D regulates COPI-independent Golgi-ER transport by recruiting the dynein-dynactin motor complex. *Nat Cell Biol*, 4(12), pp.986–992.
McDonold, C.M. & Fromme, J.C., 2014. Four GTPases differentially regulate the Sec7 Arf-GEF to direct traffic at the trans-golgi network. *Developmental cell*, 30(6), pp.759–67.
McGoldrick, P. et al., 2013. Rodent models of amyotrophic lateral sclerosis. *Biochimica et biophysica acta*, 1832(9), pp.1421–36.
Mckenney, R.J. et al., 2014. Activation of cytoplasmic dynein motility by dynactin-cargo adapter complexes. , 345(6194), pp.337–342.
McKenney, R.J. et al., 2010. LIS1 and NudE induce a persistent dynein force-producing state. *Cell*, 141(2), pp.304–314. McKeown, P.C. & Shaw, P.J., 2009. Chromatin: Linking structure and function in the nucleolus. *Chromosoma*, 118(1), pp.11–23.
Meiri, D. et al., 2014. Mechanistic insight into GPCR-mediated activation of the microtubule-associated RhoA exchange factor GEF-H1. *Nature communications*, 5, p.4857.
Menezes, M.P. et al., 2016. Pathophysiology of motor dysfunction in a childhood motor neuron disease caused by mutations in the riboflavin transporter. *Clinical Neurophysiology*, 127(1), pp.911–918.
Milanese, M. et al., 2011. Abnormal exocytotic release of glutamate in a mouse model of amyotrophic lateral sclerosis. *Journal of Neurochemistry*, 116(6), pp.1028–1042.
Minton, K., 2014. Molecular motors: Hook-ing up early endosomes. *Nature Reviews Molecular Cell Biology*, 15(5), pp.297–297.
Mitchell, J.C. et al., 2013. Overexpression of human wild-type FUS causes progressive motor neuron degeneration in an age- and dose-dependent fashion. *Acta Neuropathologica*, 125(2), pp.273–288.
Morlando, M. et al., 2012. FUS stimulates microRNA biogenesis by facilitating co-transcriptional Drosha recruitment. *The EMBO journal*, 31(24), pp.4502–10.
Morris, J., 2015. Amyotrophic Lateral Sclerosis (ALS) and Related Motor Neuron Diseases: An Overview. *The Neurodiagnostic journal*, 55(3), pp.180–94.
Muley, S.A. & Parry, G.J., 2012. Multifocal motor neuropathy. *Journal of Clinical Neuroscience*, 19(9), pp.1201–1209.
Muresan, V. & Ladescu Muresan, Z., 2016. Shared Molecular Mechanisms in Alzheimer's Disease and Amyotrophic Lateral Sclerosis: Neurofilament-Dependent Transport of sAPP, FUS, TDP-43 and SOD1, with Endoplasmic Reticulum-Like Tubules. *Neurodegenerative Diseases*, 16(1-2), pp.55–61.

Nalini, A., Lokesh, L. & Ratnavalli, E., 2004. Familial monomelic amyotrophy: A case report from India. *Journal of the Neurological Sciences*, 220(1-2), pp.95–98.
Neveling, K. et al., 2013. Mutations in BICD2, which encodes a golgin and important motor adaptor, cause congenital autosomal-dominant spinal muscular atrophy. *American journal of human genetics*, 92(6), pp.946–954.
Nishimoto, Y. et al., 2013. The long non-coding RNA nuclear-enriched abundant transcript 1_2 induces paraspeckle formation in the motor neuron during the early phase of amyotrophic lateral sclerosis. *Molecular Brain*, 6(1), p.1.
Oates, E.C. et al., 2013. Mutations in BICD2 Cause Dominant Congenital Spinal Muscular Atrophy and Hereditary Spastic Paraplegia. *American journal of human genetics*, 92(6), pp.965–73.
Olson, M.O.J., Dundr, M. & Szebeni, A., 2000. The nucleolus: An old factory with unexpected capabilities. *Trends in Cell Biology*, 10(5), pp.189–196.
Ori-McKenney, K.M. & Vallee, R.B., 2011. Neuronal migration defects in the Loa dynein mutant mouse. *Neural Development*, 6(1), p.26.
Otsu, N., 1979. A Threshold Selection Method from Gray-Level Histograms. *IEEE Transactions on Systems, Man, and Cybernetics*, 9(1), pp.62–66.
Ou, S.H. et al., 1995. Cloning and characterization of a novel cellular protein, TDP-43, that binds to human immunodeficiency virus type 1 TAR DNA sequence motifs. *Journal of virology*, 69(6), pp.3584–3596.
Padeken, J. & Heun, P., 2014. Nucleolus and nuclear periphery: Velcro for heterochromatin. *Current Opinion in Cell Biology*, 28(1), pp.54–60.
Palazzo, A., Ackerman, B. & Gundersen, G.G., 2003. Tubulin acetylation and cell motility. *Nature*, 421(6920), p.230.
Palazzo, A.F. et al., 2001. Cdc42, dynein, and dynactin regulate MTOC reorientation independent of Rho-regulated microtubule stabilization. *Current Biology*, 11(19), pp.1536–1541.
Palmer, K.J., Hughes, H. & Stephens, D.J., 2009. Specificity of Cytoplasmic Dynein Subunits in Discrete Membrane-trafficking Steps. *Molecular Biology of the Cell*, 20(11), pp.2885–2899.
Pareyson, D. & Marchesi, C., 2009. Diagnosis, natural history, and management of Charcot-Marie-Tooth disease. *The Lancet Neurology*, 8(7), pp.654–667.
Paul, L.K. et al., 2014. Agenesis of the corpus callosum and autism: A comprehensive comparison. *Brain*, 137(6), pp.1813–1829.
Philips, T. & Rothstein, J.D., 2014. Glial cells in amyotrophic lateral sclerosis. *Experimental Neurology*, 262(PB), pp.111–120.
Polymenidou, M. et al., 2011. Long pre-mRNA depletion and RNA missplicing contribute to neuronal vulnerability from loss of TDP-43 splicing of an intron within the 3′ untranslated region of its own transcript, thereby triggering nonsense mediated RNA degradation. (147 words). *Nature Neuroscience*, 14(4), pp.459–68.
Prasanth, K. V. et al., 2005. Regulating gene expression through RNA nuclear retention. *Cell*, 123(2), pp.249–263.
Quassollo, G. et al., 2015. A RhoA signaling pathway regulates dendritic Golgi outpost formation. *Current Biology*, 25(8), pp.971–982.
Ratti, A. & Buratti, E., 2016. Physiological Functions and Pathobiology of TDP-43 and FUS/TLS proteins. *Journal of Neurochemistry*, p.n/a–n/a.
Ravits, J., 2014. Focality, stochasticity and neuroanatomic propagation in ALS pathogenesis. *Experimental Neurology*, 262(PB), pp.121–126.

Renton, A.E. et al., 2011. A hexanucleotide repeat expansion in C9ORF72 is the cause of chromosome 9p21-linked ALS-FTD. *Neuron*, 72(2), pp.257–68
Renton, A.E., Chiò, A. & Traynor, B.J., 2014. State of play in amyotrophic lateral sclerosis genetics. *Nature neuroscience*, 17(1), pp.17–23.
Reyes-aldasoro, C.C., Barri, M. & Hafezparast, M., 2015. Automatic segmentation of focal adhesions from mouse embryonic fibroblasts. *ISBI*, 12, pp.548–551.
Ringholz, G.M. et al., 2005. Prevalence and patterns of cognitive impairment in sporadic ALS. *Neurology*, 65(4), pp.586–590.
Rios, R., 2014. The centrosome–Golgi apparatus nexus. *Philos Trans R Soc Lond B Biol Sci.* 369 (1650).
Roberts, A.J. et al., 2013. Functions and mechanics of dynein motor proteins. *Nature reviews. Molecular cell biology*, 14(11), pp.713–26.
Rosen, D.R. et al., 1993. Mutations in Cu/Zn superoxide dismutase gene are associated with familial amyotrophic lateral sclerosis. *Nature*, 362(6415), pp.59–62.
Rossi, S., Cozzolino, M. & Carrì, M.T., 2016. Old versus new mechanisms in the pathogenesis of ALS. *Brain Pathology*, 26(78), pp.276–286.
Rossor, A.M. et al., 2015. Phenotypic and molecular insights into spinal muscular atrophy due to mutations in BICD2. *Brain : a journal of neurology*, 138(Pt 2), pp.293–310.
Rothstein, J.D. et al., 1993. Chronic inhibition of glutamate uptake produces a model of slow neurotoxicity. *Proceedings of the National Academy of Sciences of the United States of America*, 90(July), pp.6591–6595.
Rulten, S.L. et al., 2013. PARP-1 dependent recruitment of the amyotrophic lateral sclerosis-associated protein FUS/TLS to sites of oxidative DNA damage. *Nucleic acids research*, pp.1–8
Sainath, R. & Gallo, G., 2014. The dynein inhibitor Ciliobrevin D inhibits the bidirectional transport of organelles along sensory axons and impairs NGF-mediated regulation of growth cones and axon branches. *Developmental neurobiology*, 75, pp.757–777.
Sasaki, S. et al., 2000. A LIS1/NUDEL/cytoplasmic dynein heavy chain complex in the developing and adult nervous system. *Neuron*, 28(3), pp.681–696.
Sasaki, S. et al., 2010. Alterations in subcellular localization of TDP-43 immunoreactivity in the anterior horns in sporadic amyotrophic lateral sclerosis. *Neuroscience Letters*, 478(2), pp.72–76.
Sasaki, S. et al., 2005. Complete Loss of Ndel1 Results in Neuronal Migration Defects and Early Embryonic Lethality. *Molecular and cellular biology*, 25(17), pp.7812–7827.
Scheffer, H., 2004. Spinal muscular atrophy. *Methods in molecular medicine*, 92(2), pp.343–358.
Schiavo, G. et al., 2013. Cytoplasmic dynein heavy chain: the servant of many masters. *Trends in neurosciences*, 36(11), pp.1–11.
Schofield, A. V., Steels, R. & Bernard, O., 2012. Rho-associated coiled-coil kinase (ROCK) protein controls microtubule dynamics in a novel signaling pathway that regulates cell migration. *Journal of Biological Chemistry*, 287(52), pp.43620–43629.
Schreiber, V. et al., 2002. Poly(ADP-ribose) polymerase-2 (PARP-2) is required for efficient base excision DNA repair in association with PARP-1 and XRCC1. *Journal of Biological Chemistry*, 277(25), pp.23028–23036.
Schreij, A.M. a, Fon, E. a. & McPherson, P.S., 2015. Endocytic membrane

trafficking and neurodegenerative disease. *Cellular and Molecular Life Sciences*, 73(8), pp.1–17.
Scoto, M. et al., 2015. Novel mutations expand the clinical spectrum of DYNC1H1 -associated spinal muscular atrophy. *Neurology*, 84, pp.668–679.
Sephton, C.F. et al., 2010. TDP-43 is a developmentally regulated protein essential for early embryonic development. *Journal of Biological Chemistry*, 285(9), pp.6826–6834.
Shan, X. et al., 2010. Altered distributions of Gemini of coiled bodies and mitochondria in motor neurons of TDP-43 transgenic mice. *Proceedings of the National Academy of Sciences*, 107(37), pp.16325–16330.
Shang, Y. & Huang, E.J., 2016. Mechanisms of FUS mutations in familial amyotrophic lateral sclerosis. *Brain Research*.
Shelkovnikova, T.A. et al., 2014. Compromised paraspeckle formation as a pathogenic factor in FUSopathies. *Human Molecular Genetics*, 23(9), pp.2298–2312.
Sieben, A. et al., 2012. The genetics and neuropathology of frontotemporal lobar degeneration. *Acta Neuropathologica*, 124(3), pp.353–372.
Singh, R.K. & Cooper, T.A., 2012. Pre-mRNA splicing in disease and therapeutics. *Trends in Molecular Medicine*, 18(8), pp.472–482.
Smethurst, P., Sidle, K.C.L. & Hardy, J., 2015. Review: Prion-like mechanisms of transactive response DNA binding protein of 43 kDa (TDP-43) in amyotrophic lateral sclerosis (ALS). *Neuropathology and Applied Neurobiology*, 41(5), pp.578–597.
Smith, B.N. et al., 2014. Exome-wide rare variant analysis identifies TUBA4A mutations associated with familial ALS. *Neuron*, 84(2), pp.324–331.
Smith, R. et al., 2014. Nervous translation, do you get the message? A review of mRNPs, mRNA-protein interactions and translational control within cells of the nervous system. *Cellular and molecular life sciences : CMLS*, 71(20), pp.3917–3937.
Soldati, T. & Schliwa, M., 2006. Powering membrane traffic in endocytosis and recycling. *Nature reviews. Molecular cell biology*, 7(12), pp.897–908.
Sorkin, A. & von Zastrow, M., 2009. Endocytosis and signalling: intertwining molecular networks. *Nature reviews. Molecular cell biology*, 10(9), pp.609–22.
Sreedharan, J. et al., 2008. TDP-43 Mutations in Familial and Sporadic Amyotrophic Lateral Sclerosis. *Science*, 249(March), pp.1668–1672.
Štalekar, M. et al., 2015. Proteomic analyses reveal that loss of TDP-43 affects RNA processing and intracellular transport. *Neuroscience*, 293, pp.157–170.
Stallings, N.R. et al., 2010. Progressive motor weakness in transgenic mice expressing human TDP-43. *Neurobiology of Disease*, 40(2), pp.404–414.
Stępnik, M. et al., 2015. The modulating effect of ATM, ATR, DNA-PK inhibitors on the cytotoxicity and genotoxicity of benzo[a]pyrene in human hepatocellular cancer cell line HepG2. *Environmental Toxicology and Pharmacology*, 40(3), pp.988–996.
Stewart, H. et al., 2012. Clinical and pathological features of amyotrophic lateral sclerosis caused by mutation in the C9ORF72 gene on chromosome 9p. *Acta Neuropathologica*, 123(3), pp.409–417.
Strickland, A. V et al., 2015. Mutation screen reveals novel variants and expands the phenotypes associated with DYNC1H1. *Journal of neurology*.

Swarup, V. et al., 2011. Pathological hallmarks of amyotrophic lateral sclerosis/frontotemporal lobar degeneration in transgenic mice produced with TDP-43 genomic fragments. *Brain : a journal of neurology*, 134(Pt 9), pp.2610–26.
Szafranski, K., Abraham, K.J. & Mekhail, K., 2015. Non-coding RNA in neural function, disease, and aging. *Frontiers in Genetics*, 5(FEB), pp.1–16.
Takahama, K. et al., 2013. Regulation of telomere length by G-quadruplex telomere DNA- and TERRA-binding protein TLS/FUS. *Chemistry and Biology*, 20(3), pp.341–350.
Takesono, A. et al., 2010. Microtubules regulate migratory polarity through Rho/ROCK signaling in T cells. *PloS one*, 5(1), p.e8774.
Tan, A.Y. & Manley, J.L., 2010. TLS inhibits RNA polymerase III transcription. *Molecular and Cellular Biology*, 30(1), pp.186–196.
Thyberg, J. & Moskalewski, S., 1993. Relationship between the Golgi complex and microtubules enriched in detyrosinated or acetylated aphla tubulin: studies on cells recovering from nocodazole and cells in the terminal phase of cytokinesis. *Cell & Tissue Research*, 273, pp.457–466.
Timme, W., 1917. Progressive muscular dystrophy as an endocrine disease. *Archives of Internal Medicine*, XIX(1), pp.79–104.
Tisdale, S. & Pellizzoni, L., 2015. Disease Mechanisms and Therapeutic Approaches in Spinal Muscular Atrophy. *Journal of Neuroscience*, 35(23), pp.8691–8700.
Todd, T.W. & Petrucelli, L., 2016. Insights into the pathogenic mechanisms of Chromosome 9 open reading frame 72 (C9orf72) repeat expansions. *Journal of Neurochemistry*, p.n/a–n/a
Tollervey, J.R. et al., 2011. Characterising the RNA targets and position-dependent splicing regulation by TDP-43; implications for neurodegenerative diseases. *Nature Neuroscience*, 14(4), pp.452–8.
Toropova, K. et al., 2014. Lis1 regulates dynein by sterically blocking its mechanochemical cycle. *eLife*, 3, p.e03372
Tresini, M. et al., 2015. The core spliceosome as target and effector of non-canonical ATM signalling. *Nature*, 523(7558), pp.53–58.
Tsai, K.-J. et al., 2010. Elevated expression of TDP-43 in the forebrain of mice is sufficient to cause neurological and pathological phenotypes mimicking FTLD-U. *The Journal of experimental medicine*, 207(8), pp.1661–1673.
Turinetto, V. et al., 2009. The cyclin-dependent kinase inhibitor 5, 6-dichloro-1-beta-D-ribofuranosylbenzimidazole induces nongenotoxic, DNA replication-independent apoptosis of normal and leukemic cells, regardless of their p53 status. *BMC cancer*, 9, p.281.
Udagawa, T. et al., 2015. FUS regulates AMPA receptor function and FTLD/ALS-associated behaviour via GluA1 mRNA stabilization. *Nature communications*, 6(May), p.7098.
Uday Bhanu, M. & Kondapi, A.K., 2010. Neurotoxic activity of a topoisomerase-I inhibitor, camptothecin, in cultured cerebellar granule neurons. *Neurotoxicology*, 31(6), pp.730–7.
Umar, T. & Hoda, N. ul, 2015. Selective inhibitors of phosphodiesterases: therapeutic promise for neurodegenerative disorders. *Med. Chem. Commun.*, 6, pp.2063–2080. Urnavicius, L. et al., 2015. The structure of the dynactin complex and its interaction with dynein. *Science*, 347(6229), pp.1441–1446.
Valentine, J.S., Doucette, P.A. & Zittin Potter, S., 2005. Copper-Zinc

Superoxide Dismutase and Amyotrophic Lateral Sclerosis. *Annual Review of Biochemistry*, 74(1), pp.563–593.
Vance, C. et al., 2009. Mutations in FUS, an RNA Processing Protein, Cause Familial Amyotrophic Lateral Sclerosis Type 6. *Science*, 323(5918), pp.1208–11.
Verbeeck, C. et al., 2012. Expression of Fused in sarcoma mutations in mice recapitulates the neuropathology of FUS proteinopathies and provides insight into disease pathogenesis. *Molecular Neurodegeneration*, 7(1), p.1. Available at: Molecular Neurodegeneration\npapers2://publication/doi/10.1186/1750-1326-7-53.
Vibha, D. et al., 2015. Clinical profile of Monomelic Amyotrophy (MMA) and role of persistent viral infection. *Journal of the Neurological Sciences*, 359(1-2), pp.4–7. Available at: http://dx.doi.org/10.1016/j.jns.2015.10.026.
Visser, J., de Jong, J.M.B.V. & de Visser, M., 2008. The history of progressive muscular atrophy: syndrome or disease? *Neurology*, 70(9), pp.723–727.
Vissers, L.E.L.M. et al., 2010. A de novo paradigm for mental retardation. *Nature Genetics*, 42(12), pp.1109–1112.
Vlam, L. et al., 2015. Cytokine profiles in multifocal motor neuropathy and progressive muscular atrophy. *Journal of Neuroimmunology*, 286, pp.1–4.
Wachtler, F. & Stahl, A., 1993. The Nucleolus : A Structural and Functional Interpretation. , 24(5), pp.473–505.
Wahl, M.C., Will, C.L. & Lührmann, R., 2009. The Spliceosome: Design Principles of a Dynamic RNP Machine. *Cell*, 136(4), pp.701–718.
Wang, X. et al., 2008. Induced ncRNAs allosterically modify RNA-binding proteins in cis to inhibit transcription. *Nature*, 454(7200), pp.126–30.
Wang, X., Schwartz, J.C. & Cech, T.R., 2015. Nucleic acid-binding specificity of human FUS protein. *Nucleic Acids Research*, 43(15), pp.7535–7543.
Ward, C.L. et al., 2014. A loss of FUS/TLS function leads to impaired cellular proliferation. *Cell death & disease*, 5(12), p.e1572.
Warraich, S.T. et al., 2010. TDP-43: A DNA and RNA binding protein with roles in neurodegenerative diseases. *International Journal of Biochemistry and Cell Biology*, 42(10), pp.1606–1609.
Wegorzewska, I. et al., 2009. TDP-43 mutant transgenic mice develop features of ALS and frontotemporal lobar degeneration. *Proceedings of the National Academy of Sciences of the United States of America*, 106(44), pp.18809–14.
Wheaton, M.W. et al., 2007. Cognitive impairment in familial ALS. *Neurology*, 69(14), pp.1411–1417.
Wils, H. et al., 2010. TDP-43 transgenic mice develop spastic paralysis and neuronal inclusions characteristic of ALS and frontotemporal lobar degeneration. *Proceedings of the National Academy of Sciences of the United States of America*, 107(8), pp.3858–3863.
Wu, L.S., Cheng, W.C. & Shen, C.K.J., 2012. Targeted depletion of TDP-43 expression in the spinal cord motor neurons leads to the development of amyotrophic lateral sclerosis-like phenotypes in mice. *Journal of Biological Chemistry*, 287(33), pp.27335–27344.
Wu, P. et al., 2013. Roles of long noncoding RNAs in brain development, functional diversification and neurodegenerative diseases. *Brain Research Bulletin*, 97, pp.69–80. Xiang, X. et al., 2015. Cytoplasmic dynein and early endosome transport. *Cellular and molecular life sciences : CMLS*.
Xiao, S. et al., 2015. Isoform-specific antibodies reveal distinct subcellular

localizations of C9orf72 in amyotrophic lateral sclerosis. *Annals of Neurology*, 78(4), pp.568–583.
Xu, Y., Zhang, H.-T. & O'Donnell, J.M., 2011. Phosphodiesterases in the Central Nervous System: Implications in Mood and Cognitive Disorders. In H. S. Francis, M. Conti, & D. M. Houslay, eds. *Phosphodiesterases as Drug Targets*. Berlin, Heidelberg: Springer Berlin Heidelberg, pp. 447–485.
Xu, Y.-F. et al., 2011. Expression of mutant TDP-43 induces neuronal dysfunction in transgenic mice. *Molecular Neurodegeneration*, 6(1), p.73.
Xu, Y.-F. et al., 2010. Wild-Type Human TDP-43 Expression Causes TDP-43 Phosphorylation, Mitochondrial Aggregation, Motor Deficits, and Early Mortality in Transgenic Mice. *Journal of Neuroscience*, 30(32), pp.10851–10859.
Yadav, S. & Linstedt, A.D., 2011. Golgi positioning. *Cold Spring Harbor Perspectives in Biology*, 3(5), pp.1–17.
Yadav, S., Puri, S. & Linstedt, A.D., 2009. A Primary Role for Golgi Positioning in Directed Secretion, Cell Polarity, and Wound Healing. *Molecular biology of the cell*, 20, pp.1728–1736.
Yadav, S., Puthenveedu, M. a. & Linstedt, A.D., 2012. Golgin160 Recruits the Dynein Motor to Position the Golgi Apparatus. *Developmental Cell*, 23(1), pp.153–165.
Yang, L. et al., 2014. Self-assembled FUS binds active chromatin and regulates gene transcription. *Proceedings of the National Academy of Sciences of the United States of America*, 111(50), pp.17809–14. Yasuda, K. et al., 2013. The RNA-binding protein Fus directs translation of localized mRNAs in APC-RNP granules. *The Journal of cell biology*, 203(5), pp.737–46. Yoshimura, Y. & Miki, H., 2011. Dynamic regulation of GEF-H1 localization at microtubules by Par1b/MARK2. *Biochemical and Biophysical Research Communications*, 408(2), pp.322–328.
Yu, Y. & Reed, R., 2015. FUS functions in coupling transcription to splicing by mediating an interaction between RNAP II and U1 snRNP. *Proceedings of the National Academy of Sciences of the United States of America*, 112(28), pp.8608–8613.
Yu, Z. et al., 2012. Neurodegeneration-associated TDP-43 interacts with fragile X mental retardation protein (FMRP)/staufen (STAU1) and regulates SIRT1 expression in neuronal cells. *Journal of Biological Chemistry*, 287(27), pp.22560–22572.
Zelko, I.N., Mariani, T.J. & Folz, R.J., 2002. Superoxide dismutase multigene family: A comparison of the CuZn-SOD (SOD1), Mn-SOD (SOD2), and EC-SOD (SOD3) gene structures, evolution, and expression. *Free Radical Biology and Medicine*, 33(3), pp.337–349.
Zhou, Y. et al., 2013. ALS-Associated FUS Mutations Result in Compromised FUS Alternative Splicing and Autoregulation. *PLoS Genetics*, 9(10).